Info-gap robustness assessment of reliability evaluations for the safety of critical industrial systems

Antoine Ajenjo

THÈSE DE DOCTORAT DE L'ÉTABLISSEMENT UNIVERSITÉ BOURGOGNE FRANCHE-COMTÉ

PRÉPARÉE À L'UNIVERSITÉ DE FRANCHE-COMTÉ

École doctorale n° 37

École Doctorale de Sciences Physiques pour l'Ingénieur et Microtechniques (ED SPIM)

Doctorat de Sciences pour l'Ingénieur

Par

M. Antoine AJENJO
Ingénieur SIGMA Clermont

Analyse info-gap de la robustesse d'évaluations fiabilistes pour la sûreté de systèmes industriels critiques

–

Info-gap robustness assessment of reliability evaluations for the safety of critical industrial systems

Thèse présentée et soutenue à Besançon, le 15 novembre 2022.

Composition du Jury :

Dr. François HEMEZ	Directeur de recherche, LLNL	Rapporteur
Pr. Jérôme MORIO	Directeur de recherche, ONERA & ISAE Toulouse	Rapporteur
Pr. Anas BATOU	Professeur des universités, Université Gustave Eiffel	Examinateur
Pr. Pierre-Alain BOUCARD	Professeur des universités, Université Paris-Saclay	Président
M. Emmanuel ARDILLON	Ingénieur Chercheur, EDF R&D	Co-encadrant
Dr. Vincent CHABRIDON	Ingénieur Chercheur, EDF R&D	Co-encadrant
Dr. Scott COGAN	Chargé de recherche, CNRS, UFC	Codirecteur de thèse
Dr. Emeline SADOULET-REBOUL	Maître de conférences, UFC	Codirectrice de thèse

Remerciements / Acknowledgements

Ces remerciements viennent clôturer, non sans émotion, un travail de trois ans qui représente un moment de ma vie à forte intensité.

Je souhaite exprimer en premier lieu mes profonds remerciements pour les quatre personnes, hors équipe encadrante, qui m'ont fait l'honneur de composer mon jury. Tout d'abord, je suis extrêmement reconnaissant envers mes deux rapporteurs, Messieurs François Hemez et Jérôme Morio, pour avoir accepté ce rôle. La lecture de ces deux rapports fut un moment très agréable par la bienveillance, la précision et l'expertise ressenties à travers vos questions, remarques et conseils. Nos échanges durant la soutenance n'ont qu'amplifié ce ressenti. Monsieur Pierre-Alain Boucard, vous avoir eu comme président du jury est un honneur. Je vous remercie vivement d'avoir accepté cette responsabilité et d'avoir animé cette soutenance. J'ai particulièrement apprécié vos remarques et questions pertinentes. Finalement, j'aimerais également remercier Monsieur Anas Batou pour l'intérêt porté sur ce travail et l'échange qui s'en est suivi. J'ai conscience du temps que cet exercice vous a demandé. En cette période durant laquelle les communications en présentiel ont été réduites, avoir eu la possibilité de confronter mes travaux de recherche à de tels experts demeurera un moment inoubliable et particulièrement enrichissant.

Il est maintenant temps pour moi d'exprimer toute ma gratitude envers mon équipe encadrante, sans qui ce travail n'aurait pas abouti. Mes premiers remerciements se dirigent vers mon codirecteur et ma codirectrice de thèse, Scott Cogan et Emeline Sadoulet-Reboul.

Scott, collaborer avec toi a été une expérience particulièrement enrichissante. J'ai toujours ressenti, à travers nos divers échanges, une manière unique de voir les choses avec des réflexions et propositions aussi pertinentes qu'originales. Merci de m'avoir apporté cette expertise et cette vision si particulière qui, finalement, représente une composante majeure de la recherche.

Emeline, au-delà de ton apport scientifique, tu as représenté pour moi un soutien moral considérable. Malgré un encadrement majoritairement distanciel, tu as toujours su trouver les justes mots en fonction de mes différentes phases et humeurs. Cela témoigne de ta bienveillance et de ton engagement total sur ce travail. A chacune de mes venues à Besançon, tu as systématiquement fait en sorte que je m'intègre du mieux possible.

Merci à tous les deux pour m'avoir apporté un encadrement si complet, malgré la distance. J'ai conscience des efforts que cela a pu représenter. Si j'ai passé la majorité de ma thèse en entreprise, je reste convaincu que l'environnement proposé par le FEMTO-ST et par votre encadrement est une aubaine pour tout doctorant.

J'aimerais maintenant adresser mes remerciements envers mes encadrants industriels.

Emmanuel, tu es celui qui a amené info-gap à PRISME. Tu m'as tout d'abord offert la possibilité d'effectuer mon stage de fin d'étude sous ton aile. C'est ce stage, par son contenu scientifique, l'environnement de travail et l'encadrement que tu m'as offert, qui m'a convaincu de me jeter à l'eau avec cette thèse. Je te suis extrêmement reconnaissant de m'avoir fait confiance pour cette grande aventure commune. Merci pour tous nos échanges qui ont permis d'aboutir à ce travail. Ce fut un réel plaisir que d'avoir été ton stagiaire, ton co-bureau, ton doctorant, et maintenant ton collègue.

Vincent, ces quelques lignes ne peuvent décrire toute la gratitude que je ressens d'avoir parcouru ce chemin avec toi. Ton encadrement a représenté pour moi un support crucial. Que ce soit par ton apport scientifique, ta passion, ta rigueur rédactionnelle, ton soutien moral ou encore ton aide pour mon insertion professionnelle, tu t'es démené. Tout en me laissant de l'autonomie, tu as veillé en permanence à mon bien-être durant cette épreuve et tu as su, je ne sais comment,

déceler mes phases descendantes pour me redonner de la confiance et de la motivation. Merci pour ton soutien infaillible.

Bertrand, tu as apporté bien plus que l'encadrement supposé lointain qui était convenu. Ton rôle a été déterminant dans la poursuite et la conclusion de ce travail. Ton expérience et ton efficacité ont permis d'éviter bon nombre d'obstacles. Tu as représenté une pièce maîtresse dans le bon déroulement du double encadrement et pour la prise des bonnes décisions aux bons moments. Je te suis extrêmement reconnaissant d'avoir joué ce rôle.

Merci à tous les cinq pour avoir sans cesse fait en sorte que ce double encadrement se traduise en une force pour moi et non une contrainte.

Je souhaiterais à présent remercier les deux chefs de groupe que j'ai côtoyés durant la poursuite de cette thèse. Tout d'abord, je remercie Soufien Hourrig pour m'avoir accordé cette opportunité en faisant confiance à moi et mes encadrants. Enfin, merci à Bruno Marque pour avoir pris le temps de comprendre mes travaux de thèse et, surtout, pour m'avoir intégré dans son équipe en tant qu'ingénieur chercheur.

J'ai eu la chance durant cette thèse, bien que de manière déséquilibrée, d'appartenir à deux environnements scientifiques propices à la poursuite d'une thèse et dans lesquels j'ai rencontré beaucoup de personnes qui, d'une manière ou d'une autre, ont contribué à mon bien-être. Tout d'abord, je remercie Delphine pour m'avoir aidé avec les tâches administratives en faisant preuve de beaucoup de patience et de bienveillance. J'aimerais ensuite remercier plus globalement l'ensemble de l'équipe du DMA de l'institut FEMTO-ST pour m'avoir si bien accueilli à chacun de mes passages. Merci à Gaël pour m'avoir intégré aux divers échanges du groupe. Merci à Pauline pour avoir organisé deux séminaires durant lesquels j'ai pu présenter mes travaux. J'adresse également mes remerciements envers Betty et Justine pour le travail considérable qui a été réalisé sur les différentes métriques de robustesse. Enfin, je tiens à remercier Emmanuel, Kevin et Ludovic qui ont particulièrement œuvré à ma bonne intégration et qui m'ont fait découvrir les plus beaux endroits (suivant certains critères) de cette magnifique ville qu'est Besançon.

Il est maintenant temps pour moi de remercier toutes les personnes qui font du site EDF de Chatou, et particulièrement du Bâtiment S, un endroit d'épanouissement professionnel pour tout doctorant. La qualité scientifique jumelée à la bienveillance générale des personnes que j'ai pu rencontrer sont les raisons principales de mon envie de faire cette thèse et de poursuivre l'aventure. Merci à Aurélie, Morgane, Charlène et Angélique pour votre aide précieuse sur les aspects RH et administratifs. Un grand merci à Thomas Prusek pour le temps que tu as pris à m'expliquer le fonctionnement de CATHARE. Merci également à Rachid Boulbaroud pour ta réactivité impressionnante concernant les aspects informatiques. Merci à Thibault pour avoir hébergé cette thèse au sein du projet VIGIE. Je remercie de manière générale l'ensemble du groupe P17 dans lequel c'est un plaisir et un honneur de faire partie. Merci aux anciens doctorants, Alvaro, Jérôme, Pablo, Paul, Thomas, qui ont montré la voie de l'excellence (et du bar) et qui ont facilité notre intégration en tant que stagiaires. Merci également à Claire, Elias, Julien, Laura, Marouane, Théo et tous ceux avec qui j'ai pu discuter autour d'un verre ou d'un café. Je poursuis en remerciant la fantastique équipe des stagiaires, Anne, Cardi P., Louis, Mathilde et les autres pour tous ces moments échangés. J'adresse des mentions spéciales à Clément pour s'être accordé avec moi durant les différentes phases de la thèse, à Azénor que j'ai hâte de voir survoler sa soutenance comme elle survole la pétanque, à ma co-bureau en or Vanessa avec qui il fut si réconfortant de partager toutes nos détresses, et, enfin, à Sami pour ta générosité et ta gentillesse débordantes.

L'environnement professionnel est une variable clé dans la poursuite d'une thèse. Selon moi, l'environnement extra-professionnel l'est tout autant, en particulier durant une période pandémique amplifiant le phénomène d'isolement. Dans ce contexte, je suis particulièrement reconnaissant envers mon entourage.

Tout d'abord, je suis fier d'appartenir au G1béciles et d'avoir quand même pu venir à bout de cette thèse. Merci à Aminata, Coti, Diego, Fabian, Piglette, Riton, Simsim, Valen, Williwilli. Mention spéciale à Fanfan pour m'avoir prêté son voilier même si c'était en hiver et pour m'avoir suivi dans ce voyage à vélo menant à la découverte culturelle de Barcelone. Merci également à l'équipe du 29 et en particulier à Cacho et Nono. Que de fous rires à travers toutes ces réunions en distanciel. La d1 nous tend les bras. Vouloir pouvoir.

Un grand merci (non, merci à toi !) au Salsa Club. Elian, Hakima, Jagoda et Laura, vous n'imaginez pas le bien fou que me procure chacune de nos retrouvailles.

Enfin, je tiens à remercier tout mon groupe d'amis d'enfance, dont certains datent de l'école primaire. Clem, Mathilde, Max, Mikat, Noémie, Pedro, Thibault, j'espère maintenant avoir plus de temps pour vous voir, sachant qu'à chaque fois c'est un immense bonheur.

Je remercie à présent celle qui est apparue durant cette aventure comme un cadeau du ciel. Oriane, que ce soit confinés à Nanterre ou dans le désert à contempler les étoiles, tu as été durant cette période une source de bonheur et de réconfort inépuisable. Bien que ton rôle durant cette épreuve ait été primordial, ton influence positive sur moi va bien au-delà de la réussite de cette thèse. Merci pour tout ce que tu m'apportes.

Je clôture désormais ces remerciements avec une pensée particulière pour ma famille. Merci à ma sœur pour avoir fourni tous ces efforts dans la compréhension de mon sujet de thèse. Tu as été la première (peut-être la seule) personne extérieure à être capable de le faire. J'aimerais également exprimer toute ma gratitude envers mes parents pour m'avoir apporté durant toutes ces années une éducation et un soutien inconditionnel pour lesquels je me considère privilégié. Soutenir cette thèse devant vous fut un moment spécial.

Antoine Ajenjo

Contents

List of Figures

List of Tables

Acronyms

ANN	Artificial Neural Network
ASN	Autorité de Sûreté Nucléaire
BPA	Basic Probability Assignment
BE	Best Estimate
BEPU	Best Estimate Plus Uncertainty
CATHARE	Code Avancé de ThermoHydraulique pour les Accidents de Réacteurs à Eau
cdf	cumulative distribution function
CMC	Crude Monte Carlo
DS	Dempster Shafer
FISTARR	FORM-IS-Tested Automatically-Rapid seaRch
FORM	First-Order Reliability Method
HRA	Hybrid Reliability Analysis
HPT	Hydraulic Pressurized Test
IG	Info Gap
IBLOCA	Intermediate Break Loss-Of-Coolant Accident
IRSN	Institut de Radioprotection et de Sûreté Nucléaire
IS	Importance Sampling
LS	Line Sampling
LSF	Limit-State Function
LSS	Limit-State Surface
LSTF	Large Scale Test Facility
MCF	Multi-Constraints FORM
MPFP	Most Probable Failure Point
pdf	probability density function
PLI	Perturbed Law-based Indices
QoI	Quantity of Interest
RS	Random Set
SOA	State Of the Art
SORM	Second-Order Reliability Method
SS	Subset Simulation
VoI	Value of Information
w.r.t.	With Respect To

Notations

β_{IG}	info-gap opportuneness value
$\mathrm{Bel}\left(\cdot\right)$	belief function
$C\left(\mathbf{I}_{\mathbf{y}}, \boldsymbol{\rho}_{\mathbf{Y}}\right)$	convex model in the hyperrectangle $\mathbf{I}_{\mathbf{y}}$ with the correlation matrix $\boldsymbol{\rho}_{\mathbf{Y}}$
$\mathbf{e}$	vector of unknown variables
$\widetilde{\mathbf{e}}$	vector of nominal value of $\mathbf{e}$
$f_{\mathbf{X}}$	joint pdf of $\mathbf{X}$
$F_{\mathbf{X}}$	joint cdf of $\mathbf{X}$
$\underline{F_{\mathbf{X}}}$	lower cdf of $\mathbf{X}$
$\overline{F_{\mathbf{X}}}$	upper cdf of $\mathbf{X}$
$\Gamma\left(\cdot\right)$	random set function
h	horizon of uncertainty
h_{IG}	info-gap robustness value
$m\left(\cdot\right)$	mass function
$\mathcal{M}\left(\cdot\right)$	simulation model
$\mathrm{Nec}\left(\cdot\right)$	necessity function
$n_{\mathbf{X}}$	number of random variables
$n_{\mathbf{Y}}$	number of epistemic variables
$\boldsymbol{\nu}$	vector of deterministic input variables
$\mathrm{Pl}\left(\cdot\right)$	plausibility function
$\mathbb{P}$	probability measure
P_{f}	failure probability
$\mathrm{Pos}\left(\cdot\right)$	possibility function
π	possibility distribution function
ϕ	pdf of the Gaussian distribution
Φ	cdf of the Gaussian distribution
q^{β}	quantile of order β
Q^{β}	superquantile of order β
U	IG uncertainty model
$\mathbf{U}$	vector of random variables in the standard normal space
$\mathbf{X}$	vector of random variables
$\mathbf{Y}$	vector of epistemic variables
$\mathbb{1}\left(\cdot\right)$	indicator function

CHAPTER 1

Introduction

Contents

1.1 Context

Any industrial product, whatever its purpose and its application field, must meet several criteria based on performance and safety in order to be viable. The former requirement may rely on many different interpretations as it is jointly and freely defined by the entities related to the creation or the follow-up of the product. However, a generic feature is that it must provide added value compared to what already exists. Moreover, the permanent human demand for technological and societal improvements creates a state of industrial competitivity and the necessity to always perform better. This environment naturally leads to the emergence of more and more complex systems.

Breakthrough technologies in terms of performance rarely arise without safety concerns: international highly interconnected financial networks may lead to economical crises, information technology is accompanied by intensified security threats, civil nuclear activity could lead to catastrophic consequences if it was not controlled, etc. In addition, this evolving life environment must cohabitate with natural phenomena (natural by essence but not totally disconnected to human activity) for which the potentially disastrous impacts increase together with technological improvements if not controlled. This said, new technologies may also enable to limit disasters.

In order to pursue the global performance of industrial systems while guaranteeing acceptable safety levels, safety standards have for a long time been established in different forms. In most cases, such requirements are requested by higher institutions at national or even international levels such as the ASN (Autorité de Sûreté Nucléaire) and the IRSN (Institut de Radioprotection et de Sûreté Nucléaire) for the civil nuclear activities in France, mainly operated by Électricité de France (EDF) company.

Depending on the complexity of the studied industrial system, the performance and safety quantities of interest (QoI) may be multiple. For instance, the general performance of an airplane will depend on many factors such as its fuel consumption, its cost, its passenger capacity, etc. Similarly, a system may contain several critical components that possibly interact with each other on which individual safety requirements must be met. Commonly, the whole system is divided into subsystems on which more specific requirements are identified and evaluated. Whether it is for the performance or the safety assessments, it is therefore vital to find trustworthy ways to evaluate the QoIs of the system. Such evaluations may take place during the design phase as much as during the operating phase for decision making. To do so, the most straightforward option is to build prototypes and directly evaluate their behaviors under real conditions. Obviously, this approach faces some limits such as high costs and feasibility issues. As a consequence, digital twins based on physical and mathematical models as well as numerical solvers are needed (Tao et al., 2019).

In practice, simulation models represent idealizations of reality. Indeed, they face the presence of uncertainty in two different aspects (Oberkampf and Roy, 2010). The first one concerns the numerical model itself which evaluates one or several variables of interest. The current knowledge of physical laws is insufficient to model all sorts of engineering problems in an exact theoretical framework. Complex interactions are often simplified into behaviors for which models exist. In addition, even if the theoretical frawework is available, its evaluation often relies on approximate numerical solvers. The second aspect is related to the identification and the quantification of the input quantities that play a role on the evaluation of the variables of interest. It is clear that the presence of such uncertainties strongly interferes with performance and safety assessments of the system. Solutions must be found in order to take high-stake industrial decisions in this context of uncertainty.

A first deterministic approach to guarantee the safety of a system in such an uncertain context is to evaluate its response at worst-case scenarios or to apply penalized values. However, this implies that we know the configurations that correspond to these scenarios, which is not

always straightforward. Moreover, such a methodology may lead to overconservative systems since the worst-case scenario may be very dimensioning but hardly feasible in reality. Additionaly, being in an uncertain context does not mean that no information is available, strictly speaking. Subjective information such as expert knowledge is generally available to guide the analysis. Also, real data from experiments may narrow the quantification of some input variables. In that aspect, a very large amount of works have focused on ways to quantify and propagate uncertainty through simulation models in order to take decisions based on performance and safety in a meaningful way (Morio and Balesdent, 2015). The following section summarizes such framework.

1.2 The general uncertainty quantification framework

The framework of uncertainty quantification of simulation models is often represented as the so-called "ABC diagram" as depicted in Figure 1.1 (De Rocquigny et al., 2008). The first step (Step A) corresponds to the specification of the problem on which a decision must be taken. Safety-related decisions are generally based on codified norms which define the QoIs that are directly related to the variables of interest. As mentioned in the previous section, quantifying theses variables of interest often requires a simulation model which must find a balance between an acceptable idealization of the real (and potentially unknown) input-output relations and the required computational time. Moreover, the form of a simulation model may vary from accessible analytical expressions to so-called "black-box model" (e.g. containing solvers of differential equations) for which only the input-output dataset is available.

As a simulation model basically corresponds to a function, its evaluation is naturally conditioned to the considered values of the input variables. These input variables describe relevant properties of the system itself (e.g. geometrical and material properties) as well as the environment in which the system is expected to operate (e.g. external sollicitations). It is obviously critical but not always straightforward to identify all of these input variables that play a role in the evaluation of the variables of interest. This is particularly true when simulating exceptional failures of critical systems that have never occurred. Many unprecedented catastrophies are caused by scnenarios that never had been identified. A first categorization is made between uncertain input variables denoted by $\mathbf{X}$ and known deterministic input variables denoted by $\boldsymbol{\nu}$.

The next natural step (Step B) is the quantification of the uncertain input variables. As it will be shown in Chapter 2, different representations of uncertainty have been considered depending mainly on the quantity and the type of the available information, and on their ease to be propagated and interpretated.

Uncertainty in the input variables leads to uncertain variables of interest. However, a simulation model requires fixed values of $\mathbf{X}$ and $\boldsymbol{\nu}$ to be run. The following step (Step C) is therefore to find techniques that propagate uncertainty through the simulation model. These techniques are multiple as their use depends on the analyst's choice of the QoIs which themselves depend on the involved decision criteria. One frequently encountered technique is the use of surrogate models (also called "metamodels") that are constructed through statistical learning in order to substitute the potentially time-greedy simulation model (Fang et al., 2005). The path from the variables of interest to the QoI is directed by the function denoted as $\psi(\cdot)$ whose evaluation may be of various difficulty.

Finally, inverse analyses (Step C') are often also of high interest. The idea is to use the information from samples (either simulated or experimental) of the QoI to gain more information on parameters of the simulation model and on the quantification of the input variables. A very common example is the quantification of each input variable's influence on the QoI. This is referred to as sensitivity analysis. It enables, either to identify the most influential and the noninfluential inputs (screening), or to rank the variables.

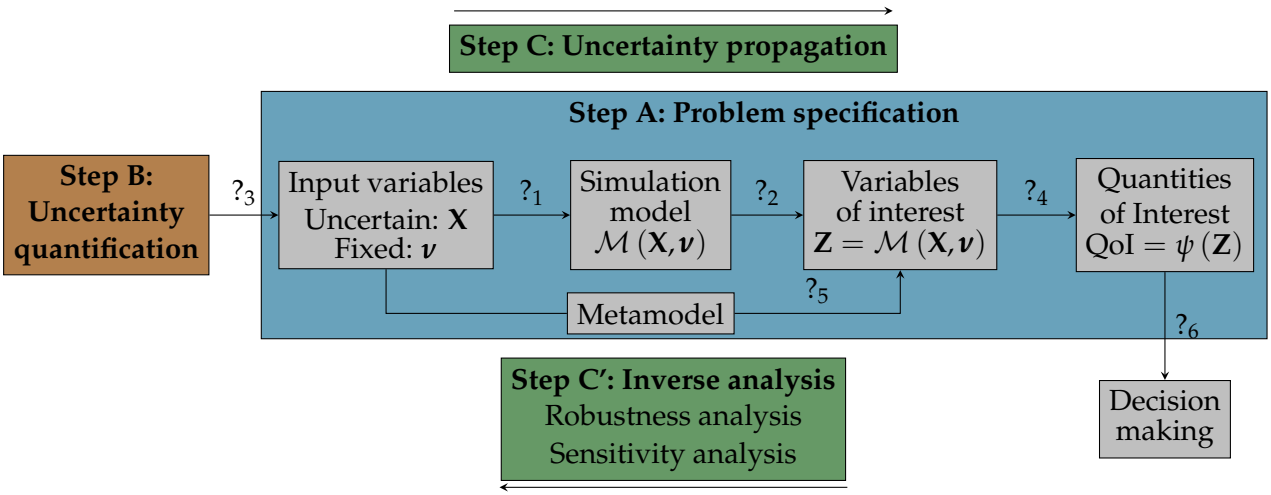

FIGURE 1.1: General uncertainty quantification and propagation framework.

Once again, this global framework represents an idealization of reality given a state of knowledge. The consideration of each box comes along with questions for which the analyst must provide answers. Depending on the analysis, some of these questions that are listed hereafter may be more or less relevant.

- $?_1$: Have all the relevant input variables that play a role on the variables of interest been identified ?
- $?_2$: How representative of the real input-output relations is the simulation model ?
- $?_3$: How representative of the available information on the input variables and how convenient to propagate are the chosen uncertainty representations ?
- $?_4$: How precise is the QoI estimator ?
- $?_5$: What is the degree of additional error brought from the metamodel ?
- $?_6$: How robust is the chosen decision w.r.t. all the previous questions ?

The last point introduces very broadly the notion of robustness of a decision w.r.t. to any additional uncertainty arising from the listed questions.

1.3 Industrial motivations

This thesis was conducted through a CIFRE industrial research agreement in partnership with EDF R&D and the Department of Applied Mechanics of the FEMTO-ST Institute (CNRS, Univ. Bourgogne Franche-Comté). This collaboration represents a typical example of the industrial need for a better understanding and a better control of uncertainty affecting the idealized representation of a system, out of which high-stakes decisions are justified.

In order to remain a world leader in the production of electricity, EDF can count on a panel of high performance and complex systems (e.g. nuclear and hydroelectric plants). These powerful facilities come along with identified risks that could potentially lead to disastrous consequences if they were not correctly handled. Therefore, the beginning and the extension of their operation represent a decision with societal repercussions that requires very strong justifications.

The complexity of the involved industrial systems and the unsimulable nature of many identified risk scenarios that may never have been observed are two main reasons that have led EDF to develop methodologies related to the uncertainty framework presented in Figure 1.1. These

methodologies have progressively included the use uncertainty quantification techniques as a more informative and less conservative way to confront uncertainty and to perform reliability risk assessments.

However, justifications based on probabilistic concepts generally bring up concerns such as:

- the acceptance and the interpretability of probabilistic QoIs that often consider a non-zero risk (e.g. very small but non zero failure probabilities);
- the more complex mathematical background required for conducting and justifying probabilistic uncertainty propagation;
- the justification of probabilistic hypotheses on which rare event quantification is very dependent and based, by definition, on very little information.

It is within this industrial context that the motivation of this thesis lies. The info-gap framework (Ben-Haïm, 2006) is investigated and adapted to probabilistic-based reliability assessments in order to quantify the robustness of these types of studies w.r.t. a lack of knowledge. Indeed, it offers the possibility to evaluate the immunity of a configuration as a function of ignorance and provides valuable insights to the decision maker. In particular, methodologies for applying the info-gap robustness framework are proposed on two real industrial applications: the mechanical integrity of penstocks involved in hydroelectric facilities and a loss-of-coolant nuclear accident scenario. As it will be described in Chapter 3, these applications are complementary in the sense that they bring forward various scientific and numerical challenges which, consequently, requires adapted methodologies for robustness evaluations.

1.4 Objectives and outline of the thesis

The main objective of this thesis is to bring insights on how to interpretate and perform an info-gap robustness analysis applied to reliability-based QoIs in order to take safe decisions. These general objectives are as follows:

- O1: Perform reliability analysis under multiple sources of uncertainty (aleatory and epistemic);
- O2: Illustrate how the info-gap and reliability assessment frameworks can be joined together for enhancing the safety-oriented decision process;
- O3: Quantify the impact of the choice of an epistemic uncertainty representation on the info-gap robustness evaluation;
- O4: Propose methodological and numerical solutions for applying info-gap robustness analysis to small failure probabilities with complex limit-state functions;
- O5: Propose methodological and numerical solutions for applying info-gap robustness analysis to high-order quantiles with time demanding numerical models.

In accordance with the objectives listed above, this manuscript is divided into several chapters whose contents are summarized hereafter.

Chapter 2 brings an overview of the reliability framework under different representations of uncertainty. After shortly describing the needs for modeling different sources of uncertainty, the general reliability framework with probabilistic random variables is presented. A few well-known techniques that are used for estimating small failure probabilities are reviewed. Then, other uncertainty representations that are less informative than probability theory are introduced together with their impact on the way to conduct a reliability analysis.

As this thesis is highly motivated by two industrial applications, Chapter 3 aims at presenting their industrial context and challenges for robustness evaluations. First, the framework associated to the reliability assessment of penstocks is presented together with the available tools for estimating the small failure probabilities induced from complex limit-state functions. Then, a nuclear-related safety application focusing on the loss of coolant in the primary system of a nuclear plant is considered. The thermal-hydraulic code CATHARE2 is briefly described before presenting the statistical methodology used for propagating uncertainty.

Chapter 4 presents the info-gap robustness method. The formulations for quantifying the notions of robustness and opportunity to uncertainty are introduced together with the notion of "value of information". In addition, some criticisms about the method are reviewed and discussed w.r.t. the objectives of this thesis and the opportunities it offers. In addition, insights about the application of info-gap and its placement within other metrics in different uncertainty contexts are given. Finally, numerical aspects involved in the application of the procedure are addressed.

As different uncertainty representations will be jointly considered in this thesis, Chapter 5 presents the context of hybrid reliability and the theory of random sets as a unifying framework for uncertainty propagation. Under this formalism, a methodology combining random set and info-gap theories is proposed for evaluating the impact of the choice of an epistemic uncertainty representation on the robustness assessment.

In Chapter 6, a methodology is proposed for efficiently evaluating the robustness related to the reliability assessments for penstocks. Adapted line sampling algorithms are implemented for estimating small failure probabilities described through complex intersection-based limit-state functions. Then, artificial neural networks are applied for accelerating the evaluation of the info-gap robustness metrics.

Finally, Chapter 7 presents the application of info-gap to the loss-of-coolant accident. As the CATHARE2 simulation code is time-greedy to evaluate, techniques based on metamodels and a unique sample dataset are tested for assessing the robustness of a quantile estimation.

The relevance of the chapters w.r.t. the different objectives is described in Table 1.1 with associated keywords. The content present in each chapter is either described as state of the art (SOA) or as a contribution (NEW).

TABLE 1.1: Summary of the thesis' content.

Keywords	**Chapter**	**Content**	**Objectives**
Aleatory uncertainty / Epistemic uncertainty / Reliability	Chapter 2	SOA	O1
Penstocks / LOCA / Failure probability / Quantile	Chapter 3	SOA	O4, O5
Info-gap / Reliability	Chapter 4	SOA/NEW	O2
Hybrid reliability / Random sets / IG Value of information	Chapter 5	NEW	O1, O3
Line sampling / Neural networks / IG robustness	Chapter 6	NEW	O4
Quantile / Superquantile / Thermal-hydraulic code	Chapter 7	NEW	O5

1.5 Publications and communications

The research contributions presented in this manuscript have also led to the published works listed herebelow.

Jour. Pap. A. Ajenjo, E. Ardillon, V. Chabridon, B. Iooss, S. Cogan and E. Sadoulet-Reboul (2022). "An info-gap framework for robustness assessment of epistemic uncertainty models in hybrid structural reliability analysis". In: *Structural Safety* 96, pp. 102196.

A. Ajenjo, E. Ardillon, V. Chabridon, S. Cogan and E. Sadoulet-Reboul (2022). "Robustness evaluation of the reliability of penstocks combining line sampling and neural networks". *Preprint / Under Review*.

Int. Conf. A. Ajenjo, E. Ardillon, V. Chabridon, S. Cogan and E. Sadoulet-Reboul (2021). "Info-gap robustness evaluation of a line-sampling-based reliability assessment of penstocks". In: *Proc. of the 13th International Conference on Structural Safety and Reliability (ICOSSAR 2021)*, Shanghai, China. (proceedings + talk)

A. Ajenjo, E. Ardillon, V. Chabridon, S. Cogan and E. Sadoulet-Reboul (2021). "Robustness Evaluation of Reliability Assessments of Pensotcks Using Info-Gap Method". In: *Proc. of the 30th European Safety and Reliability Conference and the 15th Probabilistic Safety Assessment and Management Conference (ESREL 2020 PSAM 15)*, Venice, Italy. (proceedings + talk)

A. Ajenjo, E. Ardillon, V. Chabridon, S. Cogan and E. Sadoulet-Reboul (2021). "An info-gap framework for comparing epistemic uncertainty models in hybrid structural reliability analysis". In: *Proc. of the 12th International Symposium on Imprecise Probability: Theories and Applications (ISIPTA 2021)*, Granada, Spain. (proceedings + talk)

Nat. Conf. A. Ajenjo, E. Ardillon, V. Chabridon, S. Cogan and E. Sadoulet-Reboul (2022). "Application de la méthode info-gap aux analyses de fiabilité des conduites forcées". In: *11èmes Journées Fiabilité des Matériaux et des Structures (JFMS 2022)*, Clermont Ferrand, France. (proceedings + talk)

A. Ajenjo, E. Ardillon, V. Chabridon, S. Cogan and E. Sadoulet-Reboul (2021). "Adapted line sampling and neural networks for evaluating the info-gap robustness of reliability estimates for penstocks". In: *MASCOT-NUM 2022*, Clermont Ferrand, France. (summary + poster)

1.6 Code development

The contributions of this work have been implemented using Python language. Moreover, it mainly relies on the following open-source packages:

- OpenTURNS for the definition of random variables, the use of failure probability estimation techniques and the use of global optimization algorithms;
- Numpy and Scipy for basic mathematical operations and for root finding in the context of line sampling (see Chapter 6);
- Keras and Tensorflow for the use of artificial neural networks (see Chapter 6 and Chapter 7).

CHAPTER 2

Structural reliability under different sources of uncertainty

Contents

2.1 Motivations

Robustness analysis is performed throughout this manuscript on reliability quantities of interest. As it will be illustrated in Chapter 3, this framework can be seen as a process composed of two nested layers where the inner layer corresponds to the reliability assessment. Being at the core of the entire analysis and as it is potentially perilous to evaluate in the context of rare events, it is necessary to describe the underlying definition of structural reliability and the available tools to assess it. This state-of-the-art-based chapter, although not exhaustive, aims at doing so.

After describing in Section 2.2 the different sources of uncertainty that need to be taken into account, the definition of structural reliability and some available tools to assess it are given in both the probabilistic and epistemic frameworks in Section 2.3 and Section 2.4 respectively. A simple reliability example is used to illustrate the way uncertainty is represented, how it is propagated and the resulting quantity of interest within the different frameworks.

2.2 Different sources of uncertainty

From a practical point of view, there are two key matters on which a balance should be found in order to guide the choice of the uncertainty representation:

- it must describe in the most representative and objective way the state of knowledge (and conversely of uncertainty) of all the parameters involved in the evaluation of the QoI;
- it must be propagated through the numerical model in a convenient way and yield an interpretable QoI in order to make an informed decision.

The first matter is quite obvious as it seems counter-intuitive to evaluate the impact of uncertainty through a non-representative description of the available knowledge. However, it is still of common use to translate uncertainty with (non-representative) pessimistic values in order to guarantee a safe decision. Sometimes, checking that a decision is satisfactory in a penalized configuration might bring enough information for the analyst. Thus, this first matter is conditioned to the decision at stake and the performance requirements. The second matter is also of high importance as only results that are interpretable for all the decision-makers can be used in order to make a decision and to justify it, especially for safety concerns. Yet, agreeing on the right uncertainty representation that meets both considerations is not straightforward as many configurations are possible based on the amount of information, the quality of information and the different sources of uncertainty.

The main reason that leads to the consideration of different representations is that uncertainty may take different forms (Hacking, 1975). There have been ongoing discussions on the nature of uncertainty and, therefore, the manners to treat it. More specifically, the attempts to distinguish between aleatory uncertainty (viewed as inherent variablity) and epistemic uncertainty (viewed as subjective uncertainty as a reflect of lack of knowledge) have been numerous. Many works such as in Fox and Ülkümen (2011) have enabled to better characterize some properties that separate both types of uncertainty. The work presented in Ülkümen et al. (2016) also claims that the distinction seems rather intuitive from a linguistic point of view by affecting the terms of confidence to epistemic uncertainty and likelihood to aleatory uncertainty.

However, discussions remain on the manner to treat both concepts. Although probability theory has convinced the community for the treatment of aleatory uncertainty, the numerous representations of epistemic uncertainty testify to a divergence of opinions. In addition, Der Kiureghian and Ditlevsen (2009) notice that the type of uncertainty may go from one to the other depending on the different phases of a same analysis. Still in Der Kiureghian and Ditlevsen (2009), a more global investigation is led by introducing the notion of "model universe" as the

analyst's mathematical idealizations of reality. Such idealization is necessary in practice for conducting the process of decision-making although proned to uncertainty. Seven sources of uncertainty are identified, namely inherent uncertainty in the basic probabilistic random variables, uncertainty in the choice of the probability density function (pdf) used to describe the random variables, uncertainty in the physical sub-models used to derive variables from others (the computer model $\mathcal{M}(\cdot)$ for instance), uncertainty in the parameters of the pdf, uncertainty in the parameters used in the physical sub-models, uncertainty in measurement and finally uncertainty in the mathematical or numerical tools used for estimating the quantity of interest.

Although being an important subject of research, this thesis presents no intention of further developing the distinctions between aleatory and epistemic uncertainties. Rather, it aims at evaluating how robust a decision is w.r.t. any hypothesis proned to errors. In this thesis, the probabilistic random vector $\mathbf{X}$ will contain all the random variables for which the probabilistic definition is fully trusted. The term "epistemic variable" will be used for any variable Y_i that presents one or several modeling hypotheses on which a robustness analysis is performed. Therefore, Y_i may also be a random variable whose probabilistic description is somehow considered as uncertain. As pointed out above, many sources of errors may arise in the model universe. In this thesis, robustness analysis will be concentrated on the input variables (rather than on model errors for example).

2.3 Structural reliability in the probabilistic framework

2.3.1 Core concepts of probability theory

Probability theory represents a well established and powerful framework for tackling aleatory uncertainty. It is based on the definition of a *random vector* $\mathbf{X}$ that contains $n_{\mathbf{X}}$ random variables such that $\mathbf{X} = (X_1, \cdots, X_{n_{\mathbf{X}}})^\top$. A random vector is constructed through a probability space composed of the triplet $(\Omega, \mathcal{B}(\Omega), \mathbb{P})$ where Ω is the sample space, $\mathcal{B}$ is the Borel σ-algebra and $\mathbb{P}$ is a probability measure $\mathbb{P} : \mathcal{B}(\Omega) \to [0,1]$. It follows the definition of a random vector $\mathbf{X}$ as the measurable function $\mathbf{X} : \Omega \to \mathcal{D}_{\mathbf{X}}, \omega \to \mathbf{X}(\omega) = \mathbf{x}$ where $\mathbf{x}$ is called a realization of $\mathbf{X}$ and $\mathcal{D}_{\mathbf{X}}$ is called the support (or domain) of $\mathbf{X}$.

A random vector is commonly caracterized by its *cumulative distribution function* (cdf) $F_{\mathbf{X}}(\cdot)$ expressed as:

$$F_{\mathbf{X}} : \left| \begin{array}{rcl} \mathbb{R}^{n_{\mathbf{X}}} & \longrightarrow & [0,1] \\ \mathbf{x} & \longrightarrow & \mathbb{P}(\mathbf{X} \leq \mathbf{x}) = \mathbb{P}(X_1 \leq x_1, \cdots, X_{n_{\mathbf{X}}} \leq x_{n_{\mathbf{X}}}) \end{array} \right. \tag{2.1}$$

and, when it exists, its related joint *probability density function* (pdf) $f_{\mathbf{X}}$ defined such that $f_{\mathbf{X}}(\mathbf{x}) = \frac{\partial^{n_{\mathbf{X}}} F_{\mathbf{X}}(\mathbf{x})}{\partial x_1 \cdots \partial x_{n_{\mathbf{X}}}}$. Characterizing these two functions is a key point as they enable to define the moments of a random vector such as the *mean vector* $\boldsymbol{\mu}_{\mathbf{X}}$ which reads:

$$\boldsymbol{\mu}_{\mathbf{X}} = \mathbb{E}[\mathbf{X}] = \int_{\mathcal{D}_{\mathbf{X}}} \mathbf{x} f_{\mathbf{X}}(\mathbf{x})\, d\mathbf{x} = (\mathbb{E}[X_1], \cdots, \mathbb{E}[X_{n_{\mathbf{X}}}])^\top \tag{2.2}$$

and the *variance-covariance matrix* $\boldsymbol{\Sigma}_{\mathbf{X}}$ which reads:

$$\boldsymbol{\Sigma}_{\mathbf{X}} = \mathbb{E}\left[(\mathbf{X} - \boldsymbol{\mu}_{\mathbf{X}})(\mathbf{X} - \boldsymbol{\mu}_{\mathbf{X}})^\top\right] = \int_{\mathcal{D}_{\mathbf{X}}} (\mathbf{x} - \boldsymbol{\mu}_{\mathbf{X}})(\mathbf{x} - \boldsymbol{\mu}_{\mathbf{X}})^\top f_{\mathbf{X}}(\mathbf{x})\, d\mathbf{x}. \tag{2.3}$$

The *variance* $\mathrm{Var}[X_i] = \mathbb{E}\left[(X_i - \mathbb{E}[X_i])^2\right]$, the *standard deviation* $\sigma_{X_i} = \sqrt{\mathrm{Var}[X_i]}$ and the *coefficient of variation* (for a non-zero mean value) $\delta_{X_i} = \sigma_{X_i}/\mu_{X_i}$ are related quantities that are also often used.

As the joint pdf represents the core definition of $\mathbf{X}$, methods are needed for its choice. They are based on multiple sources of information that may be combined such as experimental data,

measurements, numerical data and expert judgments. A first class of methods aims at finding the parametric distribution among a family of distributions (e.g. normal distribution, uniform distribution) that best fits the information. Parametric statistics (Wasserman, 2004) are used in that matter in order to identify the parameters of an assumed parametric distribution. A second class of methods based on nonparametric statistics assumes no underlying distribution family. Methods such as kernel density estimation (Silverman, 1986) have been proposed for directly approximating the unknown distribution. In this thesis, robustness analysis will often be performed by perturbing a nominal parametric distribution. The perturbations will either concern the parameters of a distribution while keeping its parametric definition or will directly address the parametric assumption.

2.3.2 Reliability quantities of interest

The probabilistic definition of the input variables is only a first step. Indeed, it becomes necessary to propagate the uncertainties model through the computer code $\mathcal{M}(\cdot)$ in order to quantify the variable of interest $Z = M(\mathbf{X})$, supposed scalar in this thesis. The nature of uncertainty is conserved during the propagation through the computer code which implies that Z is also a random variable that may be quantified by its cdf F_Z.

This quantification is generally not straighforward as complex behaviors may be induced from the relationship between the input pdf $f_{\mathbf{X}}(\mathbf{x})$ and the computer code $\mathcal{M}(\cdot)$. However, the complete probabilistic knowledge of the variable of interest is rarely required. Instead, statistical quantities are computed in order to bring knowledge about the variable of interest w.r.t. a decision criteria. On the one hand, one might be interested in its general probabilistic behavior by computing its mean, variance or median for example. On the other hand, one might be interested in more specific zones of the pdf such as its tails in order to quantify its extreme behavior. For instance, *small failure probabilities* or *high-order quantiles* are common quantities used for safety assessments. Such statistical quantities will be referred to as the *Quantities of Interest* (QoI). As this thesis focuses on the robustness of safety assessments, the last two QoIs will be studied, in particular small failure probabilities.

By conventionally defining failure as the event that the variable of interest z exceeds a given threshold $z_{\text{th}} \in \mathbb{R}$, the limit-state function (LSF) $g(\cdot)$ is defined as follows:

$$g(\mathbf{x}) = z_{\text{th}} - z. \tag{2.4}$$

The LSF separates the input domain into a failure domain $\mathcal{F}_{\mathbf{x}}$ and a safety domain $\mathcal{S}_{\mathbf{x}}$ such that:

$$\mathcal{F}_{\mathbf{x}} = \{\mathbf{x} \in D_{\mathbf{X}} \mid g(\mathbf{x}) \leq 0\} \tag{2.5a}$$
$$\mathcal{S}_{\mathbf{x}} = \{\mathbf{x} \in D_{\mathbf{X}} \mid g(\mathbf{x}) > 0\}. \tag{2.5b}$$

The frontier between both domains, referred to as the *limit-state surface* (LSS), represents a hypersurface in $\mathbb{R}^{n_{\mathbf{X}}}$ defined by $\mathcal{F}_{\mathbf{x}}^0 = \{\mathbf{x} \in D_{\mathbf{X}} \mid g(\mathbf{x}) = 0\}$. The failure probability P_{f} can then be defined, in an equivalent manner, as:

$$P_{\text{f}} = \mathbb{P}(g(\mathbf{X}) \leq 0) = \mathbb{P}(\mathbf{X} \in \mathcal{F}_{\mathbf{x}}) = \int_{\mathcal{F}_{\mathbf{x}}} f_{\mathbf{X}}(\mathbf{x})\, d\mathbf{x} = \int_{\mathbb{R}^{n_{\mathbf{X}}}} \mathbb{1}_{\mathcal{F}_{\mathbf{x}}}(\mathbf{x})\, f_{\mathbf{X}}(\mathbf{x})\, d\mathbf{x} = \mathbb{E}_{f_{\mathbf{X}}}[\mathbb{1}_{\mathcal{F}_{\mathbf{x}}}(\mathbf{X})]. \tag{2.6}$$

The common "Resistance - Sollicitation" ($R - S$) example is used here and in the next subsection in order to compare uncertainty propagation techniques in the different frameworks. This example simply represents the failure event as a resistance variable $X_1 = R$ being lower than a load variable $X_2 = S$. The limit-state function is therefore described as $g(R, S) = R - S$. Here, it is considered that both variables follow normal distributions such that $R \sim \mathcal{N}(\mu_R = 100, \sigma_R = 10)$ and $S \sim \mathcal{N}(\mu_S = 70, \sigma_S = 7)$. In this trivial case, the failure probability

can be evaluated analytically such that:

$$P_{\mathrm{f}} = \Phi\left(\frac{\mu_S - \mu_R}{\sqrt{\sigma_R^2 + \sigma_S^2}}\right) = \Phi\left(-\beta_c\right) \tag{2.7}$$

where $\Phi\left(\cdot\right)$ is the cdf of the Gaussian distribution and β_c is called the Cornell reliability index (Lemaire et al., 2009). The numerical application gives $P_{\mathrm{f}} = 6.99 \times 10^{-3}$.

However, the possibility of such analytical evaluation is rarely encountered in real engineering problems. Instead, several techniques have been developed in the past decades in order to estimate Eq. (2.6). The following subsection aims at presenting the most encountered ones when evaluating small failure probabilities associated to rare failure events.

2.3.3 Rare-event probability estimation techniques

Many different study configurations may be encountered in reliability analyses. Indeed, the estimation of failure probabilities depends on many factors such as:

- the (unknown) order of magnitude of the targeted failure probability;
- the computational time of the simulation model $\mathcal{M}\left(\cdot\right)$;
- the number of random variables $n_{\mathbf{X}}$;
- the complexity of the dependency between the $n_{\mathbf{X}}$ random variables;
- the degree of nonlinearity of the LSF and the possibility for multiple failure regions;
- the possibility of parallelizing the computation of the simuation model.

As a consequence, there exists quite a large panel of techniques for estimating small failure probabilities (Morio and Balesdent, 2015). What follows only represents a reduced description of the techniques that will be involved in the next chapters. After introducing the notion of transformation into the *standard normal space*, the basic technique of Crude Monte Carlo sampling is described. Then, four advanced techniques are presented, namely most-probable-failure-point-based techniques, importance sampling, subset simulation and line sampling.

Physical space to standard normal space mapping

The original physical space, called "**X**-space", may contain a mixture of different marginal distributions that possibly represent quantities with different scales. Although it will rarely be the case in this thesis, there can also be more or less complex dependencies among the random variables to be accounted for which can be modeled through the use of various copulas (see Nelsen (2006) and Lebrun (2013)). All put together, working directly in the **X**-space may be a challenging task for uncertainty propagation techniques and, therefore, for reliability assessments.

In that view, transformations have been considered and applied in order to map the **X**-space into the so-called standard normal space, also called "**U**-space", in which each random variable is independent from the others and follows a standard Gaussian distribution (such that its mean is 0 and its standard deviation is 1). Selecting Gaussian distributions gives interesting mathematical properties to the **U**-space and the transformation must be isoprobabilistic to ensure that

the probabilities of the failure event are identical in both spaces. This transformation T is defined as the $\mathcal{C}^1$-diffeomorphism:

$$\begin{aligned} T:\ \mathbb{R}^{n_\mathbf{X}} &\to \mathbb{R}^{n_\mathbf{X}} \\ \mathbf{X} &\to T(\mathbf{U}). \end{aligned} \tag{2.8}$$

This transformation is invertible such that one may switch back to the $\mathbf{X}$-space applying $\mathbf{X} = T^{-1}(\mathbf{U})$. Depending on the characteristics of the joint pdf $f_\mathbf{X}$, there exists several transformations, the most famous ones being the Nataf (Nataf, 1962) and Rosenblatt (Rosenblatt, 1952) transformations. When the physical variables are independent, this transformation is unique and expresses simply as:

$$\begin{array}{rccccc} T = T_{vu} \circ T_{xv}: & \mathcal{D}_\mathbf{X} & \to & [0,1]^{n_\mathbf{X}} & \to & \mathbb{R}^{n_\mathbf{X}} \\ & \mathbf{x} & \to & \mathbf{v} = F_\mathbf{X}(\mathbf{x}) & \to & \mathbf{u} = \Phi^{-1}(\mathbf{v}). \end{array} \tag{2.9}$$

Therefore, reliability analysis can also be performed in the standard normal space by considering the failure event $\mathcal{F}_\mathbf{u} = \{\mathbf{u} \in \mathbb{R}^{n_\mathbf{X}},\ G(\mathbf{u}) \leq 0\}$ where $G = g \circ T^{-1}$ and by keeping in mind that $\mathbb{P}(\mathbf{X} \in \mathcal{F}_\mathbf{x}) = \mathbb{P}(\mathbf{U} \in \mathcal{F}_\mathbf{u})$. This standard normal space plays an important role for some sampling and approximation techniques presented hereafter, which either use this space intrinsically (FORM-importance sampling, line sampling, directional simulation) or are implemented preferentially in it (subset simulation).

Crude Monte Carlo sampling

Crude Monte Carlo (CMC) sampling (Metropolis and Ulam, 1949) is probably the most straightforward and natural method to estimate a failure probability as it only requires a random number generator and the ability to evaluate the computer code. The method aims at estimating Eq. (2.6) by generating samples from the joint pdf $f_\mathbf{X}$. The estimation $\widehat{P}_\mathrm{f}$ can be obtained by generating n_CMC i.i.d. samples $\left(\mathbf{x}^{(i)}\right)_{1 \leq n_\mathrm{CMC}}$ according to $f_\mathbf{X}$ and evaluating the proportion of failure samples by the following empirical mean:

$$\widehat{P}_\mathrm{f} = \frac{1}{n_\mathrm{CMC}} \sum_{i=1}^{n_\mathrm{CMC}} \mathbb{1}_{\mathcal{F}_\mathbf{x}}\left(\mathbf{x}^{(i)}\right). \tag{2.10}$$

Let us note that this estimator is a random variable itself which asymptotically tends to the true failure probability as n_CMC gets larger. This is a result of the law of large numbers. The convergence rate of the estimator can be assessed through its corresponding variance estimator:

$$\widehat{\mathrm{Var}}\left[\widehat{P}_\mathrm{f}\right] = \frac{1}{n_\mathrm{CMC}} \widehat{P}_\mathrm{f}\left(1 - \widehat{P}_\mathrm{f}\right). \tag{2.11}$$

An illustration of CMC is given in Figure 2.1 in the $\mathbf{X}$-space (A) and in the $\mathbf{U}$-space (B) with 10^4 generated samples. The isoprobabilistic nature of the "$\mathbf{X}$ to $\mathbf{U}$" transformation implies the same number of failure points (the six red points) in both spaces. Let us note that, although giving the same results, there is no practical benefit in applying CMC to the standard normal space. Generally, CMC is performed in the physical space.

This basic technique has been widely applied in many different fields (Liu, 2001). However, CMC blindly explores the probabilistic space and is therefore not adapted for rare event simulations as a huge number of samples is required. As a rule of thumb, a failure probability of order of magnitude 10^{-m} requires around 10^{m+2} samples to be estimated with a targeted coefficient of

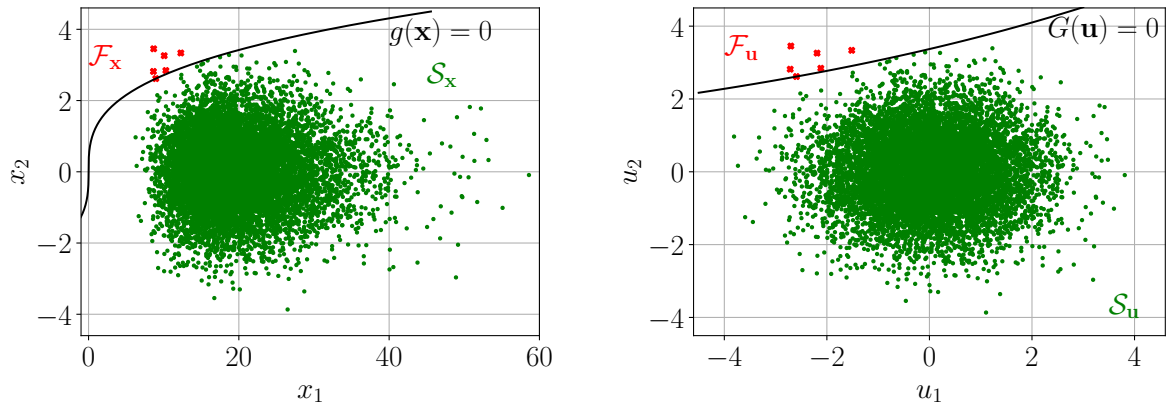

(A) (B)

FIGURE 2.1: Crude Monte Carlo in the **X**-space (A) and in the **U**-space (B).

variation of 10%. This issue is particularly limiting for assessing small failure probabilities (e.g. $< 10^{-6}$) even when the computer code is fast to evaluate.

Most-Probable-Failure-Point-based estimators

Unlike sampling methods, most-probable-failure-point (MPFP) techniques aim at addressing the failure domain by determining the point belonging to the LSS with the highest probability density in the standard normal space. When working in the standard normal space, this point simply corresponds to the closest one from the origin that belongs to $\mathcal{F}_\mathbf{u}$. Therefore, the MPFP of coordinates $\mathbf{u}^*$ is obtained by solving the following optimization problem:

$$\mathbf{u}^* = \underset{\mathbf{u}\in\mathbb{R}^{n_\mathbf{X}}}{\arg\min} \left(\mathbf{u}^\top \mathbf{u}\right) \quad \text{s.t.} \quad G\left(\mathbf{u}\right) \leq 0. \tag{2.12}$$

Note that the corresponding point in the physical space is obtained by $\mathbf{x}^* = T^{-1}(\mathbf{u}^*)$. The optimization problem is more or less challenging depending mainly on the nonlinearity of the limit-state function. Different solvers have been proposed in that matter (Rackwitz and Fiessler, 1978; Zhang and Der Kiureghian, 1994). The distance of $\mathbf{u}^*$ to the origin is the so-called Hasofer-Lind reliability index $\beta_{\text{HL}} = \|\mathbf{u}^*\|$ (Hasofer and Lind, 1974). Moreover, the unit vector that points towards the MPFP is defined as:

$$\boldsymbol{\alpha} = -\frac{\nabla_\mathbf{u} G\left(\mathbf{u}^*\right)}{||\nabla_\mathbf{u} G\left(\mathbf{u}^*\right)||} = \frac{\mathbf{u}^*}{\beta_{\text{HL}}} \tag{2.13}$$

where $\nabla\left(\cdot\right)$ is the gradient operator.

The MPFP plays a central role in many failure probability estimators and in particular in the first order reliability method (FORM) and the second order reliability method (SORM). FORM consists in linearizing the LSF through its first-order Taylor series expansion around the MPFP such that:

$$G(\mathbf{u}) \approx G_1(\mathbf{u}) = G(\mathbf{u}^*) + \nabla_\mathbf{u} G\left(\mathbf{u}^*\right)^\top \left(\mathbf{u} - \mathbf{u}^*\right). \tag{2.14}$$

Recalling that $G(\mathbf{u}^*) = 0$ by definition, one obtains the FORM estimator P_f as:

$$P_\text{f} \approx P_\text{f}^{\text{FORM}} = \mathbb{P}\left(G_1(\mathbf{U}) \leq 0\right) = \mathbb{P}\left(\frac{G_1(\mathbf{U})}{||\nabla_\mathbf{u} G\left(\mathbf{u}^*\right)||} \leq 0\right) = \mathbb{P}\left(\beta_{\text{HL}} - \boldsymbol{\alpha}^\top \mathbf{U} \leq 0\right). \tag{2.15}$$

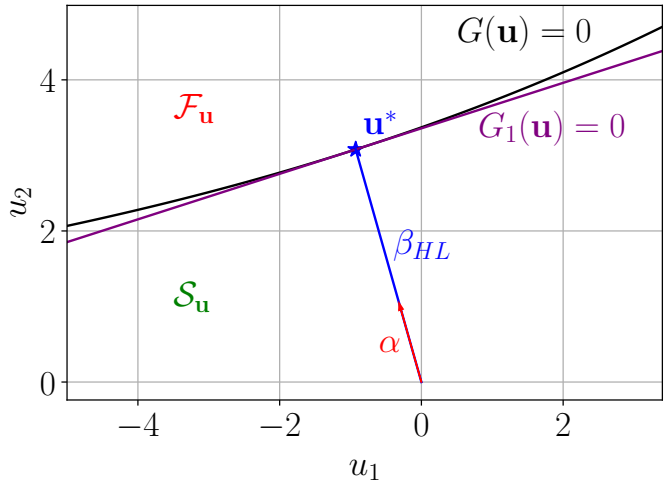

FIGURE 2.2: Graphical representation of FORM.

Finally, by noticing that $\boldsymbol{\alpha}^\top \mathbf{U}$ follows the standard Gaussian distribution, the approximation of the true failure probability yields:

$$P_\mathrm{f}^\mathrm{FORM} = \Phi\left(-\beta_\mathrm{HL}\right). \tag{2.16}$$

An illustration of FORM is given in Figure 2.2. The accuracy of the approximation naturally depends on the degree of nonlinearity of the LSF.

SORM was proposed as an extension of FORM for reducing its approximation error due the nonlinearity of the LSF. Similarly, the LSF is approximated through its Taylor series expansion but truncated at the second-order. The SORM approximation is not as straightforward as the FORM estimator and is therefore not presented here. However, the reader is referred to the three SORM estimation methods proposed by Tvedt (1990), Breitung (1984) and Hohenbichler and Rackwitz (1988).

In addition to the nonlinearity issue, the FORM and SORM approximations, as presented above, focus on a single MPFP. However the MPFP may not be unique in some applications. More generally, the probabilistic space may contain several failure domains in different locations. This information is often not available as it requires knowledge about the LSF (and therefore about the potentially expensive-to-evaluate compute code). In such cases, FORM and SORM may perform poorly. Procedures based on repeated FORM analyses have been proposed in that case in order to identify the different failure regions (Der Kiureghian and Dakessian, 1998).

Importance sampling

The idea of importance sampling is to reduce the variance of CMC by sampling according to an instrumental distribution $h_\mathbf{X}$ which will yield more failure samples than the initial distribution $f_\mathbf{X}$. This instrumental distribution can simply be integrated into the expression of the failure probability in Eq. (2.6) as follows:

$$P_\mathrm{f} = \int_{\mathbb{R}^{n_\mathbf{X}}} \mathbb{1}_{\mathcal{F}_\mathbf{x}}(\mathbf{x})\, f_\mathbf{X}(\mathbf{x})\, d\mathbf{x} = \int_{\mathbb{R}^{n_\mathbf{X}}} \mathbb{1}_{\mathcal{F}_\mathbf{x}}(\mathbf{x})\, \frac{f_\mathbf{X}(\mathbf{x})}{h_\mathbf{X}(\mathbf{x})} h_\mathbf{X}(\mathbf{x})\, d\mathbf{x} = \mathbb{E}_{h_\mathbf{X}}\left[\mathbb{1}_{\mathcal{F}_\mathbf{x}}(\mathbf{X})\, w_\mathbf{X}(\mathbf{X})\right] \tag{2.17}$$

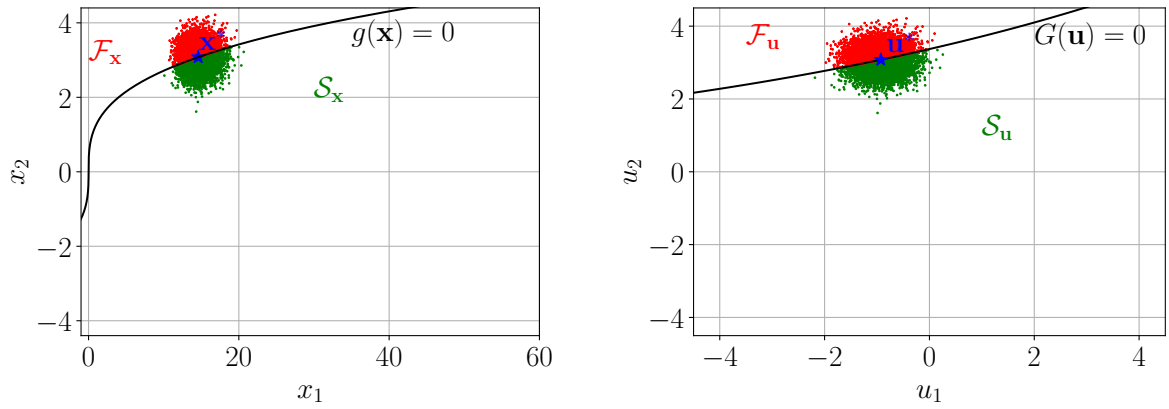

(A) (B)

FIGURE 2.3: Importance sampling in the **X**-space (A) and in the **U**-space (B).

where $w_{\mathbf{X}}(\mathbf{x}) = f_{\mathbf{X}}(\mathbf{x}) / h_{\mathbf{X}}(\mathbf{x})$ is called the likelihood ratio. As with CMC, the expectation formulation can be estimated with n_{IS} samples generated from $h_{\mathbf{X}}$:

$$\widehat{P}_{\text{f}} = \frac{1}{n_{\text{IS}}} \sum_{i=1}^{n_{\text{IS}}} \mathbb{1}_{\mathcal{F}_{\mathbf{x}}}\left(\mathbf{x}^{(i)}\right) w_{\mathbf{X}}\left(\mathbf{x}^{(i)}\right). \tag{2.18}$$

This estimator is unbiased and its corresponding variance may also be estimated as:

$$\widehat{\text{Var}}\left[\widehat{P}_{\text{f}}\right] = \frac{1}{n_{\text{IS}} - 1}\left(\frac{1}{n_{\text{IS}}} \sum_{i=1}^{n_{\text{IS}}} \mathbb{1}_{\mathcal{F}_{\mathbf{x}}}\left(\mathbf{x}^{(i)}\right) w_{\mathbf{X}}\left(\mathbf{x}^{(i)}\right)^2 - \widehat{P}_{\text{f}}^2\right). \tag{2.19}$$

It is important to note that the same formulations hold in the standard normal space. Figure 2.3 illustrates the samples generated by an instrumental distribution based on the MPFP in the physical and standard normal spaces. There is almost as many failure samples as safe samples which enables to considerably accelerate the convergence of the estimator compared to the one obtained from CMC.

The performance of this technique totally depends on the choice of the instrumental pdf $h_{\mathbf{x}}$. The theoritical optimal pdf in the physical space $h^*_{\mathbf{X}}$ is given as (Bucklew, 2004):

$$h^*_{\mathbf{X}}(\mathbf{x}) = \frac{\mathbb{1}_{\mathcal{F}_{\mathbf{x}}}(\mathbf{x}) f_{\mathbf{X}}(\mathbf{x})}{P_{\text{f}}}. \tag{2.20}$$

An equivalent expression holds in the standard normal space. This formulation is not directly usable in practice as it depends on the failure probability to be estimated. Instead, sub-optimal densities may be constructed based on three main categories:

- nonadaptive IS density based on the MPFP (see Figure 2.3);
- parametric adaptive IS based on the MPFP or using cross-entropy (Rubinstein and Kroese, 2004);
- nonparametric adaptive IS (Morio, 2011).

Throughout this thesis, IS will be performed considering an instrumental distribution constructed around the MPFP point, more precisely a standard multinormal distribution. This method is usually called FORM-IS (Melchers, 1989) since the MPFP is obtained via FORM.

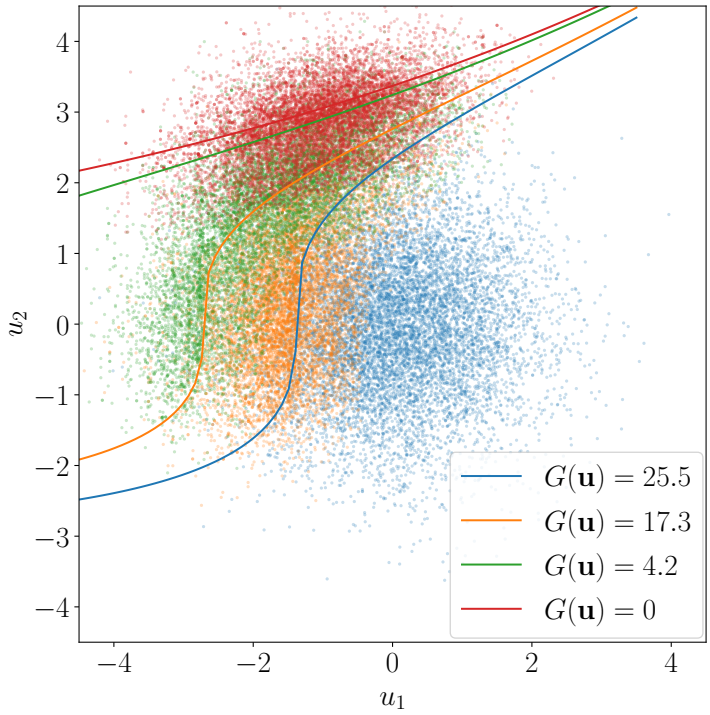

FIGURE 2.4: Graphical representation of the subset simulation procedure.

Subset simulation

The subset simulation (SS) technique (Au and Beck, 2001) is one of the multiple variants of multilevel splitting designed for reliability assessment. This technique consists in reducing the variance of the failure probability estimator by splitting the failure event into a series of failure nested events with higher probabilities of occurrence. Thus, each probability is easier to estimate.

Formally, by working in the **U**-space, the initial failure domain $\mathcal{F}_{\mathbf{u}}$ is split into m nested failure subdomains $\mathcal{F}_{\mathbf{u},n}$ with $n = 1, \cdots, m$ such that $\mathcal{F}_{\mathbf{u},n} \subset \mathcal{F}_{\mathbf{u},n-1}$. Each failure subdomain is defined with an intermediate threshold such that $\mathcal{F}_{\mathbf{u},n} = \{\mathbf{u} \in \mathbb{R}^{n_\mathbf{X}},\ G(\mathbf{u}) \leq z_n\}$ with $z_1 > z_2 > \cdots > z_m = 0$. By considering successive conditional probabilities, the failure probability reads:

$$\begin{aligned} P_\mathrm{f} &= \mathbb{P}\left(E_m\right) \\ &= \mathbb{P}\left(E_m | E_{m-1}\right) \mathbb{P}\left(E_{m-1}\right) \\ &= p_1 \prod_{n=2}^{m} p_n \end{aligned} \tag{2.21}$$

where $E_n = \{\mathbf{u} \in \mathcal{F}_{\mathbf{u},n}\}$ is the event associated to $\mathcal{F}_{\mathbf{u},n}$, $p_1 = \mathbb{P}\left(E_1\right) = \mathbb{E}_{\varphi_{n_\mathbf{X}}}\left[\mathbb{1}_{\mathcal{F}_{\mathbf{u},1}}\left(\mathbf{U}\right)\right]$ with $\varphi_{n_\mathbf{X}}$ being the $n_\mathbf{X}$-dimensional standard Gaussian pdf and $p_n = \mathbb{P}\left(E_n | E_{n-1}\right) = \mathbb{E}_{\varphi_{n_\mathbf{X}}(\cdot|E_{n-1})}\left[\mathbb{1}_{\mathcal{F}_{\mathbf{u},n}}\left(\mathbf{U}\right)\right]$ is an intermediate failure probability.

The estimator of Eq. (2.21) is given by:

$$\widehat{P_\mathrm{f}} = \widehat{p_1} \prod_{n=2}^{m} \widehat{p_n}. \tag{2.22}$$

Dedicated Monte Carlo Markov Chains algorithms, such as the standard Metropolis-Hastings

(Metropolis et al., 1953; Hastings, 1970), are used for efficiently sampling the conditional events $E_n|E_{n-1}$. Figure 2.4 illustrates an example of three intermediate LSFs with corresponding samples that lead to the true LSF (in red). In Au et al. (2007), variants of SS are proposed and tested on specific reliability problems. More recently, the possibility to combine SS with different types of metamodels has been particularly explored (Bourinet et al., 2011; Papadopoulos et al., 2012; Huang et al., 2016; Bect et al., 2017; Bourinet, 2016).

Line sampling

Line sampling (LS) technique (Koutsourelakis et al., 2004; Koutsourelakis, 2004), also known as "Axis-Orthogonal Simulation" (Tvedt, 2005), belongs to the family of directional techniques (similarly to directional sampling (Bjerager, 1988) which is not reviewed in this manuscript). It consists in dividing the $n_{\mathbf{X}}$-dimensional failure probability evaluation problem into n_{LS} one-dimensional failure probability evaluation problems. Firstly, samples belonging to a hyperplane orthogonal to a direction $\boldsymbol{\alpha}$ that points towards the LSS are generated. The technique is performed in the standard normal space. By applying an isoprobabilistic rotation $\mathbf{R}$ such that $\mathbf{V} = \mathbf{RU}$, where V_1 is a standard random variable whose outcome is parallel to $\boldsymbol{\alpha}$ and $\mathbf{V_{2:n}} = \mathbf{U}_{\boldsymbol{\alpha}}^{\perp}$ is a random vector (of size $(n_{\mathbf{X}} - 1)$) whose realization lies in the hyperplane orthogonal to $\boldsymbol{\alpha}$, the failure probability can be expressed as follows:

$$P_{\text{f}} = \int_{\mathbb{R}^{n_{\mathbf{X}}-1}} \int_{G^{\perp}\left(v_1, \mathbf{u}_{\boldsymbol{\alpha}}^{\perp}\right) \leq 0} \varphi\left(v_1\right) dv_1 \varphi_{\mathbf{U}_{\boldsymbol{\alpha}}^{\perp}}\left(\mathbf{u}_{\boldsymbol{\alpha}}^{\perp}\right) d\mathbf{u}_{\boldsymbol{\alpha}}^{\perp} \tag{2.23}$$

where $G^{\perp}\left(\left[v_1, \mathbf{u}_{\boldsymbol{\alpha}}^{\perp}\right]\right)$ is the LSF in the rotated space and $\varphi\left(\cdot\right) =$ is the pdf of the standard normal distribution. Assuming that, for any $\mathbf{u}_{\boldsymbol{\alpha}}^{\perp}$, $r\left(\mathbf{u}_{\boldsymbol{\alpha}}^{\perp}\right)$ ("r" standing for "root") is the unique solution of $G^{\perp}\left(v_1; \mathbf{u}_{\boldsymbol{\alpha}}^{\perp}\right) = 0$, the failure probability can finally be expressed as:

$$P_{\text{f}} = \int_{\mathbb{R}^{n_{\mathbf{X}}-1}} \Phi\left(-r\left(\mathbf{u}_{\boldsymbol{\alpha}}^{\perp}\right)\right) \varphi_{\mathbf{U}_{\boldsymbol{\alpha}}^{\perp}}\left(\mathbf{u}_{\boldsymbol{\alpha}}^{\perp}\right) d\mathbf{u}_{\boldsymbol{\alpha}}^{\perp} = \mathbb{E}_{\mathbf{U}_{\boldsymbol{\alpha}}^{\perp}}\left[\Phi\left(-r\left(\mathbf{u}_{\boldsymbol{\alpha}}^{\perp}\right)\right)\right]. \tag{2.24}$$

When sampling n_{LS} points that belong to the orthogonal hyperplane, the estimation of the failure probability and its corresponding variance can be estimated as follows:

$$\widehat{P}_{\text{f}} = \frac{1}{n_{\text{LS}}} \sum_{i=1}^{n_{\text{LS}}} p_{\text{f}}^{(i)} \tag{2.25}$$

$$\widehat{\text{Var}}\left(\widehat{P}_{\text{f}}\right) = \frac{1}{n_{\text{LS}}\left(n_{\text{LS}} - 1\right)} \sum_{i=1}^{n_{\text{LS}}} \left(p_{\text{f}}^{(i)} - \widehat{P}_{\text{f}}\right)^2 \tag{2.26}$$

where $p_{\text{f}}^{(i)} = \Phi\left(-r\left(\mathbf{u}_{\boldsymbol{\alpha}}^{\perp,(i)}\right)\right) = \Phi\left(-r^{(i)}\right)$ is the conditional failure probability along the $(i)^{\text{th}}$-line. A graphical representation of the LS procedure is given in Figure 2.5 which presents 50 orthogonal samples and, therefore, 50 lines parallel to $\boldsymbol{\alpha}$. Each root $r^{(i)}$ separates the corresponding line into the one-dimensional safe domain (in green for $v_1 < r^{(i)}$) and the one-dimensional failure domain (in red for $v_1 \geq r^{(i)}$).

The selected direction $\boldsymbol{\alpha}$ plays a key role on the convergence speed of the LS estimator. The optimal direction is generally the one that points towards the MPFP already defined as the vector $\boldsymbol{\alpha}$ in the paragraph related to MPFP-based estimators. Therefore, performing a FORM analysis is common before applying the LS technique. However, it is important to mention that assessing the optimal direction is not a requirement but only a way to accelerate the convergence, in the same idea that IS can be performant (in the sense of variance reduction) even without the true optimal instrumental density function. Moreover, the direction $\boldsymbol{\alpha}$ can be updated during the LS process which is one of the features proposed by De Angelis et al. (2015) and referred to

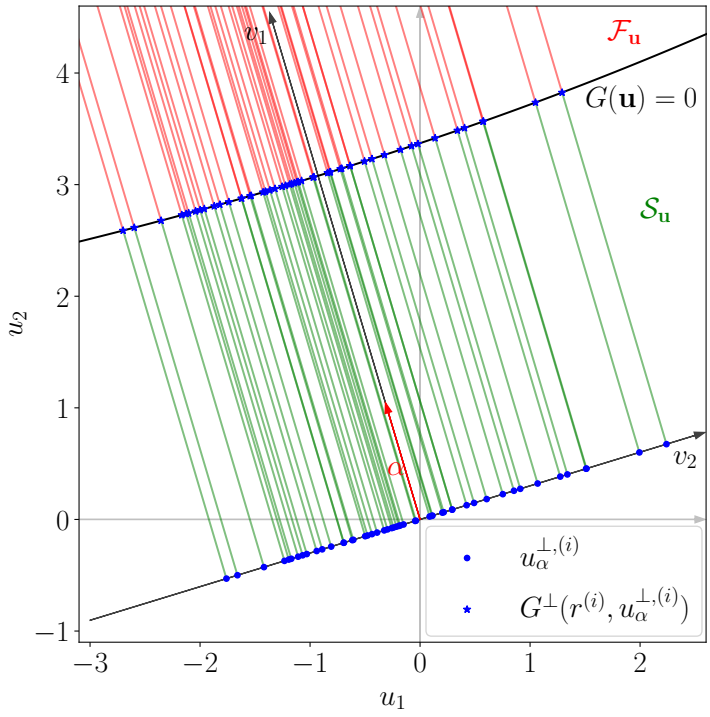

FIGURE 2.5: Graphical representation of the LS procedure.

as "Advanced Line Sampling" (ALS). The update simply consists in calculating the distance of each estimated root $r^{(i)}$ from the origin. If the distance is smaller than the one calculated with the current estimated MPFP, then the estimated MPFP is updated as such as the direction $\boldsymbol{\alpha}$.

Synthesis on failure probability estimators

In this section, a non-exhaustive list of failure probability estimators has been presented. The range of the different techniques employed with all of their numerous adaptations reflects the variety of challenges that the analyst may face when evaluating the probability of rare events. The recommendation of one technique over others is very application-based. Although its implementation is very straightforward, direct CMC is very limited as soon as failure probabilities become very small (e.g. smaller than 10^{-5}) even when the LSF is fast to evaluate.

FORM approximation is very efficient in both cases where the LSF has a high degree of linearity in the standard normal space or when only an order of magnitude of the failure probability is sufficient to the analyst. However, the optimization process does not always guarantee the obtention of the MPFP especially when the LSF is highly nonlinear. In addition, the approximation around a unique MPFP renders the analysis very localized which may lead to strong underestimations of the failure probability in the case of multiple failure regions. However, this risk can be significantly reduced if appropriate techniques are employed. The main disadvantage of FORM is that, contrary to the simulation methods, it does not propose any error estimation.

Importance sampling has proven itself highly efficient for reducing the variance of CMC with the use of an instrumental density. Indeed, sampling according to a well-chosen density enables to better reach the failure domain and reduce the number of required simulations. A popular simple choice is to use FORM information and construct a density centered on the MPFP. However, its performance strongly depends on how close the instrumental density is to the unknown

optimal density. A bad choice on the instrumental density can even yield a variance worse than the one obtained with CMC.

Subset simulation enables to transform the initial distant failure region into closer conditional failure regions. As such, it is particularly insensitive to the spread of the failure region over the entire design space. However, it has generally proven to still require a relatively high amount of simulations for reaching small variance values for low failure probabilities.

Finally, line sampling, as part of the conditional methods, intelligently transforms the $n_{\mathbf{X}}$-dimensional failure probability expression into the expectation of a one-dimensional conditional failure probability. Its convergence improves with the degree of linearity of the LSF. However, its performance is highly dependent on the direction $\boldsymbol{\alpha}$ and the number of LSF calls necessary for finding the roots. More specifically, this technique becomes also limited when undetected failure regions exist.

2.4 Structural reliability within extra-probabilistic frameworks

The probabilistic framework is a very mature and powerful way to model and propagate aleatory uncertainty. However, the exact knowledge of the joint pdf $f_{\mathbf{X}}$ is generally an assumption. Indeed, the definition of the pdf relies on more or less strong hypotheses depending on the richness of the available information (through expert judgments or experimental data). In that matter, other uncertainty representations, referred to as extra-probabilistic, have been developed for cases where information is limited.

Many types of extra-probabilistic models can be found in the literature depending on the nature of the uncertainty and the available information. The following subsections aim at presenting some that are considered in this thesis, namely convex models, evidence theory, possibility distributions and probability box (p-box) models. Their main properties and their application to reliability analysis are described. The reader is also referred to (Beer et al., 2013; Zio and Pedroni, 2013) for a clear overview of the different uncertainty models that exist and to the references in each subsection for more details about each of them. In order to maintain a coherence with the rest of the thesis, the variables that are modeled by such representations are described by the vector $\mathbf{Y} = (Y_1, \cdots, Y_{n_{\mathbf{Y}}})^\top$.

2.4.1 Convex model

Convex models (Ben-Haïm and Elishakoff, 1990) are a non-probabilistic representation of uncertainty in the sense that they consider sets without any assigned notion of measure. Their use is justified through the fact that only limited information is needed to construct them which is, in many engineering applications, more relevant than adding probability assumptions (Wang et al., 2008).

The construction of a convex set relies on the marginal intervals I_{Y_i} of each epistemic variable Y_i plus some correlation information which will define the shape of the set. When no correlation is considered, the convex set reduces to the interval representation. Different types of convex sets have been developed in order to account for correlations such as the ellipsoid model (Zhu et al., 1996; Luo et al., 2008; Kang and Zhang, 2016). More recently, the multidimensional parallelepiped model (Jiang et al., 2014; Ni et al., 2016; Zheng et al., 2018) has been proposed in order to model uncorrelated and correlated variables in a common framework.

In this thesis, a convex model is denoted as $C\left(\mathbf{I}_{\mathbf{Y}}, \boldsymbol{\rho}_{\mathbf{Y}}\right)$ where $\mathbf{I}_{\mathbf{Y}}$ is the Cartesian product of each marginal interval I_{Y_i} and $\boldsymbol{\rho}_{\mathbf{Y}}$ quantifies the correlation between each epistemic variable. As the input variables are modeled through a non-probabilistic convex set, the output QoI is a non-probabilistic interval which may be obtained through optimization, discretization or applying the "vertex" method (Dong and Shah, 1987).

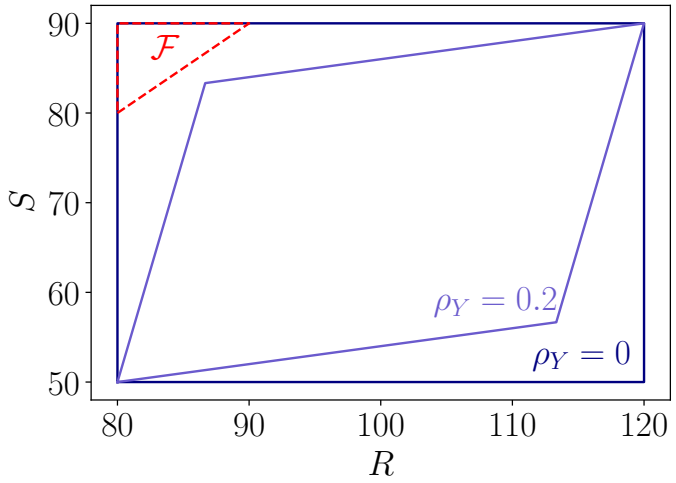

FIGURE 2.6: Illustration of the interval and parallelepiped convex models on the $R - S$ problem.

The $R - S$ example is treated by considering the parallelepiped model $C(\mathbf{I_Y}, \boldsymbol{\rho_Y})$ with $I_R = [80, 120]$, $I_S = [50, 90]$ and $\rho_{RS} = 0$ (interval model) or $\rho_{RS} = 0.2$. The shapes of both sets are shown in Figure 2.6. One can see that the interval model contains the failure domain $\mathcal{F}$ as $I_{R-S} = [-10, 70]$ while the reduced set corresponding to $\rho_{RS} = 0.2$ escapes the failure domain with $I_{R-S} = [3.33, 57.67]$.

2.4.2 Evidence theory

Evidence theory (also called Dempster-Shafer (DS) theory) (Dempster, 1967; Shafer, 1976) aims at relaxing the probabilistic framework by assigning probability masses to subsets of the uncertain variables instead of singletons. The subsets A_i of the power set $\Omega(Y_i)$ are called "focal sets" on which the *basic probability assignment* (BPA) is applied through the following mass function m:

$$m : \left| \begin{array}{rcl} \Omega(Y_i) & \longrightarrow & [0,1] \\ A_i & \longrightarrow & m(A_i) \text{ s.t. } \sum_{A \in \Omega(Y_i)} m(A_i) = 1. \end{array} \right. \tag{2.27}$$

Two measures can then be defined, namely the "belief function" $\text{Bel}(\cdot)$ and the "plausibility function" $\text{Pl}(\cdot)$, that bound the realization of any event E:

$$\text{Bel}(E) = \sum_{A_i \subseteq E} m(A_i) \tag{2.28a}$$

$$\text{Pl}(E) = \sum_{A_i \cap E \neq \emptyset} m(A_i). \tag{2.28b}$$

The belief measure can be seen as a lower probability of the event E as it adds up all the masses of each focal set that is entirely contained in E. The plausibility measure, on the other hand, can be seen as an upper probability as it adds up all the masses of each focal set that has at least one element in E. When the focal sets are singletons, the belief measure is equal to the plausibility measure and evidence theory reduces to probability theory. When there is only one focal set, it reduces to the interval representation.

Evidence theory has been widely used for reliability analysis such as in Jiang et al. (2013) or in Zhang et al. (2014) where it is combined with FORM and SORM methods. Indeed, when considering the failure event $\mathcal{F} = \{Z \in]-\infty, 0]\}$, the belief and plausibility measures yield bounds on the failure probability. To estimate these bounds, the focal sets Z of the LSF are

obtained by evaluating its extreme values in each interval obtained from the joint BPA of the inputs. Then, the bounds on the failure probability are calculated as follows:

$$\underline{P_f} = \text{Bel}(\mathcal{F}) = \sum_{Z \subseteq \mathcal{F}} m(Z) \tag{2.29a}$$

$$\overline{P_f} = \text{Pl}(\mathcal{F}) = \sum_{Z \cap \mathcal{F} \neq \emptyset} m(Z). \tag{2.29b}$$

The procedure is illustrated on the $R - S$ example. Table 2.1 presents the focal sets and corresponding BPA of both input variables and of the LSF. The maximum probability is then

TABLE 2.1: BPA of R (top line), BPA of S (left column) and extreme values of $g(R, S)$ at each joint BPA (all the rest).

S \ R	$[80, 85]$ 0.05	$[85, 90]$ 0.05	$[90, 100]$ 0.4	$[100, 110]$ 0.4	$[110, 115]$ 0.05	$[115, 120]$ 0.05
$[50, 60]$ 0.1	$[20, 35]$ 0.005	$[25, 40]$ 0.005	$[30, 50]$ 0.04	$[40, 65]$ 0.04	$[50, 65]$ 0.005	$[55, 70]$ 0.005
$[60, 70]$ 0.3	$[10, 25]$ 0.015	$[15, 30]$ 0.015	$[20, 40]$ 0.12	$[30, 55]$ 0.12	$[40, 55]$ 0.015	$[45, 60]$ 0.015
$[70, 80]$ 0.5	$[0, 15]$ 0.025	$[5, 20]$ 0.025	$[10, 30]$ 0.2	$[20, 45]$ 0.2	$[30, 45]$ 0.025	$[35, 50]$ 0.025
$[80, 85]$ 0.09	$[-5, 5]$ 0.0045	$[0, 10]$ 0.0045	$[5, 20]$ 0.036	$[15, 35]$ 0.036	$[25, 35]$ 0.0045	$[30, 40]$ 0.0045
$[85, 90]$ 0.01	$[-10, 0]$ 0.0005	$[-5, 5]$ 0.0005	$[0, 15]$ 0.004	$[10, 30]$ 0.004	$[20, 30]$ 0.0005	$[25, 35]$ 0.0005

obtained by summing all the probability masses for which the corresponding interval has at least one element that belongs to the failure domain (which corresponds to the lower bound being lower or equal to zero) and the minimum probability is obtained by summing all the probability masses for which all the elements of the corresponding interval belong to the failure domain (which corresponds to the upper bounds being lower or equal to zero). Here, the results are $\overline{P_f} = 0.025 + 0.0045 + 0.0045 + 0.0005 + 0.0005 + 0.004 = 3.9 \times 10^{-2}$ and $\underline{P_f} = 5 \times 10^{-4}$.

2.4.3 Possibility theory

Possibility theory (Zadeh, 1967; Dubois and Prade, 1980) is a special case of evidence theory where focal sets are nested. In analogy with probability theory, it is defined with the following possibility distribution function π:

$$\pi : \Omega(\mathbf{Y}) \to [0, 1] \text{ s.t. } \sup_{y \in \Omega(Y)} \pi(y) = 1. \tag{2.30}$$

It follows the definition of the possibility $\text{Pos}(\cdot)$ (also denoted as $\Pi(\cdot)$ in the literature) and necessity $\text{Nec}(\cdot)$ (also denoted as $N(\cdot)$ in the literature) measures for any subset $A \subset \Omega(\mathbf{Y})$:

$$\text{Pos}(A) = \sup_{y \in A} \pi(y) \tag{2.31a}$$

$$\text{Nec}(A) = \inf_{y \notin A} (1 - \pi(y)) = 1 - \text{Pos}(A^c) \tag{2.31b}$$

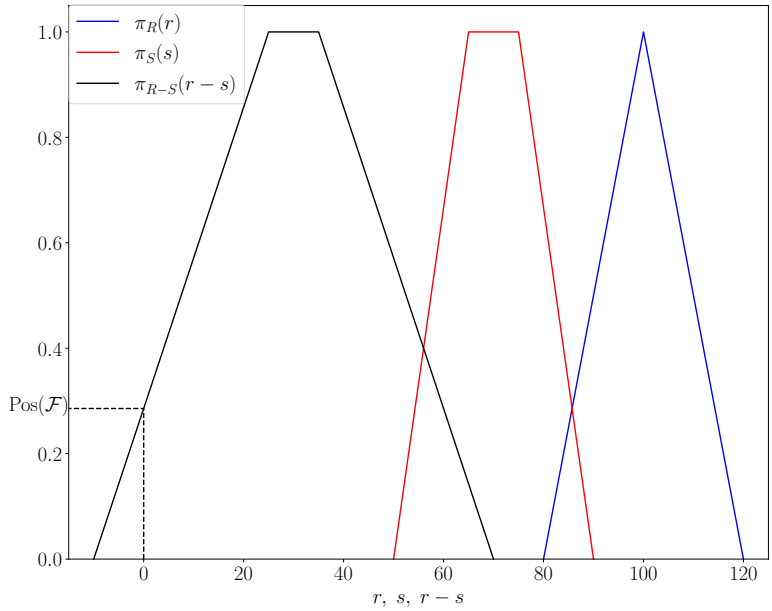

FIGURE 2.7: Illustration of the possibility distributions for the $R - S$ problem.

where A^c is the complementary event of A. So-called α-cuts are commonly associated to a possibility distribution as they represent nested confidence intervals with the following expression:

$$\left[\underline{y}_\alpha, \overline{y}_\alpha\right] = \{y, \pi(y) \geq \alpha\}. \tag{2.32}$$

The extension principle developed by Zadeh (1967) enables to propagate possibility distributions through $\mathcal{M}(\cdot)$ in order to evaluate the possibility distribution on the variable of interest $Z = \mathcal{M}(\mathbf{Y})$:

$$\pi_Z(z) = \begin{cases} \sup\{\min(\pi_1(y_1), \cdots, \pi_{n_\mathbf{Y}}(y_{n_\mathbf{Y}})) | \mathcal{M}(y_1, \cdots, y_{n_\mathbf{Y}}) = z\} & \text{if } \mathcal{M}^{-1}(z) \neq \emptyset, \\ 0 & \text{otherwise.} \end{cases} \tag{2.33}$$

Therefore, possibility distributions may also be propagated through the LSF in the context of reliability analysis. The variable of interest is also described with its corresponding possibility function on which the bounds of the failure probability are estimated as follows:

$$\overline{P_\mathrm{f}} = \mathrm{Pos}\left(\mathcal{F}_\mathbf{y}\right) = \sup_{z \in \mathcal{F}_\mathbf{y}} \pi_Z(z) \tag{2.34a}$$

$$\underline{P_\mathrm{f}} = \mathrm{Nec}\left(\mathcal{F}_\mathbf{y}\right) = \inf_{z \notin \mathcal{F}_\mathbf{y}} \left(1 - \pi_Z(z)\right) \tag{2.34b}$$

The $R - S$ example is considered by assigning a triangular possibility function to R and a trapezoidal possibility function to S. As shown in Figure 2.7, this elementary case yields a trapezoidal possibility distribution of the LSF. The bounds on the failure probability are $P_\mathrm{f} \in [0, 0.29]$.

2.4.4 Probability boxes

The probability box (p-box) framework assigns an imprecise cdf to the uncertain variable Y_i. The true, yet uncertain cdf F_Y, is bounded by an upper one $\overline{F}_Y$ and a lower one $\underline{F}_Y$ such that:

$$\overline{F}_Y(y) \leq F_Y(y) \leq \underline{F}_Y(y). \tag{2.35}$$

Two groups of p-boxes are distinguished, namely "free p-boxes" and "parametric p-boxes". Free p-boxes do not make any further assumptions other than the bounds on the true cdf. Any shape that respects the bounds and the properties of a cdf is possible. Parametric p-boxes assume that the distribution type is known or, at the very least, belongs to a parametric family. The uncertainty lies in the parameters of the distribution (e.g. mean and variance) that are modeled using simple intervals. Therefore, at equal cdf bounds, parametric p-boxes are more informative than free p-boxes by adding the information concerning the distribution type. A comparison between free and parametric p-boxes in the context of surrogate modeling for reliability assessment is given in Schöbi and Sudret (2017).

Many uncertainty models can be represented as free p-boxes. Indeed, by considering the event $\{Y \leq y\}$, plausibility and necessity measures can be seen as lower cdfs while belief and possibility measures can be seen as upper cdfs. Probability theory is retrieved when $\overline{F}_Y = \underline{F}_Y$.

Monte Carlo sampling with free p-box variables can be performed by using inverse sampling as shown by Zhang et al. (2010). With parametric p-box variables, the bounds on the failure probability are obtained through optimization in the uncertain space of the distribution parameters (Balesdent et al., 2016). A review on more advanced techniques used to reduce the computational burden when propagating free and parametric p-box variables is available in Faes et al. (2021).

The $R - S$ example is taken here by considering that $R \sim \mathcal{N}(\mu_R \in [95, 100], \sigma_R = 10)$ and $S \sim \mathcal{N}(\mu_S = 70, \sigma_S \in [5, 9])$. The induced p-boxes are depicted in Figure 2.8 as well as the resulting p-box on $Z = R - S$ considering both free and parametric cases. The p-box obtained from the parametric representation is contained in the one obtained from the free representation.

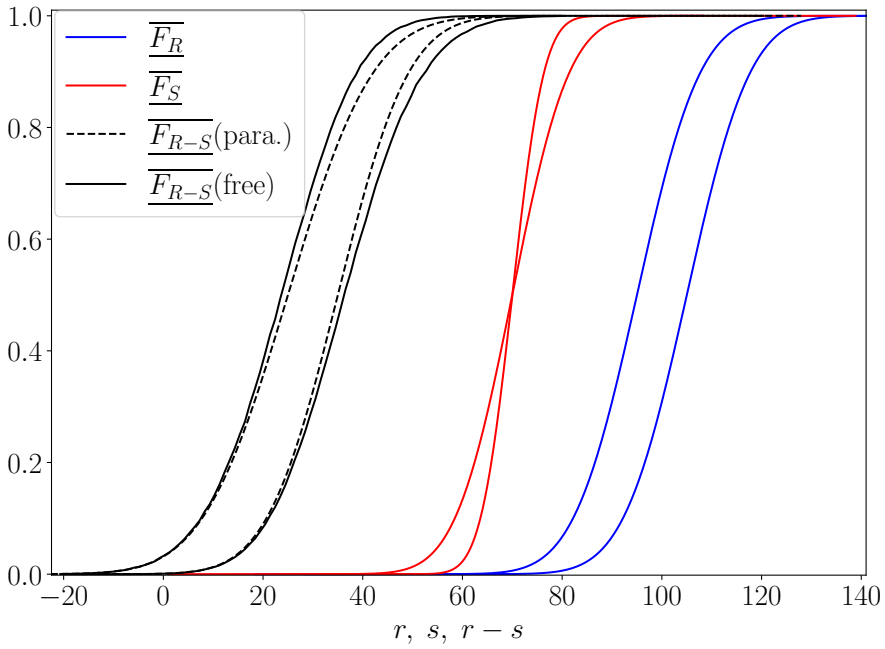

FIGURE 2.8: Illustration of the probability boxes for the $R - S$ problem.

The reason here is that the free representation allows to consider the upper and lower cdf on S which do not correspond to parametric Gaussian cdf (but rather to the combination of both Gaussian cdf at $\sigma_S = 5$ and $\sigma_S = 9$). In this case, $P_f^{\text{free}} \in \left[6.90 \times 10^{-4}, 3.18 \times 10^{-2}\right]$ and $P_f^{\text{para.}} \in \left[8.73 \times 10^{-4}, 3.16 \times 10^{-2}\right]$.

2.5 Links between the various uncertainty representations

As already mentioned in the case of p-box representation, many of these uncertainty models are closely related in the context of structural reliability. Figure 2.9 (originally proposed in Ajenjo et al. (2022)) summarizes these links that either represent a gain of information or a path from a model to another. Each number has the following meaning:

1. Bounding Y in $\left[\underline{Y}, \overline{Y}\right]$;
2. Add the information of dependency with a convex model and its coefficient of correlation;
3. Assigning weights to subsets of the interval with the mass function $m(\cdot)$;
4. Assigning a possibility distribution $\pi(\cdot)$ in the interval;
5. $Y^L = Y^U$;
6. Bounding the cdf F_Y in $\left[\underline{F}_Y, \overline{F}_Y\right]$;
7. Add the information about the probability law;
8. $\overline{F}_Y = \underline{F}_Y$;
9. $\overline{F}_Y = \text{Pl}(Y \leq y)$ and $\underline{F}_Y = \text{Bel}(Y \leq y)$ (see Baudrit and Dubois (2006) for more information);
10. Discretizing the support of the distribution into disjoint intervals of weight $m(]y_i, y_{i+1}]) = m_i = \mathbb{P}(Y \in]y_i, y_{i+1}])$ (see Baudrit and Dubois (2006) for more information).;
11. $\overline{F}_Y = \text{Nec}(Y \leq y)$ and $\underline{F}_Y = \text{Pos}(Y \leq y)$ (see Baudrit and Dubois (2006) for more information);
12. Discretizing the possibility distribution into nested intervals by equally discretizing the α-axis and assigning the weight $m_i = \alpha_i - \alpha_{i+1}$ to the corresponding interval $\left[\underline{y_i}, \overline{y_i}\right]$ which is the α_i-cut (see Baudrit and Dubois (2006) for more information).

The figure can be read from top to bottom in terms of added information where a solid line represents the path from a less informative model to a more informative one. The dotted lines represent a path from a model to another without adding information. Note that a solid line could be added from the interval to the probability boxes but has been removed here to make the diagram easier to read.

Two groups of models may be distinguished in the diagram. On the left side, the uncertainty representations are interval-based. If no information is added to the bounds of the epistemic variables, the interval model and more generally the convex model may be used. DS structures and possibility distributions enable to divide the initial interval into more or less plausible smaller intervals based on expert knowledge. These representations reduce to a deterministic value with no epistemic uncertainty. On the right side, the uncertainty representations are probability-based. The path of information goes from the free to the parametric p-box representations and finally reduces to the purely probabilistic representation. Although these two groups of models seem to be built on different theoretical frameworks, the dotted lines show how they may be related in the context of reliability. These relations will be further discussed in Chapter 5.

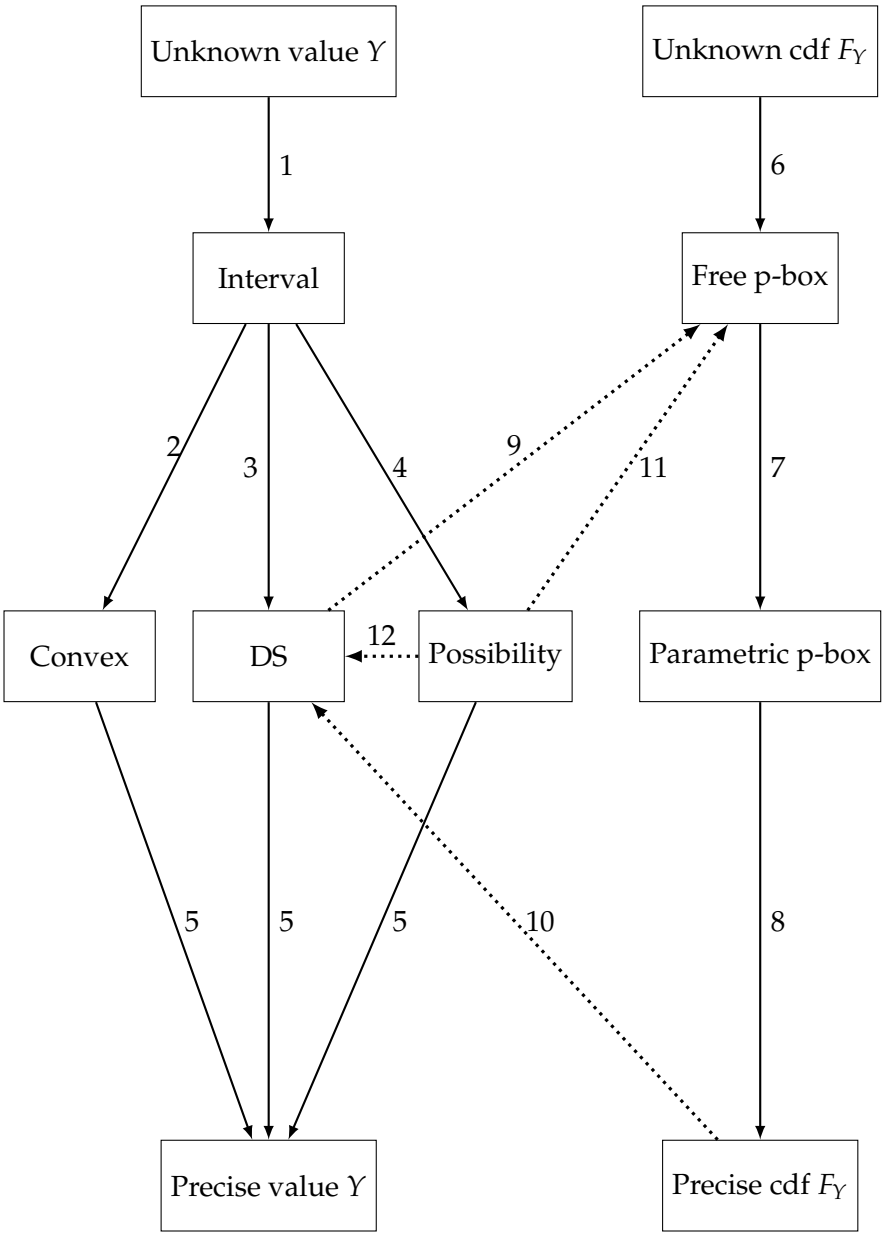

FIGURE 2.9: Diagram of the links between various uncertainty representations (solid lines ≡ added information, dotted lines ≡ no information added).

2.6 Synthesis

The framework of structural reliability in which this thesis falls has been presented. Although the overall formulation of structural reliability is well identified, the consideration of different sources and treatments of uncertainty has led to multiple uncertainty representations and, consequently, to different uncertainty propagation methods.

The probabilistic framework appears to be very mature with a panel of advanced failure probability estimation techniques which enables the analyst to tackle many different challenges involved in the evaluation of rare events. However, choosing the right estimation technique is not always straightforward especially when poor information about the LSF is available. QoIs such as failure probabilities and quantiles are increasingly considered in safety standards.

Nevertheless, their values remain the end part of an idealized framework with successive

assumptions. In particular, the probabilistic assumptions involved in the uncertainty quantification step have been pointed out leading to alternative representations, some of which have been succintly introduced in this chapter. Although bringing alternatives, the variety of available methods might confuse the analyst. Indeed, it does not seem trivial to identify unambiguously which uncertainty model and uncertainty propagation tool should be chosen.

In addition, multiple sources of uncertainty often exist within a same analysis which leads to the consideration of *hybrid reliability analysis* (HRA). There is therefore a need for a common uncertainty propagation framework. Some links between different uncertainty models have already been discussed. Chapter 4 will enhance these links with the use of a unifying framework referred to as *random set theory*. Before that, the next chapter aims at presenting the reliability analyses relevant to the two industrial application cases which motivated the work presented in this thesis.

CHAPTER 3

Motivating industrial application cases

Contents

3.1 Objectives

As mentioned in the introduction, this thesis is motivated by two industrial application cases that are relevant to the energy supplier EDF. Indeed, the large panel of industrial assets operated by EDF provides examples of physical systems for which both performance and safety are of major concerns. Moreover, the general complexity of these systems together with the rareness of the events for which safety analyses are conducted represent typical cases for which multiple sources of uncertainty, as introduced in Chapter 2, need to be accounted for.

This chapter is divided into two main sections that correspond to the presentations of the reliability of penstocks and the reliability of nuclear plant thermal-hydraulic systems w.r.t. a loss-of-coolant accident scenario, respectively. The main objectives are:

1. to describe in detail the industrial contexts that lead to the deployment of robustness analysis on the reliability assessments;

2. to describe in detail the reliability framework relevant to each analysis and the tools that are currently used for evaluating the corresponding QoIs. This is important in order to identify the challenges that the robustness analyses will have to face and, consequently, to justify the different methodologies that will be proposed in the next chapters.

3.2 Reliability of penstocks

3.2.1 Industrial context

The first industrial application case concerns the reliability study of penstocks for which the interested reader is referred to Ardillon et al. (2018), Bryla et al. (2020), and Ardillon et al. (2022) for further details than those provided in this section. Penstocks represent an assembly of pipes made of steel used to transport water under pressure from the water dam to the hydroelectric turbine. An example of such structure is given in Figure 3.1. EDF operates more than 500 penstocks in France representing a total length of over 300 km. Most of them were industrialized during the 20^{th} century after the use of many different manufacturing processes.

Due to thickness loss resulting from corrosion and to the propagation of structural defaults resulting from the welding process, their mechanical integrity must be justified at all time. The usual justification relies on diagnoses involving non-destructive thickness measurements and material properties characterizations. Then, a deterministic margin factor (MF) is evaluated as the ratio of an allowable mechanical stress over the mechanical stress present in the pipe during operation. The penstock is considered as "fit for service" if this ratio is greater that one.

The evaluation of MF depends on many variables which mainly pertain to mechanical and geometrical properties which are very sparse due to the different manufacturing processes. Therefore, the mechanical integrity needs to be justified for a very large panel of penstocks with different characteristics which justifies the need of a numerical mechanical model.

3.2.2 Mechanical model for penstocks

The MF is evaluated as the ratio between the allowable stress σ_a and the operational stress σ_o both expressed as:

$$\sigma_{\text{a}} = \min\left(\frac{R_e}{1.5}; \frac{R_m}{2.4}\right) \tag{3.1a}$$

$$\sigma_{\text{o}} = \frac{PR}{e} \tag{3.1b}$$

FIGURE 3.1: Example of a penstock operated by EDF.

where R_m is the tensile strength, R_e is the yield strength, P is the real-time controlled operating pressure in the pipe, R is the radius of the pipe and e is the thickness of the pipe. As mentioned previously, the thickness decreases through the years due to corrosion such that the resulting thickness at year N can be expressed as:

$$e(N) = e_{\text{nom}} + \Delta e_{\text{extra}} - \Delta e_{\text{corr}}(N) \tag{3.2}$$

where e_{nom} is the targeted manufacturing thickness, Δe_{extra} is the extra thickness brought by the manufacturing process and $\Delta e_{\text{corr}}(N)$ is the thickness lost after N years due to corrosion. A linear relationship is considered between the yield strength R_e and the tensile strength R_m such that:

$$R_m = AR_e - B + \varepsilon \tag{3.3}$$

where A and B are two positive real numbers and ε represents the error due to the linear approximation.

Despite non-destructive measurements being performed, the values of R_m (and consequently R_e), e and ε are not precisely known for each penstock. These variables are modeled through probabilistic distributions built upon the data obtained from these measurements and expert judgment. The historical approach to treat these uncertainties is to evaluate MF in a penalized configuration by affecting to all three variables the value $X^{\text{pen}} = \mu_X - \gamma\sigma_X$ where μ_X is the mean of the random variable, σ_X is the standard deviation of the random variable and γ is the penalization coefficient. In practice, the value $\gamma = 2$ is often used which corresponds to the 2.5% quantile.

3.2.3 The reliability model of penstocks

The approach described above considers uncertainty but propagates it through the mechanical model in a deterministic and conservative way. Hence, a reliability assessment model was developed for estimating failure probabilities at different values of γ. This semi-probabilistic approach aims at determining, for a given configuration of penstock, the value of γ that leads to a specific failure probability (e.g. 10^{-6}) in order to evaluate the degree of conservatism (or potential overestimated safety) obtained with the value $\gamma = 2$. The reliability analysis is divided through the consideration of two failure modes:

TABLE 3.1: Input probabilistic modeling of $\mathbf{X}$ for the penstock use-case.

X_i	Distribution	param. 1	param. 2	param. 3
$X_1 = R_m$ (MPa)	Lognormal	μ_{R_m}	σ_{R_m}	-
$X_2 = \varepsilon$ (MPa)	Normal	μ_ε	$\mu_\varepsilon.\omega$	-
$X_3 = \Delta e_{\text{corr}}$ (mm)	Normal	$\mu_{\Delta e_{\text{corr}}}$	$\sigma_{\Delta e_{\text{corr}}}$	-
$X_4 = \Delta e_{\text{extra}}$ (mm)	Normal	$\mu_{\Delta e_{\text{extra}}}$	$\sigma_{\Delta e_{\text{extra}}}$	-
$X_5 = a$ (mm)	Uniform	0	$a_{\max}$	-
$X_6 = K_{\text{IC}}$ (MPa.$\sqrt{\text{m}}$)	Weibull Min	$\beta_{K_{\text{IC}}}$	$\alpha_{K_{\text{IC}}}$	$\gamma_{K_{\text{IC}}}$

- the plastic collapse affecting parent metal;
- the brittle failure affecting welds.

Both are described in more details hereafter.

The plastic collapse failure mode

This failure mode, taken from the standard in (BS7910, 2015), is defined as the operating circumferential stress σ_o taking higher values than the flow stress σ_f expressed as:

$$\sigma_f = \min\left(\frac{R_m + R_e}{2}; 0.85 R_m\right). \tag{3.4}$$

The following LSF that was made independent from the in-service pressure and the pipe radius is defined at year N as:

$$G_N(\mathbf{X}, \boldsymbol{\nu}) = \sigma_f - \frac{\sigma_a\left(e_{\text{nom}} + \Delta e^{\text{pen}}\right)}{\text{MF}\left(e_{\text{nom}} + \Delta e(N)\right)} \tag{3.5}$$

where $\Delta_e(N) = \Delta e_{\text{extra}} - \Delta e_{\text{corr}}(N)$, $\mathbf{X} = \left[R_m, \Delta e_{\text{extra}}, \Delta e_{\text{corr}}, \varepsilon\right]^\top$ is the vector of random variables and $\boldsymbol{\nu}$ is the vector of deterministic input variables.

The brittle failure mode

The criterion that describes brittle failure is taken from the norm in BS7910 (2015) which defines an admissible diagram based on the two variables $L_R = \sigma_c / R_e$ and $K_R = K_I / K_{\text{IC}}$ where K_I is the stress intensity factor that depends on the height of the default a and K_{IC} is the tenacity of the material. The corresponding LSF is expressed at year N as:

$$G_N(\mathbf{X}, \boldsymbol{\nu}) = K_R(\mathbf{X}, \boldsymbol{\nu}, N) - f\left(L_R(\mathbf{X}, \boldsymbol{\nu}, N)\right) \tag{3.6}$$

where more information about the specific function $f(\cdot)$ can be found in (BS7910, 2015). This failure mode considers two additional random variables such that $\mathbf{X} = \left[R_m, \Delta e_{\text{extra}}, \Delta e_{\text{corr}}, \varepsilon, a, K_{\text{IC}}\right]^\top$. The distribution characteristics of each random variable is given in Table 3.1.

The failure event is defined as the *annual failure probability* which means that failure has not yet occurred at year N but occurs at year $N+1$ where the loss of thickness from year N to year $N+1$ is expressed through the variable Δe_{an}. Therefore, one gets $\Delta e(N+1) = \Delta e_{\text{extra}} - \Delta e_{\text{corr}}(N) - \Delta e_{\text{an}}$. By simplifying the notations such that $G_i = G_i(\mathbf{X}, \boldsymbol{\nu})$, the annual failure probability is expressed as:

$$P_{\text{f}} = \mathbb{P}\left(G_{N+1} \leq 0 \cap G_N > 0\right) = \mathbb{P}\left(G_{N+1}.G_N \leq 0\right). \tag{3.7}$$

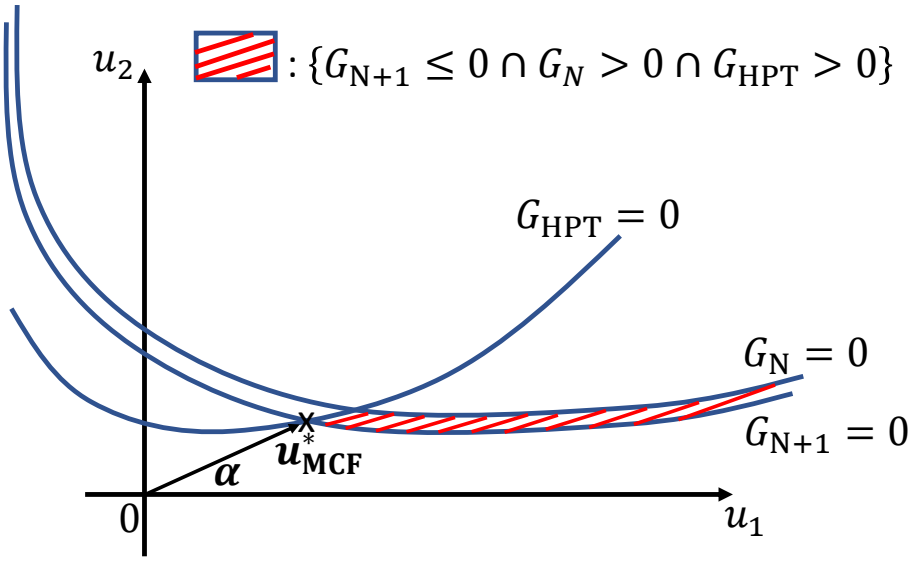

FIGURE 3.2: Illustration of typical failure domain encountered in the penstock use case in the standard normal space and principle of Multiconstraint-FORM used in the FISTARR algorithm.

The equality between the intersection and product formulations comes from the fact that the failure domain at year N is contained in the failure domain at year $N+1$ due to the monotonic behavior of the LSF w.r.t. time.

It has also been added to the analysis the fact that some penstocks are confronted to a *hydraulic pressurized test* before being operated. Therefore, the annual failure probability becomes conditioned to the event that the penstock successfully passed the test which is expressed as $G_{HPT} > 0$. The conditional failure probability at year $N+1$ therefore becomes:

$$P_f = \mathbb{P}\left(G_{N+1} \leq 0 \cap G_N > 0 \mid G_{HPT} > 0\right) \tag{3.8}$$

which leads to:

$$P_f = \frac{\mathbb{P}\left(G_{N+1} \leq 0 \cap G_N > 0 \cap G_{HPT} > 0\right)}{\mathbb{P}\left(G_{HPT} > 0\right)}. \tag{3.9}$$

The numerator in Eq. (3.9) corresponds to the probability of an intersection of three events which is depicted as the red hatched band in Figure 3.2.

This probability is usually very small (e.g. smaller than 10^{-6}) as a result of a complex narrowed failure domain. Consequently, a panel of failure probability estimators have been implemented to efficiently evaluate the annual failure probability and the annual conditional failure probability associated to both failure modes.

3.2.4 A panel of dedicated failure probability estimation techniques

The G-functions are a combination of analytical expressions which makes them fast to evaluate. Nevertheless, the fact that the failure probabilities to estimate are very small and that they must be evaluated for a very large number of configurations of penstocks prevents from the direct use of CMC. The techniques of FORM-IS and SS have therefore been used and compared with CMC results only for "high" (e.g. greater than 10^{-5}) probabilities.

The FORM-IS technique is generally preferred and SS is rather used as a backup technique for when FORM-IS gives unsufficient precision. When considering the annual failure event represented as a unique intersection between the events $G_{N+1} \leq 0$ and $G_N > 0$, the FORM

analysis is applied on G_{N+1} in order to get the MPFP $\mathbf{u}^*$ in the standard normal space. Then, the IS instrumental density is defined as a Gaussian distribution centered on the MPFP with unitary variance.

When considering the conditional annual failure event, the numerator in Eq. (3.9) involves a double intersection. In this case, sampling around the same MPFP as previously is inefficient as this point might be far from the failure domain. Instead, a *multi-constraint FORM* (MCF) analysis is performed in order to find the closest point $\mathbf{u}^*_{\text{MCF}}$ which satisfies $G_{N+1} \leq 0$ and $G_{\text{HPT}} > 0$. An illustration of such a point is given in Figure 3.2. The MCF algorithm is an important part of the method denoted "FISTARR" (for **F**ORM-**IS**-**T**ested **A**utomatically-**R**apid sea**R**ch). As the convergence of the MCF algorithm is not ensured, FISTARR consists in automatically testing an ordered list of optimization algorithms until the convergence of FORM-IS becomes acceptable.

The optimization algorithms for the MCF analysis are taken from the NLopt Python Library implemented in OpenTURNS (Baudin et al., 2017). More generally, the different estimation techniques have been implemented in a dedicated software named Persalys Penstock (Ardillon et al., 2022), which relies on the OpenTURNS library as a numerical background for the reliability assessment techniques, and which enables to define the different configurations of penstocks and the reliability analysis. For a majority of configurations, convergence is achieved within a few seconds. However, the failure probability of some configurations remains challenging to evaluate. In Chapter 5, FISTARR will be widely used while Chapter 6 will present an adaptation of LS algorithm.

3.2.5 Challenge and motivations

The info-gap (IG) robustness framework will be applied on the reliability assessment of penstocks in Chapter 5 and in Chapter 6. Indeed, some variables, especially parameters of probability distributions are not always straightforward to quantify. Interesting information would be to evaluate if some configurations of penstocks are more robust than others to these uncertainties.

Just as the standard penstock reliability analyses, these robustness analyses will imply many estimations of failure probabilities. Therefore, it will be necessary for the failure probability estimation technique to be performant both in terms of precision of the estimation and in terms of computational time.

3.3 Reliability of thermal-hydraulic systems during a loss-of-coolant accident

3.3.1 Industrial context

France is certainly one of the countries that has the most invested in civil nuclear facilities for electricity production as it is responsible for around 70% of the total national production. EDF, being the historical French electricity producer, operated nowadays 56 nuclear reactors of different capacities. This industrial sector is clearly at the center of many societal, political and scientific debates as it offers an unparalleled carbon-free way of generating electricity at potential risks that have already proven to be devastating. The commissioning and decommissioning of nuclear power plants are therefore strongly regulated, in particular, in France, by the ASN which imposes safety requirements that EDF must prove to meet with consequent justifications.

One of these requirements concerns the study of the peak cladding temperature of fuel rods in case of an Intermediate Break Loss-Of-Coolant Accident (IBLOCA) in the primary loop of a nuclear pressurized water reactor. This accidental scenario is characterized by the rapid depressurization of the primary circuit and the loss of a large mass of water in the boiler. Although the nuclear reactions in the core are automatically stopped, thermal power is still generated after the shutdown phase, mainly due to the the fission products that remain in the fuel. In this

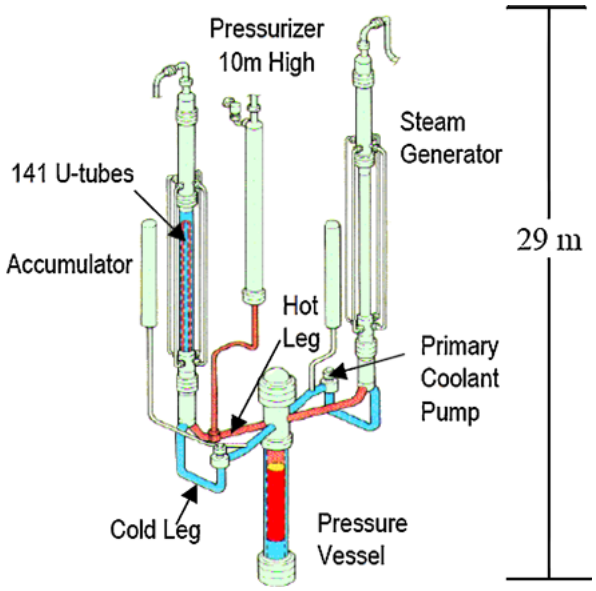

FIGURE 3.3: Scheme of the Large Scale Test Facility

situation, a saturation state can be reached in the primary water through the combined effect of the loss of coolant at the break and the continuous heat production. The main risk from this temperature rise is the possibility of fusion of the nuclear core if a certain temperature threshold is reached. The maximum temperature reached during the scenario must therefore be proven to remain below a critical value to prevent any deterioration of the reactor state.

In this thesis, this accidental scenario will be considered on a reduced model, named LSTF (Large Scale Test Facility) (Liu et al., 1997) and presented in Figure 3.3. This Japenese facility aims at simulating a pressurized water reactor that presents a reduced 1/48 volume scale. The pressure vessel is electrically heated so that it is possible to carry out physical experiments of an IBLOCA scenario (Mazgaj et al., 2016). The studied use case is related to the ROSA-2/LSTF test 2 which considers a 17% cold leg IBLOCA.

3.3.2 CATHARE2 black-box model

Nuclear systems are typical cases for which performing real experiments becomes quickly limited. However, they also represent typical systems with many interactions and complex physics. Conservative simplifications have been used during a long time to justify their operational safety. Yet, the improvements in the modeling of nuclear systems together with the increasing availability of data enabled to develop numerical simulators that are more representative of the actual behavior of nuclear installations. This lead to the intensive use of so called Best Estimate (BE) physical models (D'auria et al., 2006). In France, this resulted in the development of the BE code CATHARE (Code Avancé de ThermoHydraulique pour les Accidents de Réacteurs à Eau) which is jointly developed by the CEA, EDF, Framatome and the IRSN. The modularity of this code allows the simulation of a wide variety of accidental nuclear transients and thermal-hydraulic systems (Geffraye et al., 2011).

CATHARE2 is a system code meaning that it can represent a whole installation such as a nuclear power plant by means of different macroscopic components. These components are grouped into four main modules, namely pipes (1D flow), volumes (0D flow), a 3D vessel and boundary conditions. The thermal-hydraulic state of the system during a specific scenario is simulated by meshing the different components and solving, through an iterative Newton algorithm, a discretized six-equation model based on mass, momentum and energy conservations. The IBLOCA scenario will therefore be simulated using the code CATHARE2 that provides time

depending temperature and pressure profiles of the nuclear core assemblies as depicted in Figure 3.4.

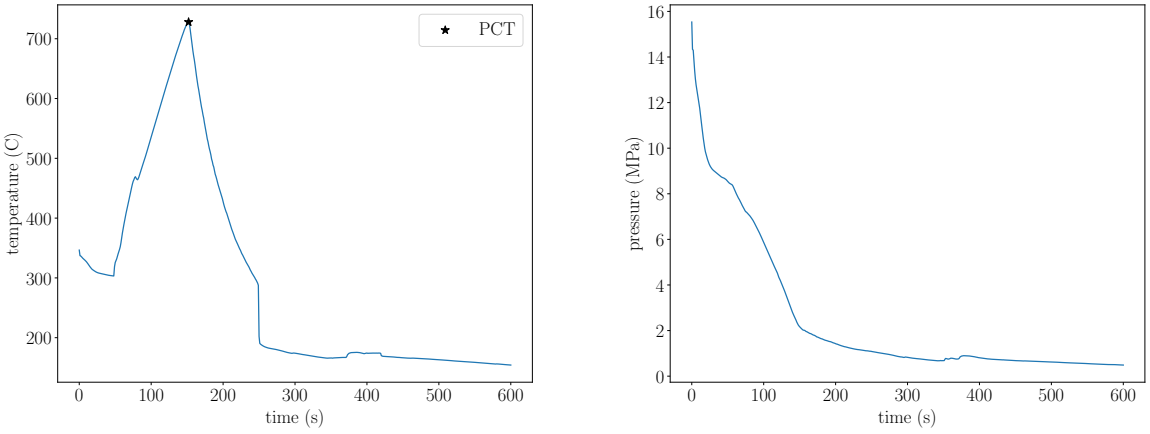

(A) (B)

FIGURE 3.4: Temperature (A) and pressure (B) profiles in the primary during an IBLOCA scenario.

The CATHARE2 code will be referred to as a black-box model due to the complexity of the mapping between the studied scenario and the resulting variable of interest (the PTC). Moreover, the required computational time for one IBLOCA scenario can go from half an hour to several hours. Consequently, useful information such as monotonic behaviors of the PTC w.r.t. to some variables or sensitivity analysis is not available. The analysis is only based on generated inputs samples and correspondind evaluated PTCs.

3.3.3 Best-estimate plus uncertainty methodology

The availability of BE models brings along the possibility to treat uncertainty in a more informative way in order to quantify the safety level of a system. This methodology is called BEPU (Best Estimate Plus Uncertainty) analysis (D'auria et al., 2012; Wilson, 2013) and has been widely considered (Iooss and Marrel, 2019; Marrel and Chabridon, 2021; Rollón De Pinedo, 2021).

The modeling of an IBLOCA scenario in pressurized water reactors can involve more than a hundred input variables which can be classified into three main categories, namely initial and limit conditions, parameters for physical models and physical correlations and finally scenario parameters. In the following BEPU analyses applied to the reduced LSTF model, the number of uncertain input variables is limited to 27 physical correlation parameters. Truncated probabilistic distributions are affected to all random variables based on data and expert knowledge. These are described in Table 3.2. The safety-related QoI generally consists in estimating a high-order quantile of the PTC which can be interpreted as a pessimistic value:

$$q^{\beta} = q^{\beta}(Z) = \inf\left\{t \in \mathbb{R}, F_Z(t) \geq \frac{\beta}{100}\right\}. \tag{3.10}$$

3.3.4 Challenge and motivations

Although the BEPU methodology represents a step forward in the modeling, the comprehension and the decision-making process related to nuclear studies, it also brings along assumptions for which regulatory authorities ask to quantify the impact. In the particular case of IBLOCA scenarios, the principal concern lies on the justification of the chosen probabilistic distributions for

TABLE 3.2: Characteristics of the 27 random variables for the LSTM IBLOCA scenario.

Variable	Bounds	Distribution	Description
X_1	$[0.74, 1.30]$	$\mathcal{N}$	Departure from nuclear boiling
X_2	$[-44.9, 63.5]$	$\mathcal{U}$	Minimum film stable temperature
X_3	$[0.4, 2.0]$	$\mathcal{LN}$	Heat transfer coefficient (HTC) for steam convection
X_4	$[0.627, 1.259]$	$\mathcal{LN}$	Wall-fluid HTC
X_5	$[0.259, 0.267]$	$\mathcal{N}$	HTC for film boiling
X_6	$[0.5, 2]$	$\mathcal{LU}$	HTC forced wall-steam convection
X_7	$[0.236, 1.412]$	$\mathcal{N}$	Liquid-interface HTC for film condensation
X_8	$[0.5, 2]$	$\mathcal{LU}$	Wall-steam friction in core
X_9	$[0.1, 10]$	$\mathcal{LN}$	Interfacial friction: steam generators outlet plena
X_{10}	$[0.1, 10]$	$\mathcal{LN}$	Interfacial friction: hot legs
X_{11}	$[0.1, 10]$	$\mathcal{LN}$	Interfacial friction: bend of the hot legs
X_{12}	$[0.1, 10]$	$\mathcal{LN}$	Interfacial friction: steam generators inlet plena
X_{13}	$[0.1, 10]$	$\mathcal{LN}$	Interfacial friction: downcomer
X_{14}	$[0.235, 3.45]$	$\mathcal{LN}$	Interfacial friction: core
X_{15}	$[0.1, 3]$	$\mathcal{LN}$	Interfacial friction: upper plenum
X_{16}	$[0.33, 3]$	$\mathcal{LN}$	Interfacial friction: lower plenum
X_{17}	$[0.33, 3]$	$\mathcal{LN}$	Interfacial friction: upper head
X_{18}	$[0.1, 10]$	$\mathcal{LN}$	Condensation downcomer
X_{19}	$[0, 2]$	$\mathcal{U}$	Condensation cold leg (intact)
X_{20}	$[0, 2]$	$\mathcal{U}$	Condensation cold leg (broken)
X_{21}	$[0.705, 2.075]$	$\mathcal{N}$	Break flow: flashing (undersaturated)
X_{22}	$[0, 12.8]$	$\mathcal{N}$	Break flow: wall-liquid friction (undersaturated)
X_{23}	$[0.53, 5.75]$	$\mathcal{N}$	Break flow: flashing delay (undersaturated)
X_{24}	$[0.456, 0.53]$	$\mathcal{N}$	Break flow: flashing (saturated)
X_{25}	$[11, 16.57]$	$\mathcal{N}$	Break flow: wall-liquid friction (saturated)
X_{26}	$[0.554, 21.54]$	$\mathcal{N}$	Break flow: global interfacial friction
X_{27}	$[0.85, 45]$	$\mathcal{U}$	Condensation jet

the quantile estimation. The use of more complex mathematical tools such as the ones involved in uncertainty quantification generally increases the difficulty to justify underlying assumptions in an interpretable way. It is within this context that the field of robustness analysis applied to BEPU studies has gained importance. In particular, the Perturbed Law-Based sensitivity Indices (PLI) framework (Lemaître et al., 2015) has been proposed and applied on quantile estimations (Sueur et al., 2016; Sueur et al., 2017; Gauchy et al., 2022) and more recently on superquantile estimations (Iooss et al., 2022). This robustness technique is closely related to sensitivity analysis as it quantifies the QoI variations w.r.t. perturbations on a nominal choice of the inputs' distributions. In Stenger et al. (2020), robustness analysis is performed within the framework of optimal uncertainty quantification (OUQ) (Owhadi et al., 2013). A maximum quantile is evaluated over a class of measures with constrained moments.

In this thesis, the IG framework will be adopted in order to quantify the robustness of 95%-order quantile and 75%-order superquantile (denoted Q^{75}) estimations w.r.t. the uncertainty affecting the inputs probabilistic assumptions. The application of IG to this industrial case can be seen as in between the works proposed in the PLI and OUQ frameworks. Indeed, the IG and PLI frameworks are closely related in the sense that perturbations on the nominal probabilistic configuration are applied progressively. Moreover, IG is related to the OUQ framework by evaluating a worst performance (a maximum quantile or superquantile) in a given uncertainty space (IG uncertainty models and moment classes in the context of OUQ).

The main challenges affecting the consideration of the IG framework to this application case

are the computational time needed for one simulated transient (around 30 minutes) and the number of uncertain variables which adds up to 27. Chapter 7 aims at proposing efficient numerical techniques and relevant IG uncertainty models which enable a feasible and interpretable quantification of the IG robustness.

3.4 Synthesis

This chapter presented the two industrial cases that motivate the application of IG in this thesis. Although both studies concern the robustness assessment of reliability-based evaluations, they face various but complementary challenges. The penstock application case has the nice feature of using fast-to-evaluate analytical expressions for formulating the LSFs. However, the rareness and the complexity of the studied failure event require very performant failure probability estimation techniques and a consequent number of LSFs evaluations. On the contrary, the reliability assessment of the PTC during an IBLOCA scenario is not confronted to the complexity of the failure event but rather to the CATHARE2 simulation model considered as a time-greedy black box code and to its high input dimension. The differences between the two application cases are summarized in Table 3.3.

TABLE 3.3: Characteristics of both industrial applications.

	Type of $M(\cdot)$	Unitary comput. time	$n_{\mathbf{X}} + n_{\mathbf{Y}}$	QoI	Event's rareness	Shape of failure domain
Penstock	Analytical	≈ 0.3 ms	$3-6$	P_{f}	high	complex
IBLOCA	Black box	≈ 30 min	27	q^{95}, Q^{75}	moderate	unknown

CHAPTER 4

The info-gap robustness framework

Contents

4.1 Motivations

Two real industrial application cases on which safety is measured through reliability assessments were presented in Chapter 3. This chapter aims at introducing the IG framework which will be applied to quantify the robustness of reliability assessments in the next chapters.

First, Section 4.2 presents a general description of the IG method. Then, Section 4.3 shows how the IG method may be applied in different contexts of uncertainty to two toy-cases with the resulting interpretations. Section 4.4 considers the placement of IG within the vast world of robustness and especially within other reliability-oriented metrics. In Section 4.5, elements are given for a proposed numerical set of guidelines that may be followed when applying the IG method to reliability assessments.

4.2 Highlight on the info-gap framework

4.2.1 A non-probabilistic view of robustness

Info-gap stands for "information gap" which is defined as the disparity between what is known and what needs to be known for taking a satisfactory decision (Ben-Haïm, 2004). The proposed framework aims at quantifying Knight's concept of "true uncertainty" for which no objective measure of probability is available as opposed to risk (Knight, 1921). Therefore, decision-making based on probabilistic concepts such as the expected utility theory (Neumann and Morgenstern, 1953) or Laplace's principle of insufficient reason are considered not suited to ignorance. In addition, even when information is available in the shape of historical data, decision-makers must be aware of the fact that data from yesterday may not be representative of tomorrow's behavior (Ben-Haïm and Smithson, 2018). In this context, optimal decisions are based on the notion of robust-satisficing (Simon, 1959) rather than performance maximization (Takewaki and Ben-Haïm, 2005; Lempert and Collins, 2007). This translates to the idea of priviledging a decision that remains satisfactory under strong deviations from an initial consideration of the system's environment rather than a decision that presents the best possible outcome based on a highly uncertain idealization of reality.

Some extra-probabilistic representations of uncertainty have already been introduced in Chapter 2 as alternatives to the probabilistic framework. Non-probabilistic convex models are generally used in the IG framework (although non-convex models may also be considered, see (Ben-Haïm, 2006, Chapter 2)). However, one major feature of an IG uncertainty model is that it is described as a function of a degree of ignorance (referred to as *horizon of uncertainty*). In that sense, an IG uncertainty model is not a unique bounded uncertain domain but rather an unbounded family of nested non-probabilistic convex sets that describes increasing uncertainty around an initial estimation.

The formulations implied in IG renders this framework applicable to basically any problem that faces uncertainty and for which the performance can be evaluated (e.g. through the computer code $\mathcal{M}(\cdot)$). Indeed, a non-exhaustive list of works related to different fields can be mentioned such as environmental-related policies (Hall et al., 2012; Matrosov et al., 2013), financial risk (Beresford-Smith and Thompson, 2007; Knoke, 2008), earthquake resilience (Takewaki et al., 2011; Kanno et al., 2017), dynamic studies (Kuczkowiak, 2014; Jaboviste et al., 2019) and many others. Although the IG framework treats uncertain parameters in a non-probabilistic way, its application to probability-based frameworks remains pertinent (Ben-Haïm, 2006, Chapter 10). Indeed, the IG framework brings the possibility to take advantage of the power of probability theory in a robust way w.r.t. the underlying hypotheses such as the definition of a pdf. In Hemez and Ben-Haïm (2004), IG is applied to parameters of a covariance matrix. In Buffe et al. (2011) and in Maugan (2017), it is applied to probabilistic distribution parameters for robustness evaluation of failure probabilities.

4.2.2 Formulation of robustness and opportunity

Let us denote by $\mathbf{d} \in \mathcal{D}$ one decision vector among the set of all possible decisions under consideration. This vector contains all the quantities that describe a studied system at the corresponding decision candidate. The IG framework proposes to quantitatively measure the notions of robustness and opportunity of the decision $\mathbf{d}$ by introducing the following *robustness function* h^*_{IG} and *opportuneness function* β^*_{IG}, both referred to as *immunity functions*:

$$h^*_{\mathrm{IG}}\left(\mathbf{d}, r^{\mathrm{cr}}\right) = \max_{h}\left\{\max_{\mathbf{e}\in U(h,\widetilde{\mathbf{e}})} R\left(\mathbf{d},\mathbf{e}\right) \leq r^{\mathrm{cr}}\right\} \tag{4.1}$$

$$\beta^*_{\mathrm{IG}}\left(\mathbf{d}, r^{\mathrm{rw}}\right) = \min_{h}\left\{\min_{\mathbf{e}\in U(h,\widetilde{\mathbf{e}})} R\left(\mathbf{d},\mathbf{e}\right) \leq r^{\mathrm{rw}}\right\} \tag{4.2}$$

where $h \in \mathbb{R}^+$ is the *horizon of uncertainty*. A closer look at these two functions is taken by describing their three pillars:

1. the *reward function*: $R\left(\mathbf{d},\mathbf{e}\right)$ associates a reward value to the decision $\mathbf{d}$ in a given state of the uncertain variables $\mathbf{e}$. This general definition allows a very broad panel of applications as the reward can directly refer to the output of a model (what was defined as variable of interest in this thesis) or to any related quantities (such as the QoIs defined in the context of reliability). In addition, several reward functions could be jointly considered as robustness and opportunity may involve different quantities;

2. the *performance requirements*: $r^{\mathrm{cr}} \in \mathbb{R}$ and $r^{\mathrm{rw}} \in \mathbb{R}$ separate the performance function output space into a tolerated outcome ($R\left(\mathbf{d},\mathbf{e}\right) \leq r^{\mathrm{cr}}$), an inadmissible outcome ($R\left(\mathbf{d},\mathbf{e}\right) > r^{\mathrm{cr}}$) and a windfall outcome ($R\left(\mathbf{d},\mathbf{e}\right) < r^{\mathrm{rw}}$). The orientation of the inequality obviously depends on the nature of the problem. If the reward function describes a financial gain, the inadmissible domain would represent rewards below the critical value. If the reward is a failure probability, the given formulation holds. The quantification of the performance requirements is not a necessary condition for conducting an IG analysis. This is shown soon after;

3. the *IG uncertainty model*: the non-probabilistic choice of uncertainty representation has been discussed in the previous subsection. Generally, the IG uncertainty model $U\left(h,\widetilde{\mathbf{e}}\right)$ is a convex set (as introduced in Chapter 2) of horizon of uncertainty $h \in \mathbb{R}^+$ containing the best estimation (also called "nominal value") $\widetilde{\mathbf{e}}$ of the uncertain vector $\mathbf{e}$. The horizon of uncertainty parametrizes, in a modular way, the size of the uncertainty space. The nominal vector $\widetilde{\mathbf{e}}$ represents the analyst's best guess about the values of the uncertain variables. It represents the deterministic quantification hypothesis of uncertain variables around which robustness and opportunity are quantified. These uncertain variables may describe different quantities such as an input variable directly or the parameters of a probabilistic distribution.

IG robustness, mathematically described in Eq. (4.1), is therefore understood as the maximum amount of uncertainty (i.e. the "widest" uncertainty space) that can be tolerated, i.e. for which the worst possible performance is still acceptable. In parallel, opportunity, mathematically described in Eq. (4.2), is understood as the minimum amount of uncertainty (i.e. the "smallest" uncertainty space) necessary for a windfall reward to become possible.

Given specific values of the performance requirements r^{cr} and r^{rw}, decision-making can be performed by assessing the best decision $\mathbf{d}^*_h = \arg\max_{\mathbf{d}\in\mathcal{D}} h^*_{\mathrm{IG}}\left(\mathbf{d}, r^{\mathrm{cr}}\right)$ in terms of robustness and the best decision $\mathbf{d}^*_\beta = \arg\min_{\mathbf{d}\in\mathcal{D}} \beta^*_{\mathrm{IG}}\left(\mathbf{d}, r^{\mathrm{rw}}\right)$ in terms of opportunity. The subscripts "h" and "β" are necessary as they reflect the trade-off between robustness and opportunity. Indeed, the best

decision in terms of robustness does not necessarily correspond to the best decision in terms of opportunity (actually it is rarely the case).

Specific values of r^{cr} and r^{rw} are not always available, and even when they are, it is generally more informative to draw the corresponding *robustness curve* and *opportuneness curve*. These curves are constructed by evaluating the bounds $\left[\underline{R}(h), \overline{R}(h)\right]$ at discretized horizons of uncertainty $h_j \in [0, h_{\max}]$ where $h_{\max}$ is the highest considered horizon of uncertainty set by the analyst. The notations $\underline{R}(h) = \min_{\mathbf{e} \in U(h,\tilde{\mathbf{e}})} R(\mathbf{d}, \mathbf{e})$ and $\overline{R}(h) = \max_{\mathbf{e} \in U(h,\tilde{\mathbf{e}})} R(\mathbf{d}, \mathbf{e})$ will be used throughout this thesis.

A key feature of the IG uncertainty models is that they are nested:

$$U(h_1, \tilde{\mathbf{e}}) \subseteq U(h_2, \tilde{\mathbf{e}}) \text{ for } h_1 \leq h_2. \tag{4.3}$$

The main consequence is that the bounds of the performance function are monotonic w.r.t. the horizon of uncertainty and, consequently, the robustness and opportuneness functions are monotonic w.r.t. the performance requirements. To understand this fact in a simpler way, if U_2 contains U_1, then it also contains the values $\mathbf{e}_{\overline{R}}$ and $\mathbf{e}_{\underline{R}}$ that led to the worst and best performances respectively in U_1.

An illustration of nested hyperrectangles with the corresponding robustness and opportuneness curves is presented in Figure 4.1. This example shows a relatively ideal decision as, for the given values r^{cr} and r^{rw}, the robustness value is "high" and the opportunity value is "low". More generally, verticality is desired on the robustness curve while horizontality is prefered on the opportuneness curve. The reader may be confused with the choice of plotting h as a function of the performance bounds as, practically, one chooses the values of h and then estimates the corresponding bounds. The reason lies in the following simplified questions that IG tries to answer:

- How wrong can my estimate be w.r.t. to a critical performance?
- How wrong does my estimate need to be w.r.t. to a windfall performance?

Drawing robustness and opportuneness curves may also suffice for the analyst to classify the best decisions without an exact prior knowledge on the performance requirements. Figure 4.2 illustrates two possible interpretations based on the robustness curves. On the one hand,

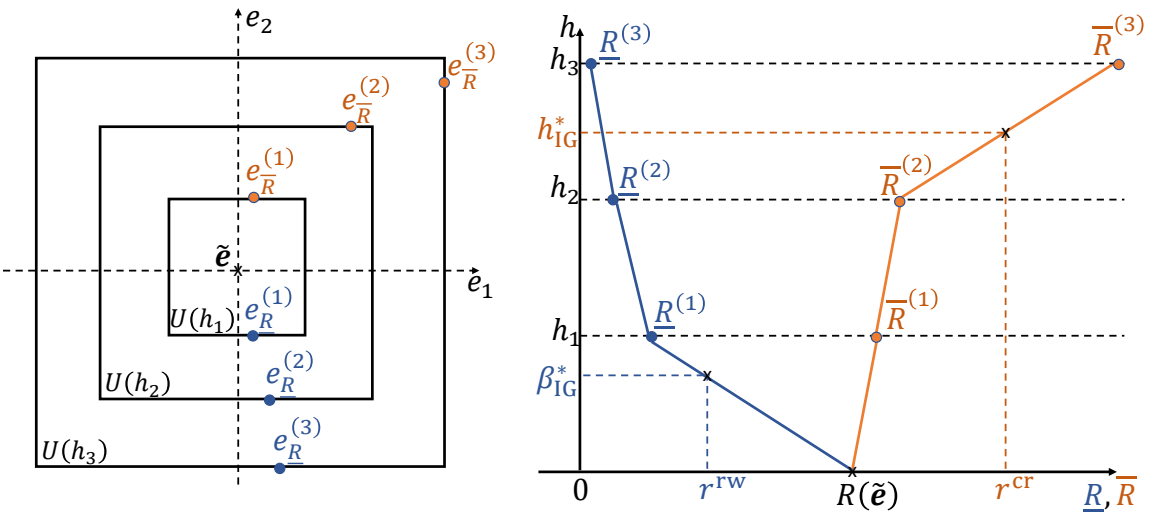

FIGURE 4.1: Example of nested convex sets (left) and associated robustness and opportuneness curves (right).

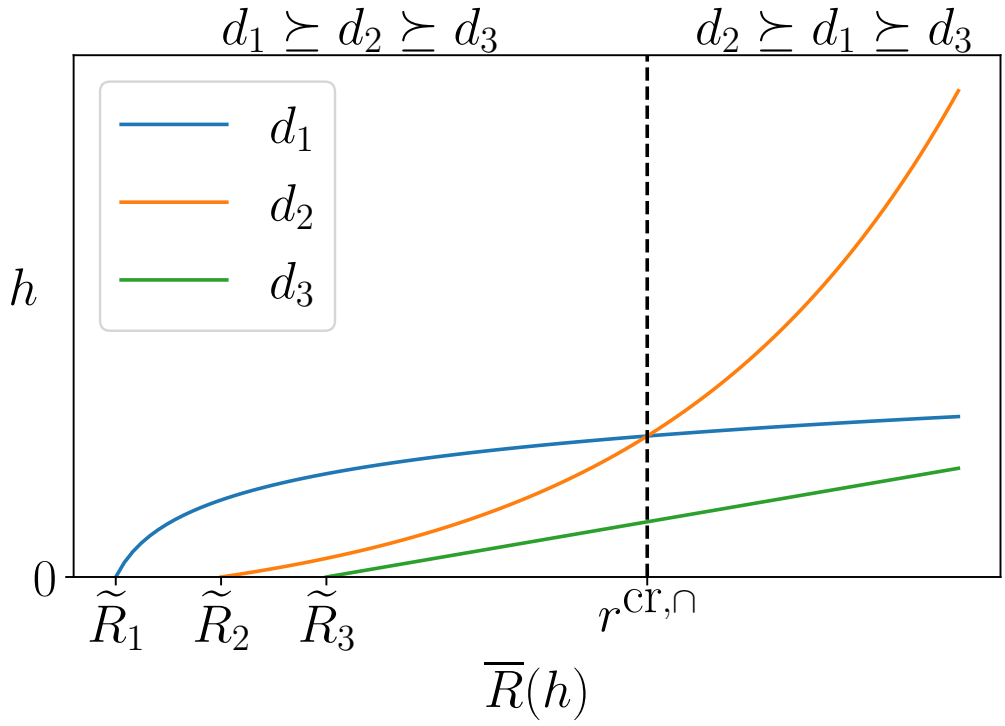

FIGURE 4.2: Different orders of preference w.r.t. robustness.

$\mathbf{d_3}$ is permanently the worst decision whether it is at nominal performance ($\widetilde{R}_3 > \widetilde{R}_2 > \widetilde{R}_1$) or considering any $h > 0$. On the other hand, the order of preference is not as straightforward between decisions $\mathbf{d_1}$ and $\mathbf{d_2}$. Indeed, both robustness curves cross each other at the intersection point $r^{\mathrm{cr},\cap}$. This means that $\mathbf{d_1}$ is more robust for critical values below the intersection point and that $\mathbf{d_2}$ is more robust otherwise. Such behavior is referred to as *reversal of preferences*.

4.2.3 Info-gap value of information

If the first analysis of the robustness and opportuneness curves does not conclude on the best decision to take, the next natural step is to ask oneself whether more information would be useful for taking the decision. How valuable is information w.r.t. the decision? First, the notion of informativeness of an IG model is defined through set inclusions. Given a same nominal vector $\widetilde{\mathbf{e}}$, U_1 is considered more informative than U_2 when the following set inclusion holds:

$$U_1\left(h, \widetilde{\mathbf{e}}\right) \subset U_2\left(h, \widetilde{\mathbf{e}}\right), \ \forall h > 0. \tag{4.4}$$

The same consequence on the bounds of the reward function as the one expressed through Eq. (4.3) is induced:

$$\underline{R_{U_2}}(h) \leq \underline{R_{U_1}}(h) \leq \overline{R_{U_1}}(h) \leq \overline{R_{U_2}}(h) \tag{4.5}$$

where $\left[\underline{R_{U_i}}(h), \overline{R_{U_i}}(h)\right]$ are the bounds of the reward function in $U_i\left(h, \widetilde{\mathbf{e}}\right)$. Finally, these relations trivially propagate to robustness and opportunity as $h^*_{\mathrm{IG}}\left(\mathbf{d}, r^{\mathrm{cr}}, U_2\right) \leq h^*_{\mathrm{IG}}\left(\mathbf{d}, r^{\mathrm{cr}}, U_1\right)$ and $\beta^*_{\mathrm{IG}}\left(\mathbf{d}, r^{\mathrm{cr}}, U_1\right) \leq \beta^*_{\mathrm{IG}}\left(\mathbf{d}, r^{\mathrm{cr}}, U_2\right)$. These simple mathematical relations are linguistically translated as the fact that information enhances robustness but impairs opportunity. A more informative environment is less prone to both negative and positive surprises.

However, the initial problem remains. Are the efforts that were put into gathering more information rewarded with more insights on the final decision? Indeed, let us first note that the strict inclusion in Eq. (4.4) does not yield strict inequalities on the extreme performances and, therefore, on robustness and opportunity. As seen in Figure 4.3, a reduced uncertainty space has no impact on the bounds if the values of $\mathbf{e}$ that led to the extreme performances in U_2 are still admissible in U_1. However, one can expect that the analyst would use the information of the location of the points in U_2 that led to the bounds of the performance to target the request of new information.

These notions are more precisely defined by the Value of Information (VoI) quantities introduced in Ben-Haïm (2006, Chapter 7) and illustrated in Figure 4.4. The four following metrics are defined:

- the *robustness premium* $\Delta h^*_{\mathrm{IG}}\left(r^{\mathrm{cr}}\right)$ represents the increment in immunity obtained after gathering more information;
- the *demand value* $\Delta r^{\mathrm{cr}}\left(h\right)$ represents the increment of additional reward that can be asked for after gathering more information;
- the *opportunity cost* $\Delta \beta^*_{\mathrm{IG}}\left(r^{\mathrm{rw}}\right)$ is the extra uncertainty that is needed for a same windfall value to remain feasible;
- the *windfall cost* $\Delta r^{\mathrm{rw}}\left(h\right)$ is the increment of windfall that vanishes with the added information.

It is also of very useful information to identify on which unknown variables the added information has the most impact w.r.t. the VoIs. This can be seen as sensitivity of the robustness/opportunity w.r.t. the amount of uncertainty in each uncertain variable. In Ferson and Tucker (2006), a pinching method is proposed in the context of p-box representation. The idea is to quantify the proportion between a metric of uncertainty on the QoI (e.g. the volume of a p-box) obtained from an uncertain representation of all unknown variables with this same metric when one variable is considered with more information (e.g. a constant value). This general sensitivity framework is compatible with the IG VoIs metrics and will be considered and more detailed in Chapter 5.

4.2.4 Criticisms addressed to the info-gap framework

The IG framework is a decision-theoretical framework that faces some criticisms, mainly addressed by Sniedovich (2010), based on two central concerns:

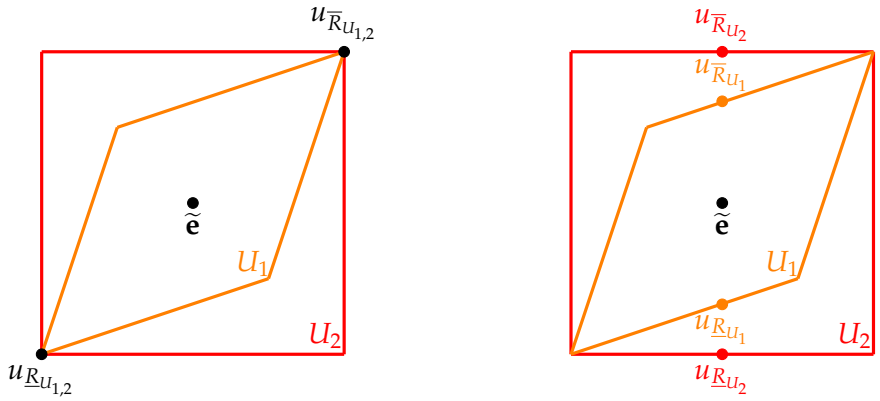

FIGURE 4.3: Case where added information has no impact on the bounds (left) and case where added information has an impact (right).

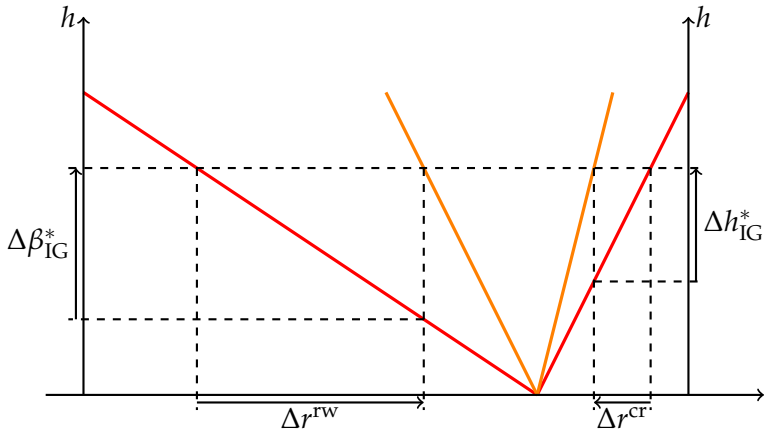

FIGURE 4.4: Info-gap value of information metrics.

1. IG decision theory is not radically different as it is a reformulation of the well-known Wald's maximin formulation,

2. IG is a local robustness method as based on radius of stability which makes it unsuitable for taking decisions under severe uncertainty as it claims itself to be.

Although it is not in this thesis' interest to end this vigorous debate, it seems important to address these claims based on mathematical proofs and the reasons why they are less relevant in the proposed context.

Wald's maximin formulation (Wald, 1950) consists in choosing the decision $\mathbf{d}^*_{\text{Wald}}$ with the best worst case. For the sake of the comparison, it is now considered that worse is lower which yields:

$$\mathbf{d}^*_{\text{Wald}} = \max_{\mathbf{d}\in\mathcal{D}} \min_{s\in S(\mathbf{d})} f(\mathbf{d}, s) \tag{4.6}$$

where $\mathbf{d}$ is one decision from the decision set $\mathcal{D}$, s is one state from all possible states S allowed from decision $\mathbf{d}$ and $f(\cdot)$ can be considered as the performance function. In order to enhance his point, Sniedovich rewrites the IG formulation as follows (the reader is referred to Sniedovich (2010) for the complete derivation):

$$\mathbf{d}^*_{\text{IG}} = \max_{\mathbf{d}\in\mathcal{D}} h^*_{\text{IG}}(\mathbf{d}, r^{\text{cr}}) = \max_{\mathbf{d}\in\mathcal{D}, h\geq 0} \min_{\mathbf{e}\in U(h,\widetilde{\mathbf{e}})} \left(h \times \mathbb{1}_{\{r^{\text{cr}}\leq R(\mathbf{d},\mathbf{e})\}}\right). \tag{4.7}$$

The similarities are indeed relevant to be addressed.

In fact, according to Sniedovich, this equivalence simply comes from the fact that IG robustness function is based on the radius of stability (Wilf, 1960) which, for the sake of comparison, is expressed here as:

$$\rho^*_{\text{SR}}(\mathbf{d}|\widetilde{\mathbf{e}}) = \max_{\rho\geq 0} \{\rho |\ c(\mathbf{d}, \mathbf{e}), \forall \mathbf{e} \in \mathcal{B}(\rho, \widetilde{\mathbf{e}})\} \tag{4.8}$$

where $\mathcal{B}(\rho, \widetilde{\mathbf{e}})$ is a "ball" centered on $\widetilde{\mathbf{e}}$ of radius ρ and $c(\mathbf{d}, \mathbf{e})$ is a list of constraints to be respected. Again, these criticisms rely on relevant remarks.

From this consideration, Sniedovich (2012) argues that IG is unsuited for decision-making under severe uncertainty. Conducting a worst-case analysis around a nominal point $\widetilde{\mathbf{e}}$ chosen in a vast uncertainty space where no region is supposed to be more likely than another only reflects local robustness which makes the analyst unaware of what may happen elsewhere. Ben-Haïm (2012) retorts that IG is not a simple local min-max analysis as it enables to consider unbounded uncertainty in order to evaluate the amount of error still acceptable w.r.t. to the analyst's consideration of nominal design.

As pointed out in Hayes et al. (2013) in the context of ecology, these discussions only emphasize the general fact that analysts should use such methods precautiously and under awareness of their underlying hypotheses and limits, especially as they involve critical systems. Considering the industrial context of this thesis, the IG framework remains very useful for justifying some decisions based on reliability assessments. The original feature of considering robustness through progressive horizons of uncertainty brings relatively interpretable insights with few information needed. Evaluating the robustness around (where "around" is allowed to be more or less large) a first estimate seems reasonable and practical with the quantities that will be dealt with in the proposed studies. This thesis does not pretend to solve problems under severe uncertainties but aims at evaluating how wrong one is allowed to be w.r.t. reliability-based hypotheses. Nevertheless, the notion of global robustness remains crucial for safety concerns since many disasters occur due to unconsidered events. However, this is out of this thesis' scope as robustness will be performed under the consideration of well identified failure modes.

4.3 Info-gap applied in different contexts of uncertainty

4.3.1 Two toy-cases

In this section, some first IG results are interpretated within different contexts by considering two analytical LSFs, usually used in optimization challenges (Molga and Smutnicki, 2005), based on the two-dimensional Rosenbrock function and the six-hump camel function. The two LSFs are expressed as:

$$g_r(x_1, x_2) = 100\left(x_2 - x_1^2\right)^2 + (x_1 - 1)^2 - 0.1 \tag{4.9}$$

for the Rosenbrock formulation and as:

$$g_c(x_1, x_2) = 500 - \left(x_1^2\left(4 - 2.1x_2^2 + \frac{x_1^4}{4}\right) + x_1x_2 + 4x_2^2\left(-1 + x_2^2\right)\right) \tag{4.10}$$

for the six-hump camel formulation. It is clear that these LSFs have no physical meaning and that they are chosen simply to point out some more general behaviors that could occur in some practical applications. Here, for the sake of the study, each LSF is viewed as one possible decision, expressed as "decision 1" for the Rosenbrock formulation and "decision 2" for the six-hump camel formulation. For example, both formulations could represent two different principal failure modes (e.g. fatigue failure and buckling failure) for two different designs that depend on the same variables x_1 and x_2. The question would then be: is design 1 more robust to uncertainty w.r.t. the failure mode associated to the Rosenbrock function than design 2 w.r.t the failure mode associated to the six-hump camel function? Some illustrative results are given considering different uncertainty contexts.

4.3.2 Non-probabilistic robustness analysis on the limit-state functions

Let us first apply the IG method directly to the LSFs w.r.t. $\mathbf{x}$. In this case, the only available information about the uncertain vector $\mathbf{x}$ is its nominal vector set at $\tilde{\mathbf{x}} = [0, 0]^T$. Both LSFs are defined such that bad performances correspond to low values. Therefore, worst performances correspond to the minimal values $\underline{g}(h) = \min_{\mathbf{x} \in U(\tilde{\mathbf{x}}, h)} g(\mathbf{x})$. In accordance with structural reliability conventions, both decisions are considered to fail for $\mathcal{F}_r = \{\mathbf{x} |\, g_r(\mathbf{x}) \leq 0\}$ and $\mathcal{F}_c = \{\mathbf{x} |\, g_c(\mathbf{x}) \leq 0\}$ which sets the critical value $g^{\text{cr}} = 0$.

The failure regions are shown in Figure 4.5. It is clear that two very distinct behaviors are induced by each LSF. On the one hand, the failure domain $\mathcal{F}_r$ defined through g_r has a very

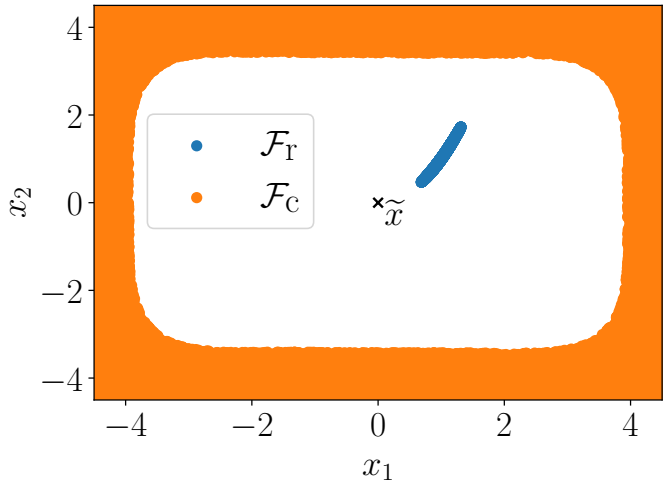

FIGURE 4.5: Failure domains $\mathcal{F}_r$ and $\mathcal{F}_c$.

restricted narrowed ellipsoid shape. On the other hand, the failure domain $\mathcal{F}_c$ defined through g_c is unbounded and surrounds the nominal value such that the safety domain is bounded.

The nested uncertainty convex models considered in this analysis are simple envelop bounds $U(\widetilde{x}_{1,2},\ h) = \{x_{1,2}|\ -h \leq x_{1,2} \leq +h\}$. With this uncorrelated interval model, Figure 4.5 suffices to understand that decision 1 is far less robust than decision 2 given the proposed failure definition. Indeed, the distance between $\widetilde{\mathbf{x}}$ and the closest point that belongs to $\mathcal{F}_r$ is shorter than the distance considering the closest point that belongs to $\mathcal{F}_c$. However, it is valuable to study the general evolution of the robustness curves. These are given in Figure 4.6 for $h \in [0, 3.5]$. In accordance with the first visual analysis, the worst performance of g_r intersects the failure criteria faster (i.e. for a smaller h) than the worst performance of g_c. Actually, the slopes of the robustness curves inform that decision 1 is poorly robust before reaching the global minima of g_r at $\mathbf{x} = [1, 1]^T$ (which becomes feasible for $h \geq 1$) and infinitly robust (vertical line) after while decision 2 seems very robust for $h < 2$ but less and less robust after. This points out the importance of the choice of the critical value g^{cr} and that drawing robustness curves brings more information than estimating a unique min-max interval.

4.3.3 Robustness analysis on probabilistic distribution parameters

The analyst may feel frustrated about the previous robustness results of decision 1. Indeed, the corresponding failure domain is very small compared to the one of decision 2 but its proximity to the nominal point renders the decision poorly robust as viewed from the IG framework. It is now supposed that the analyst gathered enough information to consider that both variables follow a normal distribution: $X_1 \sim \mathcal{N}(\mu_1, \sigma_1)$ and $X_2 \sim \mathcal{N}(\mu_2, \sigma_2)$. Uncertainty is considered either on both means (with fixed standard deviations) or on both standard deviations (with fixed means). The nominal values are set at $\widetilde{\boldsymbol{\mu}} = [0, 0]^T$ and $\widetilde{\boldsymbol{\sigma}} = [1, 1]^T$. The associated performances are now defined as the failure probability $P_\mathrm{f} = \mathbb{P}[\mathbf{X} \in \mathcal{F}_{r,c}]$ (where $\mathcal{F}_{r,c}$ denotes either $\mathcal{F}_r$ or $\mathcal{F}_c$). Therefore, bad performances are associated to high failure probabilities such that the worst values are obtained by evaluating the maximum values $\overline{P}_\mathrm{f} = \max_{\boldsymbol{\theta} \in U(\widetilde{\boldsymbol{\theta}}, h)} P_\mathrm{f}(\boldsymbol{\theta})$ where $\boldsymbol{\theta} = [\mu_1, \mu_2]^T$ or $\boldsymbol{\theta} = [\sigma_1, \sigma_2]^T$. The nested uncertainty models are again envelop bounds defined as $U(\widetilde{\mu}_{1,2}, h) = \{\mu_{1,2}|\ -h \leq \mu_{1,2} \leq +h\}$ for the means and $U(\widetilde{\sigma}_{1,2}, h) = \{\sigma_{1,2}|\ 1-h \leq \sigma_{1,2} \leq 1+h\}$ for the standard deviations with $h \in [0, 0.5]$.

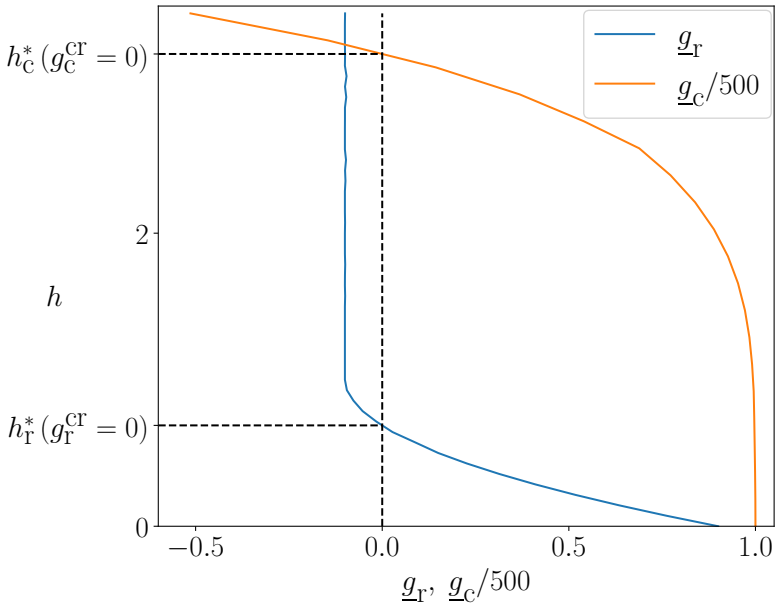

FIGURE 4.6: Robustness curves on the Rosenbrock and six-hump camel limit-state functions.

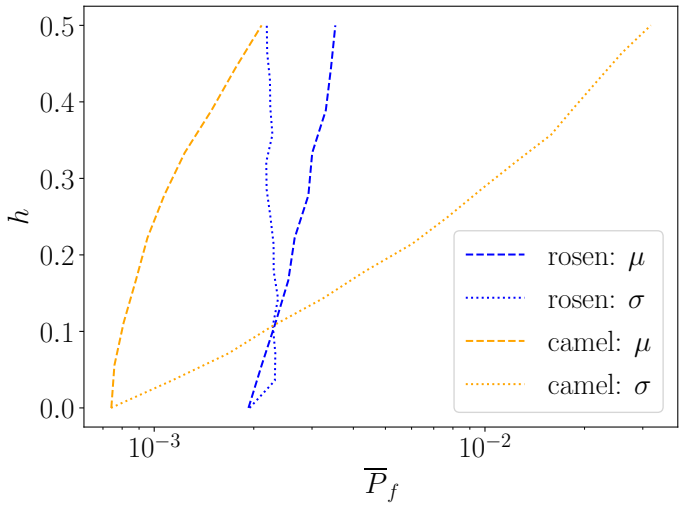

FIGURE 4.7: Robustness curves on the failure probability of the Rosenbrock and six-hump camel decisions.

Figure 4.7 presents the corresponding robustness curves. First, one can see that the nominal performance (at $h = 0$) is better (i.e. lower failure probability) for decision 2. However, decision 1 is very robust (in the given range of h) to uncertainty on its distribution parameters which is again a consequence of the narrowness of the failure domain. The uncertainty on the standard deviations has no impact while the uncertainty on the means has a slight impact as values closer to the global minima become possible. On the contrary, decision 2 is poorly robust to uncertainty on the standard deviations. Indeed, as the failure domain surrounds the nominal point $\widetilde{\mathbf{x}}$, increasing the standard deviation will increase the chances of failure in all directions. Uncertainty on the means also has a non-negligeable impact although less predominant. This smaller impact can roughly be understood by the fact that getting closer to the failure domain in one

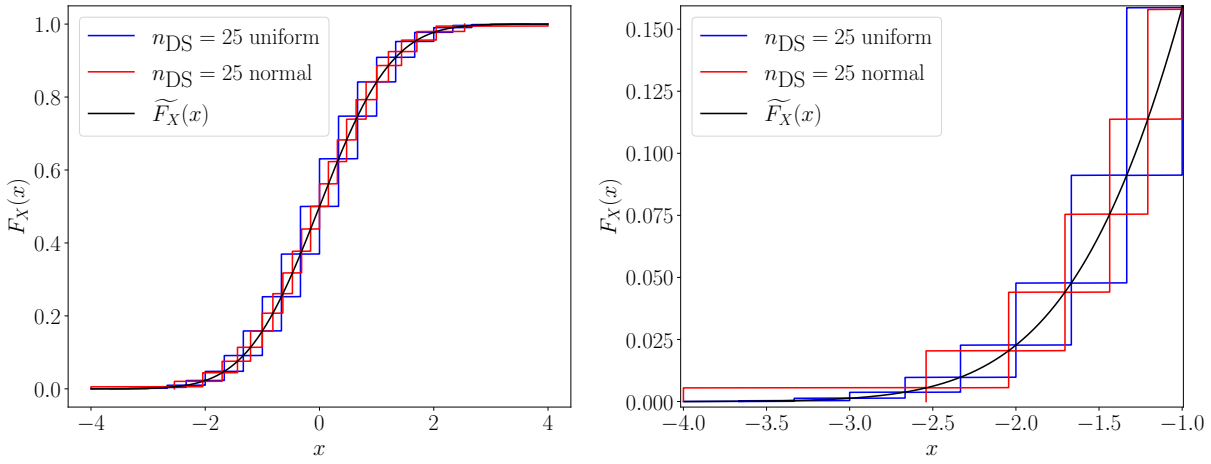

FIGURE 4.8: DS discretizations on a truncated normal distribution (A) with a zoom on the lower tail (B).

direction will reduce the number of failure samples in the other directions. The main message here is that IG is compatible with initial probabilistic hypotheses which may totally change the robustness analysis and, therefore, the associated decision.

4.3.4 Robustness analysis on the shape of the probabilistic distribution

The previous analysis considered the uncertainty on probabilistic distributions as affecting the hyperparameters. This is equivalent to a series of parametric p-box computations. However, one may be interested in considering uncertainty on the probabilistic nature of the variables. What if x_1 and x_2 do not follow perfectly parametrized normal distributions? There are many ways of considering uncertainty on a given cdf. In this analysis, two DS discretizations of the nominal cdf are proposed. This process consists in discretizing the support of the cdf F_X of a random variable X into n_{DS} disjoint intervals $[a_i, b_i]$, $i = 1, \cdots, n_{DS}$. Then, the probability mass m_i is attributed to $[a_i, b_i]$ as $m_i = F_X(b_i) - F_X(a_i)$. This will typically generate a step non-parametric p-box that envelopes F_X.

Different discretizations may be applied. In this analysis, uniform and normal discretizations are considered. The uniform type simply means that all the disjoint intervals have the same length. The normal type means that the lengths become normally wider as the intervals gets farther from the center of the support. Such discretization considers that the cdf is better justified around the mean value than around its tails (where usually less information is available). Figure 4.8 shows the p-box envelopes generated by both discretizations on a truncated normal distribution. It can be seen that the uniformly generated intervals are wider than the ones normally generated around the center of the support and that the opposite happens around the tails (approximately for $|x| > 2$ in this case). It is important to bare in mind that a uniform (or any other kind) discretization does absolutely not mean that all intervals have the same probability masses. The probability masses are defined by the nominal cdf $\widetilde{F_X}$. In Figure 4.8, the heigths of the rectangles get smaller as the intervals get farther to the center of the support whatever the choice of discretization. This is due to the fact that the nominal cdf is normal.

IG can be applied on the proposed uncertainty representation by considering reduced numbers of intervals with the increase of h. In this application, it is considered that $n_{DS}(h) = \lceil 200(1-h) \rceil$ for $h \in [0, 0.9]$ (which corresponds to a progressive reduction of intervals from 200 to 20) where $\lceil \cdot \rceil$ is the integer operator. The corresponding robustness curves for both decisions are drawn in Figure 4.9 where "DS-U" and "DS-N" correspond to uniform and normal

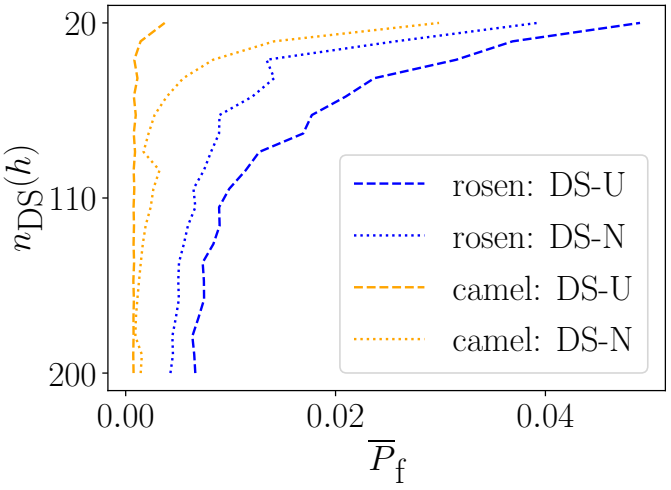

FIGURE 4.9: Robustness curves considering DS discretizations for the Rosenbrock and six-hump camel decisions.

discretizations respectively. Although some numerical errors seem to disrupt the robustness curves, their global behaviors remain interpretable. It appears that the most pessimistic discretization between the uniform one and the normal one depends on the considered LSF. The uniform one is more pessimistic for the Rosenbrock-based decision while the normal one is more pessimistic for the six-hump camel-based decision. This is explained by the fact that the failure region is rather close to the nominal point for decision 1 and rather distant for decision 2 (so that the tails of the distributions have a high impact).

4.3.5 Robustness analysis on model errors

As mentioned in Chapter 1, uncertainty on the model chosen for relating the output to corresponding inputs will not be further analyzed in the following chapters. However, it seems important to show that IG is also adapted to such robustness analysis and that model errors may also be crucial to account for. Here, the Rosenbrock-based LSF is reconsidered with the model M_1:

$$g_r^{M_1}(x_1, x_2) = a\left(x_2 - x_1^2\right)^2 + b\left(x_1 - 1\right)^2 - 0.1 \tag{4.11}$$

and the model M_2:

$$g_r^{M_2}(x_1, x_2) = 100\left(x_2 - x_1^2\right)^2 + \left(x_1 - 1\right)^2 + c\left(x_1 x_2\right)^3 - 0.1. \tag{4.12}$$

The variables a and b in M_1 could be viewed as model calibration parameters. The variable c in M_2 adds (when $c \neq 0$) a joint cubic term on x_1 and x_2 and could be understood as an error on the formulation of the model.

The shapes of the new failure domains for both models are given in Figure 4.10. It can be seen that the coefficients a and b on M_1 only have an effect on the expansion of the ellipsoid shape. However, the general shape is preserved. On the contrary, the coefficient c on M_2 considerably changes the shape of the failure domain. As soon as $c \neq 0$, the failure domain becomes unbounded. Positive values of c will reduce the initial ellipsoid shape to almost a point while adding a failure domain in another region.

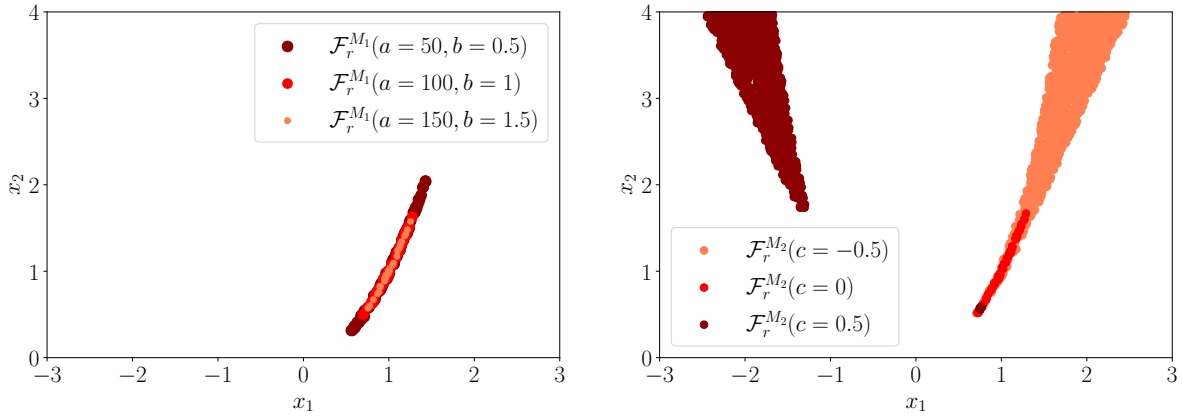

(A) (B)

FIGURE 4.10: Failure domains induced by M_1 for different values of a and b (A) and failure domains induced by M_2 for different values of c (B).

The robustnesses w.r.t. such uncertainties are analyzed. The same envelope models are considered which yields:

$$U(\widetilde{a}, h) = \{a |\ \widetilde{a}(1-h) \leq a \leq \widetilde{a}(1+h)\} \tag{4.13a}$$

$$U\left(\widetilde{b}, h\right) = \left\{b |\ \widetilde{b}(1-h) \leq b \leq \widetilde{b}(1+h)\right\} \tag{4.13b}$$

$$U(\widetilde{c}, h) = \{c |\ -h \leq c \leq h\}. \tag{4.13c}$$

The different robustness curves consider uncertainty on:

- μ_1 and μ_2 (as in Figure 4.7);
- σ_1 and σ_2 (as in Figure 4.7);
- a and b (M_1);
- c only (M_2);
- μ_1, μ_2, a and b ($\mu - M_1$);
- σ_1, σ_2, a and b ($\sigma - M_1$);
- μ_1, μ_2 and c ($\mu - M_2$);
- σ_1, σ_2 and c ($\sigma - M_2$).

The results are presented in Figure 4.11. The robustness curves show that the model error M_2 itself is more constraining than the calibration type error M_1 and its combinations with distribution parameters errors. Moreover, it can be seen that model errors may amplify the impact of distribution parameters. It is the case when jointly considering uncertainty on M_1 and $\boldsymbol{\mu}$ and it is even more blatant with the joint consideration of M_2 and $\boldsymbol{\mu}$.

4.4 Placement of info-gap within other metrics

4.4.1 Different metrics of robustness

The IG framework is far from being the only one to address quantitatively the notion of robustness. This part does not aim at describing every single robustness metric and all the

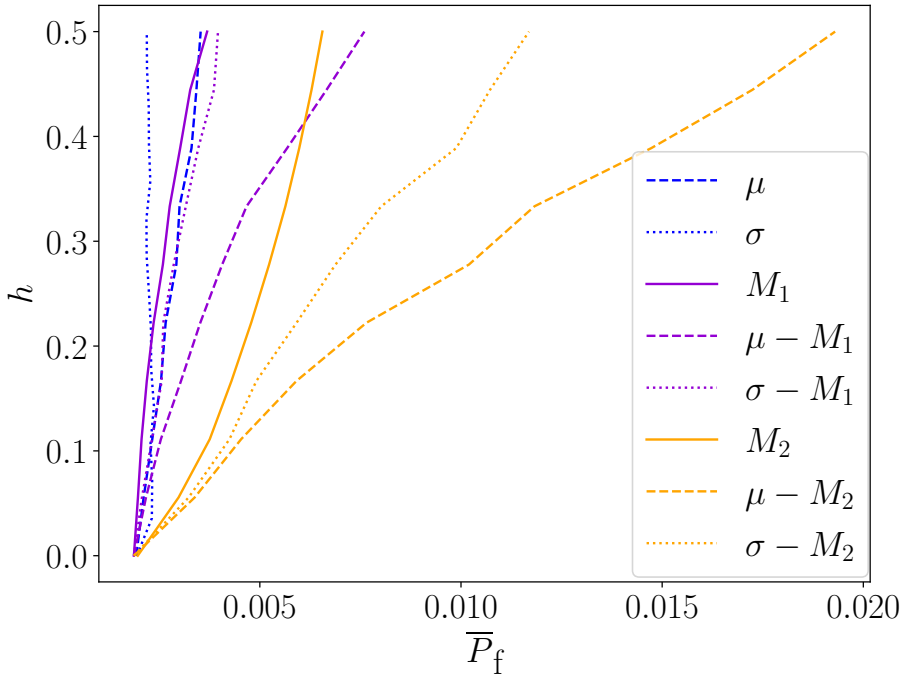

FIGURE 4.11: Robustness curves considering distribution parameters and model errors for the Rosenbrock decision.

possible links among them, but rather to give a feeling about the variety of robustness measures and the reasons that push towards the consideration of IG in this thesis.

The fact that the term of "robustness" is considered in many different contexts and for very different objectives has led to the establishment of a myriad of robustness frameworks. Giuliani and Castelletti (2016) even question the robustness of robustness analysis by illustrating the different outcomes induced by different metrics in the context of decision-making under climate change. Direct comparisons of IG with other frameworks can be found in Matrosov et al. (2013) and in Roach et al. (2016) both in the context of water resource management.

More generally, recent attempts have helped to illustrate and explain the panel of robustness metrics in the context of product development and engineering design (Göhler et al., 2016) and in the context of decision-making under deep uncertainty (McPhail et al., 2018). Let us first note that Göhler et al. (2016) enumerate up to 38 robustness metrics (with no mention of IG) classified into four groups, namely:

- sensitivity metrics;
- feasible design space metrics;
- functional expectancy and dispersion metrics;
- probability of functional compliance metrics.

More recently, McPhail et al. (2018) consider 15 robustness metrics (among them 4, including IG, are considered unsuitable for decision-making under deep uncertainty) that are not all explicitly considered in the former. The reason for this difference between both reviews is twofold.

First, it seems important to distinguish between the robustness metric itself and the different quantities involved in its assessment. The robustness metric is the quantity that enables to decide on the validity of a decision and, in the case of several considered decisions, to order them in

terms of robustness (i.e. the greatest horizon of uncertainty h^*_{IG} in the IG framework). The other involved quantities are only calculation metrics (i.e. min-max in the IG framework) that lead to the robustness metric and to its interpretability. The unifying framework proposed by McPhail et al. (2018) is very illuminating in that matter. Indeed, three transformations describe the path from the performance function of a system to the robustness value of the system, namely:

- the performance value transformation;
- the scenario subset selection;
- the robustness metric calculation.

Only when this distinction is not made, the term of robustness ends up being defined through a very large amount of metrics that have very different formulations and purposes (e.g. local sensitivity and failure probability in Göhler et al. (2016)).

The second reason is the consideration of very different contexts of uncertainty and performance. In Göhler et al. (2016), robustness to epistemic uncertainty is explicitly said not to be considered in the review. Yet, it seems important to avoid dissociating robustness to the uncertainty context dimension for such analysis as soon as robustness is viewed as the ability to guaranty a requirement in an uncertain environment which may take various forms (e.g. local perturbations, aleatory uncertainty, epistemic uncertainty, combinations of different uncertainties). In McPhail et al. (2018), on the other hand, the review focuses on the context of decision-making under deep uncertainty to the point that IG is again considered as unsuitable due to the consideration of a nominal point. The uncertainty characterization is crucial for specifying the QoI and the robustness metrics that are relevant. Moreover, robustness is intrinsically linked to the performance requirement defined by the analyst which may take many different definitions. The metrics that should be involved totally depend on whether the analysis focuses on safety issues, overall performances, best outcomes or many other concerns.

Under these considerations, the IG framework plays an important role within the field of robustness. The message is obviously not to prescribe IG as soon as the word robustness is mentioned as, once again, the uncertainty context and the performance requirement should carefully guide the choice of a metric. However, the fact that IG may be applied on any QoI (e.g. variable of interest, probability-related metrics) and that the path from knowledge to ignorance is described through a monotonic function of uncertainty enables to smoothly travel from certainty to randomness and to lack of knowledge. It makes the application of IG adapted to a wide panel of problems.

4.4.2 A closer look with other epistemic uncertainty reliability-oriented metrics

This thesis lies in the general scope of epistemic uncertainty affecting risk-oriented reliability assessments. Many strategies have been employed in such context. Some works focus on the manner to describe and propagate this type of uncertainty. A few have been introduced in Chapter 2 which basically induce more or less wide bounds on the QoI depending on the uncertainty representation. Epistemic uncertainty may also be treated stochastically as in Chabridon et al. (2017) where a Bayesian approach is considered by affecting to the uncertain distribution parameters $\boldsymbol{\Theta}$ a prior pdf $f_{\boldsymbol{\Theta}}(\boldsymbol{\theta})$. Hence, the conditional failure probability $P_{\mathrm{f}}(\boldsymbol{\Theta})$ becomes itself a random variable on which statistical quantities can be estimated such as its mean defined as the predictive failure probability $\widetilde{P}_{\mathrm{f}} = \mathbb{E}_{f_{\boldsymbol{\Theta}}}[P_{\mathrm{f}}(\boldsymbol{\Theta})]$. Robustness analysis is proposed in Stenger et al. (2020) through the Optimal Uncertainty Quantification framework (Owhadi et al., 2013) by assessing a maximum quantile over a set of probability measures under moments constraints. Although these frameworks bring valuable insights through different interpretations, it seems once again that the IG framework differs by its ability to describe immunity progressively through an increasing degree of ignorance.

Significant effort has also been put into reliability-oriented sensitivity analysis (ROSA). ROSA can be seen as an extension of sensitivity analysis of model output (SAMO) to specific QoIs involved in reliability assessments such as a failure probability. The reader is referred to Chabridon (2018, Chapter 4) for a thorough review of both sensitivity frameworks. Generally speaking, ROSA aims at quantifying the role of an input variable or of a distribution parameter on the variability of the reliability-oriented QoI. The objectives of such analysis are mainly twofold:

1. Qualitatively identifying the random variables or the distribution parameters that have no impact on the QoI. Such quantities may then be fixed to a specific value which either simplifies the reliability analysis by reducing the number of random variables (in the case of sensitivity considering random variables) or simplifies any analysis based on reliability assessments such as reliability-based design optimization (e.g. in the case of sensitivity on distribution parameters);

2. Quantitatively measuring the importance of each random variable or distribution parameter on the QoI. Such measures bring more precise insights on the impact of variability of each quantity on the QoI which is particularly fruitful for deciding on which ones more information should be requested.

ROSA applied to distribution parameters may also be seen as robustness of a reliability QoI w.r.t. variability on the underlying probabilistic hypotheses. However, the objectives are not quite the same as the ones brought by the IG framework. This basically comes from the difference between sensitivity and immunity concerns. The former identifies whose variability is the most responsible, either locally or globally, for the variability of the QoI. The latter quantifies the degree of immunity to failure that a nominal idealization of reality has. Nevertheless, both frameworks are closely linked through the following two reasons:

1. Some identical conclusions are bound to arise from both analyses;

2. Sensitivity results can bring valuable insights for conducting an IG robustness analysis. Indeed, they may inform on potential monotony of the QoI w.r.t. distribution parameters or at least narrow the uncertain space in which the extreme performances are to be found.

Moreover, a feature of high importance is that sensitivity metrics can be obtained as a by-product of the QoI estimation meaning that no extra simulation budget is required. This is particurlarly the case when estimating failure probabilities (Chabridon et al., 2018; Valdebenito et al., 2018; Zhang et al., 2020).

Among other methods, the Perturbed Law-based Indices (PLI) framework, introduced in Lemaître et al. (2015), also considers increasing levels of perturbation. It proposes a reliability-based sensitivity metric and consists in reassessing a QoI after perturbing the pdf f_i corresponding to the i-th variable. The latest expression of this sensitivity index reads (**Iooss_Verges_2021**):

$$\mathrm{PLI}_i(\delta) = \frac{\mathrm{QoI}\left(f_{X_1}, \cdots, f_{X_i,\delta}, \cdots, f_{X_{n_\mathbf{X}}}\right) - \mathrm{QoI}\left(f_\mathbf{X}\right)}{\mathrm{QoI}\left(f_\mathbf{X}\right)} \tag{4.14}$$

where $\mathrm{PLI}_i(\delta)$ is the relative change of the QoI brought by a perturbation δ on the pdf of the i-th random variable. Different types of perturbations have been proposed in this framework such as perturbations based on the Kullback-Leibler divergence measure (Lemaître et al., 2015), perturbations based on the Fisher distance (Gauchy et al., 2022), perturbations based on marginal quantile constraints and Wasserstein loss minimization (Il Idrissi et al., 2022) and perturbations in the standard normal space (**Iooss_Verges_2021**). A noticeable similarity with the IG framework is that the PLI is not estimated for a single perturbation but rather in a range of perturbations in order to compare the curves obtained from each perturbed variable. Therefore, the order

of importance of each variable may depend on the degree of perturbation. The main difference is that the PLI indice corresponds to a relative change induced by a one-dimensional perturbation while the IG framework considers the extreme performances in a multidimensional uncertain space. However, searching for the extreme performances or the extreme relative changes leads to the same conclusion. Thus, the PLI framework can be seen as a one-dimensional particular case of IG when the performance function corresponds to a relative change and the uncertainty model corresponds to one of the different density perturbation methods proposed.

4.5 Numerical procedure for applying info-gap to reliability assessment

Applying the IG framework to reliability assessments may induce very time-greedy computations which greatly depend on the following considerations:

- the method used for finding the worst QoI at a given horizon of uncertainty h_j;
- the convergence speed of one QoI estimation (that may vary for different values of $\mathbf{e}$);
- the possibility to use metamodels and unique-sample-based techniques;
- the number of considered discretized horizons of uncertainty n_h.

Some elements relevant to each concern are discussed.

4.5.1 Search of the worst QoI

When the QoI is a failure probability or a quantile, the problem consists in finding its maximum value in the uncertain space $U\left(h_j, \widetilde{\mathbf{e}}\right)$ which is of dimension $n_{\mathbf{e}}$. Therefore, the point $\mathbf{e}^* = \left[e_1^*, \cdots, e_k^*, \cdots, e_{n_{\mathbf{e}}}^*\right]^\top$ to be found reads:

$$\mathbf{e}^* = \underset{\mathbf{e} \in U\left(h_j, \widetilde{\mathbf{e}}\right)}{\arg\max}\, \mathrm{QoI}\left(\mathbf{e}\right). \tag{4.15}$$

Different levels of knowledge (or assumed hypotheses) about the behavior of the QoI w.r.t. e_k allow different strategies:

- the maximum of the QoI is known to be obtained at a specific bound value of e_k. This is always true for monotonic behaviors but may also be true for non-monotonic behaviors. In this case, each uncertain variable involved by this feature is set to $e_k^* = \overline{e_k\left(h_j\right)}$ where $\overline{e_k\left(h_j\right)}$ is either the minimum or the maximum value of $e_k\left(h_j\right)$ in $U\left(h_j, \widetilde{\mathbf{e}}\right)$. The dimension of the initial optimization problem is reduced by the number of concerned uncertain variables;
- the maximum of the QoI is obtained at an unknown bound value of e_k. This is equivalent to the previous point except that it is not known if it is the maximum or the minimum of e_k that is involved. In this case, the vertex method may be used which evaluates the QoI at each combination of extreme values of all concerned variables e_k. The dimension of the initial optimization problem is again reduced by the number of concerned uncertain variables. However, the vertex method can sometimes require more evaluations (i.e. $2^{n_{\mathbf{e}}}$) than optimization algorithms for high dimensions;
- the maximum of the QoI is known to be obtained in a specific range of e_k that is narrower than the entire interval. In this case the dimension of the optimization is unchanged but the optimization domain is reduced;

- no hypothesis is made. In such case, MC sampling or optimization algorithms should be used. It is important to recall that, most of the time, the performance QoI $(\mathbf{e})$ is itself a realization of a random variable. Hence, using gradient-based optimization algorithms may be tricky. In this thesis, global optimization procedures will be considered.

The reader is referred to Appendix B for some first comparisons between the optimization, the sampling and the vertex methods.

4.5.2 Performance of the QoI estimator

This concern has already been exposed in Chapter 2 with the introduction of several small failure probability estimation techniques. Again, such a panel tries to bring solutions to the many different combinations of possible issues to be faced (e.g. nonlinearity of the LSF, complex geometrical shape of the failure domain, high dimensionality). A good performance of the QoI estimation technique is vital as it may represent the underlying objective function in an optimization algorithm. The performance should be defined in terms of overall precision of the estimation technique and overall computational time for any $\mathbf{e}\left(h_j\right) \in U\left(h_j, \widetilde{\mathbf{e}}\right)$. Indeed, consequent overestimations or underestimations may cause the optimization algorithm to struggle. Moreover, even a small reduction of the computational time involved for one estimation will induce a high gain for the cumulated computational time as the QoI may be estimated hundreds or even thousands of times. However, it may seem unnecessary to estimate with the same level of convergence every single value of QoI $(\mathbf{e})$, in particular the values that are trusted to be lower than the final maximum value.

4.5.3 Use of surrogate models and unique-sample-based techniques

For some physical systems, the numerical computer code $\mathcal{M}(\cdot)$ may require more than several hours to evaluate the performance of one configuration of inputs. In such cases, even variance reduction techniques are not directly applicable for assessing small failure probabilities based on the costly LSF. In that context, significant effort has been put into the use of surrogate models for uncertainty propagation. From a general point of view, a surrogate model is an approximation $\widetilde{\mathcal{M}}$ of the true relation $\mathcal{M}$ between an output and its corresponding input configuration. It is built upon a certain number of true input-output samples that is considerably smaller than the number of evaluations required for the analysis to be carried out. Various surrogate-based methods have been adapted and applied in the context of reliability analysis such as polynomial chaos expansion (Blatman, 2009), Gaussian process (Li, 2012), support vector machines (Deheeger, 2008) or artifical neural networks (Papadrakakis and Lagaros, 2002; Papadopoulos et al., 2012).

Other techniques have been proposed for estimating several failure probabilities based on a unique input-output dataset. In Yuan (2013), weighted approaches combined to MC, SS and IS are proposed to evaluate failure probabilities from a single reliability analysis very easily as it only requires the calculation of a ratio of densities. In Yuan et al. (2020), the line sampling roots obtained given one input distribution parameters are transformed in order to estimate failure probabilities with different input distribution parameters without having to search for the new roots. In Yuan et al. (2021) and Chabridon et al. (2017), failure probabilities (or more precisely, predictive failure probabilities in Chabridon et al. (2017)) are estimated from a unique set of samples generated in the augmented space $(\mathbf{X}, \boldsymbol{\Theta})$ where $\boldsymbol{\Theta}$ is an instrumental probabilistic distribution on the distributional parameters $\boldsymbol{\theta}$. The methods developed in Yuan (2013), Yuan et al. (2020), and Yuan et al. (2021) are shortly described in Appendix A.

4.5.4 The discretization of the horizon of uncertainty

From a practical aspect, the robustness curve is built from the values $\left(\overline{\text{QoI}}\left(h_j\right)\right)_{1\leq j\leq n_h}$ where n_h is the number of discretized horizons of uncertainty such that $h_j \in [0, h_{\max}]$ and $h_{\max}$ is the highest horizon of uncertainty considered during the analysis. The choice of discretization basically depends on the degree of nonlinearity of the robustness curve (which is not known in advance), the degree of precision needed for taking the decision and the computational budget. One can imagine cases where a single worst case evaluation at $h_j = h_{\max}$ suffices to conclude that the decision is safe enough w.r.t. to a predefined level of requirement. However, more evaluations are needed as soon as the analyst is interested in the route taken by robustness or, said differently, the speed at which very bad performances are attained.

4.6 Synthesis

In this chapter, the IG framework was presented first in its general formulation and application. It has been seen how the notions of robustness and opportunity to uncertainty can be quantified in order to take an informed decision. Moreover, IG VoI metrics have been introduced as a means to quantify to what extent a more informative uncertainty model simultaneously enhances robustness while limiting opportunity. Both the strength and the criticisms attributed to the IG method rely on the fact that uncertainty is considered as a progressive degree of ignorance from the hypothesis of a nominal design (certainty) to a conceptual unbounded uncertain space (complete ignorance). Some will argue that considering a nominal state of the system in the analysis reduces IG to local robustness and therefore makes it unsuitable under deep uncertainty. However, it seems that, in the context of this thesis, this framework is particularly practical and insightful for either justifying or refuting a decision based on the analyst's best idealization of reality which often represents the context of an industrial application.

It is argued in this thesis that IG nonprobabilistic uncertainty models and the probability-based reliability frameworks must not be seen as antagonistic frameworks. Rather, their combination offers the possibility to take advantage of the probabilistic framework while justifying its underlying hypotheses.

The placement of IG within other metrics related to the consideration of epistemic uncertainty has briefly been discussed. The IG framework finds its originality and relevance in its way to describe uncertainty and its interpretation of robustness and opportunity. However, other reliability-based metrics with an important literature background, such as reliability-oriented sensitivity analysis, remain relevant in the context of IG robustness applied to reliability assessments.

Finally, applying IG to reliability assessments implies a possibly challenging numerical framework that combines several inner boxes, as presented in Figure 4.12, that each requires an efficient procedure. The main ones have been presented and their consideration highly depends on the application case. Chapters 6 and 7 each develop their own procedure relevant to each industrial case presented in Chapter 3.

However, the considered framework is by nature a typical case of hybrid reliability analysis. Chapter 5 introduces the random set theory in order to solve the induced uncertainty propagation challenges. Although the IG method requires very few hypotheses, the robustness analysis depends on the choice of a nominal configuration and on the employed uncertainty model. Moreover, it has been seen that several more or less informative uncertainty representations exist. Chapter 5 aims at evaluating the impact of a choice of epistemic uncertainty representation on the robustness analysis by combining both the random set and IG frameworks.

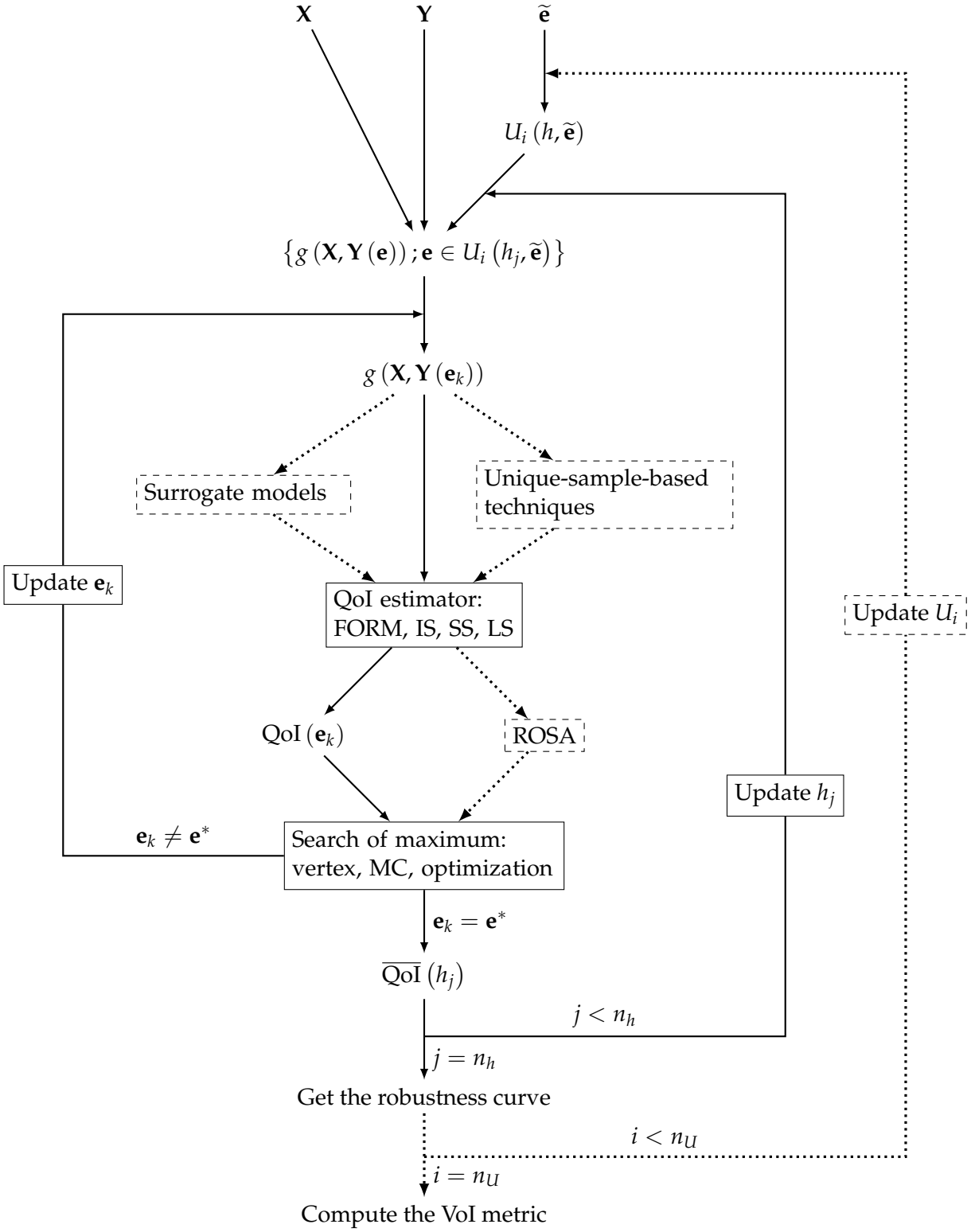

FIGURE 4.12: Overall procedure for evaluating IG robustness curve to reliability assessments.

CHAPTER 5

Comparison of uncertainty representations in terms of info-gap robustness

Contents

This chapter is adapted from the following reference:
A. Ajenjo, E. Ardillon, V. Chabridon, B. Iooss, S. Cogan and E. Sadoulet-Reboul (2022). "An info-gap framework for robustness assessment of epistemic uncertainty models in hybrid structural reliability analysis". In: *Structural Safety* 96, pp. 102196.

5.1 Motivations

The general robustness analysis procedure presented in Chapter 4 depends on how the epistemic uncertainty is modeled. Two different convex models may lead to different maximum values of failure probabilities which in turn lead to the following question: to what extent does the choice of the epistemic uncertainty representation affect a robustness analysis? In this chapter, in the context of HRA, a methodology is proposed to assess, within the IG framework, the robustness of small failure probabilities w.r.t. the choice of a specific representation of epistemic uncertainty on the uncertain variables. To do so, the different epistemic uncertainty models introduced in Chapter 2 are considered using the random set (RS) theory. This methodology enables to compare the IG metrics presented in Chapter 4 - the robustness and opportuneness curves and the demand value - obtained from different uncertainty representations, but also to highlight their implicit relationships.

The chapter is organized as follows: Section 5.2 reviews the LSF formulations involved in HRA and how RS theory can be used to evaluate them; Section 5.3 describes the framework that is used and how IG and RS theory are combined to compare uncertainty representations; Section 5.4 shows the results of the methodology applied to two academic examples and the industrial case that concerns the reliability of penstocks; finally Section 5.5 proposes some discussions about the presented study.

5.2 Random set for hybrid reliability

5.2.1 Hybrid reliability

This study falls in the scope of rare event estimation under HRA, meaning that the uncertain vector can be divided into two vectors, namely $\mathbf{X}$ and $\mathbf{Y}$ where $\mathbf{X}$ is a random vector with a fully determined pdf $f_{\mathbf{X}}$ and $\mathbf{Y}(\mathbf{e})$ contains the input variables subject to epistemic uncertainty and described by one of the representations introduced in Chapter 2. The most available literature involving small failure probability estimation under HRA corresponds to the representation of $\mathbf{Y}$ with interval models. Many works such as in (Yang et al., 2015; Zhang et al., 2018; Xiao et al., 2019) propose methods to decrease the computational burden of estimating the failure probability bounds when random and interval variables are associated. The combination of random variables and convex models have also been considered as in (Kang and Luo, 2010) with ellipsoid convex models or in (Liu and Elishakoff, 2020) with multidimensional parallelepiped convex models. Kriging is used in (Yang et al., 2015) for speeding interval MC analysis when propagating random and p-box variables together. Multi-level kriging is considered in (Schöbi and Sudret, 2017) in both contexts of free and parametric p-box. Combinations of random variables with evidence and possibilistic variables for failure probability estimation are less encountered. An example with evidence theory is found in (Du, 2006) where FORM is used for solving a unified uncertainty analysis. It is reminded that the framework of possibility representation of probabilistic distribution parameters (which creates fuzzy random variables) as performed in (Valdebenito et al., 2020) is not considered in this thesis.

For a given realization $\mathbf{x}$ of the random vector $\mathbf{X}$, the hybrid limit-state function $g(\mathbf{x}, \mathbf{Y})$ is no longer a scalar value but an interval which will depend on the representation of $\mathbf{Y}$. As such, it is not possible to directly use the techniques introduced in Chapter 2 for estimating a single failure

probability. Instead, only its bounds denoted by $\left[\underline{P_f}, \overline{P_f}\right]$ can be computed with the following general expressions:

$$\underline{P_f} = \min_{\mathbf{Y} \in U_\mathbf{Y}} \mathbb{P}\left[g\left(\mathbf{X}, \mathbf{Y}\right) \leq 0\right] \tag{5.1a}$$

$$\overline{P_f} = \max_{\mathbf{Y} \in U_\mathbf{Y}} \mathbb{P}\left[g\left(\mathbf{X}, \mathbf{Y}\right) \leq 0\right] \tag{5.1b}$$

where $U_\mathbf{Y}$ represents the set of intervals that define $\mathbf{Y}$. Estimating these bounds using small failure probability estimator techniques require a common framework which is brought by random sets theory.

5.2.2 Random sets

The general definition of a random set (RS) (Molchanov, 2005) relies on a probability space based from the triplet $(\Omega, \sigma_\Omega, \mathbb{P})$ and a measurable space $(\mathcal{A}, \sigma_\mathcal{A})$. A RS $\Gamma(\cdot)$ represents the following measurable mapping:

$$\Gamma : \left| \begin{array}{ccc} \Omega & \longrightarrow & \mathcal{A} \\ \boldsymbol{\alpha} & \longrightarrow & \Gamma\left(\boldsymbol{\alpha}\right) \end{array} \right. . \tag{5.2}$$

As such, a RS is similar to a random variable whose realization is a set (called focal element) in $\mathcal{A}$ (called focal set), not a scalar (Alvarez, 2006). The probability of an event E can then be expressed through the probability measure $\Pr = \mathbb{P} \circ \Gamma^{-1}$ as:

$$\Pr\left[E\right] = \mathbb{P}\left\{\Gamma\left(\boldsymbol{\alpha}\right) \in E, \boldsymbol{\alpha} \in \Omega\right\}. \tag{5.3}$$

In the general case, the value of the above probability is not measurable but one can evaluate its bounds as:

$$\underline{\Pr}\left(E\right) = \mathbb{P}\left(\left\{\boldsymbol{\alpha} \in \Omega : \Gamma\left(\boldsymbol{\alpha}\right) \subseteq E, \Gamma\left(\boldsymbol{\alpha}\right) \neq \emptyset\right\}\right) \tag{5.4a}$$

$$\overline{\Pr}\left(E\right) = \mathbb{P}\left(\left\{\boldsymbol{\alpha} \in \Omega : \Gamma\left(\boldsymbol{\alpha}\right) \cap E \neq \emptyset\right\}\right). \tag{5.4b}$$

The reader may notice that these expressions are close to the ones introduced in Chapter 2 when presenting DS evidence theory. Actually, it appears that RS theory is a generalization of evidence theory for an infinite number of focal elements.

The previous definitions enable to link RS theory with the different uncertainty representations introduced in Chapter 2 in the special case where (Alvarez et al., 2018):

- $\Omega = [0,1]^{n_\alpha}$,
- $\sigma_\Omega = \mathcal{B}\left(\Omega\right)$,
- $\mathbb{P} = \mu_C$ for some copula C (Nelsen, 2006) which will be the independent one in this chapter (see Apendix C for the consideration of the Gaussian copula),
- the focal elements are hyperrectangles of dimension n_α.

These links are depicted for $n_\alpha = 1$ in Figure 5.1 which gives the corresponding RS for each type of uncertainty representation. A RS can also describe a convex set in a similar way as it describes an interval in the sense that any vector $\boldsymbol{\alpha}$ (of dimension equal to the dimension of the convex set) yields the same convex set. Therefore, the interval and convex models are special cases where the RS is actually a constant set as the function does not depend on $\boldsymbol{\alpha}$. The probability model is a special case where the random set is a random singleton. The deterministic representation is a special case where the RS is a constant singleton.

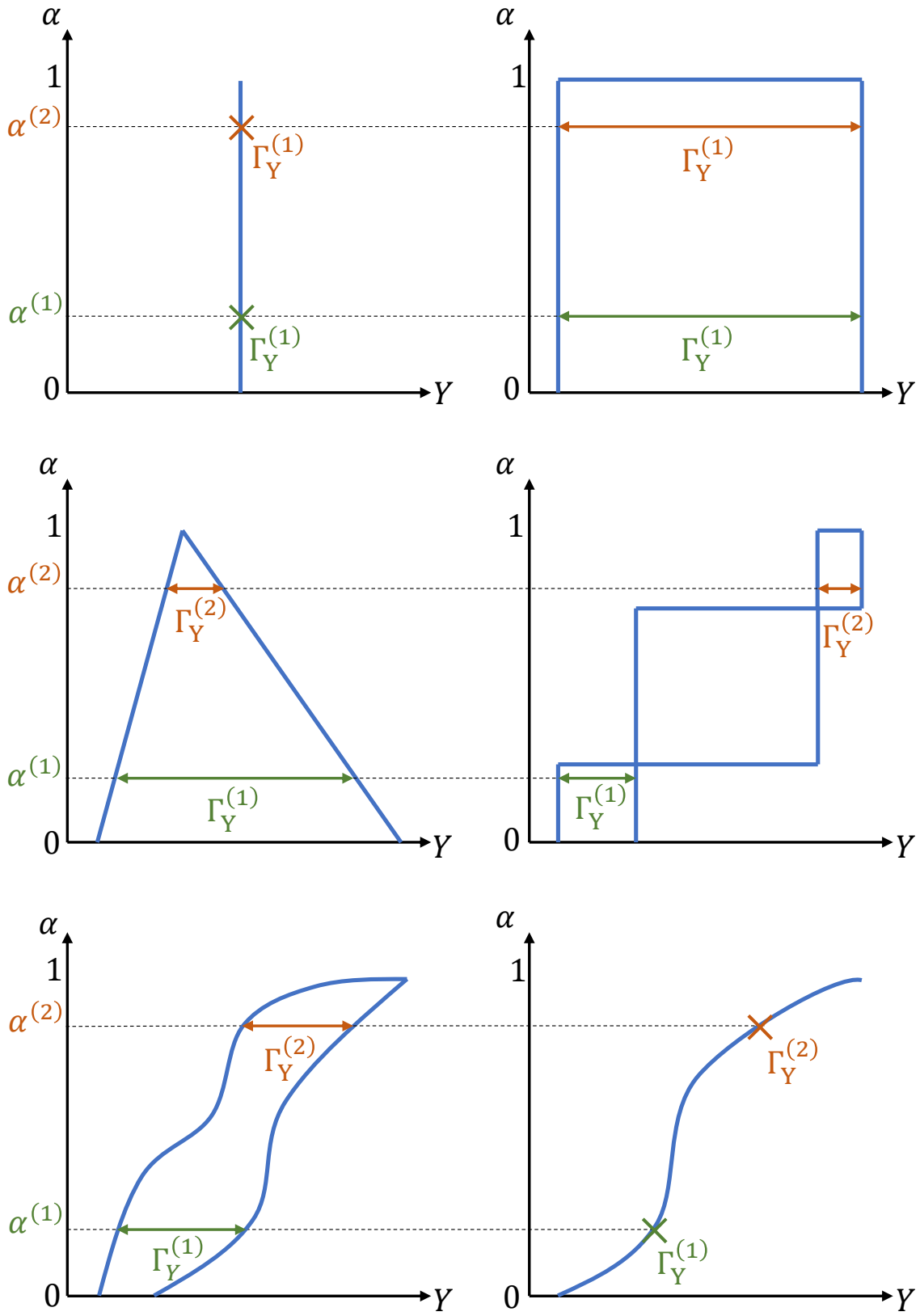

FIGURE 5.1: Random sets associated to a constant value (top left), interval model (top right), possibility distribution (middle left), DS structures (middle right), free p-box (bottom left) and probabilistic cdf (bottom right).

5.2.3 Random sets in the reliability framework

The RS framework is applicable to reliability analysis by particularizing the previous general event E to the failure event $\mathcal{F}$. Some first applications involving failure probability estimations can be found in (Tonon and Bernardini, 2000; Tonon et al., 2000a; Tonon et al., 2000b). In addition, the works proposed in (Alvarez and Hurtado, 2014; Alvarez et al., 2017; Alvarez et al., 2018) enable to well relate hybrid reliability analysis to classical probabilistic reliability analysis through the use of RS. Indeed, the sample space is now composed of the two extreme failure domains:

$$\underline{\mathcal{F}_{\boldsymbol{\alpha}}} = \left\{\boldsymbol{\alpha} \in \Omega : \Gamma(\boldsymbol{\alpha}) \subseteq \mathcal{F}_{(\mathbf{X},\mathbf{Y})}, \Gamma(\boldsymbol{\alpha}) \neq \emptyset\right\} = \left\{\boldsymbol{\alpha} \in \Omega : \underline{g}(\boldsymbol{\alpha}) \leq 0\right\} \tag{5.5a}$$

$$\overline{\mathcal{F}_{\boldsymbol{\alpha}}} = \left\{\boldsymbol{\alpha} \in \Omega : \Gamma(\boldsymbol{\alpha}) \cap \mathcal{F}_{(\mathbf{X},\mathbf{Y})} \neq \emptyset\right\} = \{\boldsymbol{\alpha} \in \Omega : \overline{g}(\boldsymbol{\alpha}) \leq 0\} \tag{5.5b}$$

where the extreme LSFs are expressed as:

$$\overline{g}(\boldsymbol{\alpha}) = \max_{\Gamma_{(X,Y)}(\boldsymbol{\alpha})} g(\boldsymbol{\alpha}) \tag{5.6a}$$

$$\underline{g}(\boldsymbol{\alpha}) = \min_{\Gamma_{(X,Y)}(\boldsymbol{\alpha})} g(\boldsymbol{\alpha}). \tag{5.6b}$$

It follows, in the case of an independent copula, the expressions of the bounds on P_f as:

$$\overline{P_\mathrm{f}} = \int_\Omega \mathbb{1}_{\underline{g}(\boldsymbol{\alpha})\leq 0} d\boldsymbol{\alpha} \tag{5.7a}$$

$$\underline{P_\mathrm{f}} = \int_\Omega \mathbb{1}_{\overline{g}(\boldsymbol{\alpha})\leq 0} d\boldsymbol{\alpha}. \tag{5.7b}$$

The HRA problem thus reduces to two standard reliability analyses for which standard estimation methods may be used. Figure 5.2 shows the equivalent representations from the original space to the $\boldsymbol{\alpha}$-space to the standard normal space for a case where Y_1 follows a possibility distribution and Y_2 is represented through a p-box (here, there is no random variable X). The original space has a unique LSF but the samples of the input variables are sets (rectangles here). The $\boldsymbol{\alpha}$-space contains the two extreme LSF and the samples are uniformly distributed in the unit hypercube. The red rectangle in the physical space corresponds to the red sample in the $\boldsymbol{\alpha}$-space. The fact that the rectangle is fully contained within the physical failure domain means that the maximum of the LSF in the set is negative ($\overline{g}(\boldsymbol{\alpha}) \leq 0$). Similarly, the two orange rectangles in the physical space correspond to the two orange samples in the $\boldsymbol{\alpha}$-space. The fact that the rectangles intersect with the physical failure domain means that the minimum of the LSF in the set is negative ($\underline{g}(\boldsymbol{\alpha}) \leq 0$). Naturally, the failure domain defined through the maximum of the LSF is contained within the failure domain defined through the minimum of the LSF. Finally, as $\boldsymbol{\alpha}$ is probabilistically defined, classical isoprobabilistic transformations can be used to travel into the standard normal space.

However, it is important to notice, as pointed out in (Alvarez et al., 2017), that when considering only interval or parametric p-box models on $\mathbf{Y}$, the bounds obtained using the RS framework are larger than the ones obtained by applying a straightforward search for the maximum and minimum of the failure probability in the interval domain (on the physical variables or the distributional parameters). For example, with the interval model, the following equations hold:

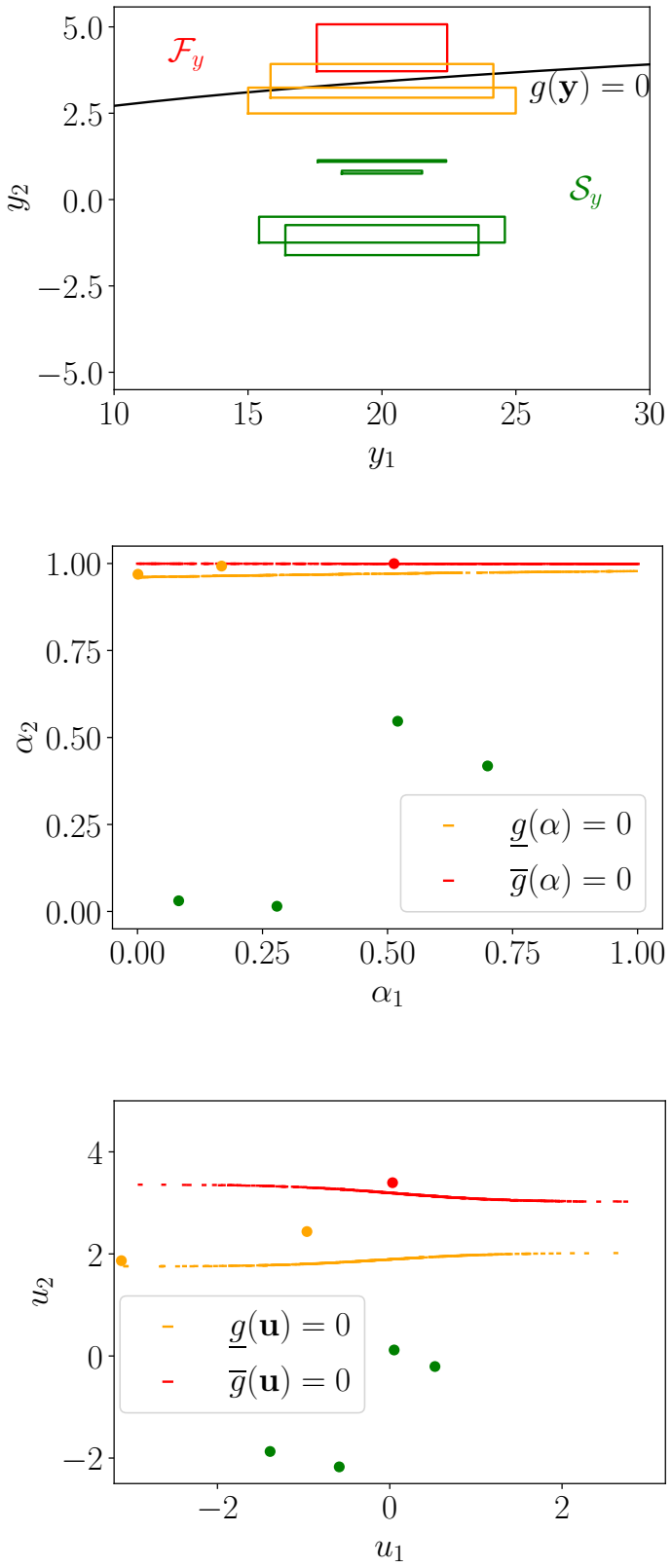

FIGURE 5.2: Equivalence from the physical **x**-space (top) to the random set $\boldsymbol{\alpha}$-space (middle) to the standard **u**-space (bottom).

$$\Pr\left[\max_{\Gamma_{(X,Y)}(\boldsymbol{\alpha})} g(\boldsymbol{\alpha}) \leq 0\right] \leq \min_{\mathbf{Y}\in\mathcal{D}_{\mathbf{Y}}} \Pr\left[g(\mathbf{X},\mathbf{Y}) \leq 0\right] \tag{5.8a}$$

$$\Pr\left[\min_{\Gamma_{(X,Y)}(\boldsymbol{\alpha})} g(\boldsymbol{\alpha}) \leq 0\right] \geq \max_{\mathbf{Y}\in\mathcal{D}_{\mathbf{Y}}} \Pr\left[g(\mathbf{X},\mathbf{Y}) \leq 0\right]. \tag{5.8b}$$

Actually, it can be shown that the failure domain associated to $\underline{g}(\boldsymbol{\alpha}_{\mathbf{X}}, \boldsymbol{\alpha}_{\mathbf{Y}})$ is the union of all the sampled failure domains generated from the interval model (on the physical variables or the distributional parameters) while the failure domain associated to $\overline{g}(\boldsymbol{\alpha}_{\mathbf{X}}, \boldsymbol{\alpha}_{\mathbf{Y}})$ is the intersection of them. Figure 5.3 illustrates this point on a LSF based on the Rosenbrock function where the com-

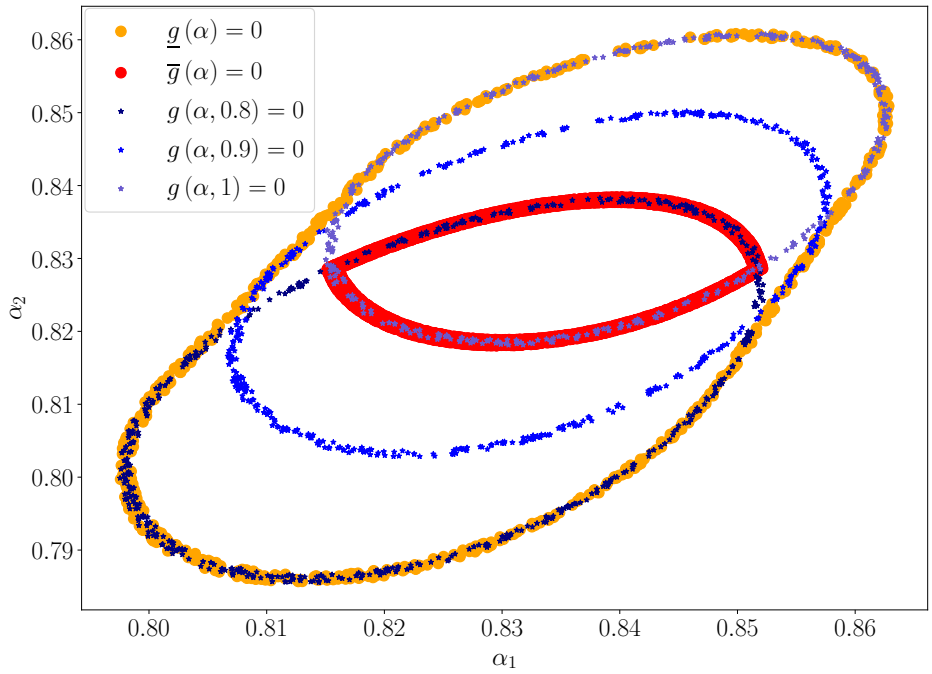

FIGURE 5.3: Comparison of the LSS with the RS framework and the LSS sampled from an interval for the Rosenbrock function.

ponents α_1 and α_2 are associated to two standard Gaussian distributions and Y is represented as an interval in $[0.8, 1]$ (which could be associated to a component α_3 but it is not necessary here). The union and intersection of only three LSS samples for $Y = \{0.8, 0.9, 1\}$ suffice to explain how both extreme RS-based LSS are constructed. The conditions at which the expressions in Eq. (5.8) become either equalities or strict inequalities are mathematically formulated in (Alvarez et al., 2017). Basically, the strict inequality is obtained when the values of $\mathbf{Y}$ that lead to the extreme LSF change for different samples $\boldsymbol{\alpha}_{\mathbf{X}}^{(i)}$. This mixture of different epistemic values is not allowed when directly performing optimization in the epistemic space as each bound of the failure probability is obtained at a single value $\mathbf{Y}^*$ (one for each bound). In practice, this divergence is intensified with complex interactions between both probabilistic and epistemic variables within the LSF.

5.3 Proposed info-gap framework for uncertainty representations comparison

5.3.1 Hybrid reliability analysis framework

The goal in this chapter is to analyse the effect of the choice of an epistemic uncertainty model on the IG robustness and opportunity of a reliability quantity of interest. Hence, the bounds on the failure probability implied in the HRA framework need to be estimated at each discretized value of the horizon of uncertainty. In order to compare the effect of each epistemic uncertainty model, the bounds on the failure probability are estimated considering that all variables in $\mathbf{Y}$ are described by a single epistemic uncertainty representation. The process is then repeated for all epistemic representations considered for the comparison. The different epistemic models for which results are shown in this chapter are:

- interval model;
- parallelepiped convex model (see Appendix D);
- possibility triangular distribution;
- possibility trapezoidal distribution;
- DS structures;
- free and parametric p-boxes;
- probabilistic uniform distribution.

In order to estimate the bounds on the failure probability, Eqs. (5.7a) and (5.7b) need to be evaluated through a double loop process. The inner loop which corresponds to the search of the minimum and maximum of the limit-state function for one realization of the random set $\Gamma(\boldsymbol{\alpha})$ may be performed using an optimization algorithm. The outer loop corresponds to the estimation method of the failure probability which may rely on any of the techniques introduced in Chapter 2. As an inner optimization loop is involved, HRA usually requires more evaluations of the limit-state function than a standard reliability analysis. Moreover, the lower bound of the failure probability to be estimated may be very small (e.g. such that $P_\mathrm{f} < 10^{-5}$). Therefore, in this chapter, the outer loop is mainly performed with FORM-IS. The Subset Simulation algorithm is also used in order to verify the results. However, let us note that several other advanced sampling methods could have been used here (e.g. directional sampling, line sampling).

5.3.2 Comparison by means of info-gap robustness and opportuneness curves

As seen in Chapter 4, the IG framework quantifies the notions of robustness and opportuneness to uncertainty by building nested convex sets around a nominal state which represents the analyst's best guess. An interesting feature is that it enables to compare different possible decisions in view of choosing the one that maximizes the robustness given a critical performance. IG analysis can also be used to assess the VoI induced by a more informative input model. Indeed, the different decisions can be directly linked to the choice of different uncertainty models $U_i\left(h, \widetilde{\mathbf{Y}}\right)$ that each has its own degree of information. Therefore, it is possible to compare robustness and opportuneness curves of different uncertainty models for $\mathbf{Y}$ by considering the random set function Γ_i as the IG uncertainty model as follows:

$$U_i\left(h, \widetilde{\mathbf{Y}}\right) = \Gamma_i(\alpha, h) \tag{5.9}$$

with:

$$\Gamma_i : \left| \begin{array}{rcl} [0,1]^{n_{\mathbf{Y}}} \times \mathbb{R}^+ & \longrightarrow & \mathcal{D}_{\mathbf{Y}}\left(h, \widetilde{\mathbf{Y}}\right) \\ (\boldsymbol{\alpha}, h) & \longrightarrow & \Gamma_i\left(\boldsymbol{\alpha}, h\right) \end{array} \right. \tag{5.10}$$

where $[0,1]^{n_{\mathbf{Y}}}$ is the unit hypercube and $\mathcal{D}_{\mathbf{Y}}$ is the support of $\mathbf{Y}$ that grows around the nominal vector $\widetilde{\mathbf{Y}}$ when the horizon of uncertainty h increases:

$$\mathcal{D}_{\mathbf{Y}}\left(h, \widetilde{\mathbf{Y}}\right) = \left\{ \mathbf{Y} : \widetilde{\mathbf{Y}}\left(1-h\right) \leq \mathbf{Y} \leq \widetilde{\mathbf{Y}}\left(1+h\right) \right\}, h \geq 0. \tag{5.11}$$

The robustness and opportuneness functions defined in Chapter 4 translate with the proposed methodology to:

$$h^*_{\mathrm{IG}} = \max_h \left\{ \overline{P}_{\mathrm{f}}\left(\Gamma_i\right) \leq P_{\mathrm{f}}^{\mathrm{cr}} \right\} \tag{5.12}$$

$$\beta^*_{\mathrm{IG}} = \min_h \left\{ \underline{P}_{\mathrm{f}}\left(\Gamma_i\right) \leq P_{\mathrm{f}}^{\mathrm{rw}} \right\} \tag{5.13}$$

where $P_{\mathrm{f}}^{\mathrm{cr}}$ and $P_{\mathrm{f}}^{\mathrm{rw}}$ are the critical and reward failure probabilities respectively. Practically, the robustness and opportunity curves are plotted by estimating $\overline{P}_{\mathrm{f}}$ and $\underline{P}_{\mathrm{f}}$ for a certain number n_h of horizons of uncertainty that belong to a chosen interval $h_j \in [0, h_{\max}]$, $j = 1, \cdots, n_h$. Let us note that in Eq. (5.10), the random set function is only applied on $\mathbf{Y}$ for the sake of conciseness. In the application cases, the random set function also takes into account the random vector $\mathbf{X}$ as in Eqs. (5.6a) and (5.6b).

Whatever the type of uncertainty model that is used for $\mathbf{Y}$, for a given level of horizon of uncertainty h, the same support is used to compare bounds obtained from each model which enables a meaningful comparison. Moreover, the fact that bounds are calculated for increasing horizons of uncertainty and, therefore, growing supports, enables a comparison in terms of robustness (upper bound $\overline{P}_{\mathrm{f}}$) and opportuneness (lower bound $\underline{P}_{\mathrm{f}}$) functions. The larger the support, the more impact the choice of the uncertainty model has on the bounds of the failure probability.

The following quantity $R^{(ij)}_{\overline{P}_{\mathrm{f}}}$ is defined in this chapter as the demand value between a less informative uncertainty model $\mathcal{U}_i$ and a more informative uncertainty model $\mathcal{U}_j$ and is used as the VoI metric:

$$R^{(ij)}_{\overline{P}_{\mathrm{f}}} = 1 - \frac{\overline{P}_{\mathrm{f}}\left(\Gamma_i\left(\boldsymbol{\alpha}, h\right)\right)}{\overline{P}_{\mathrm{f}}\left(\Gamma_j\left(\boldsymbol{\alpha}, h\right)\right)} \tag{5.14}$$

The value of this metric, which is negative as $\overline{P}_{\mathrm{f}}\left(\Gamma_i\left(h\right)\right) \geq \overline{P}_{\mathrm{f}}\left(\Gamma_j\left(h\right)\right)$, shows how the added information from model $\mathcal{U}_i$ to model $\mathcal{U}_j$ diminishes, in terms of percentage, the upper bound of the failure probability. A similar metric could be defined with the lower bound to quantify how a more informative model reduces the best possible outcome. This last metric is not used in this chapter since, in the context of a reliability analysis, the main concern is to understand how the worst possible outcome may be reduced with more information.

5.3.3 Sensitivity to the gain of information

Sensitivity analysis aims at identifying the variables that have a significant impact on the quantity of interest in order to simplify the numerical model or to help the analyst decide where to judiciously allocate resources (Ferson and Tucker, 2006). Many metrics exist depending on the analyst's objective. In this chapter, a simple metric is defined in order to identify the epistemic variables where added information contributes the most to the global gain of information on the bounds of the probability of failure. The idea is then to compare the demand value $R_{\overline{P}_{\mathrm{f}}}$ obtained by considering a more informative uncertainty representation on one variable at a time and compare it with the value obtained when considering all variables at once. The following metric

is defined:

$$S_{Y_k}^{(ij)} = \frac{R_{\overline{P_f}}^{(ij)(k)}}{R_{\overline{P_f}}^{(ij)}}. \tag{5.15}$$

where:

$$R_{\overline{P_f}}^{(ij)(k)} = 1 - \frac{\overline{P_f}\left(\Gamma_i\left(\boldsymbol{\alpha}, h\right)\right)}{\overline{P_f}\left(\Gamma_j^{(k)}\left(\boldsymbol{\alpha}, h\right)\right)} \tag{5.16}$$

with $\Gamma_j^{(k)} = \left[\Gamma_i\left(\alpha_1, h\right), \cdots, \Gamma_j\left(\alpha_k, h\right), \cdots, \Gamma_i\left(\alpha_{n_{\mathbf{Y}}, h}\right)\right]^\top$. This metric gives the contribution of information gained from an uncertainty model to a more informative one brought by each variable. The metric depends on the horizon of uncertainty which means that a variable may be informative for some range of horizon of uncertainty and less informative for other values. This characteristic can contribute valuable knowledge to the decision-making process.

5.3.4 Proposed methodology

This section aims at summarizing the steps that are followed to apply the proposed methodology to three reliability problems. The different steps are presented in Figure 5.4 where each box is detailed as follows:

1. Compute the limit-state function $g\left(\mathbf{X}, \mathbf{Y}\right)$, build a comparison group $\mathbf{G}$ that contains different uncertainty models M_i to be compared, define the values of the horizon of uncertainty h_j for which the bounds on the failure probability will be estimated, associate the joint cumulative distribution function $F_{\mathbf{X}}\left(\mathbf{x}\right)$ to $\mathbf{X}$ and the nominal values $\widetilde{\mathbf{Y}}$ to $\mathbf{Y}$;

2. Get the random set function Γ_i that corresponds to the uncertainty model M_i as presented in Table 1;

3. Compute the support $\mathcal{D}_{\mathbf{Y}}\left(h_j, \widetilde{\mathbf{Y}}\right)$ as defined in Eq. (5.11) which enables to compute the random set function $\Gamma_i\left(\boldsymbol{\alpha}, h_j\right)$ as defined in Eq. (5.10);

4. For each discretized value h_j, estimate the bounds on the failure probability where each random variable α_k follows the standard uniform distribution and each corresponding realization is either the maximum value of the limit-state function in $\Gamma_i\left(\boldsymbol{\alpha}, h_j\right)$ (estimation of $\underline{P_f}$) or the minimum value (estimation of $\overline{P_f}$) obtained with an optimization algorithm. The privileged method used to estimate the probabilities is FORM-IS but SS is also used as a verification method;

5. Once the bounds on the failure probability are obtained for each discretized horizon of uncertainty h_j and for each uncertainty model M_i, the VoI metric $R_{\overline{P_f}}$, as defined in Eq. (5.14), is evaluated;

6. Show the robustness ($\overline{P_f}$) and opportuneness ($\underline{P_f}$) curves obtained with each uncertainty model M_i and show the surface plot $R_{\overline{P_f}}\left(h\right)$ which is a function of h and the two different uncertainty models that are compared in terms of information.

Note that the sensitivity analysis is not present in Figure 5.4. The only addition is the estimation of $\overline{P_f}\left(\Gamma_j^{(k)}\left(\boldsymbol{\alpha}, h\right)\right)$ in Eq. (5.16) which requires to consider the more informative model M_j on one variable Y_k at a time and compute $S_{Y_k}^{(ij)}$ as defined in Eq. (5.15).

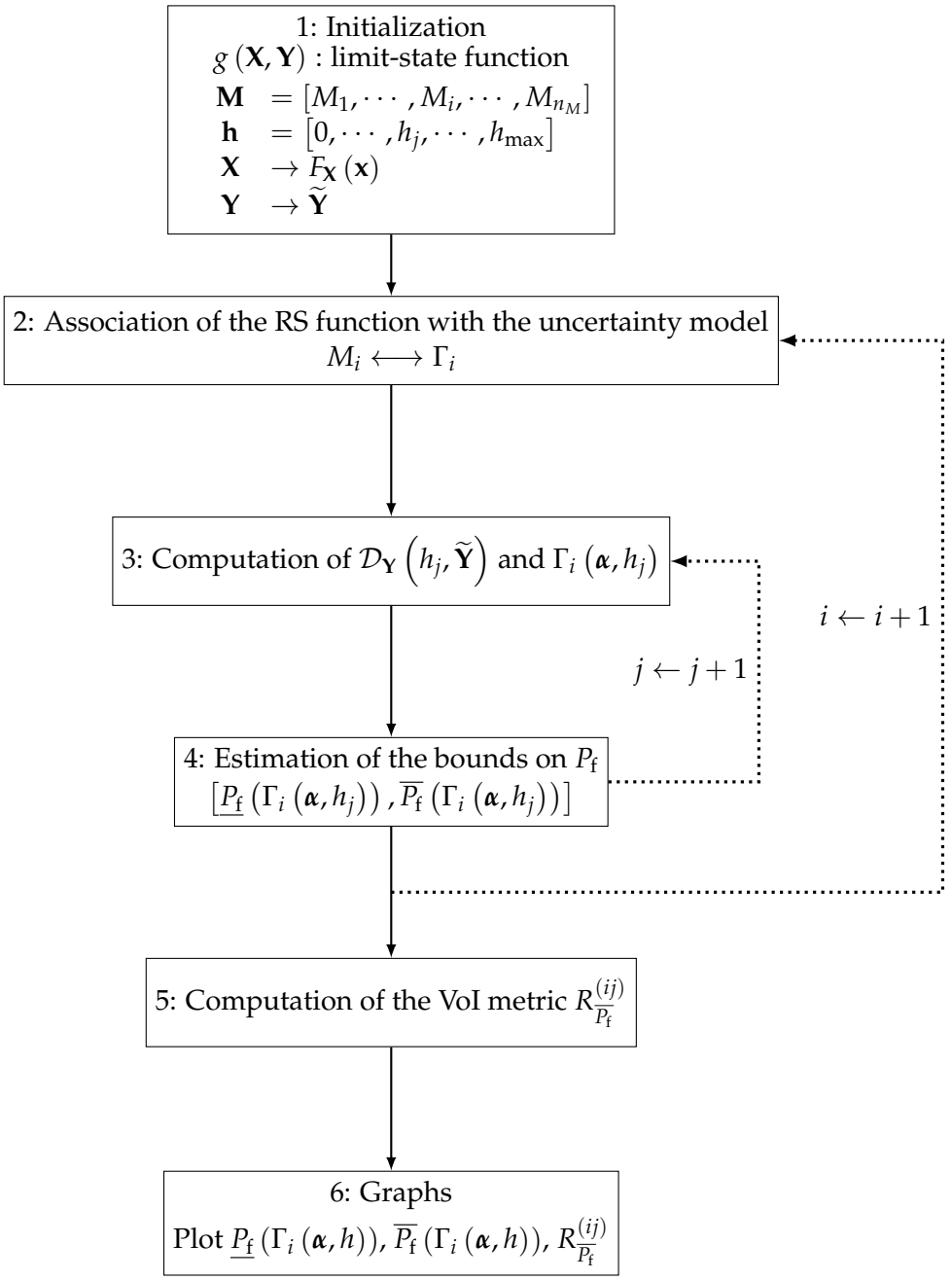

FIGURE 5.4: Workflow of the proposed methodology.

5.4 Application cases

5.4.1 Test cases and numerical tools used

The methodology that is proposed in this chapter is applied on two academic examples, or toy-cases, and to the reliability analysis of penstocks. The two academic examples correspond to modified versions of the three-dimensional Rosenbrock function and a two-degree-of-freedom oscillator system. The main objective is to compare the robustness and opportuneness curves obtained from various uncertainty models with increasing level of informativeness. Therefore, the following groups of comparison are created:

- $\mathbf{M}_1$: interval RS, interval DIRECT, trapezoidal possibility distribution, triangular possibility distribution, probabilistic uniform distribution;

- $\mathbf{M}_2$: interval RS, parallelepiped convex model;
- $\mathbf{M}_3$: free p-box, parametric p-box.

The group $\mathbf{M}_1$ corresponds to added information represented by the solid lines 4 and 5 in Figure 2.9 from Chapter 2 and the solid line that could have been plotted between the interval and probability models. When considering the interval model, a distinction is made between "interval RS" which means that the bounds on the failure probability are estimated using RS theory and "interval DIRECT" which means that the bounds are estimated by using the global optimization algorithm DIRECT (Jones et al., 1993; Finkel, 2003) directly on the failure probability. The group $\mathbf{M}_2$ corresponds to added information represented by the solid line 2. The group $\mathbf{M}_3$ corresponds to added information represented by the solid line 7.

Robustness and opportuneness curves are also presented in order to verify numerically the links between possibility distributions, DS theory, p-boxes and probability distributions. The following groups of comparison are defined for that purpose:

- $\mathbf{M}_4$: triangular possibility distribution, DS structures, free p-box;
- $\mathbf{M}_5$: DS structures, probabilistic uniform distribution.

The group $\mathbf{M}_4$ corresponds to the dotted lines 9, 11 and 12 in Figure 2.9. The group $\mathbf{M}_5$ corresponds to the dotted line 10.

Parametric p-box results are also obtained using the DIRECT algorithm in the hyperrectangle resulting from each uncertain hyperparameter of the distribution law represented as an interval. For all the other models, the bounds are estimated using the RS framework. Moreover, hybrid limit-state functions are shown with the Rosenbrock function and the previously defined VoI metric is computed. The methodology was numerically implemented with Python using mainly the Scipy package to solve the optimization problems (scipy.optimize module) arising from the hybrid limit-state functions, and the OpenTURNS software (Baudin et al., 2017) to estimate failure probabilities using mainly FORM-IS but also Subset Simulation for verification. When available, the robustness and opportuneness curves are given with their corresponding 95% confidence interval (which will be depicted with dotted lines).

5.4.2 Toy case 1: the Rosenbrock function

The first toy case has the following limit-state function based on the Rosenbrock function in three dimensions:

$$g(\mathbf{X}, Y) = 100\left(Y - X_2^2\right)^2 + (X_2 - 1)^2 + 100\left(X_2 - X_1^2\right)^2 + (X_1 - 1)^2 - 3 \tag{5.17}$$

where X_1 and X_2 follow standard Gaussian distributions and Y is the only epistemic variable with a nominal value of $\widetilde{Y} = 0.9$. Robustness and opportuneness curves are obtained by estimating the bounds $\left[\underline{P}_\mathrm{f}, \overline{P}_\mathrm{f}\right]$ for $n_h = 15$ horizon levels for $h \in [0, 0.19]$. As Y has a single component, the convex model reduces to the interval model. The groups of uncertainty models on which results are provided are $\mathbf{M}_1$, $\mathbf{M}_3$, $\mathbf{M}_4$ and $\mathbf{M}_5$. The fact that the input dimension here is $n_\alpha = n_X + n_Y = 3$ enables to draw the isolines of both LSSs $\underline{g}(\boldsymbol{\alpha}, h) = 0$ and $\overline{g}(\boldsymbol{\alpha}, h) = 0$ in the $\boldsymbol{\alpha}$-space for different values of h and different uncertainty models. Note that the $\boldsymbol{\alpha}$-space is the unit hypercube of dimension $n_X + n_Y$ and that α_{X_i} represents the quantile order of X_i.

$\mathbf{M}_1$ results

The isolines of the limit-state functions for the interval model on Y are shown in Figure 5.5, where the failure domain lies in the ellipsoid shape. Since, for a given h, Y is a unique interval, its corresponding random set is the same interval and does not depend on α_Y. Therefore, for a given

h, the failure domain is a surface. The isolines are given at increasing horizons of uncertainty $h \in [0, 0.19]$ which is why the plot is three-dimensional. One can see how $\underline{g}(\boldsymbol{\alpha}, h) = 0$ (used for $\overline{P_f}$ estimation) gradually expands with h while $\overline{g}(\boldsymbol{\alpha}, h) = 0$ (used for $\underline{P_f}$ estimation) gradually reduces as expected.

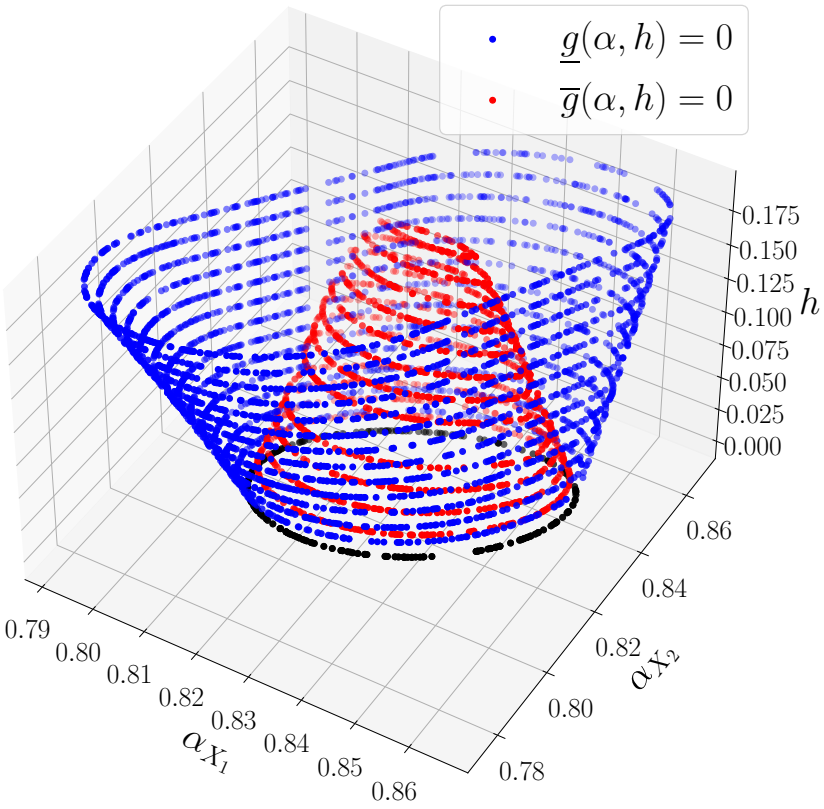

FIGURE 5.5: Illustration of limit-state surfaces $\underline{g}(\boldsymbol{\alpha}, h) = 0$ and $\overline{g}(\boldsymbol{\alpha}, h) = 0$ for the interval representation for the Rosenbrock function.

Figure 5.6 compares the isolines of the LSSs between the triangular and trapezoidal distributions at a given horizon level $h = 0.19$. In this case, the dimension of $\boldsymbol{\alpha}$ is 3 which means that the failure domain is a volume which is why it is illustrated for a single value of h. For a given $\boldsymbol{\alpha}$, the corresponding random set induced by the triangular distribution is contained in the random set induced by the trapezoidal distribution. This explains why the failure volume obtained from the triangular model is contained in the one obtained from the trapezoidal model when considering the limit-state function $\underline{g}(\boldsymbol{\alpha}, h) = 0$ while the opposite happens when considering the limit-state function $\overline{g}(\boldsymbol{\alpha}, h) = 0$.

The analysis of the limit-state functions already gives a strong intuition on the inclusions of the bounds on the failure probability obtained from the different uncertainty representations in $\mathbf{M}_1$. Figure 5.8.(A) presents the robustness and opportuneness curves for the four different uncertainty models. The expected inclusions are obtained. One can notice that the extreme failure probabilities remain close to the nominal result except for the lower failure probabilities obtained with the interval model and considering RS theory (i.e. interval RS). This could be expected looking at Figure 5.5 as the ellipses shrink considerably when the horizon of uncertainty grows. Nevertheless, computing the results of the interval model using the optimization method (i.e. interval DIRECT) yields very different results as the bounds on the failure probability become very tight, even tighter than the bounds obtained from the trapezoidal model. This

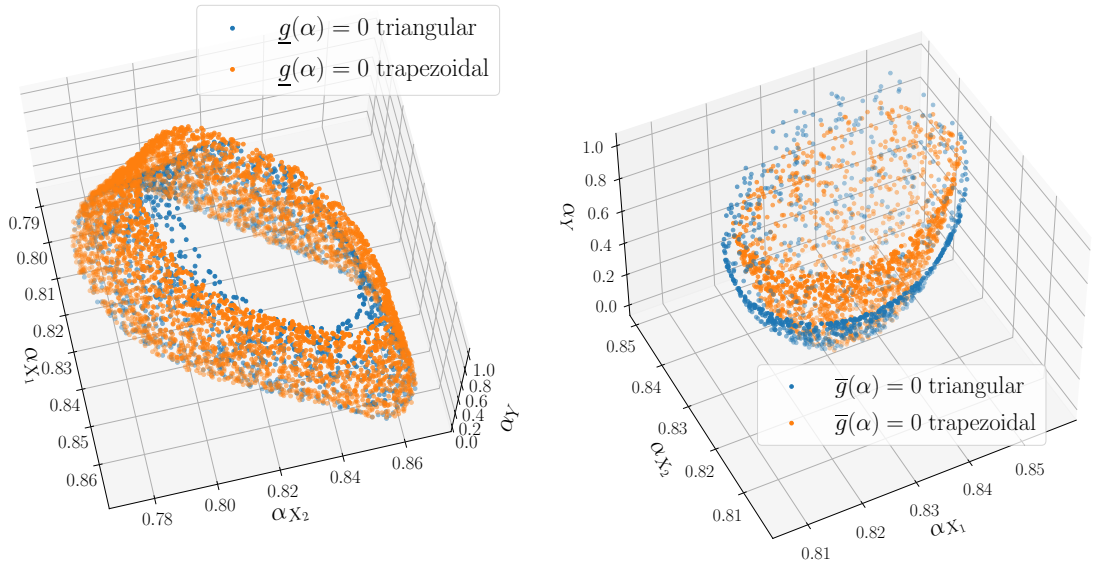

(A) (B)

FIGURE 5.6: Comparison of $\underline{g}(\boldsymbol{\alpha}) = 0$ (A) and $\overline{g}(\boldsymbol{\alpha}) = 0$ (B) for the triangular and trapezoidal uncertainty models.

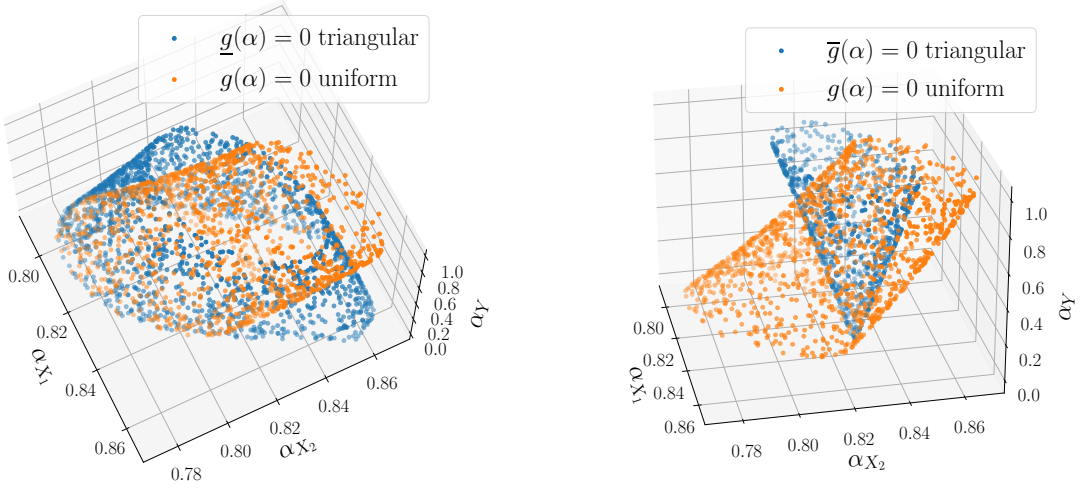

(A) (B)

FIGURE 5.7: Comparison of $\underline{g}(\boldsymbol{\alpha}) = 0$ (A) and $\overline{g}(\boldsymbol{\alpha}) = 0$ (B) for the triangular and uniform uncertainty models.

is probably caused by the strong non-linearity of the limit-state function.

M_3 results

Here, the free p-box and parametric p-box models are compared. It is recalled that, for an equivalent support, the parametric p-box model is more informative than the free p-box model which implies the bounds on the failure probability of the second model to be contained in the

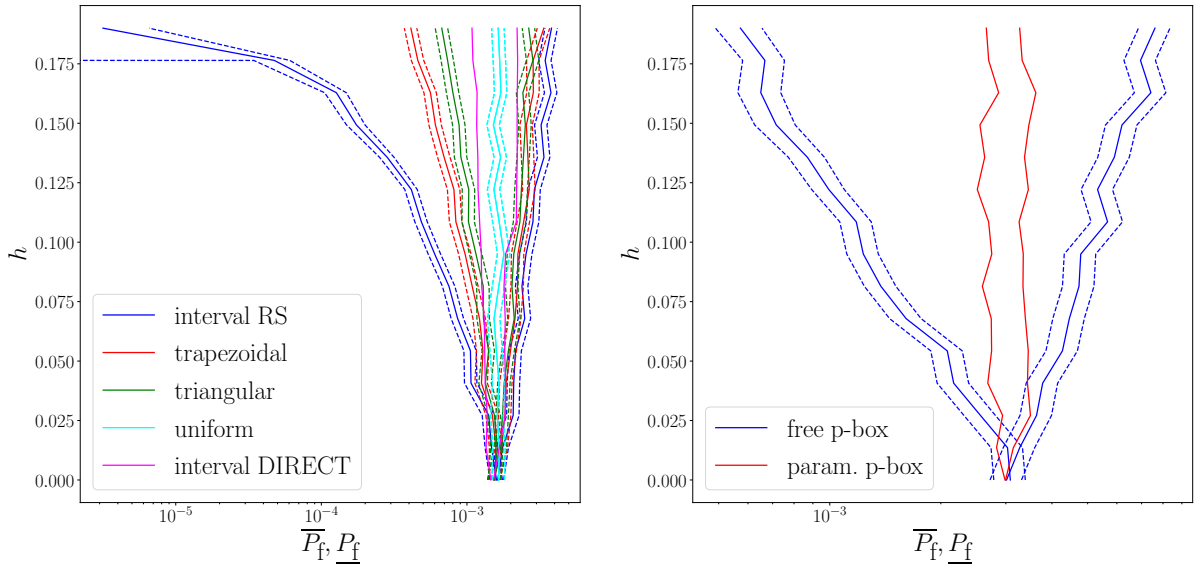

(A) (B)

FIGURE 5.8: Robustness and opportuneness curves for the groups $\mathbf{M}_1$ (A) and $\mathbf{M}_3$ (B) for the Rosenbrock function.

bounds of the first model. The p-box models (free and parametric) are constructed by considering a Gaussian distribution on Y: $Y \sim \mathcal{N}\left(0.9, \sigma^2\right)$ with $\sigma \in [1-h, 1+h]$. The parametric p-box results are obtained by performing an optimization using the DIRECT algorithm on σ. Figure 5.8.(B) presents the robustness and opportuneness curves. One can see a strong difference in behavior as the bounds induced by the parametric p-box model barely expand. This difference can again be explained by the strong non-linearity of the model.

$\mathbf{M}_4$ and $\mathbf{M}_5$ results

The $\mathbf{M}_4$ comparison aims, firstly, at numerically illustrating the relation between the triangular possibility distribution and its equivalent free p-box representation and, secondly, the link between the triangular possibility distribution and its discretized DS model. The $\mathbf{M}_5$ comparison aims at numerically illustrating the link between the probabilistic uniform cdf and its discretized DS model. Figure 5.9 compares the limit-state functions between the triangular model and its equivalent p-box at $h = 0.19$. It does seem that the limit-state functions of both representations have the same volume, though having a different shape. Note that, even if the different scales make it hard to see, the failure domain $\overline{g}\left(\boldsymbol{\alpha}\right) \leq 0$ is still included in the failure domain $\underline{g}\left(\boldsymbol{\alpha}\right) \leq 0$ for both representations as expected.

Figure 5.10 compares the robustness and opportuneness curves for both comparisons and numerically confirms the expected results, despite the noise induced by the failure probability estimations.

5.4.3 Toy-case 2: a non-linear oscillator system

The second toy-case corresponds to an adapted version of a two-degree-of-freedom oscillator as shown in Figure 5.11 and seen in (Der Kiureghian and De Stefano, 1991; Chabridon et al., 2017). The system is composed of two masses m_p and m_s, two springs of stiffnesses k_p and k_s, two damping ratios ζ_p and ζ_s and is subjected to a white noise base acceleration of intensity S_0. By denoting F_s as the force capacity of the secondary spring, the reliability of the system is

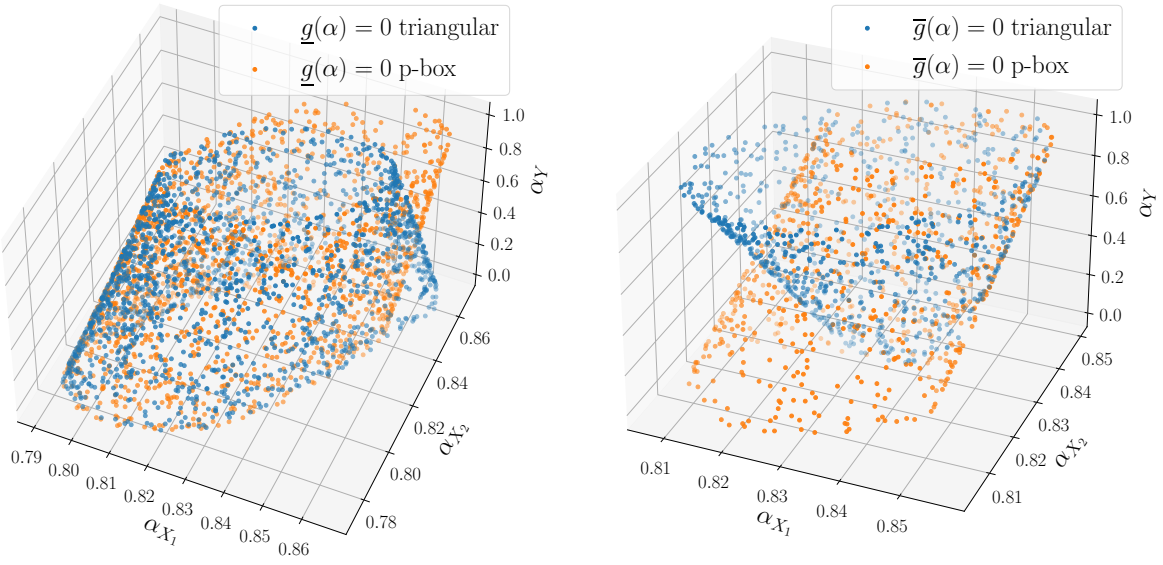

(A) (B)

FIGURE 5.9: Comparison of $\underline{g}(\alpha) = 0$ (A) and $\overline{g}(\alpha) = 0$ (B) for the triangular and triangular-pbox uncertainty models.

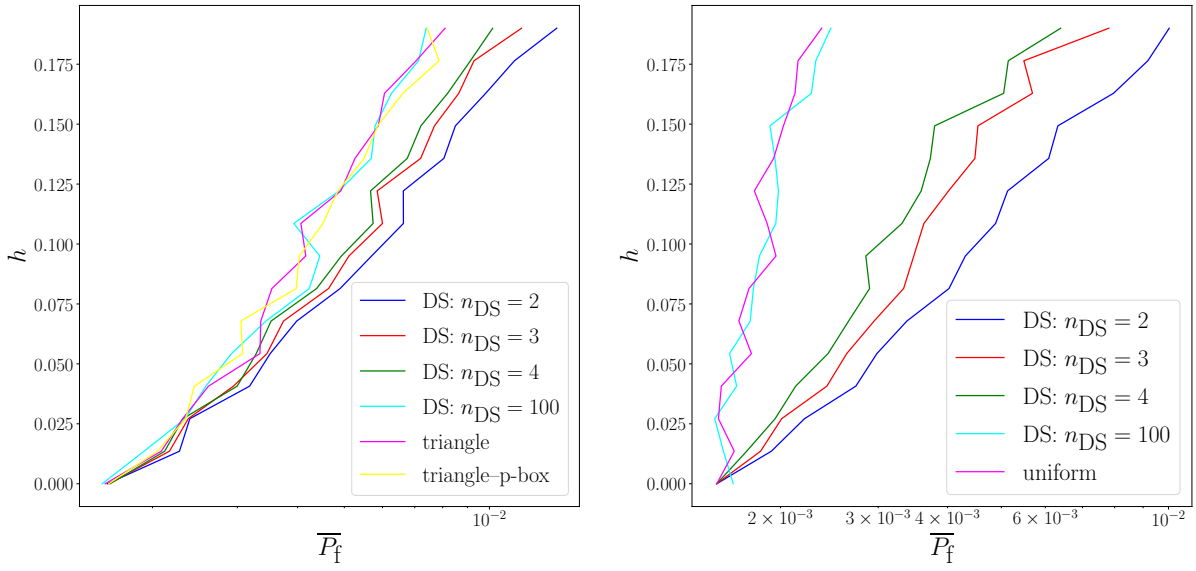

(A) (B)

FIGURE 5.10: Robustness curves for the groups $\mathbf{M}_4$ (A) and $\mathbf{M}_5$ (B) for the Rosenbrock function.

expressed through the following limit-state function:

$$g(\mathbf{X}, \mathbf{Y}) = F_s - 3k_s \sqrt{\frac{\pi S_0}{4\zeta_s \omega_s^3} \left[\frac{\zeta_a \zeta_s}{\zeta_p \zeta_s \left(4\zeta_a^2 + r^2\right) + \gamma \zeta_a^2} \frac{\left(\zeta_p \omega_p^3 + \zeta_s \omega_s^3\right) \omega_p}{4\zeta_a \omega_a^4} \right]} \tag{5.18}$$

where $\gamma = m_s/m_p$ is the mass ratio, $\omega_p = \left(k_p/m_p\right)^{1/2}$ and $\omega_s = \left(k_s/m_s\right)^{1/2}$ the natural frequencies, $\omega_a = \left(\omega_p + \omega_s\right)/2$ the average frequency ratio, $\zeta_a = \left(\zeta_p + \zeta_s\right)/2$ the average damping

ratio and $r = \left(\omega_p - \omega_s\right)/\omega_a$ a tuning parameter. The random vector $\mathbf{X}$ gathers $n_X = 3$ independent random variables whose probabilistic modeling is given in Table 5.1. The epistemic vector $\mathbf{Y}$ is of dimension $n_Y = 5$ and its epistemic characteristics are given in Table 5.2. One supposes here that nominal values are known for the stiffnesses, the damping ratios and the force capacity.

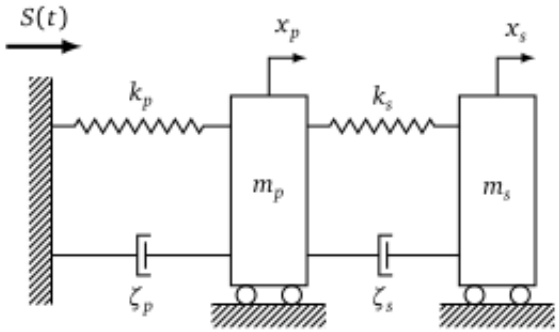

FIGURE 5.11: Two-degree-of-freedom damped oscillator.

The horizon of uncertainty is discretized into 10 values in $[0, 0.05]$. The groups of comparison that are studied are $\mathbf{M}_1$ and $\mathbf{M}_2$.

TABLE 5.1: Input probabilistic modeling of $\mathbf{X}$.

Variable X_i	Distribution	Mean μ_{X_i}	δ
$X_1 = m_p$ (kg)	Lognormal	1.5	10%
$X_2 = m_s$ (kg)	Lognormal	0.01	10%
$X_3 = S_0$ (m.s^{-2})	Lognormal	100	10%

TABLE 5.2: Epistemic characteristics of $\mathbf{Y}$.

Variable Y_i	$\widetilde{Y}_i$
$Y_1 = k_p$ (N.m^{-1})	1
$Y_2 = k_s$ (N.m^{-1})	0.01
$Y_3 = \zeta_p$ (1)	0.05
$Y_4 = \zeta_s$ (1)	0.02
$Y_5 = F_s$ (N)	11

$\mathbf{M}_1$ results

Before showing the robustness and opportuneness curves for all representations, Figure 5.12 compares these curves for the trapezoidal representation estimated using the FORM-IS and Subset Simulation algorithms. The curves obtained by evaluating the hybrid limit-state functions using the vertex method (Dong and Shah, 1987) (which states that the extreme values of the limit-state function are obtained at combinations of the extreme values of Y_i) instead of an optimization algorithm are also given in the same figure. The curves suggest a high confidence in the results obtained with the FORM-IS algorithm and seem to confirm the hypothesis introduced with the vertex method.

The robustness and opportuneness curves are given in Figure 5.13.(A) and the corresponding VoI surface plot in Figure 5.13.(B). Once again, the minimum failure probability with the interval-RS model quickly decreases compared to the other representations including the interval-DIRECT model. This is not so much the case for the maximum failure probability for which the highest values of $R_{\overline{P}_f}$ are obtained from the triangle representation to the uniform representation.

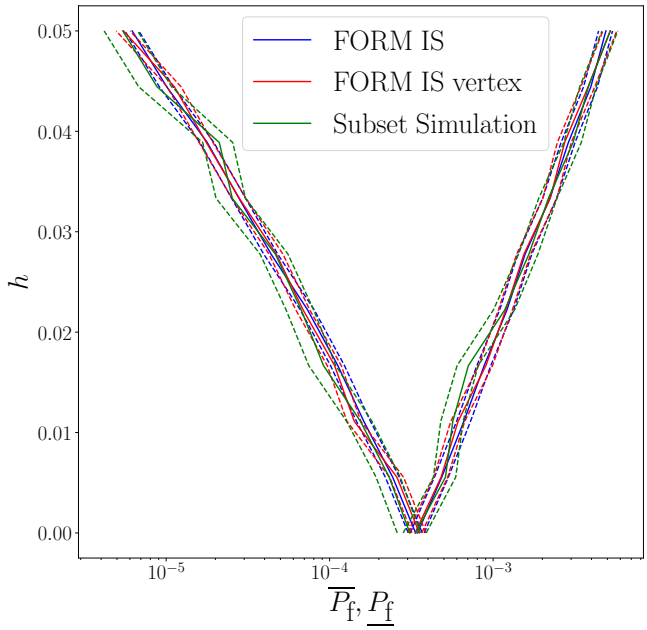

FIGURE 5.12: P_f estimators comparison for the oscillator case.

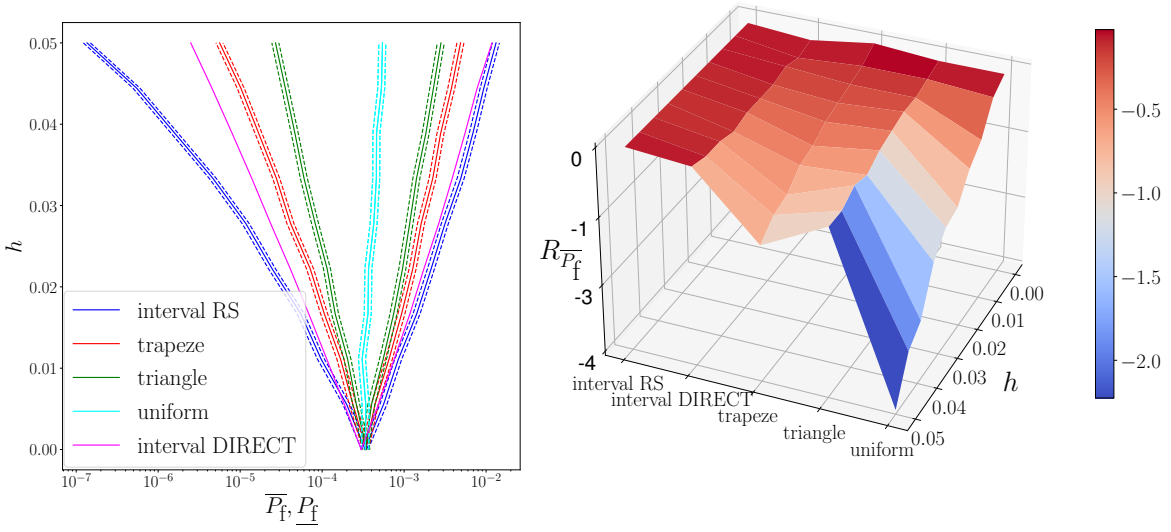

(A) (B)

FIGURE 5.13: Robustness and opportuneness curves (A) and VoI metric (B) considering the $\mathbf{M}_1$ group for the non-linear oscillator case.

$\mathbf{M}_2$ results

Here, the multi-parallelepiped uncertainty model is used to model the epistemic vector by considering an equal coefficient of linear correlation $\rho_{k_p\zeta_p} = \rho_{k_s\zeta_s} = \rho$. Figure 5.14 presents the robustness and opportuneness curves for different values of the coefficient of correlation. The 95% confidence intervals are not depicted for the sake of clarity. As expected, the higher the coefficient of correlation in terms of absolute value, the narrower the bounds on the failure

probability. Nevertheless, the bounds will shrink significantly as soon as a non-zero coefficient of correlation is given but the results between a low or high coefficient do not considerably differ.

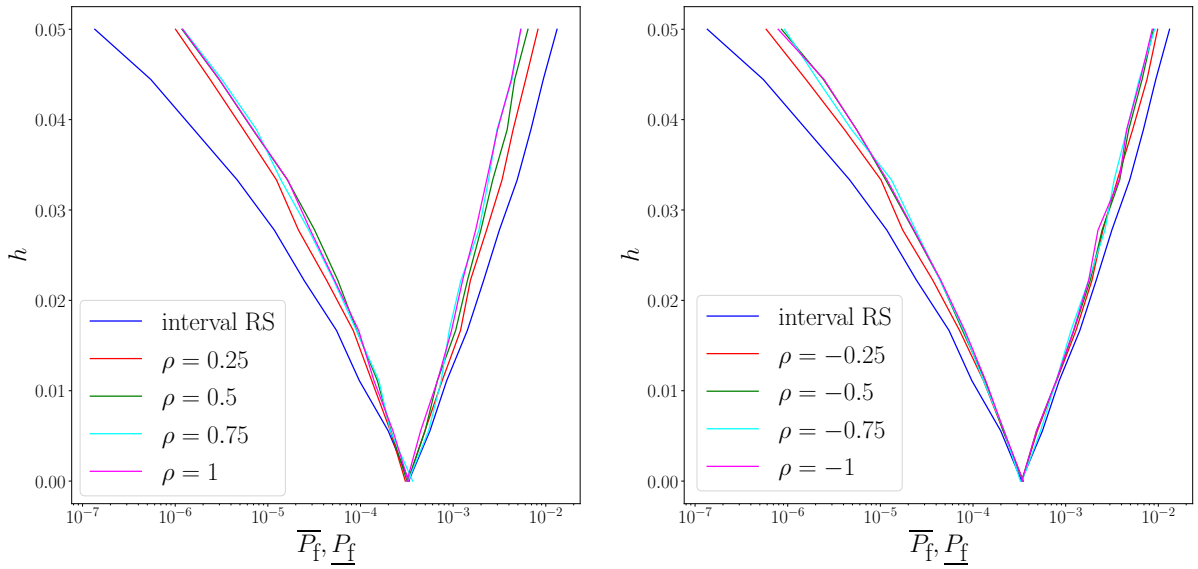

(A) (B)

FIGURE 5.14: $\mathbf{M}_2$ comparison for positive coefficients of correlation (A) and $\mathbf{M}_2$ comparison for negative coefficients of correlation (B).

5.4.4 Reliability assessment of penstocks

In this section, the methodology is applied to the reliability of penstocks associated to brittle failure mode. Note that this application is illustrative: the choice of epistemic variables should be further substantiated. It is meant to demonstrate the feasibility of the methodology on a more complex industrial use-case. The conditional annual failure probability is of interest and the characteristics of $\mathbf{X}$ and $\mathbf{Y}$ are given in Tables 5.3 and 5.4 respectively.

TABLE 5.3: Input probabilistic modeling of $\mathbf{X}$ for the penstock use-case.

Variable X_i	Distribution	Param 1	Param 2	Param 3
$X_1 = R_m$ (MPa)	Lognormal	480	24	-
$X_2 = \Delta e_{\text{extra}}$ (mm)	Normal	0	0.25	-
$X_3 = \Delta e_{\text{corr}}$ (mm)	Normal	1	0.4	-
$X_4 = \varepsilon$ (MPa)	Normal	0	16.816	-
$X_5 = K_{IC}$ (MPa.$\sqrt{\text{m}}$)	Weibull Min	90	4	20

TABLE 5.4: Epistemic characteristics of $\mathbf{Y}$ for the penstock use-case.

Variable Y_i	$\widetilde{Y}_i$
$Y_1 = e_{\text{nom}}$ (mm)	8
$Y_2 = \Delta e_{\text{an}}$ (mm)	0.06
$Y_3 = a$ (mm)	2

It should be pointed out that calculating a conditional probability using RS theory is not as straightforward as in Eqs. (5.7a) and (5.7b). Indeed, one cannot express in a trivial way the

maximum or the minimum of the failure probability as a function of the maximum or minimum of both limit-states $G_{N+1} \times G_N$ and G_{HPT}. Nevertheless in this case, as $\mathbf{Y}$ has a greater impact on $G_{N+1}.G_N$ than G_{ht}, the following simplification is performed:

$$\overline{P}_{\text{f}} \approx \frac{\Pr\left[\min_{\Gamma(\boldsymbol{\alpha})}\left(G_{N+1}.G_N\right) \leq 0 \cap G_{\text{HPT}}\left(\boldsymbol{\alpha}^*\right) \geq 0\right]}{\Pr\left[G_{\text{HPT}}\left(\boldsymbol{\alpha}^*\right) \geq 0\right]} \tag{5.19}$$

where $\boldsymbol{\alpha}^* = \arg\min\left(G_{N+1}.G_N\right)$. In this industrial use-case, only the maximum failure probability $\overline{P}_{\text{f}}$ will be of interest. The results of the groups of comparison $\mathbf{M}_1$, $\mathbf{M}_2$ and $\mathbf{M}_3$ are given in the following.

$\mathbf{M}_1$ results

The FORM-IS algorithm is, once again, the first choice to estimate the probabilities. Nevertheless, it is necessary to verify the results with another algorithm. Figure 5.15 compares the robustness curves obtained with the FORM-IS and the Subset Simulation algorithms considering the interval model on $\mathbf{Y}$. Despite being less smooth, the results obtained with the Subset Simulation algorithm are very similar to those obtained with FORM-IS.

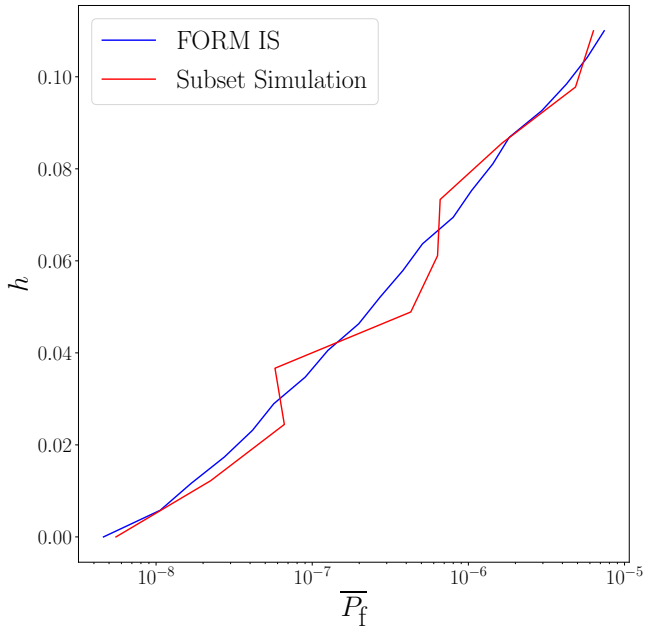

FIGURE 5.15: P_{f} estimators comparison for the penstock use-case.

Figure 5.16.(A) shows the robustness curves of $\mathbf{M}_1$ and Figure 5.16.(B) shows the corresponding VoI surface plot of the VoI metric $R_{\overline{P}_{\text{f}}}$. Once again, the probabilistic information of a uniform distribution considerably reduces the maximum failure probability and therefore improves the robustness. The difference between both interval results is also quite significant.

Figure 5.17 presents the sensitivity results from the interval to the trapezoidal representations. The classification of the most influential variables on the information is quite clear whatever the horizon of uncertainty as the added information on e_{nom} has a strong influence, on K_{IC} a non-negligible influence and on Δe_{an} a very weak influence.

$\mathbf{M}_2$ results

Figure 5.18.(A) presents the results with the multi-parallelepiped model by considering a coefficient of correlation $\rho = \rho_{Y_1 Y_2}$ between e_{nom} and Δe_{an}. It seems that a negative coefficient

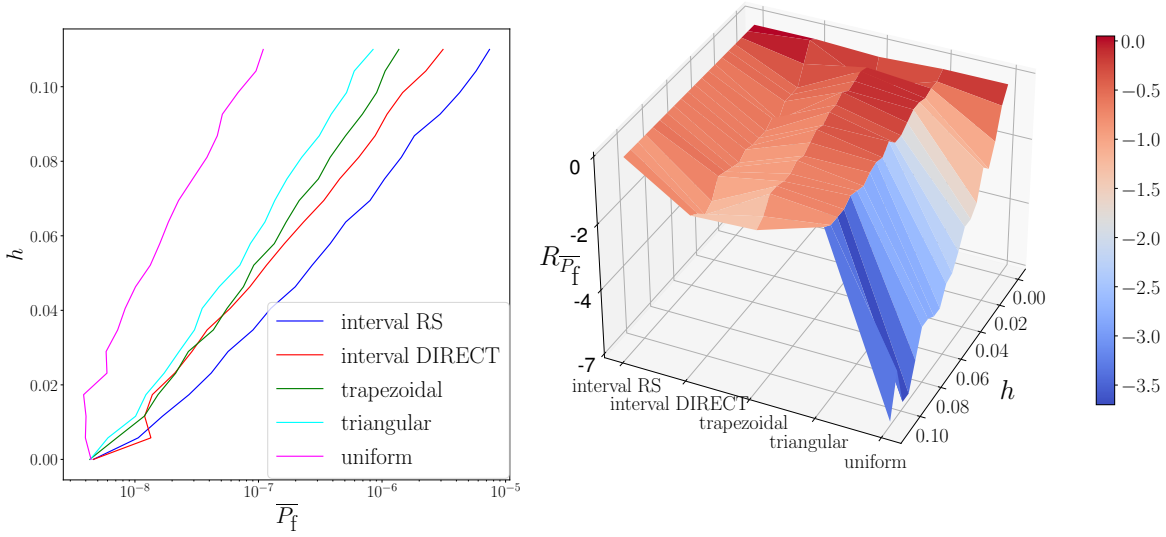

(A) (B)

FIGURE 5.16: Robustness curves (A) and VoI metric (B) considering the $\mathbf{M}_1$ group for the penstock use-case.

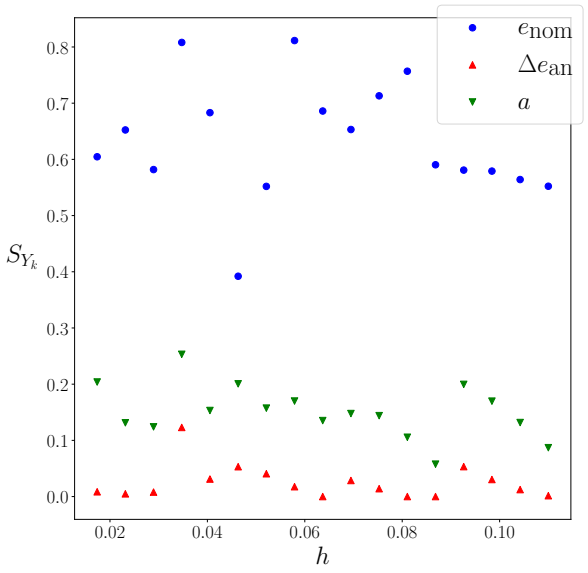

FIGURE 5.17: Sensitivity analysis from the interval to the trapezezoidal representations for the penstock use-case.

of correlation has no impact on the robustness while a positive coefficient has a very limited impact.

$\mathbf{M}_3$ results

The p-box model is constructed by considering a Gaussian distribution for Y_i: $Y_i \sim \mathcal{N}\left(\widetilde{Y}_i, \sigma_i^2\right)$ with $\sigma_i \in [\widetilde{\sigma}_i(1-h), \widetilde{\sigma}_i(1+h)]$ and $\widetilde{\sigma} = [0.4, 0.003, 0.1]^\top$. For this case, the horizon of uncertainty belongs to $h \in [0, 0.5]$. The parametric p-box results are still obtained by performing an

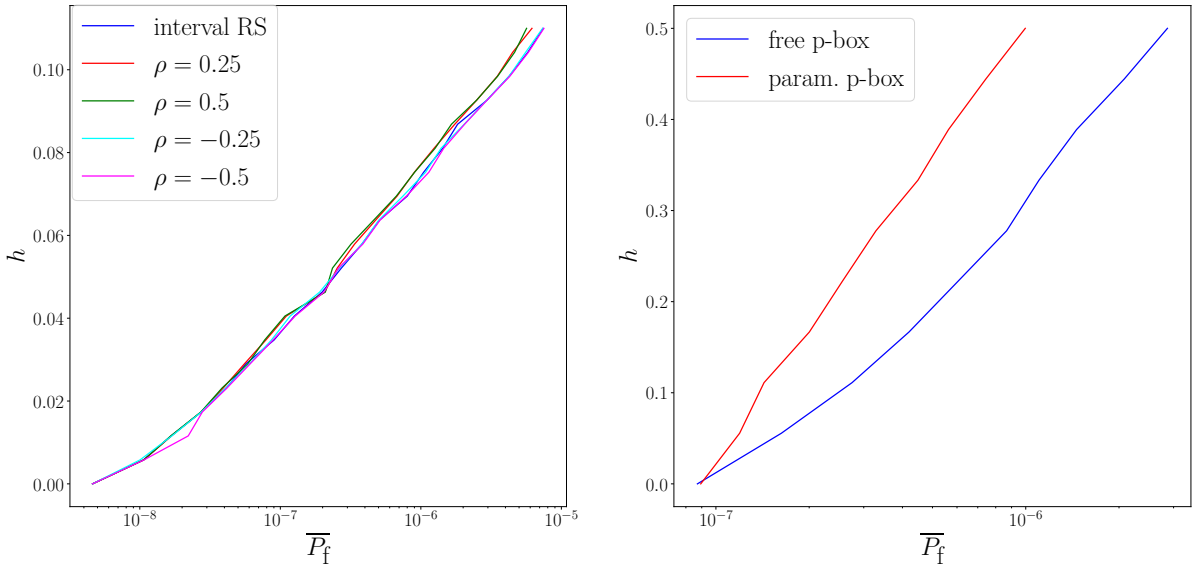

(A) (B)

FIGURE 5.18: Robustness curves for the groups $\mathbf{M}_2$ (A) and $\mathbf{M}_3$ (B) for the penstock use-case.

optimization using the DIRECT algorithm on σ. Figure 5.18.(B) presents the robustness curves for both representations. The added information in the parametric p-box improves the robustness as expected.

5.5 Discussions

This section aims in a first place at summarizing all the results from above w.r.t. the objective of this work which is to analyse the effect of different models of uncertainty on a robustness analysis in the context of HRA. The use-cases enable to numerically translate the links presented in Figure 2.9 by constructing and comparing opportuneness and robustness curves. These links, and therefore the comparison, are divided into two main groups. The first one, which involves the comparison groups M_1, M_2 and M_3, shows in what extent a more informative uncertainty model may affect robustness and opportunity. Indeed, adding information will often lead to a gain in robustness (the model can tolerate more uncertainty) and a loss in opportunity (more uncertainty is needed for a positive unexpected outcome). In the context of HRA, this notion is seen as a narrowing of the bounds of the failure probability until reaching a unique value for purely probabilistic or deterministic models. The more the support of the epistemic variables grows the more narrowing is observed. On the other hand, the more informative a model is the more dependent the quantity of interest is on the hypothesis made. Nevertheless, the benefits of acquiring information strongly depend on the decision-making context. Indeed, in the case of safety assessment for which very small failure probabilities are estimated, a gain of information is way more valuable if it affects the robustness curve rather than the opportuneness curve.

The behavior of the numerical model (i.e. the limit-state functions in the case of HRA) w.r.t. the epistemic variables also has a key role on the value of information. For example, a monotonous behavior will yield the same bounds on the failure probability whether free or parametric p-boxes are considered. A reduced convex set (i.e. more informative) will have no impact on the robustness curve if the worst performance was initially obtained at a point that is still contained in the more informative set. In most practical cases, such information may unfortunately only be available after the robustness analysis.

The second main group concerns the comparison groups M_4 and M_5 which emphasize some links between different uncertainty models in the framework of this chapter. More precisely, it numerically confirms that possibility distributions and DS structures may also be seen as free p-boxes and that probability and possibility distributions may be considered as DS structures (with a loss of information that depends on the discretization process). This is interesting for two main reasons. The first one is related to the fact that all these uncertainty models with different interpretations and mathematical foundations may be intimidating for an average decision maker. These links show how different models can be closely related in the context of HRA. The second reason is that it enables to widen the use of smart numerical methods initially established for a specific uncertainty framework such as p-boxes for which a lot of content is proposed.

Additionally, this section wants to clarify the use of the proposed methodology. The IG framework is initially built for taking robust decisions in the context of strong uncertainty. The present work does certainly not aim at ranking any uncertainty representation nor does it want to emphasize the proposed methodology for performing an IG analysis. The choice of an uncertainty model strongly depends on the available information and on the context in which a decision must be made (e.g. a safety requirement). The IG method brings an additional tool for confronting a decision to the hypotheses that were made in order to take that decision. Therefore, it is complementary with the probabilistic framework for decisions based on reliability quantities. The possible combination of the different uncertainty models considered through random set theory together with the IG framework offers a wide range of possibilities for conducting a suitable robustness analysis on reliability quantities.

5.6 Synthesis

In this Chapter, a methodology was proposed in order to analyse the robustness of the upper bound of a failure probability w.r.t. different epistemic uncertainty representations in input. In the context of hybrid reliability analysis, the random set framework is suitable to model and propagate different representations of uncertainty to estimate reliability quantities of interest such as bounds on a failure probability. An IG robustness analysis was performed by considering each type of uncertainty model in an increasing support of the epistemic variables.

This methodology enabled to compare robustness and opportuneness curves between uncertainty models that are more or less informative for two academic examples and one industrial use-case related to the reliability assessment of hydraulic penstocks. As expected, it is seen that increasing the support of the epistemic variables leads to increasing the effect of the choice of the uncertainty model on the bounds of the failure probability and therefore on the robustness analysis. The objective of this study is not to determine the best representation of uncertainty, as this depends on the available information, but to provide insights about the impact (in terms of robustness) of the uncertainty model.

In the following chapters, robustness will be performed considering uncertainty on a nominal probabilistic distribution. Therefore, the p-box representation will be considered.

CHAPTER 6

Line sampling-based algorithms for the robustness assessment of penstocks

Contents

This chapter is adapted from the following reference:
A. Ajenjo, E. Ardillon, V. Chabridon, S. Cogan and E. Sadoulet-Reboul (2022). "Robustness evaluation of the reliability of penstocks combining line sampling and neural networks". *Preprint*.

6.1 Motivations

The overall motivation of this chapter is twofold. First, an illustrative IG robustness analysis is applied to the failure mode of penstocks associated to plastic collapse. Line sampling is adapted to this simpler reliability assessment study before presenting numerical aspects and typical results induced by the IG analysis. Secondly, robustness applied to the more challenging conditional brittle failure mode is considered. A numerical procedure that appears to be performant for evaluating the IG robustness on the reliability assessment of penstocks is followed. As already mentioned in Chapter 3, the main challenges that appear when estimating the failure probability of a penstock is the rareness of the failure event and the particular geometry of the failure domain defined through event intersections. The last matter becomes even more binding when considering conditional failure probabilities. However, the bright side is that the involved LSFs are analytical, and therefore fast to evaluate, and that some knowledge about the LSFs is available.

Robustness analysis is firstly performed in Section 6.2 on the plastic collapse failure mode which presents a first implementation of line sampling. Then, Section 6.3 presents adaptations of line sampling to the brittle failure mode conditional to the success of the hydraulic test. Section 6.4 describes the methodology applied for building robustness curves and validates the line sampling algorithms. Finally, Section 6.5 proposes a combination of two artificial neural networks with the line sampling algorithm to reduce computational time.

6.2 Robustness analysis applied to the plastic collapse failure mode

6.2.1 First application of line sampling

As a reminder from Chapter 3, the annual failure probability related to the plastic collapse failure mode is expressed as:

$$P_{\mathrm{f}} = \mathbb{P}\left(G_{N+1}\left(\mathbf{X}\right) \leq 0 \cap G_N\left(\mathbf{X}\right) > 0\right) = \mathbb{P}\left(G_{N+1}\left(\mathbf{X}\right).G_N\left(\mathbf{X}\right) \leq 0\right). \tag{6.1}$$

The random vector involved in this failure mode is $\mathbf{X} = [R_m, \Delta e_{\mathrm{corr}}, \Delta e_{\mathrm{extra}}, \varepsilon]$ for which the probabilistic characteristics can be retrieved in Chapter 3 in Table 3.1. The monotonic decrease of the annual LSF over the years due to corrosion implies that the studied failure domain actually represents a narrowed band (the failure domain at year $N+1$ contains the failure domain at year N). Hence, importance sampling algorithms only based on the MPFP may still generate a lot of samples outside of the band, at least in their standard version. In this chapter, the line sampling technique already introduced in Chapter 2 is implemented. Indeed, this technique enables to tackle directly the LSFs.

However, the formulation proposed in Eq. (2.24) needs to be reconsidered as the underlying hypothesis of the unicity of the root $r\left(\mathbf{u}_{\boldsymbol{\alpha}}^{\perp,(i)}\right)$ is not met due to the geometry of the failure domain. Indeed, by denoting $G_N^{\perp,(i)} = G_N\left(v_1, \mathbf{u}_{\boldsymbol{\alpha}}^{\perp,(i)}\right)$ and $G_{N+1}^{\perp,(i)} = G_{N+1}\left(v_1, \mathbf{u}_{\boldsymbol{\alpha}}^{\perp,(i)}\right)$, Figure 6.1 shows the two roots $r_1^{(i)}$ and $r_2^{(i)}$ to be considered which bound the one-dimensional failure domain along the i-th line. The fact that two roots need to be accounted for simply rewrites the

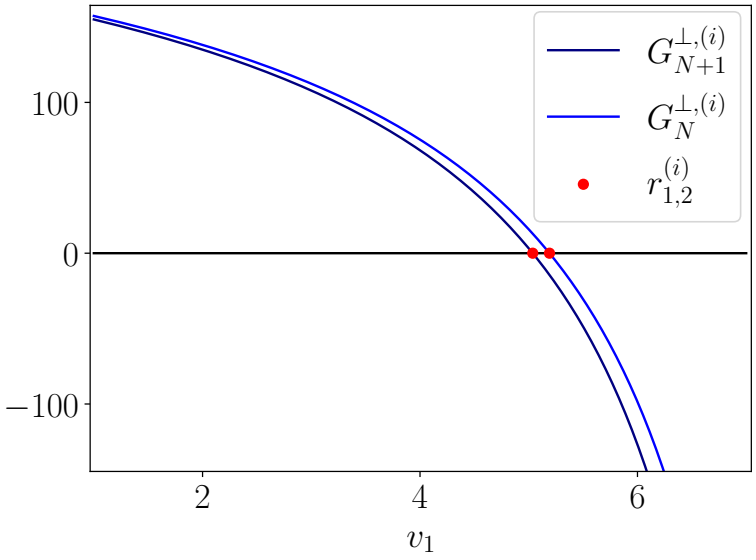

FIGURE 6.1: Two roots involved along a sampled line for the plastic failure mode.

failure probability as:

$$P_{\mathrm{f}} = \int_{\mathbb{R}^{n_{\mathbf{X}}-1}} \left[\Phi\left(-r_1\left(\mathbf{u}_{\boldsymbol{\alpha}}^{\perp}\right)\right) - \Phi\left(-r_2\left(\mathbf{u}_{\boldsymbol{\alpha}}^{\perp}\right)\right)\right] \varphi_{\mathbf{U}_{\boldsymbol{\alpha}}^{\perp}}(\mathbf{u}_{\boldsymbol{\alpha}}^{\perp}) d\mathbf{u}_{\boldsymbol{\alpha}}^{\perp} \tag{6.2}$$

which yields the following estimator:

$$\widehat{P}_{\mathrm{f}} = \frac{1}{n_{\mathrm{LS}}} \sum_{i=1}^{n_{\mathrm{LS}}} p_{\mathrm{f}}^{(i)} = \frac{1}{n_{\mathrm{LS}}} \sum_{i=1}^{n_{\mathrm{LS}}} \Phi\left(-r_1^{(i)}\right) - \Phi\left(-r_2^{(i)}\right). \tag{6.3}$$

The generic procedure to estimate the failure probability with the LS estimator is presented in Algorithm 1. First, the optimal direction $\boldsymbol{\alpha}$ is obtained after a FORM analysis. Then, n_{LS} points are generated according to the standard Gaussian distribution before being projected into the orthogonal hyperplane. Finally, the two roots $r_1^{(i)}$ and $r_2^{(i)}$ are assessed along each line using the "Newton" algorithm proposed in the Python optimization package in SciPy (`scipy.optimize`).

Algorithm 1 – LS procedure for plastic failure mode.

$P_{\mathrm{f}} \leftarrow 0$
Find $\boldsymbol{\alpha}$ # FORM results
Generate $\mathbf{u} \sim \mathcal{N}(0,1)$
for $i : 1 \rightarrow n_{\mathrm{LS}}$ **do**
  $\mathbf{u}_{\boldsymbol{\alpha}}^{\perp,(i)} \leftarrow \mathbf{u}^{(i)} - \left(\mathbf{u}^{(i)}.\boldsymbol{\alpha}\right)\boldsymbol{\alpha}$ # projection on the orthogonal hyperplane
  Search for $r_1^{(i)}$ and $r_2^{(i)}$
  $p_{\mathrm{f}}^{(i)} = \Phi\left(-r_1^{(i)}\right) - \Phi\left(-r_2^{(i)}\right)$ # failure lies in $\left[r_1^{(i)}, r_2^{(i)}\right]$
  $P_{\mathrm{f}} \leftarrow P_{\mathrm{f}} + p_{\mathrm{f}}^{(i)}$
$P_{\mathrm{f}} \leftarrow P_{\mathrm{f}} / n_{\mathrm{LS}}$

The procedure for the LS estimator is now tested on four different configurations of penstocks. The convergence of the estimated failure probabilities is compared with the convergence

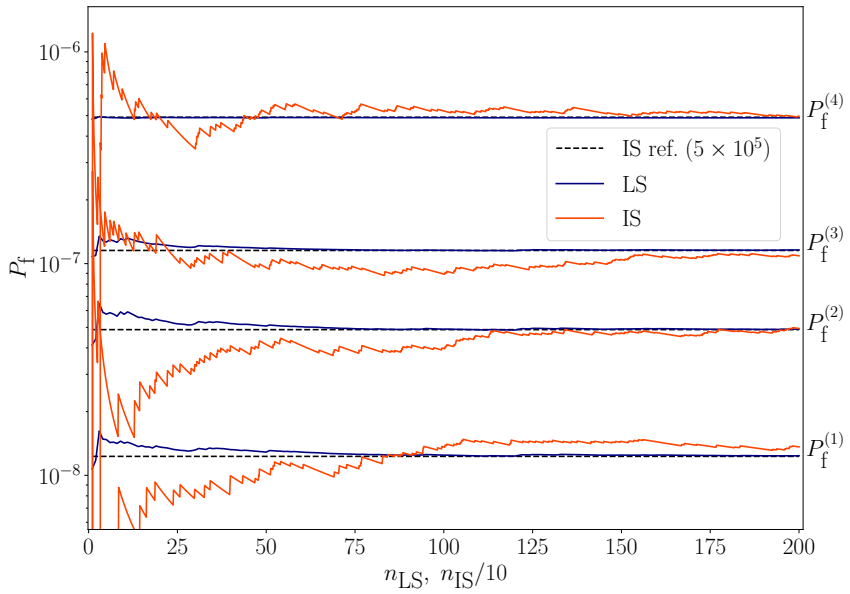

FIGURE 6.2: Comparison of P_f estimation obtained with each LS algorithm and the IS algorithm on four configurations of penstock.

of the FORM-IS algorithm and the reference value, denoted as "IS ref." obtained with the FORM-IS algorithm with $n_{IS} = 5 \times 10^5$ samples. The results are presented in Figure 6.2. The abscissa axis represents the number of LS iterations n_{LS} and the number of IS iterations n_{IS} divided by 10. This means, for example, that 2×10^2 LS iterations correspond to 2×10^3 IS iterations. One IS iteration implies 2 LSF evaluations (one for each LSF) while one LS iteration requires an average of 9 total LSF evaluations for finding both roots. These first results show that both estimators are very performant. In particular, the LS algorithm only needs a very few number of iterations for an acceptable estimation. Such behavior reveals a probable high degree of linearity of the two LSSs.

6.2.2 Info-gap analysis

The fact that the G-functions are fast to evaluate and that the LS estimator converges rapidly enables a direct application of the IG framework. The IG uncertain vector is defined as $\mathbf{e} = \left[\widetilde{e}_{\text{nom}}, \widetilde{\Delta e}_{\text{an}}, \widetilde{\mu}_{R_m}, \widetilde{\mu}_{\Delta e_{\text{corr}}}, \widetilde{\sigma}_{\Delta e_{\text{extra}}}, \widetilde{\omega}\right]$. This illustrative choice jointly considers non-probabilistic input variables and probability distribution parameters. Interesting information is to evaluate the robustness of different configurations of penstocks in order to detect if some are more robust than others despite an equal or a lower nominal performance. Figure 6.3.(A) presents the robustness curves obtained using the `GN_ORIG_DIRECT_L` optimization algorithm at each of the 10 values of $h_j \in [0, 0.4]$ for 39 configurations that have a range of nominal performances roughly between 10^{-9} and 10^{-6}. It appears that most of these robustness curves reveal same behaviors such that only a very few of them intersect with others. This is confirmed with Figure 6.3.(B) which presents the robustness values associated to a critical failure probability set at 10^{-5} as a function of the nominal performance. It is expected that the closer the nominal performance to the critical value, the less robust the configuration. However, it is interesting to look at potential vertical dispersion at close nominal values. In this application, the maximum dispersion is around 4% which confirms that no configuration is way more or way less robust to the considered uncertainty than the others.

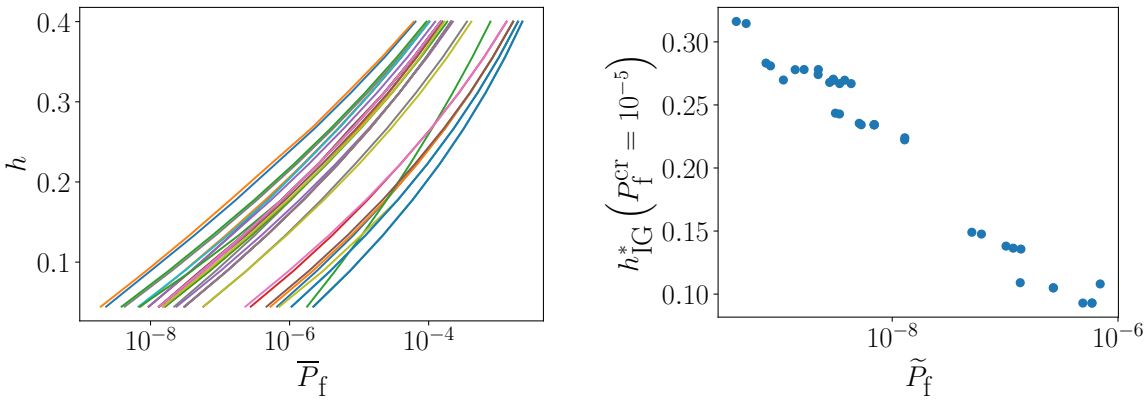

(A) (B)

FIGURE 6.3: Robustness curves for many different nominal configurations of penstocks (A) and correlation between nominal performance and robustness (B).

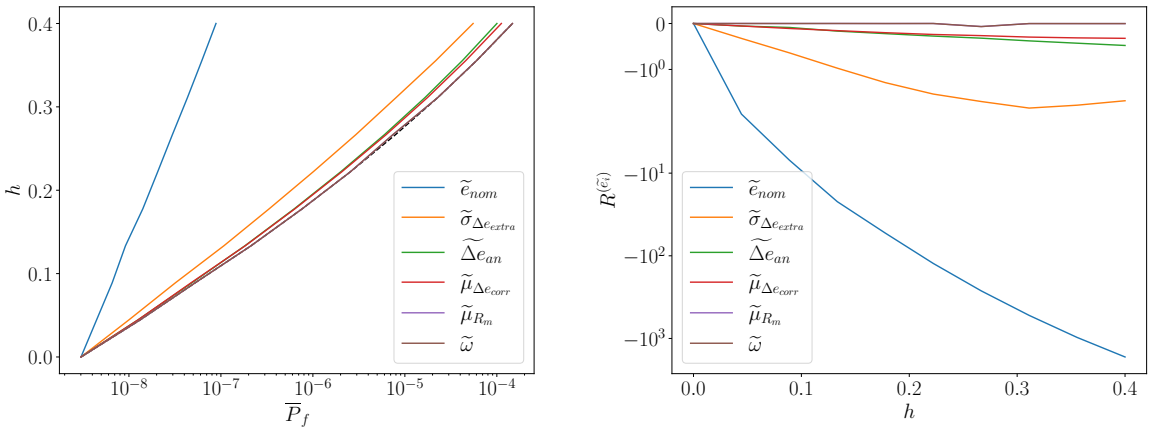

(A) (B)

FIGURE 6.4: Robustness curve obtained for each uncertain variable fixed at nominal value (the black dotted curve corresponds to all variables considered uncertain) (A) and corresponding demand values (B).

Figure 6.4.(A) shows the new robustness curves when each uncertain variable is set to its nominal value while the others remain uncertain and Figure 6.4.(B) quantifies the demand value introduced in Chapter 5 for each fixed uncertain variable. The added information on e_{nom} clearly stands out and renders the other results almost irrelevant. It seems important to notice that the IG results are conditioned to the way that the horizon of uncertainty parametrizes the range of each uncertain variable. In this thesis, the relative error model is mostly used and similarly applied to each uncertain variable even on variables that have a nominal value very close to zero. The analyst must make sure that the horizon of uncertainty broadens the uncertainty range of each variable in a representative way. Let us mention that weights on each uncertain variable may be applied in that matter.

6.3 A line-sampling-based procedure adapted to the brittle failure mode

6.3.1 Challenge for the application of line sampling

The conditional annual failure probability is recalled:

$$P_{\text{f}} = \frac{\mathbb{P}\left(G_{N+1} < 0 \cap G_N \geq 0 \cap G_{\text{HPT}} \geq 0\right)}{\mathbb{P}\left(G_{\text{HPT}} \geq 0\right)} \tag{6.4}$$

In penstock reliability assessments, considering such a conditional probability is particularly relevant for brittle fracture. The involved random variables are $\mathbf{X} = \left[R_m, \Delta e_{\text{extra}}, \Delta e_{\text{corr}}, \varepsilon, a, K_{\text{IC}}\right]^\top$ for which the probabilistic characteristics can also be retrieved in Chapter 3 in Table 3.1. In the following, only the numerator probability in Eq. (6.4) will be of interest as it is the most challenging one to estimate. Indeed, the double-intersection-based failure domain becomes even more restricted than the one involved in Section 6.2. This can be understood in a first place from Figure 3.2. Depending on the sample $\mathbf{u}_{\boldsymbol{\alpha}}^{\perp}$ and the direction $\boldsymbol{\alpha}$, two cases can be encountered:

- either the failure band is never reached, which results in the fact that there is no root;
- or the failure band is reached in which case there are two roots denoted r_1 and r_2.

As a consequence, the LS algorithm must again be adapted for taking into account these two possibilities. First, let us remark that the double intersection may actually be described following three equivalent mathematical formulations of the same event:

$$\begin{aligned} E_1 &= \left\{\max\left(G_{N+1}, -G_N, -G_{\text{HPT}}\right) \leq 0\right\}, \\ E_2 &= \left\{G_{N+1}.G_N \leq 0 \cap G_{\text{HPT}} > 0\right\}, \\ E_3 &= \left\{G_{N+1} \leq 0 \cap G_N > 0 \cap G_{\text{HPT}} > 0\right\}. \end{aligned} \tag{6.5}$$

In the following, the event E_i is to be understood as the same event $E = E_1 = E_2 = E_3$ described by the i-th formulation. The following notations are used: $G_{\max} = \max\left(G_{N+1}, -G_N, -G_{\text{HPT}}\right)$ and $G_{\text{prod}} = G_{N+1}.G_N$. Figures 6.5 and 6.6 represent the several LSF $G_{N+1}^{\perp}\left(v_1\right)$, $G_N^{\perp}\left(v_1\right)$, $G_{\text{HPT}}^{\perp}\left(v_1\right)$ and $G_{\max}^{\perp}\left(v_1\right)$ for two different samples $\mathbf{u}_{\boldsymbol{\alpha}}^{\perp,(i)}$. As the functions $G_{N+1}^{\perp}$, $G_N^{\perp}$ and $G_{\text{HPT}}^{\perp}$ are decreasing, the composed function $G_{\max}^{\perp}$ first decreases with $G_{N+1}^{\perp}$ and then increases either with $-G_N^{\perp}$ or $-G_{\text{HPT}}^{\perp}$. Actually, there are three distinguishable cases:

1. the two roots correspond to $G_{N+1}^{\perp} = 0$ and $G_N^{\perp} = 0$ as in the example in Figure 6.5;
2. the root of $G_{\text{HPT}}^{\perp} = 0$ is smaller than the root of $G_{N+1}^{\perp} = 0$ which implies no solution for $G_{\max}^{\perp} = 0$ as in the example in Figure 6.6,
3. the two roots correspond to $G_{N+1}^{\perp}$ and $G_{\text{HPT}}^{\perp}$ (much rarer). Typically, this happens when the root of $G_{\text{HPT}}^{\perp} = 0$ is between the roots of $G_{N+1}^{\perp} = 0$ and $G_N^{\perp} = 0$.

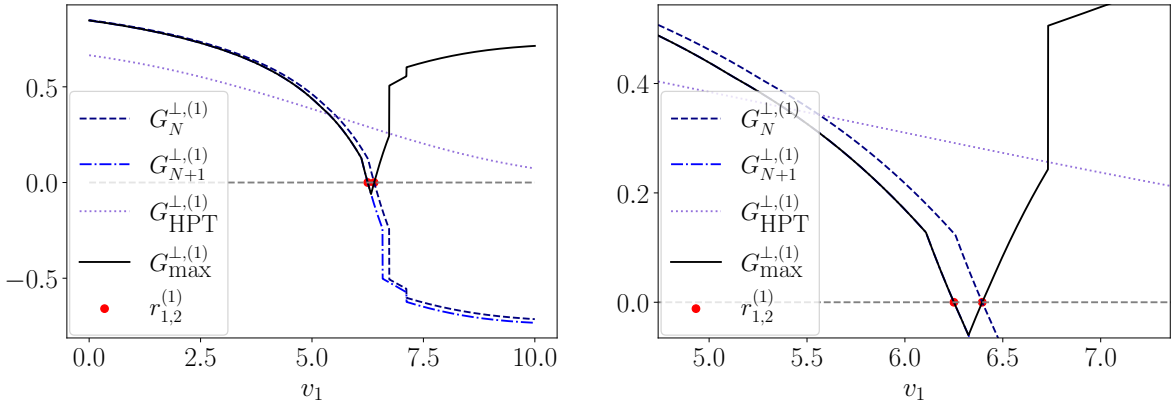

(A) (B)

FIGURE 6.5: Values of $G_j^{\perp,(i)}$ in function of v_1 for a case with two roots (A) on which a zoom is performed (B).

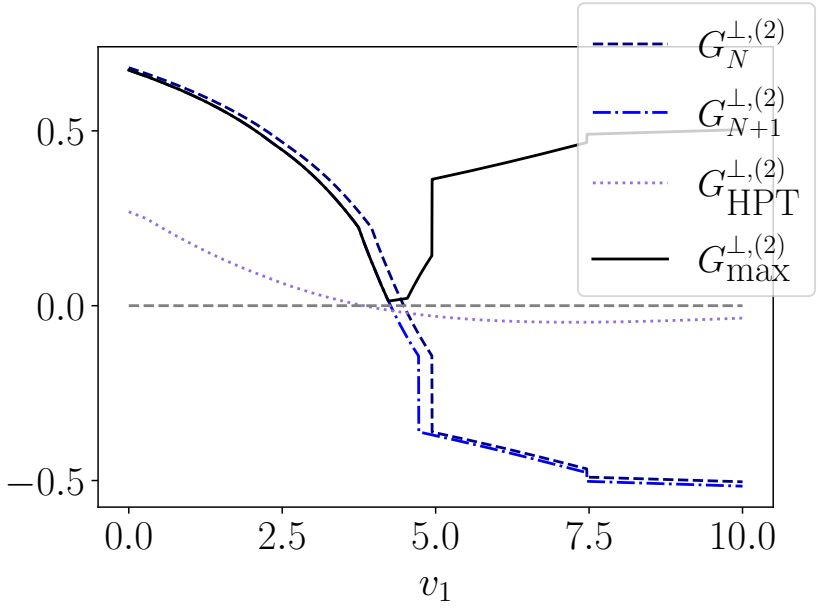

FIGURE 6.6: Values of $G_j^{\perp,(i)}$ in function of v_1 for a case with no roots (see the $G_{\max}^{\perp,(i)}$ curve).

The one-dimensional failure probability associated to the i-th line is now expressed as:

$$p_{\mathrm{f}}^{(i)} = \begin{cases} \Phi\left(-r_1^{(i)}\right) - \Phi\left(-r_2^{(i)}\right) \text{ if } r_{1,2}^{(i)} \text{ exist,} \\ 0 \text{ otherwise.} \end{cases} \tag{6.6}$$

The LS algorithm must now be able to assess the existence of roots for each sampled line. In the following section, three algorithms constructed in accordance with the events E_1, E_2 and E_3 are proposed in order to efficiently solve this zero/multiple root search problem.

6.3.2 Proposition of three adapted line sampling procedures

Algorithm 2 presents the new general LS procedure (in the standard normal space) used to estimate the failure probability which is very close to 1, except for the fact that the initial direction $\boldsymbol{\alpha}$ is now obtained from the MCF algorithm and that the roots may not exist. Moreover,

Algorithm 2 – General LS procedure (for possible two roots).

$P_{\mathrm{f}} \leftarrow 0$
Find $\boldsymbol{\alpha}, \mathbf{u}^*_{\mathrm{MCF}}$ # MCF results
Generate $\mathbf{u} \sim \mathcal{N}(0,1)$
for $i : 1 \rightarrow n_{\mathrm{LS}}$ **do**
  $\mathbf{u}_{\boldsymbol{\alpha}}^{\perp,(i)} \leftarrow \mathbf{u}^{(i)} - \left(\mathbf{u}^{(i)}.\boldsymbol{\alpha}\right)\boldsymbol{\alpha}$ # projection on the orthogonal hyperplane
  Search for $r_1^{(i)}$ and $r_2^{(i)}$ # see Algorithms 3 and 4
  if $r_1^{(i)}$ and $r_2^{(i)}$ exist **then**
    $p_{\mathrm{f}}^{(i)} = \Phi\left(-r_1^{(i)}\right) - \Phi\left(-r_2^{(i)}\right)$ # failure lies in $\left[r_1^{(i)}, r_2^{(i)}\right]$
    if $\|\mathbf{u}_{\boldsymbol{\alpha}}^{\perp,(i)} + r_1^{(i)}\boldsymbol{\alpha}\| < \|\mathbf{u}^*_{\mathrm{MCF}}\|$ **then** # advanced line sampling
      $\mathbf{u}^* \leftarrow \mathbf{u}_{\boldsymbol{\alpha}}^{\perp,(i)} + r_1^{(i)}\boldsymbol{\alpha}$
      $\boldsymbol{\alpha} \leftarrow \mathbf{u}^*/\|\mathbf{u}^*\|$
  else
    $p_{\mathrm{f}}^{(i)} = 0$ # failure is never reached
  $P_{\mathrm{f}} \leftarrow P_{\mathrm{f}} + p_{\mathrm{f}}^{(i)}$
$P_{\mathrm{f}} \leftarrow P_{\mathrm{f}}/n_{\mathrm{LS}}$

if valid roots are found and if the point corresponding to the first root has a smaller distance to the origin than the previous optimal point $\mathbf{u}^*$, then $\mathbf{u}^*$ and the optimal direction $\boldsymbol{\alpha}$ are updated. This is a feature of the so-called "adaptive line sampling" (De Angelis et al., 2015) which is useful in this case as the MCF algorithm may not always give the best possible direction.

The procedures used to find the roots when considering the events E_1 (related to $G_{\max}$) and E_2 (related to G_{prod}) are both presented in Algorithm 3 as they are quite similar. Algorithm 4 is proposed to find the roots when considering only the event E_3. It is important to keep in mind that the choice of the event does not impact the position of the roots but only the procedure to find them. Indeed, the event E_1 is only composed of one function which is supposed to be always decreasing first and then always increasing. As it is formulated as the maximum value of three different functions, its shape may not be smooth. The corresponding procedure in Algorithm 3 (in blue) aims at estimating the minimum value of the function. If the minimum value is negative, then the first root and the second root are searched in its neighborhood (before and after). If the minimum value is positive, then no root exists and p_{f} is set to 0. The procedure applied for the event E_2 and described in Algorithm 3 (in red) is quite similar to the one for the event E_1. E_2 is composed of the two functions G_{HPT} which is supposed always decreasing and

Algorithm 3 – Roots search with the events E_1 and E_2.

$m^{(i)} = \min_{v_1} G^{\perp}_{\max}(v_1)$
$m^{(i)} = \min_{v_1} G^{\perp}_{\text{prod}}(v_1)$
if $m^{(i)} < 0$ **then** # else case 2
  Find $r_1^{(i)} < m^{(i)}$ s.t. $G^{\perp}_{\max}\left(r_1^{(i)}\right) = 0$
  Find $r_2^{(i)} > m^{(i)}$ s.t. $G^{\perp}_{\max}\left(r_2^{(i)}\right) = 0$ # case 1 or 3
  Find $r_1^{(i)} < m^{(i)}$ s.t. $G^{\perp}_{\text{prod}}\left(r_1^{(i)}\right) = 0$
  if $G^{\perp}_{\text{HPT}}\left(r_1^{(i)}\right) > 0$ **then** # else case 2
    Find $r_2^{(i)} > m^{(i)}$ s.t. $G^{\perp}_{\text{prod}}\left(r_2^{(i)}\right) = 0$ # case 1
    if $G^{\perp}_{\text{HPT}}\left(r_2^{(i)}\right) < 0$ **then**
      Find $r_2^{(i)}$ s.t. $G^{\perp}_{\text{HPT}}\left(r_2^{(i)}\right) = 0$ # case 3

Algorithm 4 – Roots search with the event E_3.

Find $r_1^{(i)}$ s.t. $G^{\perp}_{N+1}\left(r_1^{(i)}\right) = 0$
if $G^{\perp}_{\text{HPT}}\left(r_1^{(i)}\right) > 0$ **then** # else case 2
  Find $r_2^{(i)} > r_1^{(i)}$ s.t. $G^{\perp}_{N}\left(r_2^{(i)}\right) = 0$ # case 1
  if $G^{\perp}_{\text{HPT}}\left(r_2^{(i)}\right) < 0$ **then**
    Find $r_2^{(i)}$ s.t. $G^{\perp}_{\text{HPT}}\left(r_2^{(i)}\right) = 0$ # case 3

$G_{\text{prod}} = G_{N+1}.G_N$ which is supposed always decreasing first and then always increasing. It is necessary, in this case, to verify the position of the root of G_{HPT}. If it appears before the first root of G_{prod} then there is no solution. Otherwise, the second root to be kept is the smallest one between the root of G_{HPT} and the second root of G_{prod}.

The event E_3 is composed of the three supposed decreasing functions G_{N+1}, G_N and G_{HPT}. These functions taken one by one are generally smoother but may still present discontinuities in some cases. If the root of G_{HPT} is smaller than the root of G_{N+1} then there is no solution. Otherwise, the second root to be kept is the smallest one between the root of G_{HPT} and the root of G_N. This algorithm is therefore based on a sequential roots search strategy. The algorithms corresponding to the events E_1, E_2 and E_3 are respectively denoted by A_{E_1}, A_{E_2} and A_{E_3}.

6.3.3 Numerical comparison of the three line sampling algorithms

The numerical tools used to perform the minimization and the roots search are taken from the Python optimization package in SciPy (`scipy.optimize`). The minimization is conducted with the "`bounded`" algorithm which uses the Brent method to find a local minimum in an interval. The root search is conducted either with the "`toms748`" algorithm (Alefeld et al., 1995) in A_{E_1} and A_{E_2} or the "`newton`" algorithm in A_{E_3} as the functions involved are more regular. Each algorithm must be able to treat the three cases mentioned in Section 6.3.1. The first two cases are frequent while the third case is rarer. Depending on which algorithm is used, the efforts needed to find the roots (or to find out that there is no root) to deal with each case will differ. This is presented in Table 6.1 where "Minimization" corresponds to the search of a minimum either for

TABLE 6.1: Operations performed for each event.

Algorithm		Minimization	Roots search	G_{HPT} evaluations
A_{E_1}	Case 1	1	2	0
	Case 2	1	0	0
	Case 3	1	2	0
A_{E_2}	Case 1	1	2	2
	Case 2	1	1	1
	Case 3	1	3	2
A_{E_3}	Case 1	0	2	2
	Case 2	0	1	1
	Case 3	0	3	2

TABLE 6.2: Performances of each LS algorithm (A_{E_1}, A_{E_2}, A_{E_3}).

	A_{E_1}	A_{E_2}	A_{E_3}	IS
$\bar{\#}G_{N+1}$-calls	19162	22524	8484	5×10^4
$\bar{\#}G_N$-calls	19162	22524	3062	5×10^4
$\bar{\#}G_{\text{HPT}}$-calls	19162	1516	996	5×10^4
$\sum \bar{\#}G_i$	57486	46564	13530	1.5×10^5
$\bar{t}(s)$	4.13	3.90	2.21	6.10

$G_{\max}$ or G_{prod}, "Roots search" corresponds to the number of times a root is searched and "G_{HPT} evaluations" is the number of evaluations of G_{HPT} at a given root.

From Table 6.1, one can expect the algorithm A_{E_3} to be the least demanding in number of code evaluations and the algorithm A_{E_2} to be the most demanding one. This conjecture is verified by estimating 500 failure probabilities corresponding to different input probabilistic distribution parameters with each LS algorithm for a total number of iterations $n_{\text{LS}} = 1 \times 10^3$. The averages $\bar{\#}G_{N+1}$-calls, $\bar{\#}G_N$-calls and $\bar{\#}G_{\text{HPT}}$-calls of the number of evaluations $\#G_i$ of each single limit-state function are calculated as well as the average time $\bar{t}$ required for estimating one failure probability. The number of evaluations that come from the MCF algorithm used for both the LS method and the IS method is not given here as it is the same for all the methods and as it is low compared to the total number of evaluations.

The results are presented in Table 6.2 and confirm what was expected from Table 6.1. A_{E_3} requires more than three times less total evaluations than A_{E_2} and more than four times less than A_{E_1}. The ratios in terms of computational time are not the same as for the number of total evaluations as it depends on other factors such as the different functions that are used. Nevertheless, one failure probability estimation with A_{E_3} seems to be almost twice as fast as the two others. It cannot yet be said if the LS algorithms are more efficient than the IS algorithm as it depends on the numbers of iterations n_{LS} and n_{IS}. What can be said is that one IS iteration implies (in the current version of FISTARR) three limit-state evaluations (one for each single limit-state function) and one LS iteration implies roughly an average of 57 total evaluations with A_{E_1}, 46 total evaluations with A_{E_2} and 13 total evaluations with A_{E_3}.

The comparison is now made by looking at the evolution of the estimated failure probability using the three proposed LS algorithms with the IS algorithm and the reference value, denoted as "IS ref." obtained by performing the MCF importance sampling with $n_{\text{IS}} = 10^6$ samples. The IS algorithm is again performed using OpenTURNS. The results are presented in Figure 6.7. The comparison is presented on four different configurations of penstocks. One first interpretable result is that the three LS algorithms give identical curves for all four probabilities. The seed of the random generator being set at an identical value, this means that the three algorithms find exactly the same roots which is what is expected. The comparison with the IS curve shows

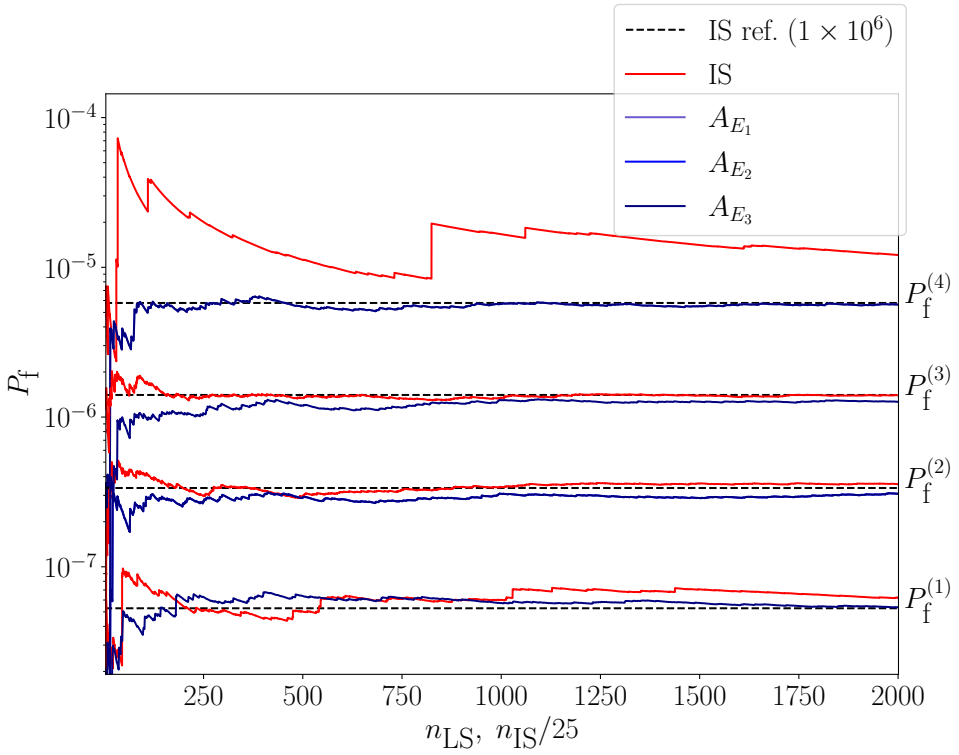

FIGURE 6.7: Comparison of P_f estimation obtained with each LS algorithm and the IS algorithm.

that the three LS algorithms are efficient. Indeed, while the IS curve seems to converge rapidly towards the reference value for some configurations (see the middle probabilities), it also seems that the convergence is slower in some cases (see the lowest curve and especially the highest curve). From this initial comparison whose number of experiments is too small to draw any final conclusion, the LS algorithms seem relevant for applying IG. In the following, A_{E_3} is chosen over A_{E_1} and A_{E_2} for the reliability assessment of penstock as it performs faster. The following section strengthens the comparison by analysing robustness curves obtained using the different failure probability estimators.

6.4 Methodology for robustness evaluation

6.4.1 Comparison of robustness curves

The IG uncertain variables considered in this study are the following distribution parameters grouped in the vector $\mathbf{e} = \boldsymbol{\theta} = [\mu_{\Delta e_{\text{corr}}}, \mu_{\Delta e_{\text{extra}}}, a_{\max}, \beta_{K_{\text{IC}}}]^\top$. The uncertainty model $U\left(h, \widetilde{\boldsymbol{\theta}}\right)$ considered is again the basic hyperrectangle convex model defined as the Cartesian product of all intervals of each uncertain parameter. For a given horizon of uncertainty h, the interval of the parameter θ_i is defined as $I_{\theta_i} = \left[\widetilde{\theta}_i\,(1-h)\,, \widetilde{\theta}_i\,(1+h)\right]$ if $\widetilde{\theta}_i$ is non-zero or $I_{\theta_i} = [-h, h]$ otherwise. Moreover, the nominal values are set to $\widetilde{\boldsymbol{\theta}} = [1, 0, 4, 90]^\top$. For this application, it has been chosen to construct the robustness curves with 10 values $h_i \in [0; 0.2]$. The maximum of the failure probability is searched using again the "`GN_ORIG_DIRECT_L`" optimization algorithm implemented in the `NLopt` Python library with a maximum number of 500 evaluations.

The objective is first to compare on one nominal configuration of penstock the robustness curves obtained using the A_{E_3} and IS algorithms as failure probability estimators with the reference curve. The comparison is made in terms of robustness curves (see Figure 6.8), relative error

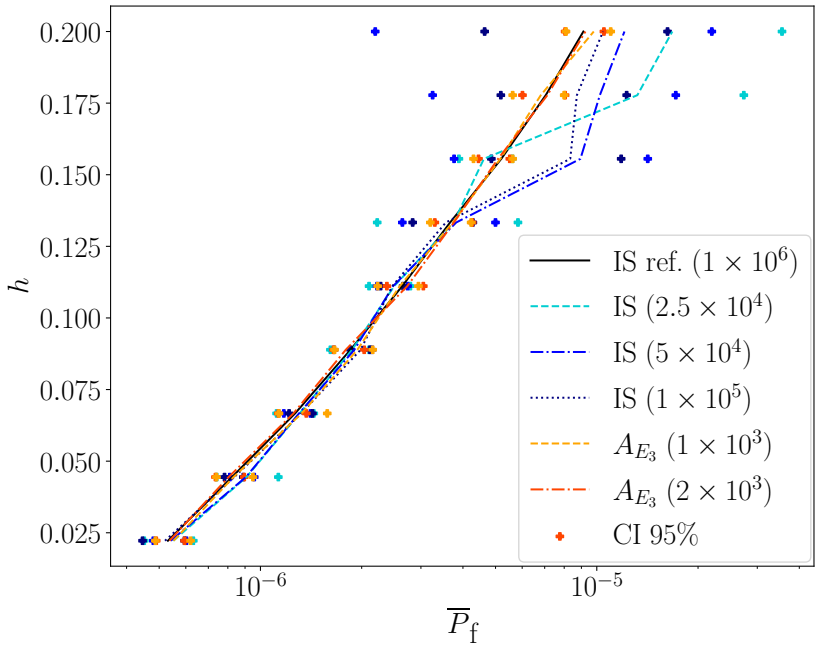

FIGURE 6.8: Comparison of robustness curves obtained with the proposed LS algorithm A_{E_3} and the IS algorithm.

η_{P_f} with the reference curve (see Figure 6.9) and cumulative calculation time (see Figure 6.10) considering $n_{\mathrm{IS}} \in \{2.5 \times 10^4, 5.0 \times 10^4, 1.0 \times 10^5\}$ and $n_{\mathrm{LS}} \in \{1.0 \times 10^3, 2.0 \times 10^3, 3.0 \times 10^3\}$. It appears from Figures 6.8 and 6.9 that the IS algorithms perform rather well in general, except for the three last values of h for which the robustness curves deviate from the reference curve. However, even in this less favorable case, the optimization process will automatically provide conservative results ($\overline{P}_{\mathrm{f}}$ is overestimated) and the confidence intervals contain the reference curve: their performance remains acceptable even in this case. Note that these non adaptive IS algorithms could be further optimized; moreover, other optimization algorithms than LD_MMA in the multi-constraint design point may converge better. This deviation does not seem to happen with the proposed algorithm A_{E_3} for which the robustness curves remain close to the reference curve. Moreover, the proposed LS algorithms seem also efficient in terms of cumulative computational time as shown in Figure 6.10. Although no definitive conclusion can be made regarding the comparative efficiency of the proposed algorithms with the IS ones, the adapted LS algorithms seem to be well suited in this context of robustness analysis.

6.4.2 Synthesis on the line sampling algorithms

Drawing robustness curves requires an efficient failure probability estimator over the whole uncertainty space. Indeed, as optimization is performed repeatedly, only a few bad estimations suffice to make the robustness curve deviate. In addition to a general trend to provide conservative results that could be observed from FORM-IS in standard penstock reliability evaluations, the fact that the optimization algorithm used is global and that it searches for a maximum value will generally tend to make the errors conservative which is preferred for safety assessments. Moreover, a criterion based on the coefficient of variation of each failure probability estimation could be used to insure a sufficient convergence at each evaluation.

However, the IG robustness analysis is therefore very instructive on the efficiency of the failure probability estimator in the considered uncertainty space. The proposed adapted line sampling algorithms represent an interesting alternative as they manage to better target the

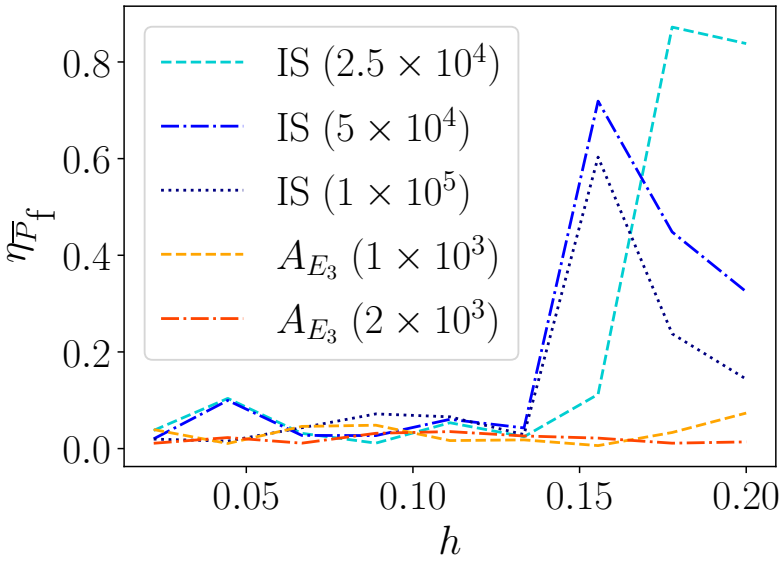

FIGURE 6.9: Comparison of the error $\eta_{\overline{P}_f}$ of each algorithm w.r.t. the reference robustness curve.

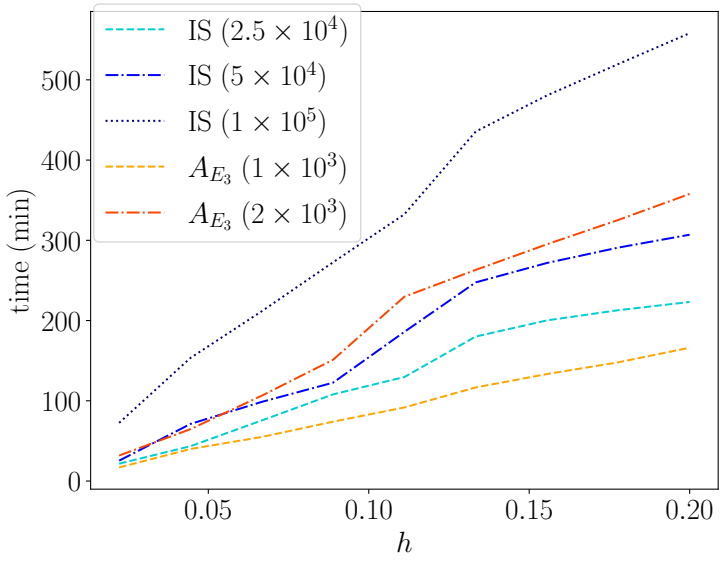

FIGURE 6.10: Cumulative computational time for obtaining the robustness curves.

restricted failure domain and correctly estimate the roots. In this reliability application, the partial knowledge on the behaviors of each limit-state function is helpful for adapting the root search. Nevertheless, each LS iteration still requires a large number of G-functions evaluations. The following section presents a method that aims at training artificial neural networks (ANN) in order to predict the roots for any sampled line and for any uncertain vector $\boldsymbol{\theta}$ during the robustness analysis.

6.5 Combination of two artificial neural networks for the line sampling roots prediction

6.5.1 Problem statement

As the G-functions involved in Eq. (6.4) are a series and a combination of analytical expressions, a single failure probability estimation may be obtained within a few seconds. Nevertheless, when considering no information that could simplify the optimization process such as a monotonic behavior with respect to the epistemic distribution parameters, applying the IG method as it is done in the previous section requires the evaluation of several thousands of failure probabilities. Therefore, being able to reduce the computational time of one probability evaluation remains relevant. Chapter 4 already introduced the potential use of surrogate models. They often substitute the expensive G-function. This is not relevant in the present application as the G-functions are not expensive to evaluate. It is considered here to use the surrogate models in order to directly evaluate the existence and (when they exist) the values of the roots for any joint vector $(\mathbf{u}, \boldsymbol{\theta})$. As the G-functions are relatively fast to compute, several thousand training samples may be considered for building predictive surrogate models. Therefore, the choice made in this application is to use ANNs rather than other types of surrogate models such as kriging or polynomial chaos expansions.

Chapter 4 also introduced methods that evaluate many failure probabilities using a unique input dataset. In this application, the method from (Yuan, 2013) called "weighted importance sampling" (WIS) seems the most appropriate as it only requires the calculation of a ratio of densities. This method will also be part of the comparison when computing robustness curves.

6.5.2 Generalities on artifical neural networks

This part does not aim at giving an extended description of ANNs but only at presenting the basic notions necessary to understand how they may be of use for reliability analysis. ANNs represent a mathematical structure that processes information from an input layer to an output layer through hidden layers (Jain et al., 1996). The information is passed from one layer to another with some specific functions called "artificial neurons" as illustrated in Figure 6.11. Each neuron belonging to the layer $l^{(i)}$ receives as an input, a linear combination on the outputs $s_k^{(i-1)}$ of the neurons of the previous layer $l^{(i-1)}$ with weights $w_{k,j}^{(i)}$ and a bias term $b_j^{(i)}$. The input is then processed with an activation function $f^{(i)}$ whose output $s_j^{(i)}$ is passed to the neurons of the next layer. This simple mechanism is depicted in Figure 6.11. In this application, fully connected feedforward ANNs are considered which simply correspond to architectures where the information only goes from all the neurons of layer $l^{(i-1)}$ to all the neurons of layer $l^{(i)}$ (but not between neurons of a same layer which is the case for recurrent neural networks).

An ANN may learn complex relationships between inputs and outputs by training it with an available dataset (e.g. composed of inputs-output realizations). Indeed, by performing back-propagation through gradient descent (Hecht-Nielsen, 1989), the ANN is able to update the values of the weights $w_{k,j}$ and the biases b_j such that the errors (defined through a loss function) between the output dataset and the ANN outputs are minimized. The application range of such

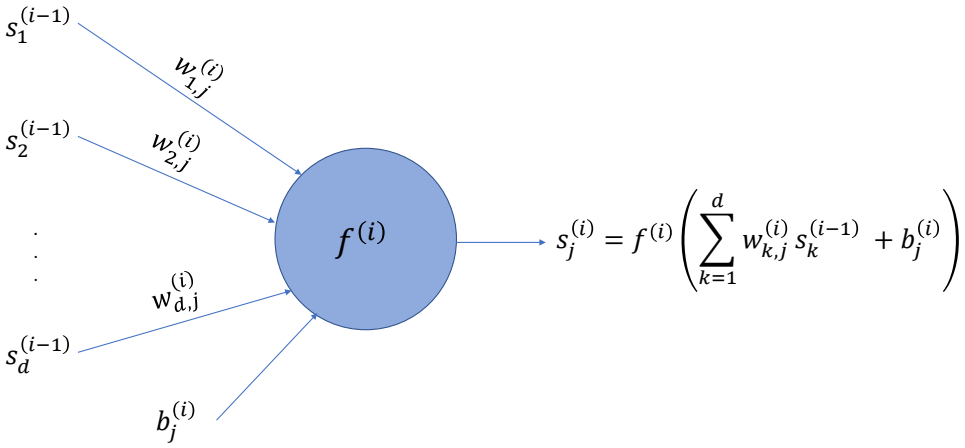

FIGURE 6.11: Representation of a single artificial neuron.

networks is very wide as ANNs may be used for classification and regression problems. Moreover, it is able to treat all sorts of information (Liu et al., 2017). Therefore, ANNs also find their use in reliability analyses as surrogate models, most often to replace an expensive limit-state function. In Papadrakakis and Lagaros (2002), Papadopoulos et al. (2012) and Zio and Pedroni (2010), ANNs are combined with Monte Carlo simulation, subset simulation and line sampling respectively. A review of their use in the context of reliability analysis is proposed in (Chojaczyk et al., 2015). In the present work, ANNs are combined with LS in order to directly predict the roots associated to each $\mathbf{u}_{\alpha}^{\perp}$ drawn from the LS algorithm.

6.5.3 Proposed methodology based on artificial neural networks

ANNs are combined to the LS-based A_{E_3} algorithm, which has been identified as the most efficient in Subsection 6.4.1, in order to reduce the computational time required for obtaining a robustness curve. What makes the A_{E_3} still time consuming is that it requires a large number of evaluations of the G-functions, first to assess the existence of roots and, second, to evaluate their values. The objective here is to be able, for any joint sample $(\mathbf{u}, \boldsymbol{\theta})$, to predict the answers of the two previous problems based on training samples $(\mathbf{u}, \boldsymbol{\theta})^{\text{train}}$. The fact of considering the probabilistic standard vector $\mathbf{u}$ together with the epistemic uncertain vector $\boldsymbol{\theta}$ as the input of the ANN enables to create a single surrogate model applicable during the whole IG analysis.

Two types of ANNs are jointly proposed. First, a classification ANN, denoted by ANN_1, is necessary in order to predict if roots exist or not for a given sample $(\mathbf{u}, \boldsymbol{\theta})^{(i)}$. Then, a regression ANN, denoted as ANN_2, is used to predict the values of both roots when they exist. The procedure that is followed to build both ANNs is presented hereafter:

1. Generate n_{train} training and n_{val} validation samples of $\mathbf{u}$ according to the independent standard Gaussian distribution;

2. Generate n_{train} training and n_{val} validation samples of $\boldsymbol{\theta}$ according to the uniform distribution with the bounds $\left[\underline{\boldsymbol{\theta}}\left(h_{\max}\right), \overline{\boldsymbol{\theta}}\left(h_{\max}\right)\right]$ with a user-defined $h_{\max}$;

3. For each $\left(\mathbf{u}^{(i)}, \boldsymbol{\theta}^{(i)}\right)^{\text{train}}$ and $\left(\mathbf{u}^{(i)}, \boldsymbol{\theta}^{(i)}\right)^{\text{val}}$, assess the existence or not of roots using algorithm A_{E_3}. Any joint vector for which no root exists is denoted $(\mathbf{u}, \boldsymbol{\theta})^{(0)}$ while the others are denoted $(\mathbf{u}, \boldsymbol{\theta})^{(1)}$;

4. Build and learn the surrogate model ANN_1 with the samples $(\mathbf{u}, \boldsymbol{\theta})^{\text{train}}$ and validate its performance with the samples $(\mathbf{u}, \boldsymbol{\theta})^{\text{val}}$;

5. Build and learn the surrogate model ANN_2 with the samples $(\mathbf{u}, \boldsymbol{\theta})^{(1),\text{train}}$ and validate its performance with the samples $(\mathbf{u}, \boldsymbol{\theta})^{(1),\text{val}}$.

A lot of parameters may be tuned when building ANNs such as the number of layers, the number of neurons per layer or the type of loss and accuracy metrics. Both ANNs are built using the Python libraries Keras and Tensorflow. More information about the architectures and parameters of ANN_1 and ANN_2 for the penstock use-case is given in Appendix E.

A small number of errors in the roots classification may lead to unfixable errors especially as less compensation will take place with highly efficient ANNs. One way of treating this issue is to consider a multi-fidelity approach and to combine the classification surrogate model ANN_1 with the initial algorithm A_{E_3} for estimating $P_\text{f}(\boldsymbol{\theta})$. Indeed, for a given joint vector $(\mathbf{u}, \boldsymbol{\theta})$, the output of ANN_1 corresponds to the probability that roots exist. Therefore, if the output is close to 0, one can have strong confidence that no root exists. On the contrary, if the output is close to 1, one can have strong confidence that some roots exist. However, if the output takes a value close (where close might be quantified by the analyst) to 0.5, then one might want to check the correct answer with the A_{E_3} algorithm. Consequently, by defining the security value $s \in [0, 0.5]$, the hybrid multi-fidelity method denoted by "A_{E_3}-ANN" is proposed. Thus, it simply adds the following operation:

- if the output $\text{ANN}_1\left(\mathbf{u}^{(i)}, \boldsymbol{\theta}^{(i)}\right) \in [0.5 - s; 0.5 + s]$, one can estimate the roots using A_{E_3};
- otherwise, one can reasonably trust the result obtained from ANN_1.

The complete procedure is depicted in Figure 6.12.

6.6 Application cases

6.6.1 Rosenbrock function

The methodology is first applied to a LSF based on the Rosenbrock function in two dimensions:

$$g(X_1, X_2) = 100\left(X_2 - X_1^2\right)^2 + (X_1 - 1)^2 - 0.01 \tag{6.7}$$

where $X_1 \sim \mathcal{N}(\theta_1, 1)$ and $X_2 \sim \mathcal{N}(\theta_2, 1)$. Indeed, this toy-case has a similar problematic as the penstock reliability problem in terms of root search. As depicted in Figure 6.13.(A) for $\theta_1 = 1.5$ and $\theta_2 = 0$, the limit-state function takes on a very narrow elliptic shape. Due to this geometry and to the fact that the limit-state function is not formulated as an intersection, the LS algorithm A_{E_1} is best suited. However, Figure 6.13.(B) shows that a large number of LS iterations and IS samples are needed in order to converge to the reference failure probability.

The ANN-based methodology is applied by considering $n_\text{train} \in \left[1 \times 10^3, 3 \times 10^4\right]$, $n_\text{val} = 0.2 n_\text{train}$, $\Theta_1 \sim \mathcal{U}(0, 3)$ and $\Theta_2 \sim \mathcal{U}(-1, 1)$. The four following metrics relevant to the performance of ANN_1 and ANN_2 are defined:

- "false root" is the proportion of wrongly declared existing roots from ANN_1;
- "forgotten root" is the proportion of existing roots forgotten by ANN_1;

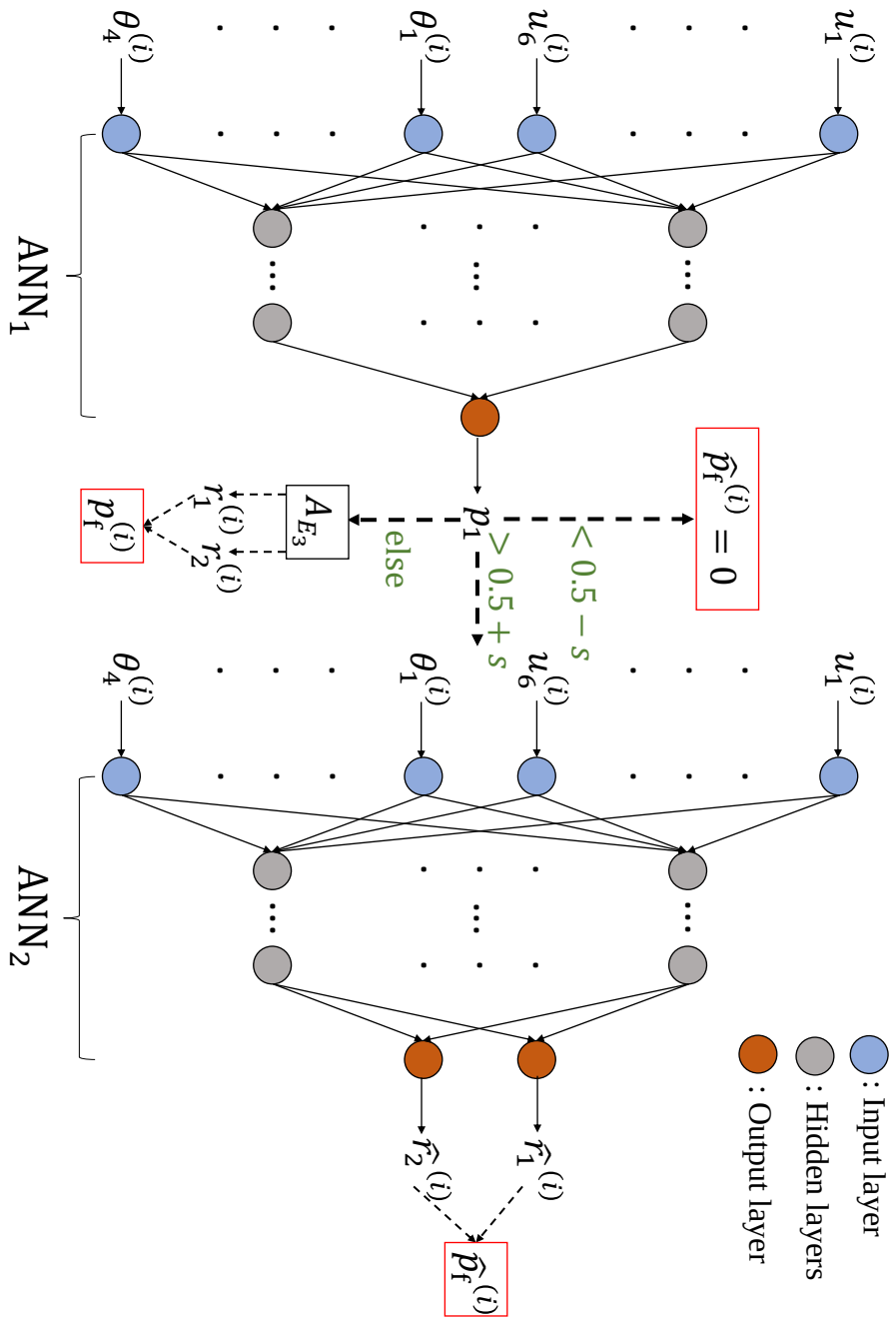

FIGURE 6.12: Illustration of the methodology combining ANNs and A_{E_3} for the reliability of penstocks.

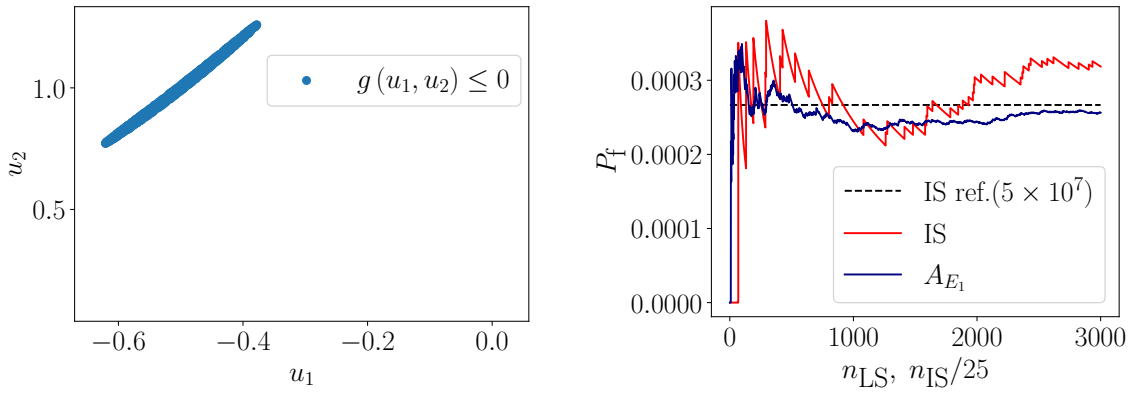

(A) (B)

FIGURE 6.13: Illustration of a limit-state function (A) and comparison of the evolution of P_f with A_{E_1} and with importance sampling (B) for the Rosenbrock function and for $\theta_1 = 1.5$ and $\theta_2 = 0$.

- $Q^2(r_1)$ is the coefficient of preditivity calculated on the first root r_1 in common between ANN_1 and A_{E_1};
- $Q^2(r_2)$ is the coefficient of preditivity on the second root r_2 in common between ANN_1 and A_{E_1}

where the coefficient of predictivity has the following expression:

$$Q^2(r_i) = 1 - \frac{\sum_{j=1}^{n_{r_i}} \left(r_i^{(j)} - \widehat{r}_i^{(j)}\right)^2}{\sum_{j=1}^{n_{r_i}} \left(r_i^{(j)} - \overline{r}_i^{(j)}\right)^2} \tag{6.8}$$

where n_{r_i} is the number of real roots predicted by ANN_1, $r_i^{(j)}$ the roots obtained with A_{E_1}, $\widehat{r}_i^{(j)}$ the roots obtained with ANN_2 and $\overline{r}_i^{(j)}$ the mean on all roots.

The values of these metrics are calculated on 3×10^3 new testing samples $(\mathbf{u}, \boldsymbol{\theta})^{\text{test}}$. Note that the availability of such testing samples is not always present for more time-demanding applications. Figure 6.14 presents the impact of the number of training samples on the four metrics. Except for $n_{\text{train}} = 1000$ where the proportion of forgotten roots is high (actually it is equal to the true proportion of existing roots meaning that ANN_1 misjudged every single existing root), the proportions of wrong classifications quickly become very low (typically lower than 1%). It also appears that the coefficients of predictivity of both roots are very high (typically greater than 99%) even for $n_{\text{train}} = 1000$.

The methodology is now tested with $n_{\text{train}} = 3 \times 10^4$ at three randomly chosen uncertain vectors $\boldsymbol{\theta}^{(i)}$: $\boldsymbol{\theta}^{(1)} = [2.37, 0]^\top$, $\boldsymbol{\theta}^{(2)} = [0.84, -0.99]^\top$ and $\boldsymbol{\theta}^{(3)} = [0.88, -0.08]^\top$. One can see in Figure 6.15.(A) that ANN_1 manages very well to predict the lines for which roots exist and that ANN_2 is very precise on the estimation of $r_{1,2}$ although the zoom in Figure 6.15.(B) seems to show that the elliptic shape is simplified by two lines. These good visual performances are confirmed with the comparison of the failure probabilities estimations presented in Figure 6.16. In this case, the proportions of forgotten roots (0.44%, 0.1% and 0.18%) and the proportions of false roots (0.02%, 0.04% and 0%) are very low such that there is no need to apply the security value s.

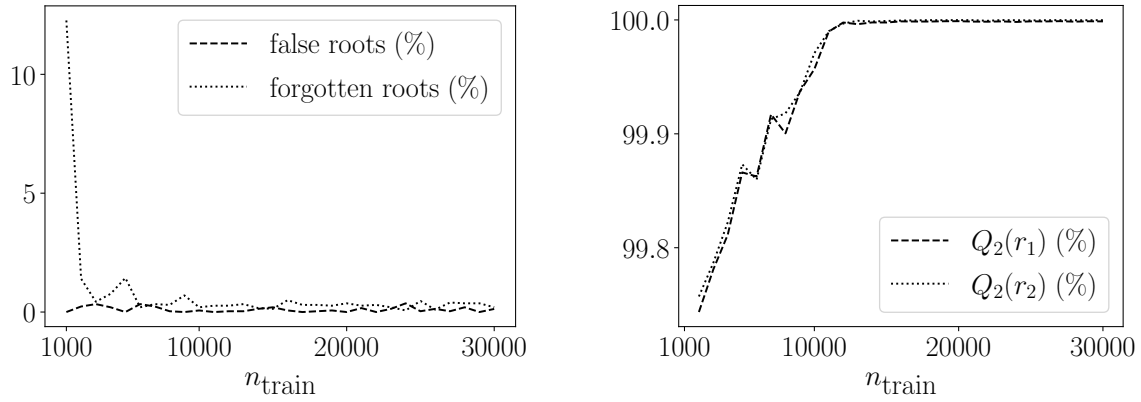

(A) (B)

FIGURE 6.14: Illustration of the performances of ANN_1 (A) and ANN_2 (B) on testing samples in function of the number of training samples on the Rosenbrock function.

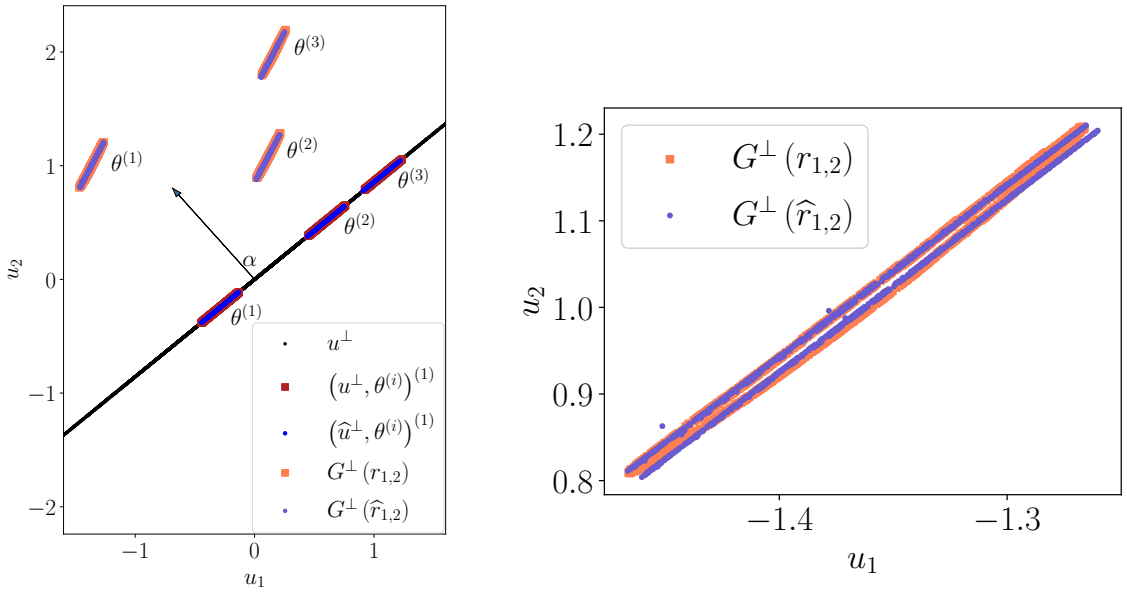

(A) (B)

FIGURE 6.15: Illustration of the performances of ANN_1 and ANN_2 for three distribution parameters vectors (A) with a zoom on one limit-state (B) for the Rosenbrock function.

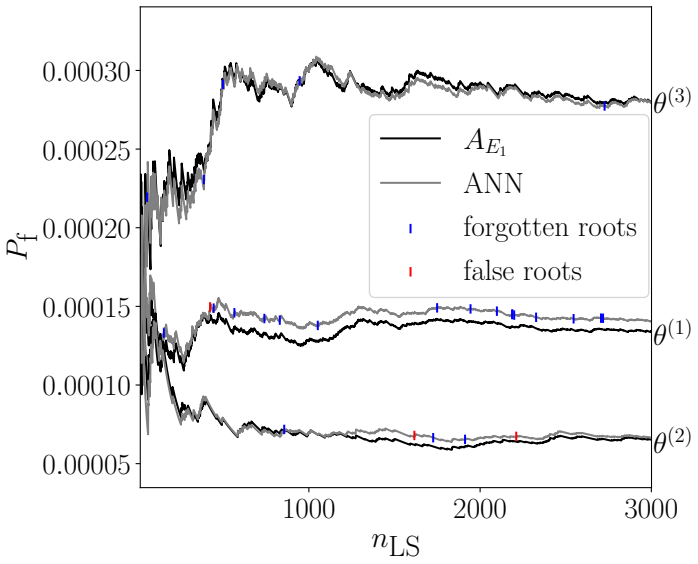

FIGURE 6.16: Comparison of the evolution of P_f with A_{E_1} and the ANNs for three distribution parameters vectors for the Rosenbrock function.

TABLE 6.3: ANNs metric values on $\boldsymbol{\theta}^{(1)}$ and $\boldsymbol{\theta}^{(2)}$.

	false roots (%)	forgotten roots (%)	$Q^2(r_1)$ (%)	$Q^2(r_2)$ (%)
$\boldsymbol{\theta_1}$	0.16	0.63	99.8	99.7
$\boldsymbol{\theta_2}$	1.6	0.06	99.7	99.7

6.6.2 Reliability of penstocks

The ANN methodology is now applied to the reliability assessment of penstocks. The vector of uncertain distribution parameters is $\boldsymbol{\theta} = [\mu_{\Delta e_{corr}}, \mu_{\Delta e_{extra}}, a_{max}, \beta_{K_{IC}}]^\top$ with the following nominal vector $\widetilde{\boldsymbol{\theta}} = [1, 0, 4, 90]^\top$. The maximum value of the horizon of uncertainty having been set at $h_{max} = 0.2$, the training is performed considering $\Theta_1 \sim \mathcal{U}(0.8, 1.2)$, $\Theta_2 \sim \mathcal{U}(-0.2, 0.2)$, $\Theta_3 \sim \mathcal{U}(3.1, 4.9)$ and $\Theta_4 \sim \mathcal{U}(71, 109)$. Again, the values of the four testing metrics are calculated on 3×10^3 new testing samples for $n_{train} \in [1 \times 10^3, 3 \times 10^4]$ and $n_{val} = 0.2 n_{train}$. The results shown in Figure 6.17 reveal good performances but for a higher number of training samples compared to the results obtained on the Rosenbrock function. One may notice that the coefficient of predictivity related to r_2 is always lower than the one related to r_1. A possible explanation is that the first root always corresponds to the limit-state function G_{N+1} whereas the second root either corresponds to G_N (in most cases) or to G_{HPT} which may be a more challenging feature to understand for ANN_2.

The procedure is now tested on the two distribution parameters samples $\boldsymbol{\theta}^{(1)} = [1,\ 0,\ 4,\ 90]^\top$ and $\boldsymbol{\theta}^{(2)} = [1.2,\ -0.2,\ 4.8,\ 108]^\top$ as they both represent the nominal point and one of the vertex points respectively. The results with the A_{E_3} algorithm and the ANNs are compared for $n_{train} = 3 \times 10^4$. The values of the four testing metrics are given in Table 6.3 for $n_{LS} = 3 \times 10^3$.

Figure 6.18 compares the values of $r_{1,2}^{(i)}$ obtained from the ANN and from A_{E_3} at both distribution parameters vectors $\boldsymbol{\theta}^{(1)}$ and $\boldsymbol{\theta}^{(2)}$. The comparisons of the evolution of $P_f\left(\boldsymbol{\theta}^{(1)}\right)$ and $P_f\left(\boldsymbol{\theta}^{(2)}\right)$ with the two algorithms are presented in Figure 6.19. The evolution of $P_f(\boldsymbol{\theta}_1)$ with both algorithms is almost identical. Indeed the number of wrong classifications from ANN_1 is very low and ANN_2 seem to predict both roots with high precision. The evolution of $P_f(\boldsymbol{\theta}_2)$ with

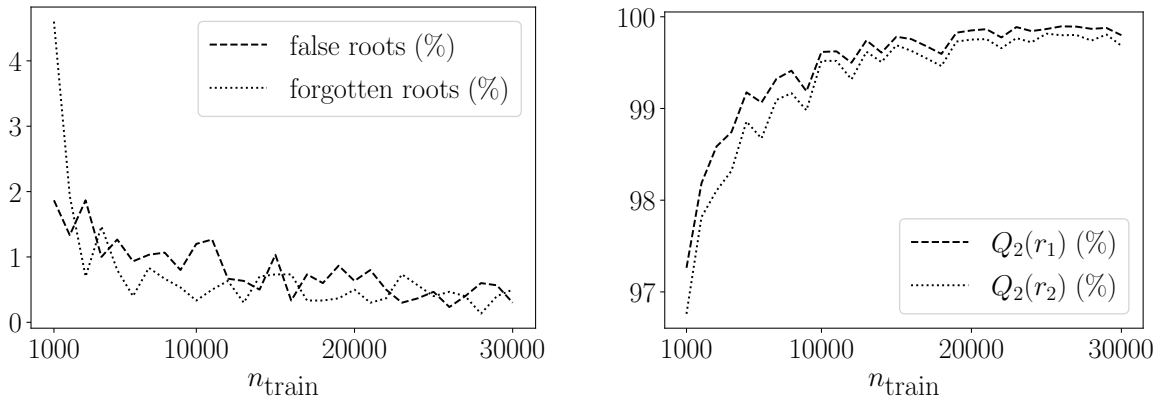

(A) (B)

FIGURE 6.17: Illustration of the performances of ANN_1 (A) and ANN_2 (B) on testing samples in function of the number of training samples on the penstock use-case.

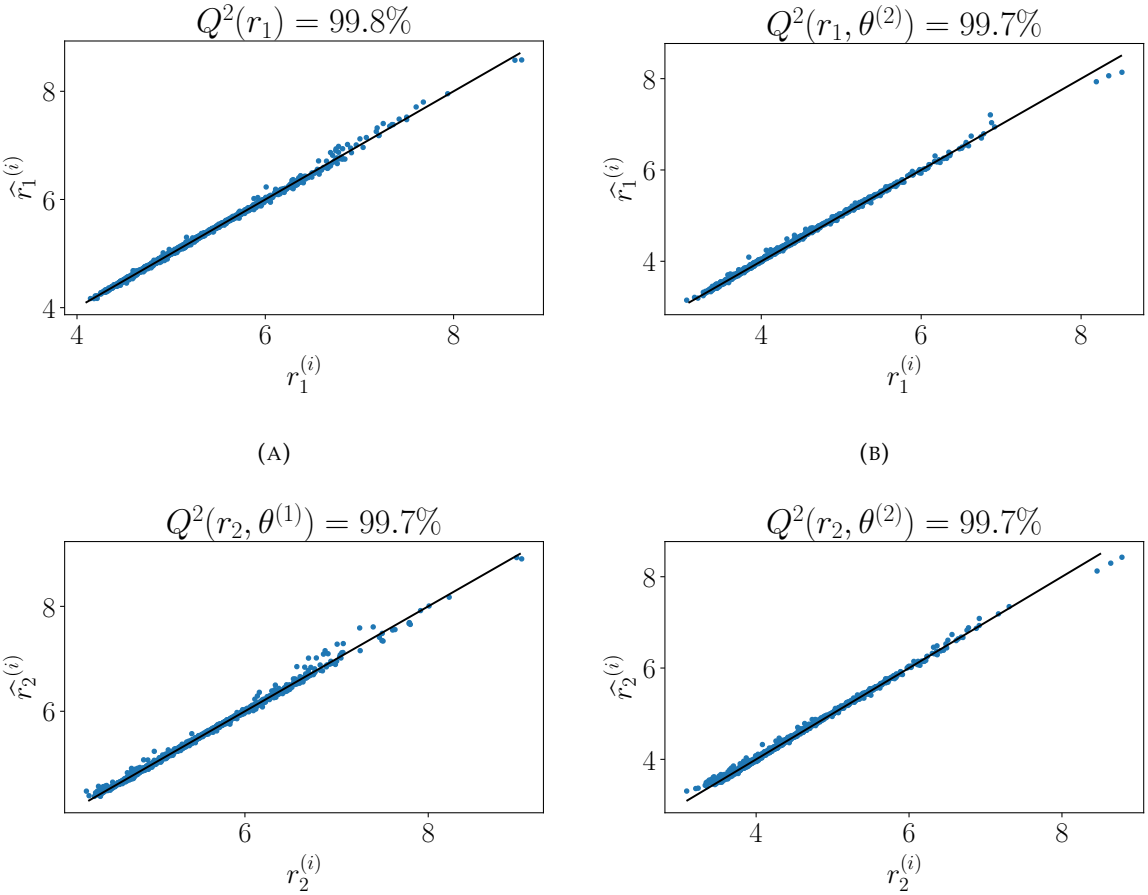

(A) (B)

(C) (D)

FIGURE 6.18: Comparison between the values of $r_1^{(i)}$ and $r_2^{(i)}$ from A_{E_3} and from the ANN at $\boldsymbol{\theta}^{(1)}$ (A,C) and $\boldsymbol{\theta}^{(2)}$ (B,D).

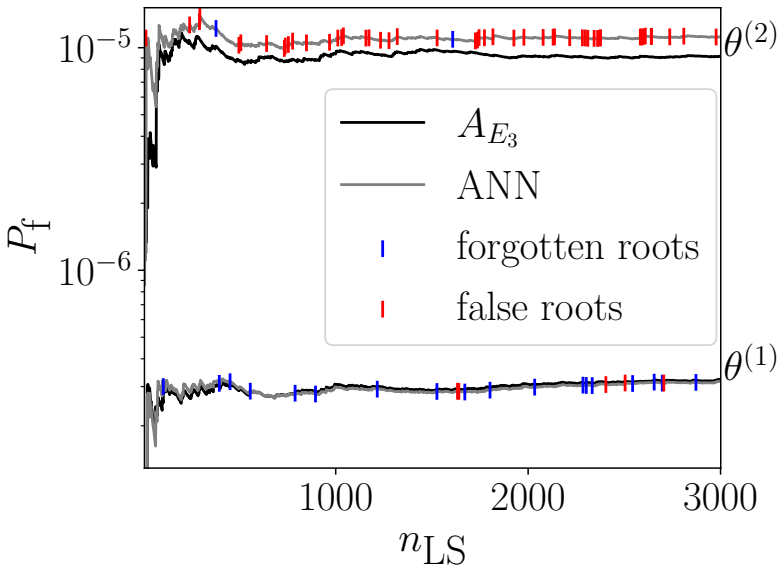

FIGURE 6.19: Evolution of $P_f\left(\boldsymbol{\theta}^{(1)}\right)$ and $P_f\left(\boldsymbol{\theta}^{(2)}\right)$ with A_{E_3} and the ANNs.

the ANNs is slightly overestimated which may be caused either by the evaluation of many false roots or by an overestimation of each single $p_f^{(i)}$. It is hard to tell from Figure 6.18.(F) if the single failure probabilities are overestimated as most predictions seem slightly underestimated but the worst predictions correspond to a few overestimated predictions. However, Figure 6.19 clearly shows a relatively large proportion (1.6%) of false roots which will automatically increase the estimated failure probability. To improve the estimation of $P_f(\boldsymbol{\theta}_2)$, the security value s may be used to reduce the number of false roots. Figure 6.20 presents the evolution of $P_f(\boldsymbol{\theta_2})$ for three different values of s. As expected, increasing the value of s brings the probability estimation curve closer to the one obtained with A_{E_3}. The side effect is that increasing s automatically increases the number of G-functions evaluations. However, Figure 6.21 reveals that a very large proportion of the output of ANN_1 is either very close to 0 or very close to 1 meaning that the verification process remains occasional.

6.6.3 Application to the estimation of robustness curves

The proposed methodology is used for estimating the robustness curves. The comparison is made by considering the following failure probability estimators: "A_{E_3} 2×10^3" which estimates P_f with A_{E_3} for $n_{LS} = 2 \times 10^3$, "A_{E_3}-ANN" which uses ANN_1 and ANN_2 applying the security value $s = 0.3$ for $n_{LS} \in \left[1 \times 10^3, 2 \times 10^3\right]$, "WIS 1×10^5" which uses the Weighted Importance Sampling algorithm in (Yuan, 2013) with a unique importance sampling of 10^5 samples considering $\boldsymbol{\theta} = \widetilde{\boldsymbol{\theta}}$ and "IS ref" as the same reference curve as in the previous robustness comparisons. Again, the comparison is made in terms of robustness curves (see Figure 6.22), error with the reference curve (see Figure 6.23) and cumulative computational time (see Figure 6.24).

Figures 6.22 and 6.23 reveal accurate estimations of the robustness curves using the ANNs and using the WIS approach. Actually, it shows that using the WIS approach by using a unique importance sampling of 1×10^5 samples reduces the errors that were obtained when repeatedly using the IS algorithm. A further reduction could be achieved by combining WIS with optimized FORM-IS algorithms leading to a lower sample size. In Figure 6.24, it can be seen how the use

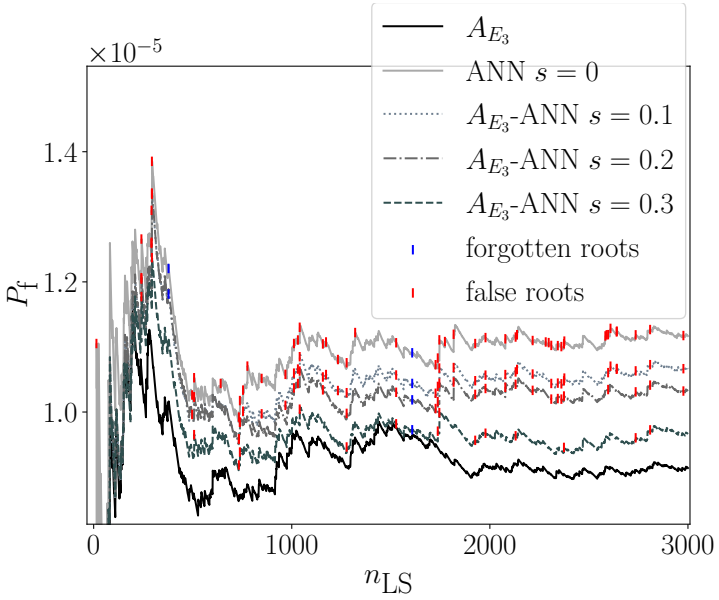

FIGURE 6.20: Evolution of $P_f(\boldsymbol{\theta_2})$ for different security values.

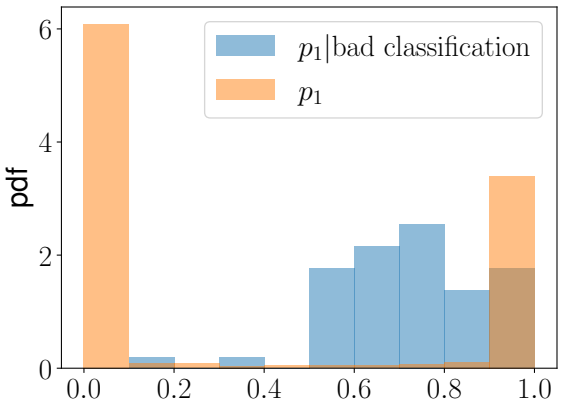

FIGURE 6.21: The pdf of the probability output p_1 of ANN_1 compared to its pdf conditioned to bad classifications for $\boldsymbol{\theta}^{(2)}$.

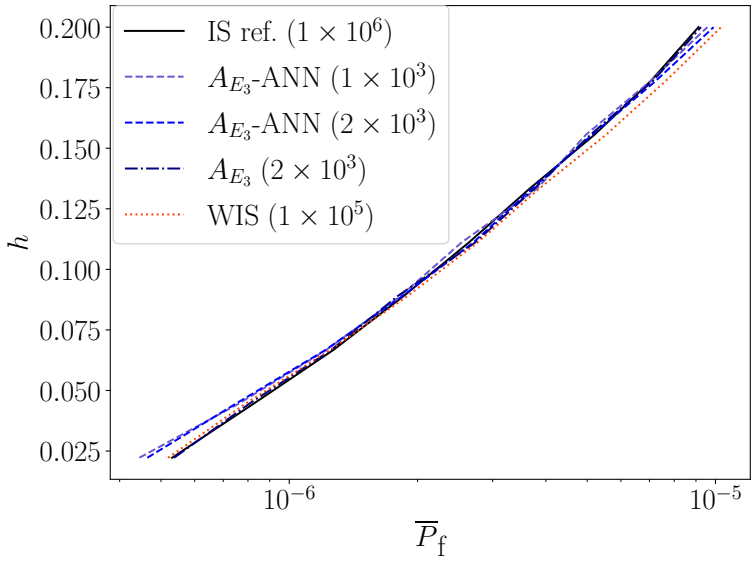

FIGURE 6.22: Robustness curves obtained with the A_{E_3}, A_{E_3}-ANN and WIS algorithms.

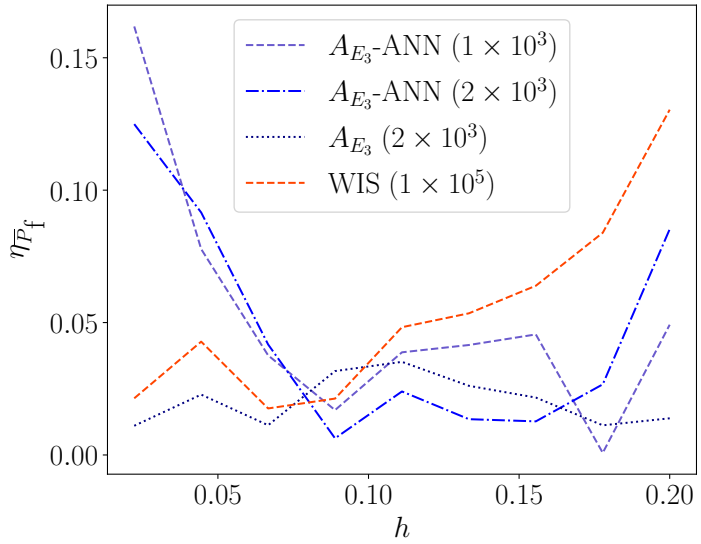

FIGURE 6.23: Relative error on the robustness curves obtained with the A_{E_3}, A_{E_3}-ANN and WIS algorithms.

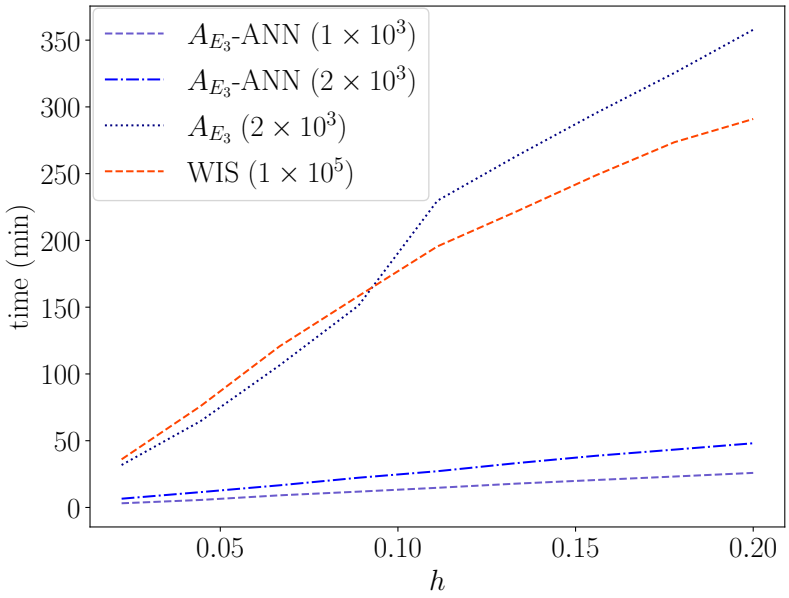

FIGURE 6.24: Cumulative computational time for obtaining the robustness curves obtained with the A_{E_3}, A_{E_3}-ANN and WIS algorithms.

of ANNs considerably reduces the computational time even when considering a security value $s = 0.3$.

Insightful information obtained as a post-processing result from an IG analysis is the values of the uncertain parameters that led to the worst performances according to the optimization algorithm. Figure 6.25 presents these values where $h^*(\theta_i^*)$ is a scaling value such that $h^*(\theta_i^*) = \theta_i^*/\widetilde{\theta}_i - 1$ for $i = \{1,3,4\}$ (non-zero nominal value) and $h^*(\theta_i^*) = \theta_i^*$ for $i = 2$ (zero nominal value). This figure shows in a standardised way the relative position of the uncertain parameters that led to the highest failure probabilities w.r.t. each increasing interval defined by h_j. It is clearly apparent that the failure probability is monotonic w.r.t. the uncertain parameters. Therefore, the vertex method could have substituted the DIRECT algorithm. However, this represents a post-processing information that was not assumed before the IG analysis. This result may also guide the analyst when searching for more information about the uncertain parameters. For example, if new information reveals that the uncertain parameter actually lies in the "good" area w.r.t. robustness, then there is no need to gather more information (unless to check if it can counterbalance penalizing effects from the other uncertain parameters). On the contrary, if penalizing values do appear to be very likely, the analyst would want to gather more information in order to better know how close this penalizing value is to the critical value that leads to the critical performance.

Finally, the fact that the robustness curves are relatively fast to generate thanks to the use of ANNs enables to re-estimate robustness curves in order to evaluate the demand value $R^{\widetilde{e}_i}$ when considering iteratively each uncertain parameter at its nominal value. These results are given in Figure 6.26. The most impacting uncertain parameter is still quite predominant, although far less than the one observed considering the plastic collapse failure mode.

6.7 Conclusion

In this chapter, the line sampling technique was adapted to each failure mode for which the reliability assessment of penstocks is evaluated. The failure domain associated to plastic collapse

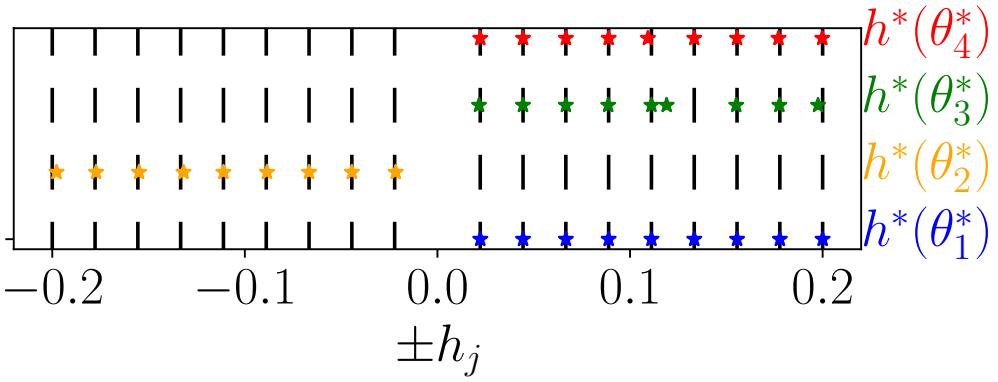

FIGURE 6.25: Values of the uncertain distribution parameters that led to the maximum failure probabilities.

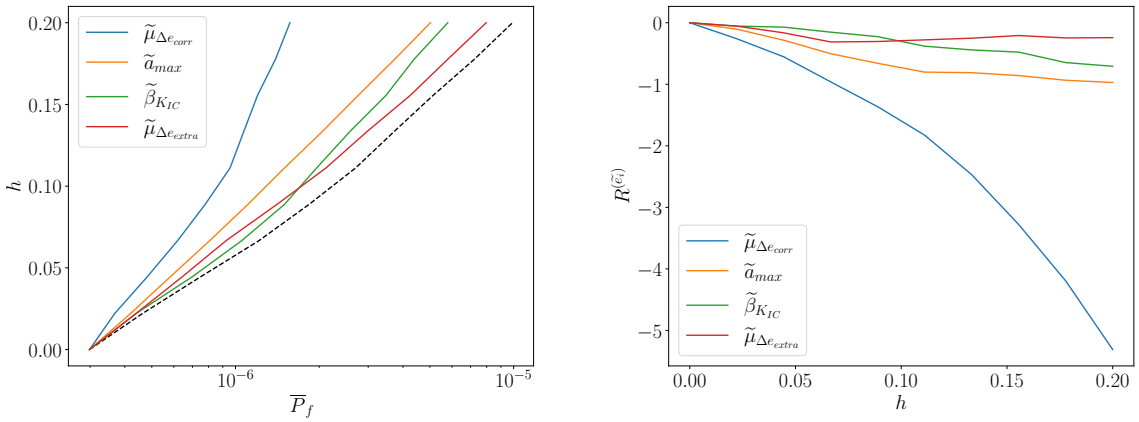

(A) (B)

FIGURE 6.26: Robustness curve obtained for each uncertain variable fixed at its nominal value (the black dotted curve corresponds to all variables considered uncertain) (A) and corresponding demand values (B)

is simpler to tackle and the proposed line sampling algorithm converges very efficiently. Thus, the IG framework could be applied without needing computational time reduction techniques. The robustness results on a panel of penstock configurations did not reveal any configuration that stands out.

Then, the challenging reliability problem induced by brittle failure is tackled by the use of three customized LS algorithms (A_{E_1}, A_{E_2} and A_{E_3}) based on three equivalent formulations of the complex limit-state function made of a double intersection of events. While considering the root search differently, each algorithm yields similar estimations of the failure probability. The good performances of the proposed algorithms are enhanced with their use for estimating robustness curves. The algorithm A_{E_3}, based on a sequential root search, appears to be more efficient in this case.

Finally, the root search procedure is improved in terms of computational time with the use of two artificial neural networks. The first one enables to predict the existence (or not) of roots for any given line search and for any value of the epistemic uncertain vector $\boldsymbol{\theta}$. The second one predicts the values of both roots when they exist. Although the ANNs performance metrics are very good, a few bad predictions may lead to non-negligible errors on the failure probability. Therefore, a security value is proposed in order to decide whether the classification ANN should be trusted or whether the initial algorithm should be used. The methodology is then tested and proven to be very efficient for estimating IG robustness curves.

The use of neural networks is motivated by the fact that the limit-state functions involved in the industrial use case are relatively fast to evaluate which enables a large dataset for the training process. In many practical applications, such a large dataset may not be available due to time-consuming numerical models. In this case, it would be necessary to consider other types of surrogates models such as Gaussian process regression. In particular, methods based on active learning such as in (Song et al., 2021) may present a high interest especially if there is a way to apply it in the augmented space which includes the uncertain distribution parameters.

Moreover, the high computational cost for estimating IG robustness curves is due to the choice of not making any assumption when successively searching for the maximum failure probability at each horizon of uncertainty h. The a posteriori results show that the vertex method could be used in this application case which would considerably reduce the number of failure probability estimations.

The application of IG on the loss-of-coolant accident presented in the next chapter is a typical case for which the procedure employed in this chapter becomes intractable.

CHAPTER 7

Robustness assessment for a complex thermal-hydraulic industrial case

Contents

7.1 Motivations

In this chapter, the IG framework is applied to the risk analysis related to the IBLOCA scenario as already presented in Chapter 3. The QoIs are the quantile and the superquantile of the peak cladding temperature evaluated using the CATHARE2 code which simulates the accidental transient. The main difficulties that arise in this study are the computational time needed for one simulated transient (around 30 minutes) and the number of uncertain variables which adds up to 27. The former challenges the application of the IG method for the obvious reason that many QoI evaluations are involved while each one of them would require several days to be obtained. The latter is challenging as the pdfs describing all the involved random variables present various properties which makes the definition of a unique IG uncertainty model complex. Moreover, high dimensionality very often drives down the performances of some numerical procedures such as metamodels.

The objective motivating the following sections is to propose and compare methodologies that enable the application of the IG framework despite the aforementioned challenges. In particular, two original IG uncertainty models based on the standard normal space and DS structures are proposed as well as two different numerical procedures used for estimating both QoIs from a unique set of samples. First, Section 7.2 develops the proposed IG methodologies by describing the studied QoIs, the IG uncertainty models and the numerical procedures for efficiently estimating the QoIs. Then, Section 7.3 presents the application of the overall methodology to a toy case and to the IBLOCA risk analysis.

7.2 Info-gap problem statement

7.2.1 Risk-oriented quantities of interest

The usual QoI studied in BEPU analysis is the quantile q^β of order β (Prosek and Mavko, 2007) which takes the following formulation:

$$q^\beta = \inf\{t \in \mathbb{R} \mid F_Z(t) \geq \frac{\beta}{100}\}. \tag{7.1}$$

By generating N i.i.d. realizations $\left\{\mathbf{x}^{(n)} = \left(x_1^{(n)}, \cdots, x_{n_\mathbf{X}}^{(n)}\right)\right\}_{1\leq n\leq N}$ from the random vector $\mathbf{X}$ and evaluating the corresponding output values $\left\{z^{(n)} = \mathcal{M}\left(\mathbf{x}^{(n)}\right)\right\}_{1\leq n\leq N}$, the empirical estimator of the quantile reads:

$$q_N^\beta = \inf\left\{t \in \mathbb{R} \mid \frac{1}{N}\sum_{n=1}^{N} \mathbb{1}_{z^{(n)}\leq t} \geq \frac{\beta}{100}\right\}. \tag{7.2}$$

In practice, the 95%-order ($\beta = 0.95$) is often considered for the IBLOCA application case.

More recently, the superquantile was added as a relevant QoI (Labopin-Richard et al., 2016). Indeed, by representing the expectation of the variable of interest over a specific range of values (e.g. the safety-relevant tail of the distribution), it better explains its behavior in the region of interest than the quantile alone. The superquantile Q^β of order β reads:

$$Q^\beta = \mathbb{E}\left(\frac{Z\mathbb{1}_{Z\geq q_N^\beta}}{1-\frac{\beta}{100}}\right) \tag{7.3}$$

with the corresponding empirical estimator:

$$Q_N^\beta = \frac{1}{N(1-\frac{\beta}{100})} \sum_{n=1}^{N} z^{(n)} \mathbb{1}_{z^{(n)} \geq q_N^\beta}. \tag{7.4}$$

In practice, the 75%-order will be considered ($\beta = 0.75$) as in Iooss et al. (2022). It is noted, at this point, that the quantile and superquantile notations between the theoritical and empirical formulations are purposely confounded in order to ease the notations defined in the following sections.

7.2.2 Info-gap uncertainty models

The probabilistic definition of the 27 random variables present in the LSTF reduced model can be found in Table 3.2 which reveals the presence of four families of parametric distributions: normal distributions, lognormal distributions, uniform distributions and loguniform distributions. A common property of all the involved quantities is that they are bounded which implies that the pdfs are truncated. In the studies related to CATHSBI, the principal concern about the probabilistic definition of $\mathbf{X}$ lies in the choice of the marginal parametric distributions rather than the bounds of the quantities that are considered to be known (Baccou et al., 2019).

In this study, each random variable will be considered uncertain, although not all at the same time. In the same way as previously, $\mathbf{X}$ will denote the random vector of certain random variables while $\mathbf{Y}$ refers to the uncertain random vector. Therefore, each random variable will sometimes belong to $\mathbf{X}$ and other times to $\mathbf{Y}$. In this chapter, two different IG uncertainty models are considered.

Case 1: parametric p-box in the standard normal space

The historical way for density perturbations proposed in the context of PLI estimation (Lemaître et al., 2015; Sueur et al., 2017; Iooss and Le Gratiet, 2019) is to shift specific moments (e.g. the mean or the variance) of the uncertain pdf by a value δ. As several pdfs may be eligible to such a perturbed moment, the retained pdf is the one that minimizes the Kullback-Leibler divergence from the nominal pdf $\widetilde{f}_{\mathbf{Y}}$. This implies that the perturbed pdf does not necessarily belong to the same parametric distribution family. For instance, shifting the mean of a nominal uniform distribution will not result in a uniform distribution as the bounds are fixed. Using such approach is straightforward in some cases (e.g. perturbing a normal distribution) but may be more challenging in others (e.g. perturbing lognormal distributions).

In this context, Perrin and Defaux (2019) proposed to apply the perturbations in the standard normal space. This method presents two main advantages. First, as all nominal distributions become Gaussian, applying a perturbation on one moment comes back to considering a normal distribution with the corresponding perturbed moment. Secondly, as all the uncertain random variables have the same nominal moments, their perturbations are easier to compare. Figure 7.1 shows the perturbed pdfs back in the physical space for the four families of distribution present in Table 3.2 when perturbing the mean μ_s of the Gaussian distribution.

This method is used for defining the IG uncertainty model. In the following applications, only uncertainty on the mean vector $\boldsymbol{\mu}_s$ of the Gaussian distributions related to $\mathbf{Y}$ will be considered. Hence, as in Chapter 6, the IG problem reduces to a succession of parametric p-box problems as the robustness function becomes:

$$h^*_{U_1,\mathrm{QoI}} = \max_{h \in \mathbb{R}^+} \left\{ \max_{\boldsymbol{\mu}_s \in U_1(h,\tilde{\boldsymbol{\mu}}_s)} \mathrm{QoI}\left(Z|\boldsymbol{\mu}_s\right) \leq \mathrm{QoI}^{\mathrm{cr}} \right\}. \tag{7.5}$$

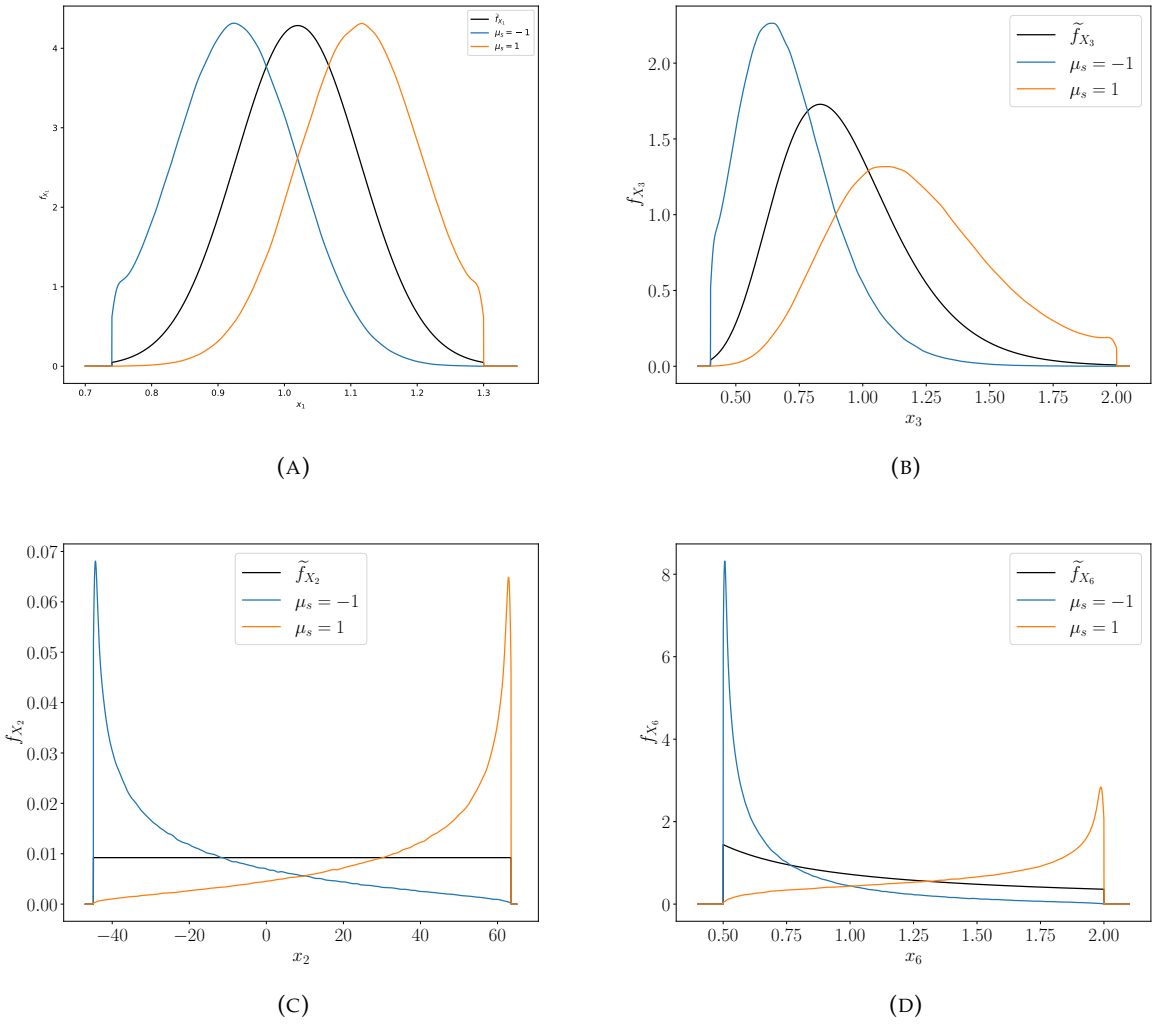

FIGURE 7.1: Perturbed distributions of a normal pdf (A), lognormal pdf (B), uniform pdf (C) and loguniform pdf (D) back in the physical space after perturbation of the standard mean μ_s.

where $\text{QoI}\left(Z|\boldsymbol{\mu}_s\right) = \text{QoI}\left(Z\left(T^{-1}\left(\mathbf{U}\right)\right)|\boldsymbol{\mu}_s\right)$ refers either to the quantile or the superquantile estimators conditional to $\boldsymbol{\mu}_s$ and $U_1\left(h, \widetilde{\boldsymbol{\mu}}_s\right) = \times_{i=1}^{n_\Upsilon}\left[-h, +h\right]$.

Case 2: free p-box based on Dempster-Shafer structures

The second IG uncertainty model that is considered in this chapter is based on the DS discretization already introduced in Chapter 4. As a reminder, the idea consists in discretizing the support of each uncertain random variable Y_i into n_{DS} disjoint intervals $\left[a_{i,j}, b_{i,j}\right]_{1\leq j\leq n_{\text{DS}}}$ with given mass probabilities:

$$m_{i,j} = F_{Y_i}\left(b_{i,j}\right) - F_{Y_i}\left(a_{i,j}\right). \tag{7.6}$$

This method is equivalent to considering a free p-box representation. It enables to smoothly travel from a perfectly known cdf (i.e. a very high value of n_{DS}) to the unique interval representation (i.e. $n_{\text{DS}} = 1$). Figure 7.2 shows examples of induced p-box representations for the four families of distribution present in Table 3.2.

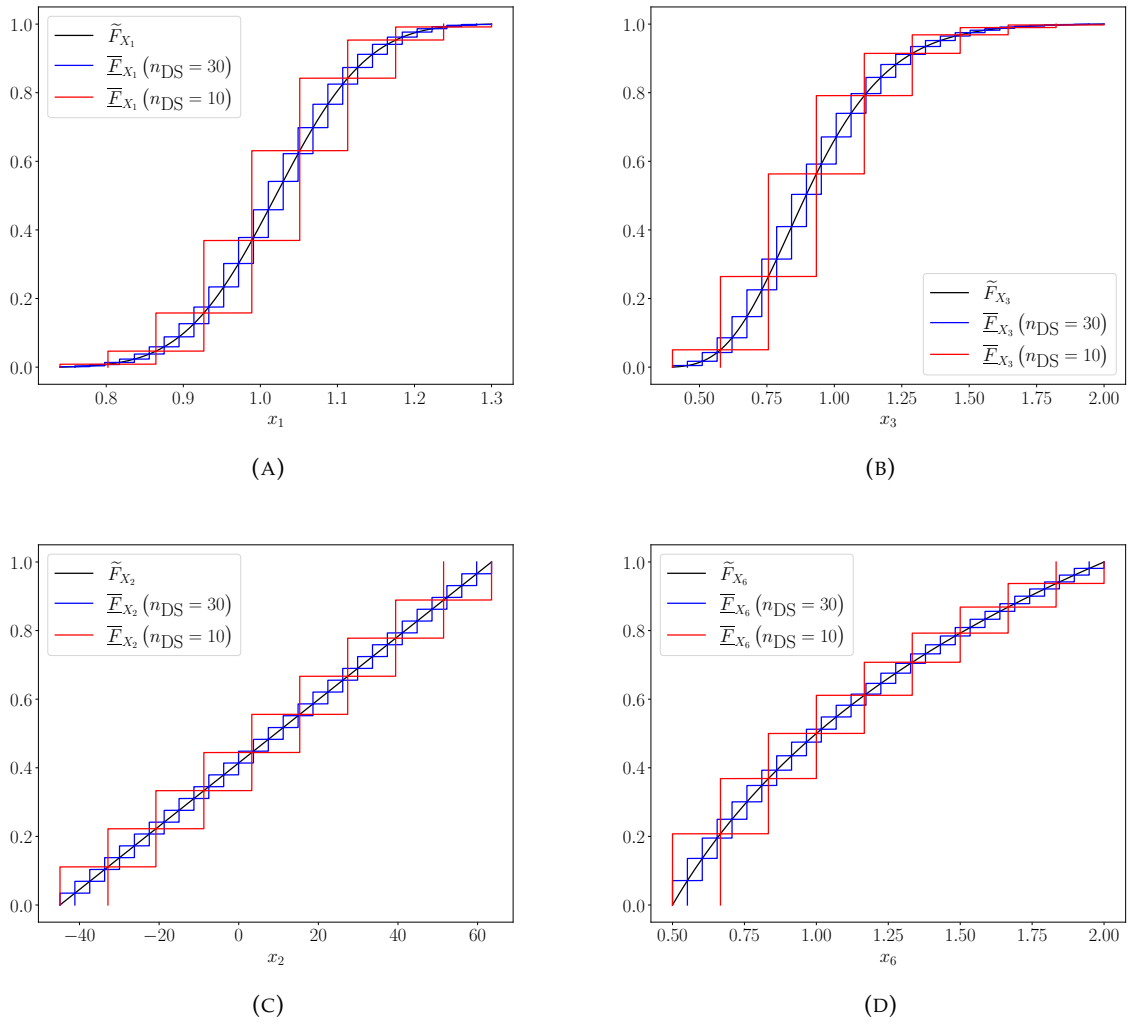

FIGURE 7.2: Dempster-Shafer discretization of a normal cdf (A), lognormal cdf (B), uniform cdf (C) and loguniform cdf (D) for $n_{\text{DS}} = 10$ and $n_{\text{DS}} = 30$.

As the cdfs of the uncertain random variables belong to a p-box, the cdf of the output random variable Z also belongs to a p-box such that $\underline{F}_Z\left(z\right) \leq F_Z\left(z\right) \leq \overline{F}_Z\left(z\right)$. Therefore, in order to

apply the IG robustness framework, it is necessary to search for the output cdf that belongs to this envelop and gives the worst performances (i.e. the highest quantile $\overline{q}^{\beta}_{F_Z}$ and superquantile $\overline{Q}^{\beta}_{F_Z}$ values). When considering the search of the worst quantile, the problem writes:

$$\overline{q}^{\beta}_{F_Z} = \sup_{\underline{F}_Z \leq F_Z \leq \overline{F}_Z} \left[\inf\{t \in \mathbb{R} \mid F_Z(t) \geq \frac{\beta}{100}\} \right]. \tag{7.7}$$

In the context of quantile optimization over a probability measure μ that belongs to a moment class $\mathcal{A}$, the following duality was proven in (Stenger et al., 2020):

$$\overline{q}^{\beta}_{\mu \in \mathcal{A}} = \inf\{t \in \mathbb{R} \mid \inf_{\mu \in \mathcal{A}} F_{\mu}(t) \geq \frac{\beta}{100}\}. \tag{7.8}$$

Therefore, in the present context, one gets:

$$\overline{q}^{\beta}_{F_Z} = \inf\{t \in \mathbb{R} \mid \min_{\underline{F}_Z \leq F_Z \leq \overline{F}_Z} F_Z(t) \geq \frac{\beta}{100}\}. \tag{7.9}$$

Figure 7.3, still inspired from (Stenger et al., 2020), illustrates this point. Moreover, by reminding

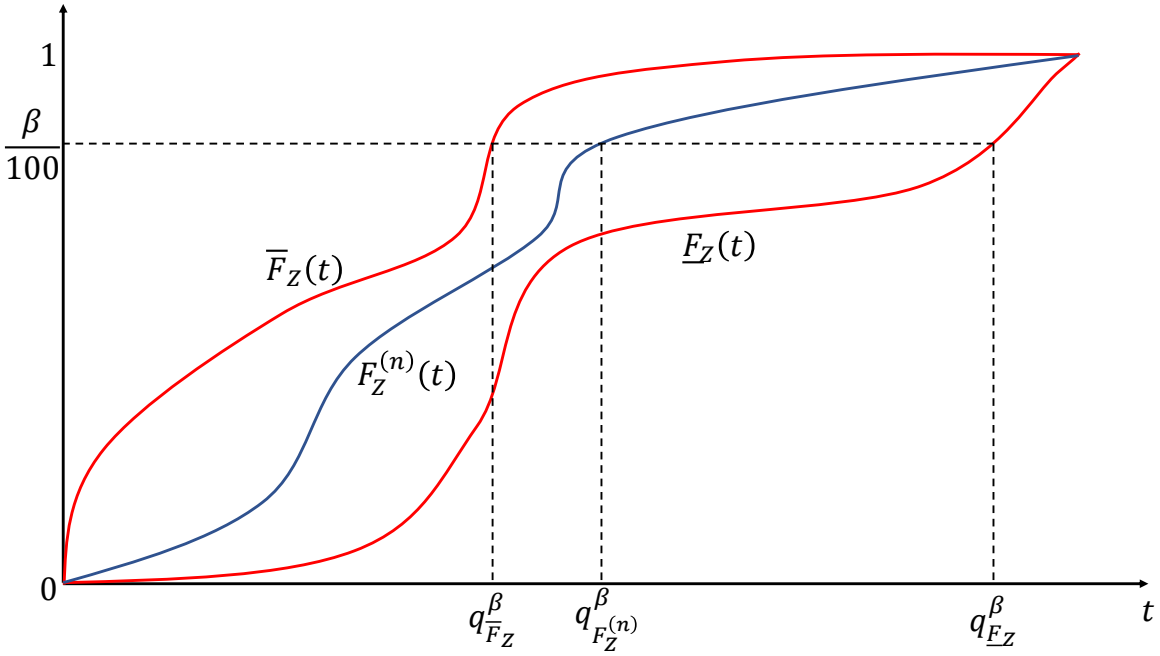

FIGURE 7.3: Illustration of the maximum quantile as the quantile of the lowest CDF of Z.

that $F_Z(t) = \mathbb{P}\left(Z\left(\mathbf{X}, \mathbf{Y}\right) \leq t\right)$, random set theory as introduced in Chapter 5 can be applied such that:

$$\min_{\underline{F}_Z \leq F_Z \leq \overline{F}_Z} F_Z(t) = \int_{[0,1]^{n_{\boldsymbol{\alpha}}}} \mathbb{1}_{\{\overline{z}(\boldsymbol{\alpha}) \leq t\}} d\boldsymbol{\alpha} \tag{7.10}$$

with:

$$\overline{z}\left(\boldsymbol{\alpha}\right) = \max_{(\mathbf{X},\mathbf{Y}) \in \Gamma_{(\mathbf{X},\mathbf{Y})}(\boldsymbol{\alpha})} z(\mathbf{X}, \mathbf{Y}). \tag{7.11}$$

Similarly to the estimation of bounds on the failure probability in Chapter 5, the estimation of the worst quantile is obtained by generating samples $\boldsymbol{\alpha}^{(n)}$ from the uniform distribution and

computing the maximum value of z in each corresponding random set $\Gamma\left(\boldsymbol{\alpha}^{(n)}\right)$.

However, the previous derivations do not appear to be as straightforward when considering the superquantile. Therefore, this method will only be applied to the quantile by considering $n_{\mathrm{DS}}(h)$ as a decreasing function of h such that:

$$h^*_{U_2} = \max_{h\in\mathbb{R}^+}\left\{\max_{F_Z\in\underline{F}_Z(n_{\mathrm{DS}}(h))} q^{95}_{F_Z} \leq q^{95,\mathrm{cr}}\right\}. \tag{7.12}$$

7.2.3 Quantile and superquantile estimation methods

The previous proposed IG uncertainty models imply either several searches of the highest quantile and superquantile w.r.t. $\boldsymbol{\mu}_s$ or many searches of the maximum peak cladding temperature in the corresponding random sets. In both cases, considering the computational time of one single peak cladding temperature estimation, it is unfeasible to solve these IG problems using directly the CATHARE2 code $\mathcal{M}(\cdot)$. In this context, two different numerical procedures are investigated.

Method 1: reverse importance sampling

The idea behind the reverse importance sampling (RIS) (Hesterberg, 1996) technique is to use a unique set of samples $\left(\mathbf{x}^{(n)},\mathbf{y}^{(n)},\mathbf{z}^{(n)}\right)_{1\leq n\leq N^r}$ for estimating $\mathrm{QoI}(\boldsymbol{\theta})$ at different values of the uncertain distribution parameters $\boldsymbol{\theta}$. By considering that $\left(\mathbf{x}^{(n)},\mathbf{y}^{(n)}\right)$ are generated according to $f_{\mathbf{X}}$ and to the nominal joint pdf $\widetilde{f}_{\mathbf{Y}}$, the RIS estimation $\widehat{q}^{\beta}_{N^r}(\boldsymbol{\theta})$ of the quantile is obtained as:

$$\widehat{q}^{\beta}_{N^r}(\boldsymbol{\theta}) = \inf\{t\in\mathbb{R} \mid \widehat{F}^{N^r}_Z(t|\boldsymbol{\theta}) \geq \frac{\beta}{100}\} \tag{7.13}$$

where

$$\widehat{F}^{N^r}_Z(t|\boldsymbol{\theta}) = \frac{\sum_{n=1}^{N^r} L^{(n)}(\boldsymbol{\theta})\,\mathbb{1}_{z^{(n)}\leq t}}{\sum_{n=1}^{N^r} L^{(n)}(\boldsymbol{\theta})} \tag{7.14}$$

with $L^{(n)}$ being the likelihood ratio expressed as:

$$L^{(n)}(\boldsymbol{\theta}) = \frac{f_{\mathbf{Y}}\left(y^{(n)}|\boldsymbol{\theta}\right)}{\widetilde{f}_{\mathbf{Y}}\left(y^{(n)}\right)}. \tag{7.15}$$

Similarly, the estimation $\widehat{Q}^{\beta}(\boldsymbol{\theta})$ of the superquantile reads:

$$\widehat{Q}^{\beta}_{N^r}(\boldsymbol{\theta}) = \frac{1}{N^r(1-\frac{\beta}{100})}\sum_{n=1}^{N^r} z^{(n)}\mathbb{1}_{z^{(n)}\geq\widehat{q}^{\beta}_{N^r}(\boldsymbol{\theta})}L^{(n)}(\boldsymbol{\theta}). \tag{7.16}$$

The performance of this technique reduces as soon as the unique set of samples becomes less representative of $f_{\mathbf{Y}}(\mathbf{y}|\boldsymbol{\theta})$, i.e. when the values in $\boldsymbol{\theta}$ are far away from $\widetilde{\boldsymbol{\theta}}$. Some practical recommendations are given in Iooss et al. (2022) for that matter.

As this method is based on the likelihood ratio of parametric distributions, it can only be applied in this application when considering the IG uncertainty model in the standard normal space and not based on the DS discretization. With $\boldsymbol{\theta} = \boldsymbol{\mu}_s$, the IG robustness function simply becomes:

$$\widehat{h}^*_{U_1,\mathrm{QoI}} = \max_{h\in\mathbb{R}^+}\left\{\max_{\boldsymbol{\mu}_s\in U_1(h,\widetilde{\boldsymbol{\mu}}_s)} \widehat{\mathrm{QoI}}(\boldsymbol{\mu}_s) \leq \mathrm{QoI}^{\mathrm{cr}}\right\}. \tag{7.17}$$

Method 2: metamodel with artificial neural networks

The idea with this method is to substitute the time-greedy CATHARE2 code $\mathcal{M}(\cdot)$ with a metamodel $\widehat{\mathcal{M}}(\cdot)$ that approximates its behavior. Artifical neural networks are again chosen for that task as the input dimension is relatively large and as a few thousand of training samples will be available. However, other techniques such as Gaussian process could have been chosen (Iooss and Marrel, 2019). By denoting $\widehat{\widehat{z}} = \widehat{\widehat{\mathcal{M}}}(\mathbf{x}, \mathbf{y})$ the estimation of the peak cladding temperature provided by the ANN trained on N^t samples, the estimation $\widehat{\widehat{q}}^{\beta}_{N^t}$ of the quantile reads:

$$\widehat{\widehat{q}}^{\beta}_{N^t} = \inf\left\{ t \in \mathbb{R} \mid \frac{1}{N^t}\sum_{n=1}^{N} \mathbb{1}_{\widehat{\widehat{z}}^{(n)} \leq t} \geq \frac{\beta}{100} \right\} \tag{7.18}$$

and the estimation $\widehat{\widehat{Q}}^{\beta}_{N^t}$ of the superquantile reads:

$$\widehat{\widehat{Q}}^{\beta}_{N^t} = \frac{1}{N(1-\frac{\beta}{100})}\sum_{n=1}^{N^t} \widehat{\widehat{z}}^{(n)} \mathbb{1}_{\widehat{\widehat{z}}^{(n)} \geq \widehat{\widehat{q}}^{\beta}_{N^t}}. \tag{7.19}$$

As $\widehat{\mathcal{M}}(\cdot)$ is fast to compute, it can be used to estimate the IG robustness functions in both considered uncertainty models such that:

$$\widehat{\widehat{h^*_{U_1,\mathrm{QoI}}}} = \max_{h\in\mathbb{R}^+}\left\{ \max_{\boldsymbol{\mu}_s \in U_1(h,\widetilde{\boldsymbol{\mu}}_s)} \widehat{\widehat{\mathrm{QoI}}}(\boldsymbol{\mu}_s) \leq \mathrm{QoI}^{\mathrm{cr}} \right\}. \tag{7.20}$$

considering the uncertainty model in the standard normal space and

$$\widehat{\widehat{h^*_{U_2}}} = \max_{h\in\mathbb{R}^+}\left\{ \max_{F_Z \in \underline{\overline{F}}_Z(n_{\mathrm{DS}}(h))} \widehat{\widehat{q^{95}_{F_Z}}} \leq q^{95,\mathrm{cr}} \right\} \tag{7.21}$$

considering the DS discretization uncertainty model.

7.3 Application cases

7.3.1 Application to a cantilever tube

This first application case related to the cantilever tube illustrated in Figure 7.4 aims at studying some first IG results on the quantile and superquantile obtained using the RIS technique. The variable of interest considered in this application case is the maximum von Mises stress $\sigma_{\max} = \sqrt{\sigma_x^2 + 3\tau_{xz}^2}$ at the support of the tube of diameter d, thickness t, length L_1 and subjected to a torsional moment T, external lateral forces F_1 and F_2 and an axial force P.

The normal stress σ_x is expressed as:

$$\sigma_x = \frac{P + F_1\sin\theta_1 + F_2\sin\theta_2}{A} + \frac{Md}{2I} \tag{7.22}$$

where $A = \pi\left(d^2 - (d-2t)^2\right)/4$ is the cross-sectional areal, $M = F_1L_1\cos\theta_1 + F_2L_2\cos\theta_2$ is the bending moment and $I = \pi\left(d^4 - (d-2t)^4\right)/64$ is the second moment of inertia and the shear stress τ_{xz} is expressed as:

$$\tau_{xz} = \frac{Td}{4I}. \tag{7.23}$$

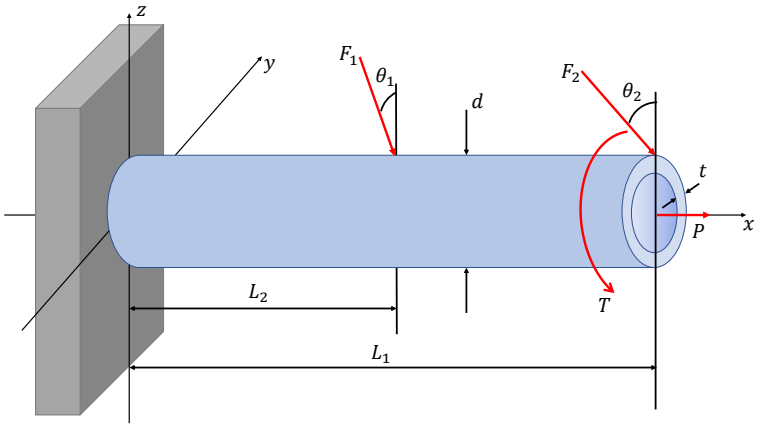

FIGURE 7.4: Illustration of the cantilever tube.

.

The properties of the ten truncated distributions are given in Table 7.1.

TABLE 7.1: Input probabilistic modeling of **X** for the cantilever tube model.

Variable X_i	Distribution	param. 1	param. 2	Bounds
$X_1 = P$ (kN)	Gumbel	$\beta = 12$	$\gamma = 1.2$	$[8, 16]$
$X_2 = t$ (mm)	Normal	$\mu = 5$	$\sigma = 0.25$	$[3.8, 6.2]$
$X_3 = d$ (mm)	Normal	$\mu = 42$	$\sigma = 2.1$	$[32, 52]$
$X_4 = L_1$ (mm)	Uniform	$a = 115$	$b = 125$	$[115, 125]$
$X_5 = L_2$ (mm)	Uniform	$a = 55$	$b = 65$	$[55, 65]$
$X_6 = F_1$ (kN)	Normal	$\mu = 3$	$\sigma = 0.3$	$[2, 4]$
$X_7 = F_2$ (kN)	Normal	$\mu = 3$	$\sigma = 0.3$	$[2, 4]$
$X_8 = \theta_1$ (degrees)	Normal	$\mu = 5$	$\sigma = 1$	$[0, 10]$
$X_9 = \theta_2$ (degrees)	Normal	$\mu = 10$	$\sigma = 2$	$[5, 15]$
$X_{10} = T$ (N.m)	Normal	$\mu = 90$	$\sigma = 9$	$[60, 120]$

Figure 7.5 shows the convergence of the nominal quantile and superquantile estimators when increasing the number of samples. It appears, in this case, that the estimators get close to their reference value quite soon and that the superquantile estimator is slightly more precise for a same value N.

Figure 7.6 now shows the convergence of the RIS quantile and superquantile estimators at four negative values of μ_s considering $Y = [d]$. The estimators seem less stable for higher absolute values of μ_s and require more samples for approaching the reference values. The fact that the RIS estimators seem to underestimate the reference values is not a behavior to be generalized as the same set of 10^4 samples was used for generating all the curves.

Finally, Figure 7.7 compares the quantile and superquantile robustness curves obtained using the RIS estimators for $N^r = 3000$ (solid lines) with the reference ones obtained by regenerating samples from each perturbed distributions (dotted lines). It appears that the estimated robustness curves on the quantile are quite close to the reference ones although larger errors are observed when considering three uncertain variables. The estimated robustness curves on the superquantile present larger deviations than for the quantile especially for $n_{\mathbf{Y}} = 1$ and $n_{\mathbf{Y}} = 2$. In the general case, larger deviations are expected when increasing the number of uncertain variables. Indeed, adding uncertain variables will necessarily increase the highest values of quantile and superquantile which makes the unique set of sample less representative (very few samples are actually above the predicted quantile and superquantile).

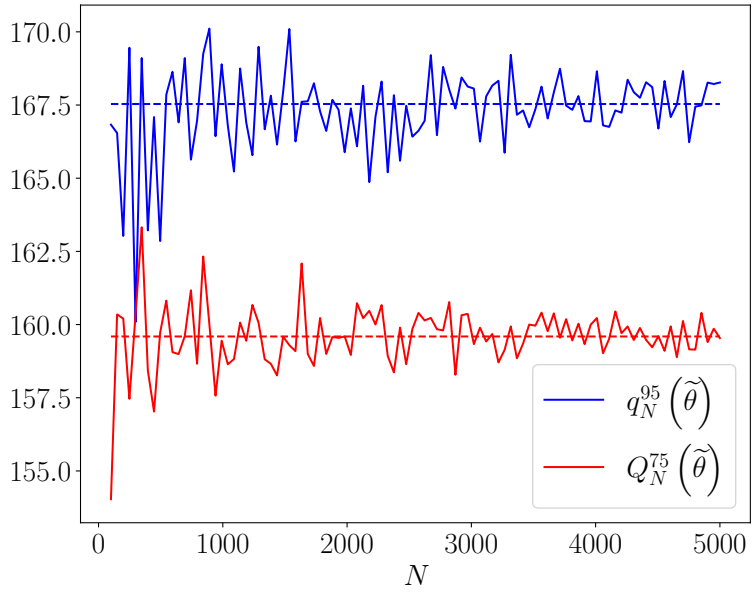

FIGURE 7.5: Convergence of the nominal quantile q_N^{95} and nominal superquantile Q_N^{75} when increasing the number of samples N for the cantilever tube model. The dotted lines are the reference values.

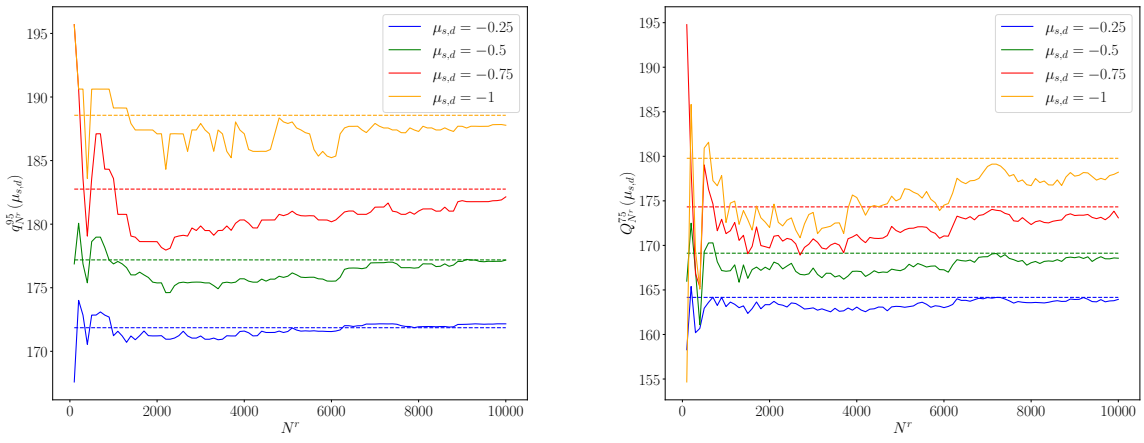

(A) (B)

FIGURE 7.6: Convergence of the RIS quantile (A) and superquantile (B) estimators at four values of μ_s corresponding to d. The dotted lines are the reference values.

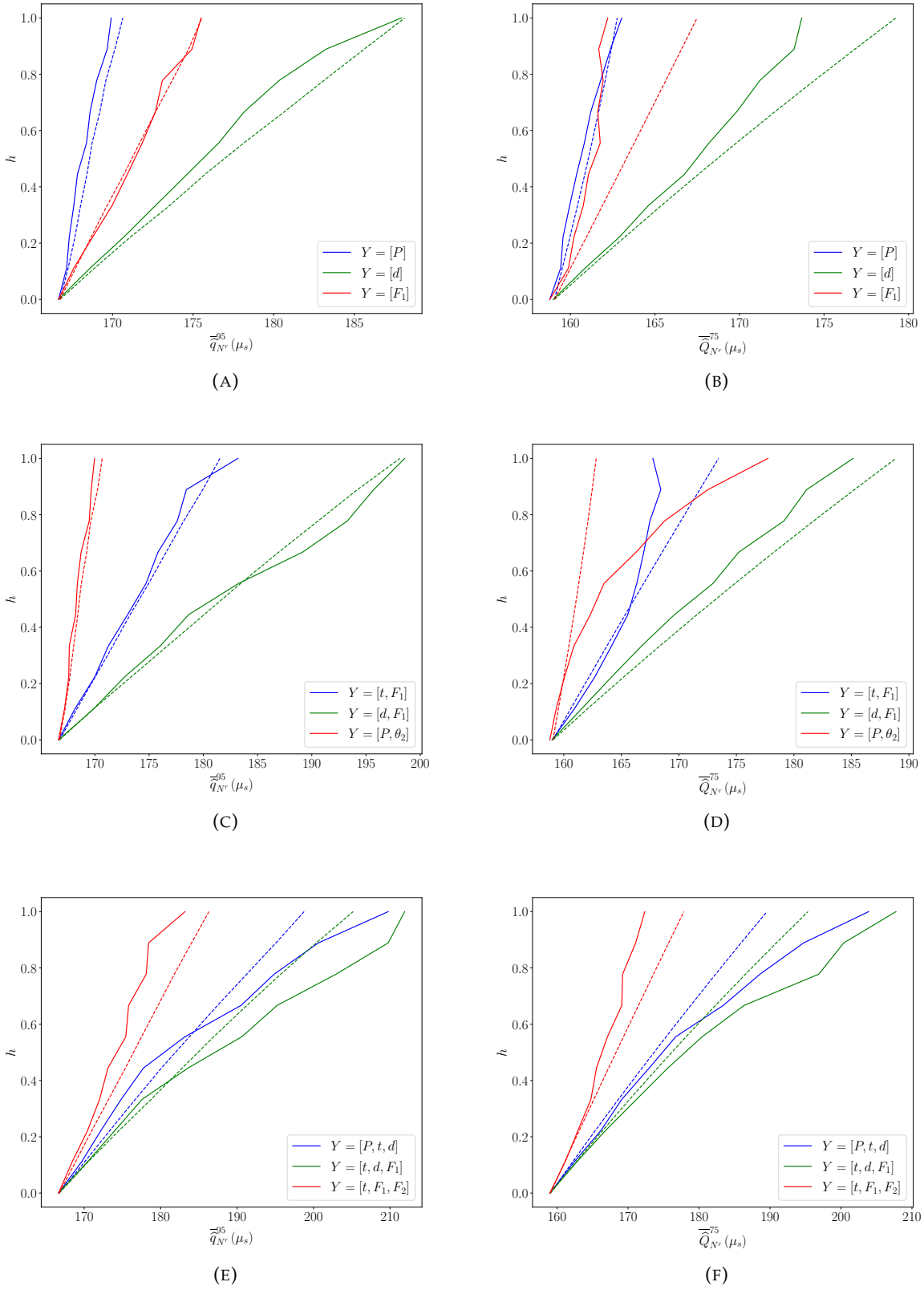

FIGURE 7.7: Robustness curves obtained using the RIS estimators (solid lines) to be compared with the reference curves (dotted lines) for the quantile and superquantile considering $n_Y = 1$ (A and B), $n_Y = 2$ (C and D) and $n_Y = 3$ (E and F).

7.3.2 Application to the intermediate break loss of coolant accident

The complete methodology detailed in Section 7.2 is now applied to the IBLOCA scenario. The first step is to generate the samples that will be used for the RIS estimators and for training the ANN. A total of $N^r = 3000$ MC samples are generated according to the nominal pdf $\widetilde{f}_{\mathbf{X}}$. Figure 7.8 shows the convergence of the nominal quantile and superquantile empirical estimators.

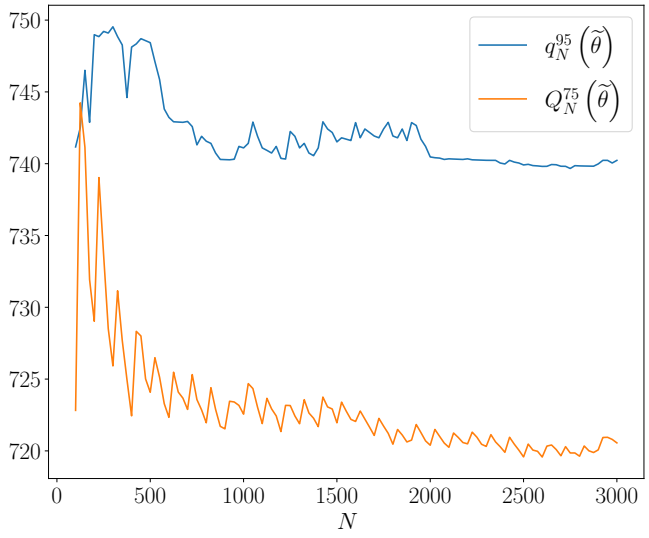

FIGURE 7.8: Convergence of the nominal quantile and superquantile estimated from the 3000 MC samples.

In order to train the ANN, an additional set of 3000 samples was generated considering a uniform distribution in the bounds of $\mathbf{X}$. The reason for choosing a uniform distribution is that the application of the IG framework implies covering the entire uncertain space. Other sampling techniques such as latin hypercube sampling (McKay et al., 2000) could have been more judicious for a better coverage. Moreover, adaptive sampling could also be of interest as it is more important to well describe the uncertain areas where the worst QoIs are to be expected than the rest of the uncertain space. The first 300 realizations of the uniform set of samples are used for validating the performance of the ANN during the training (but are not used for updating the ANN weights during training). This number is kept the same no matter the number of training samples N^t in order to compare performances on a same set of validation samples. However, in the case where, for intance, only 400 samples are available, a more relevant distribution would be recommanded (e.g. 350 training samples and 50 validation samples). Several ANNs are constructed for $N^t \in [100, 4700]$. When $N^t \leq 2700$, only uniformly generated samples are considered. When $N^t > 2700$, Monte Carlo samples are added to all the uniformly generated samples. Note that once the ANN is trained, the number of ANN predicted samples used for the empirical estimation of $\widehat{\widetilde{q}}_{N^t}^{95}$ and $\widehat{\widetilde{Q}}_{N^t}^{75}$ is not necessarily the same as N^t. In the following, this number will be equal to 3000 no matter the value of N^t.

Figure 7.9 shows how the coefficient of predictivity Q^2 evaluated on the validation samples evolves w.r.t. the number of training samples. It appears that this performance metric improves rather quickly up to $N^t = 1000$ and more slowly after.

Figure 7.10.(A) presents the values of the quantile and the superquantile on the 1000 MC samples that are never used for the construction of the ANNs. The solid lines show both QoIs estimated from the ANNs w.r.t. the number of training samples and the dotted lines show the

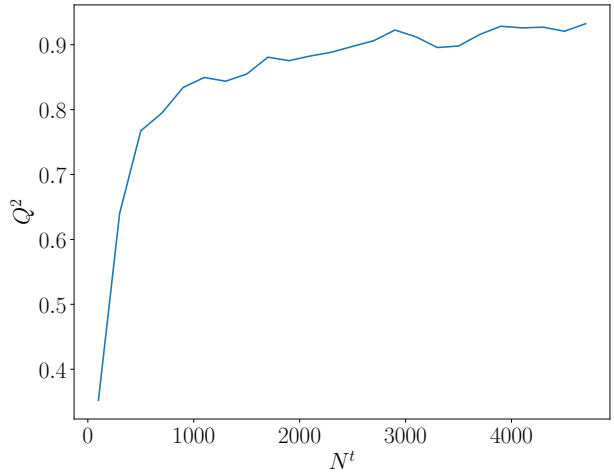

FIGURE 7.9: Evolution of Q^2 for increasing numbers of training samples.

empirical estimators from the MC samples. The estimations obtained from the ANN begin to be acceptable for $N^t > 2000$ and get very close to the empirical estimators for $N^t > 3000$. Similar trends are observed between the quantile and the superquantile estimation curves. This is understandable as ANNs that overestimate (respectively underestimate) the higher values of z will necessarily overestimate (respectively underestimate) the quantile and the superquantile estimations. The scatter plot between the same 1000 MC peak cladding temperatures $z^{(n)}$ and their ANN estimations $\widehat{\widehat{z}}^{(n)}$ is given in Figure 7.10.(B) for $N^t = 500$ and $N^t = 3100$. Clearly, the better trained ANN yields estimations that are closer to the dotted line representing exact estimations. Some of these estimations are still quite far from their reference value even for $N^t = 3100$. However, although the lower values of z seem to be generally overestimated by both ANNs, the predictions of the higher values do not appear, in average, to be overestimated nor underestimated for $N^t = 3100$ (while they tend to be more often underestimated for $N^t = 500$). This explains why the quantile and the superquantile estimations are precise despite the coefficient of predictivity not being that close to 1.

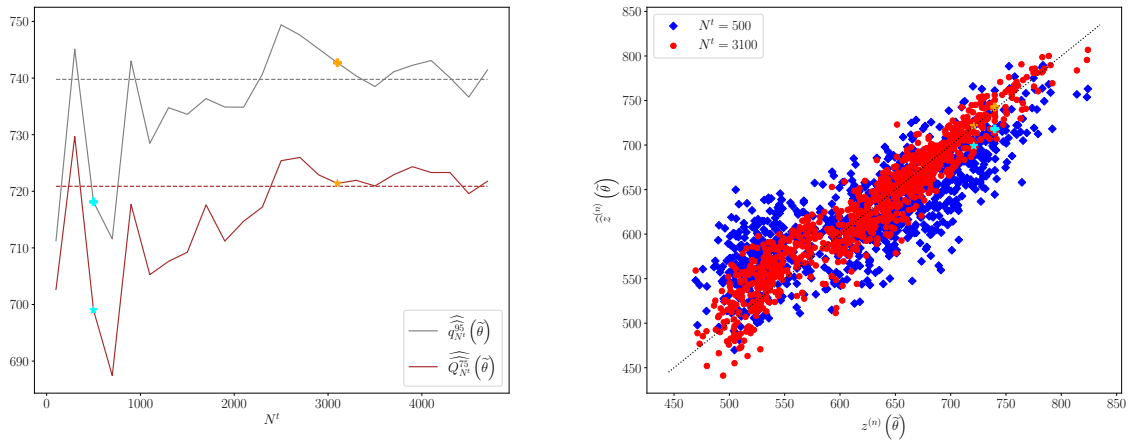

(A) (B)

FIGURE 7.10: Convergence of the ANN estimator at the nominal configuration (A) and scatter plot obtained from the ANN on the 1000 MC samples.

The RIS and ANN estimators are now compared jointly considering the IG uncertainty model U_1 based on the standard normal space. Before applying the IG framework, Figure 7.11 compares the convergence of the estimators w.r.t. N^r (for the RIS estimator) and N^t (for the ANN estimator) on four perturbation values of the standard mean related to the variable X_{22}. Figure 7.11.(A) compares the quantile estimator while Figure 7.11.(B) compares the superquantile estimator. A first interpretation is that the ANN curves relevant to the quantile and the superquantile all have trends that are similar to the ones observed in Figure 7.10.(A) (equivalent to $\mu_s = 0$). This could suggest that the general behaviors of the ANN identified at the nominal configuration are extendable to any configuration. This could be understood from the fact that the ANNs are mostly trained and totally validated on uniformly generated samples. Secondly, the curves obtained from the RIS quantile estimator are quite stable, especially for $N^r > 2000$. Moreover, they seem to globally meet the ANN curves, except at $\mu_s = -1$ which yields more noticeable deviations. On the contrary, the evolution of the RIS superquantile estimators are highly chaotic, especially at $\mu_s = -0.5$ and $\mu_s = -1$. The potential reasons for this instability, despite the quantile estimations being stable, are not clearly identified.

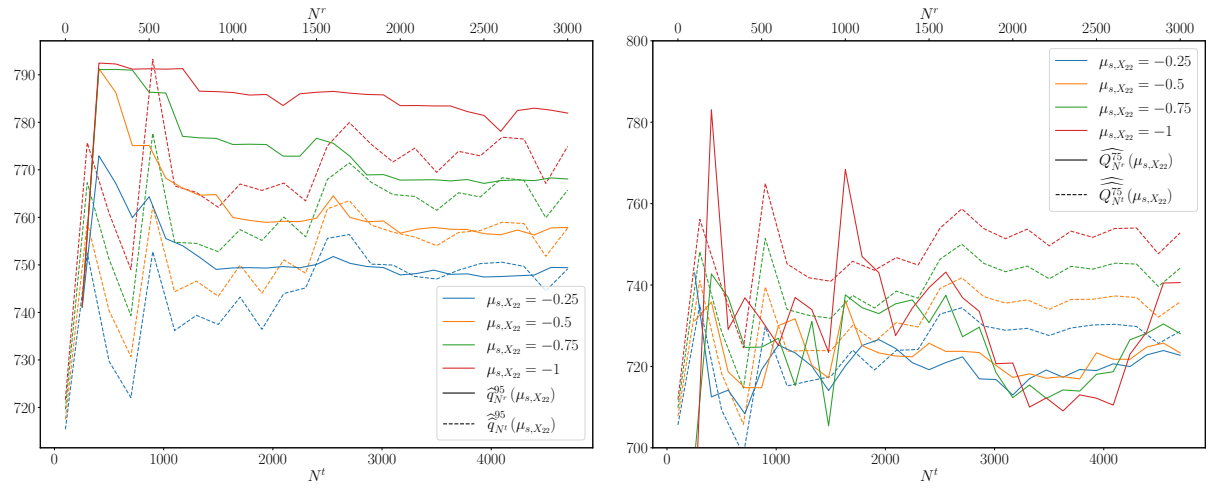

(A) (B)

FIGURE 7.11: Convergence of the RIS estimator (solid lines) and the ANN estimator (dotted lines) on the quantile (A) and the superquantile (B) at four different values of μ_s related to X_{22}.

The RIS and ANN estimators are now integrated in the IG procedure for estimating robustness curves considering $N^r = 3000$ and $N^t = 3100$. As the total number of uncertain variables is high, considering all of them at once would, most likely, yield very pessimistic temperatures as worst-case scenarios are cumulated. Instead, robustness curves are first estimated considering each uncertain variable alone. Then, combinations including the variables that affect the most the robustness are analyzed. This is a hypothesis as one could imagine that a variable alone may have very little effect on the robustness but may reveal a strong influence when associated to other uncertain variables. Figure 7.12 presents the most pessimistic robustness curves relevant to the uncertainty model based on the standard mean for $n_{\mathbf{Y}} = \{1, 2, 3\}$. These results are again obtained using the DIRECT optimization algorithm. The RIS-based robustness curves are only given for $n_{\mathbf{Y}} = \{1, 2\}$ on the quantile and $n_{\mathbf{Y}} = 1$ on the superquantile. Indeed, as it could be expected from the preliminary results in Figure 7.11.(B), the RIS superquantile results are quite unstable. The RIS quantile results are more in accordance with the ANN results, at least for identifying the group of uncertain variables that lead to the most pessimistic curves. Note that the IG robustness curves for $n_{\mathbf{Y}} = 1$ are equivalent to looking at the positive values (because worse means higher) of the PLI estimators that have been considered many times for

similar application cases by using the RIS technique. However, noticeable deviations from the ANN results are observed for higher values of h and when increasing the dimension $n_{\mathbf{Y}}$. Yet, the ANN-based robustness curves, although being stable and coherent, remain estimations and, therefore, cannot be considered as reference values.

Finally, Figure 7.13 presents the ANN-based robustness curves considering the uncertainty model based on a DS discretization for $n_{\text{DS}} \in [5, 100]$. The maximum value in each sampled random set is estimated using the DIRECT algorithm. The group of most impacting uncertain variables is similar to the one obtained from the uncertainty model based on the standard mean, although the most penalizing variable changes from X_{22} to X_{12}. It can be observed from every robustness curve that the maximum quantile is not affected much for numbers of intervals higher than 40. Yet, robustness worsens much faster for lower numbers of intervals. This point can be seen again in Figure 7.14 which gives the most part (for β in $[5, 95]$) of the predicted peak cladding temperature p-box envelop for $n_{\text{DS}} = \{5, 20, 50\}$ and for $\mathbf{Y} = [X_{12}, X_{22}]$. The envelop for $n_{\text{DS}} = 5$ is very wide with a temperature range of around 100 degrees for the predicted 95%-order quantile. On the contrary, the envelop for $n_{\text{DS}} = 50$ is almost reduced to a unique cdf (the predicted nominal output cdf).

7.4 Conclusion

In this chapter, G was applied in different ways for assessing the robustness of two new reliability estimates for the peak cladding temperature during an IBLOCA scenario. Although 95%-order quantiles and 75%-order superquantiles are generally easier to estimate than very low failure probabilities, the computational time required for a CATHARE2 simulation makes the reliability analysis, and therefore its IG application, challenging. Two original IG uncertainty models were proposed. The first one, based on the perturbation of moments in the standard normal space, enables an easier application and interpretation of a unique horizon of uncertainty affecting all uncertain variables. The second one, based on a DS discretization of the nominal cdf, enables to consider comparable perturbations in a non-parametric way. This uncertainty representation which comes back to considering free p-box required to reuse the random set theory framework.

The computational burden associated to CATHARE2 simulations implied the investigation of two substitution procedures. First, the RIS method, already used for PLI estimations, enables to reevaluate perturbed QoIs from a unique set of realizations. Additionally, ANN-based metamodels were trained in order to substitute the CATHARE2 model with predictive models that are much faster to evaluate. These two methods were then applied for estimating robustness curves. Comparable results were obtained for the robustness of the quantile as both methods identified the same group of impacting uncertain variables. Yet, some deviations appear especially for higher values of h and for increasing numbers of considered uncertain variables. On the contrary, the robustness of the superquantile obtained with the RIS estimator is quite chaotic and difficult to interpretate. The curves obtained from the ANN estimator are much smoother.

The main limitation of the employed methodology is the lack of confidence intervals on the final results. The fact that the highly trained ANNs revealed precise quantile and superquantile estimations at the nominal configuration does not imply equivalent performances for perturbed configurations. However, the fact that the robustness curves are smooth and that the same impacting variables are identified shows the stability of the estimator. Nevertheless, there is no guarantee that the metamodel did not miss any particular uninditified feature of the real input-output relation. Note that confidence intervals could have been obtained on the RIS estimations using the bootstrap technique as in Iooss et al. (2022). Moreover, more conservative results can be obtained using Wilks formula.

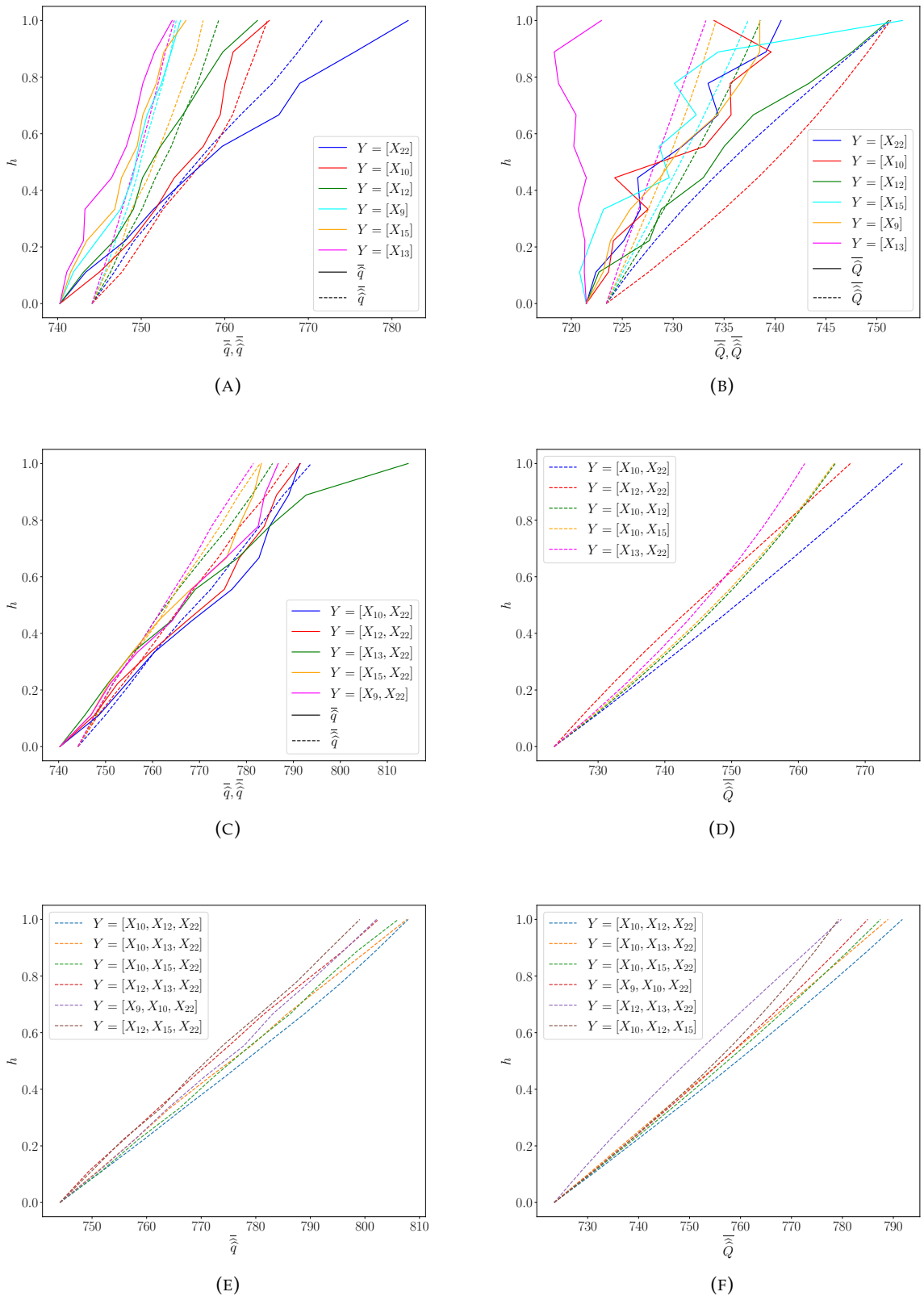

FIGURE 7.12: Robustness curves relevant to the standard mean on the quantile (A,C,E) and the superquantile (B,D,F) obtained with the RIS and ANN estimators for increasing numbers of uncertain variables.

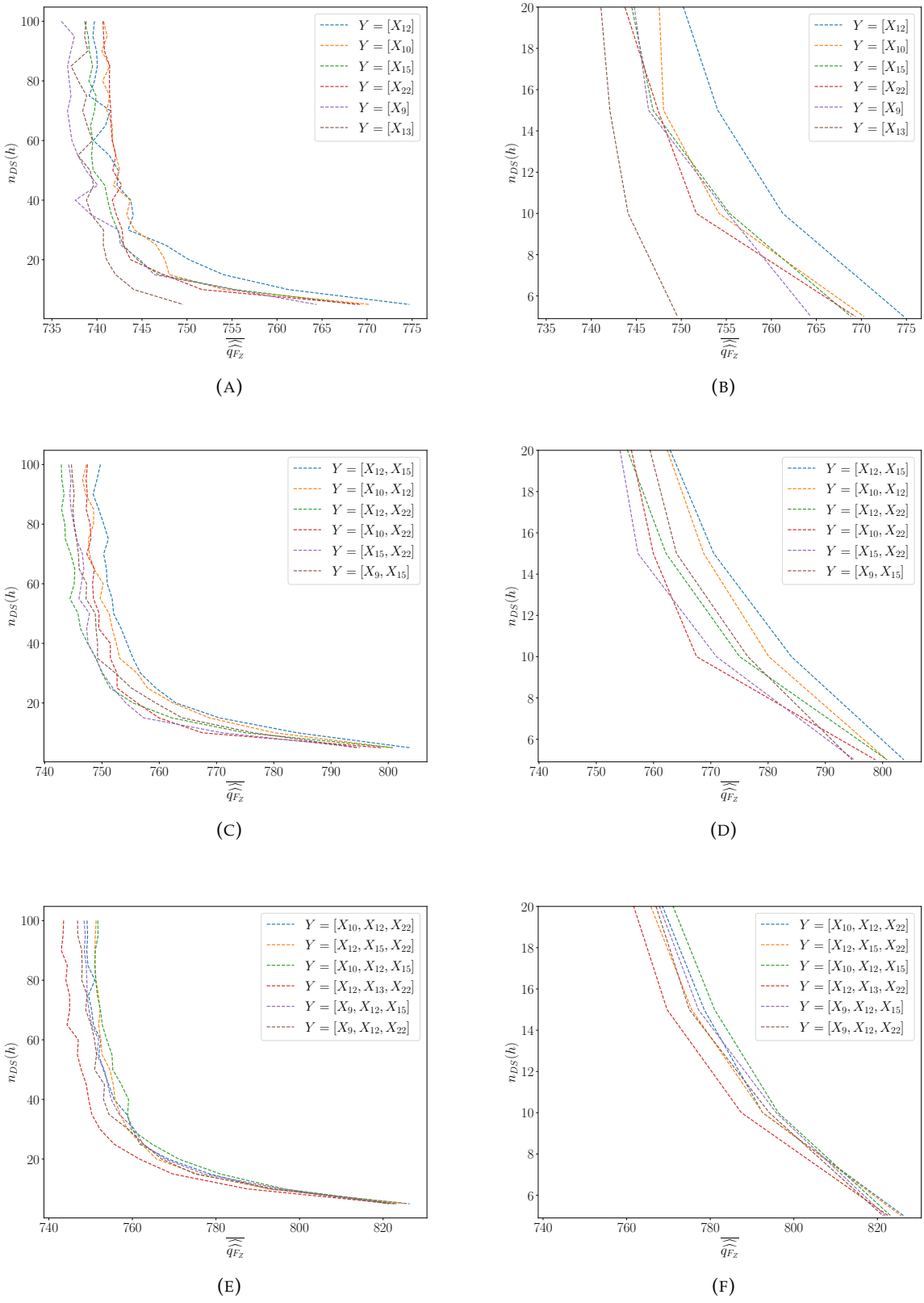

FIGURE 7.13: Robustness curves (ANN estimators) relevant to the DS discretization on the quantile with a zoom on lower values of n_{DS} (B,D,F).

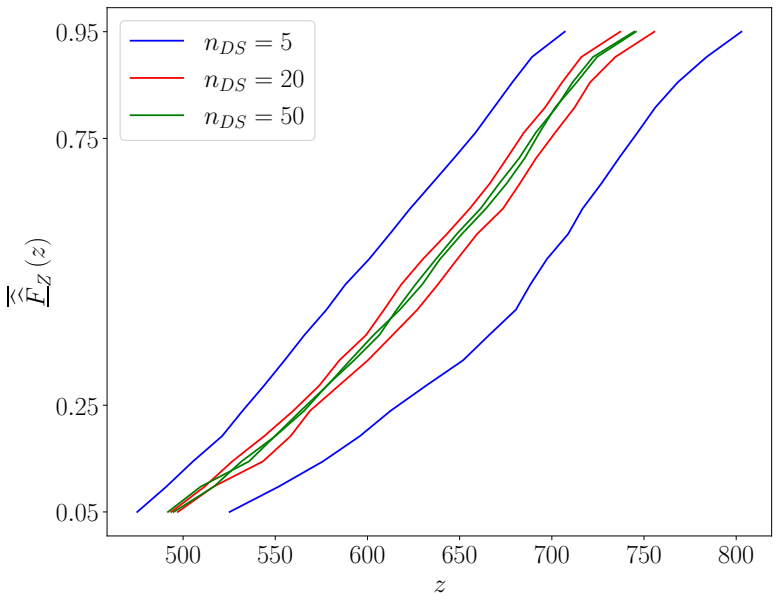

FIGURE 7.14: Predicted p-box envelop of the peak cladding temperature for different numbers of intervals and for $\mathbf{Y} = [X_{12}, X_{22}]$.

Another identified perspective for the use of RIS would be to investigate if the consideration of an augmented space for generating the unique set of samples would enable better performances at higher horizons of uncertainty and in higher dimensions. Indeed, such an augmented space should yield more samples above the real pertubed quantile and superquantile values. Moreover, it would be interesting to analyze results obtained from metamodels that focus their learning on specific regions of the uncertain space. Indeed, the proposed application tends to show that well predicting in average the highest values of the variable of interest may be sufficient for good estimations on the quantile and the superquantile.

CHAPTER 8

General conclusion and perspectives

General conclusion

The central motivation leading to the realization of this thesis was to develop methodologies that could evaluate the robustness of reliability estimates w.r.t. lack of knowledge that may influence safety-related industrial decisions. Indeed, although probability theory offers quite a powerful framework for quantifying and propagating uncertainty through computer codes, it remains crucial to confront high-stakes decisions to their underlying assumptions. In that matter, the info-gap framework was investigated as it proposes a generalizable framework that quantifies the notion of robustness.

After a general description of the IG method, its adaptation to reliability-based quantities of interest was formulated. In particular, it was shown in Chapter 4, through the consideration of different uncertainty contexts, how the IG framework may bring valuable insights. Although a key aspect of the IG theory is its non-probabilistic representation of uncertainty, it should not be viewed as an opponent to the use of probabilistic concepts, but rather as a complementary framework. Indeed, the modular characteristic of IG uncertainty models offers many possibilities for perturbing nominal configurations. Moreover, the notion of horizon of uncertainty creates a progressive path from probabilistic representations to non-probabilistic ones. However, despite using relatively approachable mathematical concepts for quantifying the notion of robustness, the application of IG on reliability QoIs may imply a burdensome numerical procedure.

A first challenge that appears when applying IG to reliability QoIs is the possible coexistence of several uncertainty representations that can be listed into three categories: purely probabilistic, extra-probabilistic and non-probabilistic. Although they each have their specific propagation framework as described in Chapter 2, their joint consideration is more complex especially for rare-event evaluation as advanced techniques are needed. In that matter, it was shown in Chapter 5 how random set theory enables to transform a hybrid reliability analysis into two standard reliability analyses. More specifically, random set functions were used as info-gap uncertainty models in order to evaluate the impact of different uncertainty representations on the robustness evaluation and, therefore, on the decision. An IG value of information metric was proposed to quantify this impact. The results show that the choice of an uncertainty representation may have a great influence on the robustness curves. This paradoxically confirms the interest in conducting robustness evaluations at the same time as it shows that the robustness evaluation itself is subject to the choice of uncertainty representation.

The application of the IG framework on reliability QoIs was supported by two real and complementary industrial use cases. First, IG was applied in Chapter 6 to small failure probability estimations assessing the reliability of penstocks. In this application, the rareness of the conditional failure event and the complex geometrical shape of the failure domain challenged the

estimation of failure probabilities and, consequently, its robustness assessment. As the application of IG implies global optimization over the failure probability, its estimator must be efficient all over the IG uncertainty space. In that matter, the line sampling technique was investigated. The original binary roots search problem was expressed considering three equivalent formulations to which algorithms were proposed. Finally, the robustness evaluation was accelerated by combining two artificial neural networks trained in an augmented space composed of the standard and the IG uncertainty spaces. The ANNs proved their efficiency in assessing the existence and predicting the values of the line sampling roots for any sampled line and for any perturbed distribution parameters. Precise robustness curves were therefore obtained at a reasonable computational time.

The second application of IG described in Chapter 7 was related to reliability assessments on a nuclear accidental scenario. As opposed to the reliability of penstocks, the challenge for estimating the involved QoIs does not lie in the rareness and complexity of the event but directly in the time needed for computing the variable of interest. Hence, only a limited amount of inputs-output realizations had to be considered for the entire IG analysis. First, two original IG uncertainty models were proposed: one based on perturbations in the unifying standard normal space and the other one based on a Dempster-Shafer discretization of the nominal cdfs. They both enable a comparable interpretation of the IG horizon of uncertainty but require different numerical procedures for evaluating worst performances. Finally, two techniques based on limited sets of realizations were employed for estimating the QoIs; one used the reverse importance sampling trick and the other one substituted the computer code with artifical neural networks. The robustness curves on the quantile and the superquantile obtained from both methods were compared. While the ANN-based robustness curves appear to be smooth and coherent, the RIS ones seem hardly interpretable on the superquantile and limited to low horizons of uncertainty and to very small dimensions (up to 2) of uncertain variables on the quantile.

In this thesis, IG was applied in many different ways for evaluating the robustness of reliability assessments. The safety-related performance functions went from very small failure probabilities to 95%-order quantiles and 75%-order superquantiles. The IG uncertainty models also took various forms, namely based on random set functions, parametric p-box in the physical space, parametric p-box in the standard normal space and free p-box from a Dempster-Shafer discretization. Many numerical techniques were used to facilitate the IG application. Artificial neural networks were implemented either to directly substitute the computer model or during an intermediary step of failure probability estimations. Re-estimation techniques were also considered with weighted importance sampling and reverse importance sampling. This variety of mathematical concepts only goes to show the modularity of the IG framework and how its numerical implementation is conditioned to the considered use case. Finally, the expansion of the general numerical toolbox offered from the literature in various relevant scientific fields, such as advanced QoIs estimation techniques, efficient optimization algorithms, sensitivity analysis, metamodels or high performance computing, makes the application of IG on reliability assessments more and more feasible.

However, the numerous scientific fields involved in the application of IG on reliability estimates also means that this thesis alone does not suffice to cover all the different paths that could be explored. A few of them, that seem particularly relevant in the author's view, are listed hereafter.

Perspectives

Placing IG within other metrics.

The original features that distinguish IG to other frameworks were already discussed. However, a deeper comparison, both theoretically and numerically, would provide better insight into the similarities and dissimilarities of IG with other metrics in the context of reliability-based decision making. In particular, the notion of VoI in reliability studies (Straub et al., 2022; Alibrandi et al., 2022) and the notion of reliability-oriented sensitivity under epistemic uncertainty (Chabridon et al., 2018; Schöbi and Sudret, 2019; Sarazin et al., 2021) are gaining much interest. An interesting study would be to analyze when these different frameworks lead to the same conclusions, or, on the contrary, diverge.

Taking into account the dependency structure on the inputs.

The potential presence of dependency was mostly omitted in this thesis, although representing a fundamental topic. In the context of hybrid reliability, dependency can be present either between random variables, between epistemic variables or between both. Note that the use of convex models in IG is a first way to deal with correlation between the uncertain variables. The random set framework, as shown in (Alvarez et al., 2018) and shortly in Appendix C, enables to represent the three dependency cases through the use of copulas. However, it seems that more work is still needed to better interpret these dependency structures. Another related interesting topic to pursue would be to apply IG uncertainty models directly on the dependency structure as it is often not well known in real engineering studies. A first application can be found in Hemez and Ben-Haïm (2004). The use of imprecise copulas can also be found in Zhang and Shields (2020).

Investigating the application of IG on model errors.

Both applications of IG to real industrial reliability studies present in this thesis focused on uncertainty affecting input variables and assumed a deterministic model to represent the relation between the inputs and the variable of interest. However, as it was briefly illustrated in Chapter 4, model errors can actually by more damaging to the reliability esimation than errors on the input variables. The choice of models often relies on hypotheses both on the real physical behavior and on the equations resolutions. Therefore, it would be interesting to analyze how the modularity of IG uncertainty models may be of use in that matter. Some first applications can be found (Atamturktur et al., 2015) in the context of model calibration and in (Ben-Haïm and Hemez, 2020) where IG is applied to an appriximation model used to solve partial differential equations.

Investigating the contribution of sensitivity analysis to compute robustness curves.

Although representing a very mature and important field of the general UQ framework, sensitivity analysis was not the object of this thesis (except through VoI metrics). The different objectives involved in sensitivity and IG immunity analyses were briefly discussed in Chapter 4. However, it seems that sensitivity analysis could be of great help when conducting IG robustness evaluations in two main aspects:

1. Identifying non-influential uncertain variables in order to reduce both the reliability problem dimension and the IG uncertainty model dimension and to ease some numerical techniques such as the construction of metamodels;

2. Guiding the search of the worst performance value in each uncertainty space.

A large panel of sensitivity metrics is available in the literature both for SAMO and ROSA purposes. This field is also gaining interest in the context of imprecise probabilities such as in Schöbi

and Sudret (2019) where imprecise Sobol indices are defined. It seems therefore interesting to investigate to what extent these metrics could be of use, especially as some can be obtained together with the QoI estimation (Valdebenito et al., 2018; Zhang et al., 2020)

Combining adaptive numerical procedures between optimization algorithms and approximation techniques.

The performance of the numerical scheme involved in the application of IG to reliability quantities depends on three main components that are connected: the successive optimization problems, the potential need for a metamodel and the QoI estimator. The nested iterative nature of IG uncertainty models together with the specific metric of interest (a worst performance) makes the IG framework very prone to the use of adaptive techniques. The optimization process at a given horizon of uncertainty should use the results from the previous horizons of uncertainty. One could perform the optimizations considering increasing horizons of uncertainty by only searching in the added uncertainty space. One could also perform optimization in the largest uncertainty space first which means that the contained uncertainty spaces (for decreasing horizons of uncertainty) have already been partially explored. The same idea could also be investigated for the estimation of failure probabilities. The fact that the succesive maximum failure probabilities are by definition higher than the nominal failure probability means that the "hardest" (i.e. rarest event) estimation has already been performed. Finally, adaptive metamodels would also be of interest as better predictions are needed in specific zones of the uncertainty space than in others (e.g. values around the penalizing LSSs for failure probabilities and extreme values for extreme quantiles). All of these considerations treated in a joint framework could considerably improve the estimation of robustness curves.

Extending IG's paradigm to less conservative robustness assessments.

The context of deep uncertainty in which the IG framework places itself leads to considering non-probabilistic uncertainty models and, consequently, worst and best performances. As such, it clearly quantifies the notion of immunity. From another angle, the analysis may seem overconservative in some cases (e.g. high number of uncertain variables, conservatism already included in other forms, availability of some information). In this case, it would seem interesting to keep the notion of horizon of uncertainty but to investigate other metrics than the extreme performances such as quantiles of different orders. This implies a probabilistic representation of the epistemic variables. When the performance function is a failure probability and the epistemic variables are distribution parameters, the Bayesian hierarchical model is retrieved such that the failure probability is a random variable itself. This context was particularly studied in (Chabridon, 2018) for efficiently estimating predictive failure probabilities (i.e. the expectation of the failure probability) and could be extended with the notion of horizon of uncertainty.

Improving the probability of failure estimators.

This perspective is general and not specific to the application of the IG method. However, as it was seen in Chapter 6, the performance of the reliability estimator plays an important role in the precision of the robustness curve and in the cumulated computational time. Even a small reduction of the unitary computational time can lead to a non-negligible gain at the end of the IG process.

Bibliography

Ajenjo, A., E. Ardillon, V. Chabridon, B. Iooss, S. Cogan, and E. Sadoulet-Reboul (2022). "An info-gap framework for robustness assessment of epistemic uncertainty models in hybrid structural reliability analysis". In: *Structural Safety* 96, p. 102196.

Alefeld, G.E., F.A. Potra, and Y. Shi (1995). "Algorithm 748: enclosing zeros of continuous functions". In: *ACM Transactions on Mathematical Software* 21, pp. 327–344.

Alibrandi, U., L.V. Andersen, and E. Zio (2022). "Informational probabilistic sensitivity analysis and active learning surrogate modelling". In: *Probabilistic Engineering Mechanics*, p. 103359.

Alvarez, D.A. (2006). "On the calculation of the bounds of probability of events using infinite random sets". In: *International Journal of Approximate Reasoning* 43, pp. 241–267.

Alvarez, D.A. and J.E. Hurtado (2014). "An efficient method for the estimation of structural reliability intervals with random sets, dependence modeling and uncertain inputs". In: *Computers and Structures* 142, pp. 54–63.

Alvarez, D.A., J.E. Hurtado, and J. Ramírez (2017). "Tighter bounds on the probability of failure than those provided by random set theory". In: *Computers and Structures* 189, pp. 101–113.

Alvarez, D.A., F. Uribe, and J.E. Hurtado (2018). "Estimation of the lower and upper bounds on the probability of failure using subset simulation and random set theory". In: *Mechanical Systems and Signal Processing* 100, pp. 782–801.

Ardillon, E., P. Bryla, and A. Dumas (2018). "Probabilistic optimization of margins for plastic collapse in the mechanical integrity diagnoses of penstocks". In: *Congrès Lambda Mu 21 "Maîtrise des risques et transformation numérique: opportunités et menaces"*. Reims, France.

— (2022). "Penstock reliability assessments: some results and developments". In: *Proc. of the 13th International Conference on Structural Safety and Reliability (ICOSSAR'22)*. Shanghai, China.

Atamturktur, S., Z. Liu, S. Cogan, and H. Juang (2015). "Calibration of imprecise and inaccurate numerical models considering fidelity and robustness: a multi-objective optimization-based approach". In: *Structural and Multidisciplinary Optimization* 51, pp. 659–671.

Au, S.-K. and J. L. Beck (2001). "Estimation of small failure probabilities in high dimensions by subset simulation". In: *Probabilistic Engineering Mechanics* 16, pp. 263–277.

Au, S.-K., J. Ching, and J. L. Beck (2007). "Application of subset simulation methods to reliability benchmark problems". In: *Structural Safety* 29, pp. 183–193.

Baccou, J. et al. (2019). "Development of good practice guidance for quantification of thermal-hydraulic code model input uncertainty". In: *Nuclear Engineering and Design* 354, p. 110173.

Balesdent, M., J. Morio, and L. Brevault (2016). "Rare event probability estimation in the presence of epistemic uncertainty on input probability distribution parameters". In: *Methodology and Computing in Applied Probability* 18, pp. 197–216.

Baudin, M., A. Dutfoy, B. Iooss, and A.L. Popelin (2017). "OpenTURNS: An industrial software for uncertainty quantification in simulation". In: *Handbook of Uncertainty Quantification*. Ed. by R. Ghanem, D. Higdon, and H. Owhadi. Springer, pp. 2001–2038.

Baudrit, C. and D. Dubois (2006). "Joint propagation and exploitation of probabilistic and possibilistic information in risk assessment". In: *IEEE Transactions on Fuzzy Systems* 14, pp. 593–608.

Bect, J., L. Li, and E. Vazquez (2017). "Bayesian Subset Simulation". In: *SIAM/ASA Journal of Uncertainty Quantification* 5, pp. 762–786.

Beer, M., S. Ferson, and V. Kreinovich (2013). "Imprecise probabilities in engineering analyses". In: *Mechanical Systems and Signal Processing* 37, pp. 4–29.

Ben-Haïm, Y. (2004). "Uncertainty, probability and information-gaps". In: *Reliability Engineering and System Safety* 85, pp. 249–266.

— (2006). *Info-Gap Decision Theory: Decisions under Severe Uncertainty*. Academic Press.

Ben-Haïm, Y. and I. Elishakoff (1990). *Convex Models of Uncertainties in Applied Mechanics*. Elsevier Science Publisher.

Ben-Haïm, Y. and F. Hemez (2020). "Richardson extrapolation: an info-gap analysis of numerical uncertainty". In: *Journal of Verification, Validation and Uncertainty Quantification* 5, p. 021004.

Ben-Haïm, Y. and M. Smithson (2018). "Data-based prediction under uncertainty: CDF-quantile distributions and info-gap robustness". In: *Journal of Mathematical Psychology* 87, pp. 11–30.

Ben-Haïm, Y. (2012). "Why risk analysis is difficult, and some thoughts on how to proceed". In: *Risk Analysis* 32, pp. 1638–1646.

Beresford-Smith, B. and C.J. Thompson (2007). "Managing credit risk with info-gap uncertainty". In: *Journal of Risk Finance* 8, pp. 24–34.

Bjerager, P. (1988). "Probability integration by directional simulation". In: *Journal of Engineering Mechanics* 114, pp. 1288–1302.

Blatman, G. (2009). "Adaptive sparse polynomial chaos expansionsfor uncertainty propagation and sensitivity analysis". PhD thesis. Université Blaise Pascal – Clermont II.

Bourinet, J.-M. (2016). "Rare-event probability estimation with adaptive support vector regression surrogates". In: *Reliability Engineering and System Safety* 150, pp. 210–221.

Bourinet, J.-M., F. Deheeger, and M. Lemaire (2011). "Assessing small failure probabilities by combined subset simulation and support vector machines". In: *Structural Safety* 33, pp. 343–353.

Breitung, K. (1984). "Asymptotic Approximations for multinormal integrals". In: *Journal of Engineering Mechanics* 110, pp. 357–366.

Bryla, P., E. Ardillon, and A. Dumas (2020). "Méthodes probabilistes appliquées à l'évaluation de l'intégrité des conduites forcées". In: *Congrès Lambda Mu 22 "Les risques au cœur des transitions"*. Le Havre, France.

BS7910 (2015). "Guide to methods for assessing the acceptability of flaws in metallic structures". In: *British Standard Institute*.

Bucklew, J. A. (2004). *Intoduction to Rare Event Simulation*. Springer Series in Statistics. Springer-Verlag New York, Inc.

Buffe, F., E. Pillet, S. Cogan, and M. Guedri (2011). "Robust optimization of a spacecraft structure". In: *Proc. of the 12th European Conference on Spacecraft Structures, Materials and Mechanical Testing*.

Chabridon, V. (2018). "Reliability-oriented sensitivity analysis under probabilistic model uncertainty". PhD thesis. University Clermont Auvergne.

Chabridon, V., M. Balesdent, J-M Bourinet, J. Morio, and N. Gayton (2017). "Evaluation of failure probability under parameter epistemic uncertainty: application to aerospace system reliability assessment". In: *Aerospace Science and Technology* 69, pp. 526–537.

Chabridon, V., M. Balesdent, J.-M. Bourinet, J. Morio, and N. Gayton (2018). "Reliability-based sensitivity estimators of rare event probability in the presence of distribution parameter uncertainty Author links open overlay panel". In: *Reliability Engineering and System Safety* 178, pp. 164–178.

Chojaczyk, A.A., A.P. Teixeira, L.C. Neves, J.B. Cardoso, and C. Guedes Soares (2015). "Review and application of Artificial Neural Netorks models in reliability analysis of steel structures". In: *Reliability Engineering and System Safety* 12, pp. 78–89.

D'auria, F., A. Bousbia-Salah, A. Petruzzi, and A. Del Nevo (2006). "State of the art in using best estimate calculation tools in nuclear technology". In: *Nuclear Engineering and Technology* 38, pp. 11–32.

D'auria, F., C. Camargo, and O. Mazzantini (2012). "The Best Estimate Plus Uncertainty (BEPU) approach in licensing of current nuclear reactors". In: *Nuclear Engineering and Design* 248, pp. 317–328.

De Angelis, M., E. Patelli, and M. Beer (2015). "Advanced Line Sampling for efficient robust reliability analysis". In: *Structural Safety* 52, pp. 170–182.

De Rocquigny, E., N. Devictor, and S. Tarantola (2008). *Uncertainty in industrial practice: a guide to quantitative uncertainty management*. Wiley.

Deheeger, F. (2008). "Couplage mécano fiabiliste : 2 SMART - méthodologie d'apprentissage stochastique en fiabilité". (in French). PhD thesis. Université Blaise Pascal – Clermont II.

Dempster, A. P. (1967). "Upper and lower probabilities induced by a multivalued mapping". In: *The Annals of Mathematical Statistics* 38, pp. 325–339.

Der Kiureghian, A. and T. Dakessian (1998). "Multiple design points in first and second-order reliability". In: *Structural Safety* 20, pp. 37–49.

Der Kiureghian, A. and M. De Stefano (1991). "Efficient Algorithm for Second-Order Reliability Analysis". In: *Journal of Engineering Mechanics ASCE* 117, pp. 2904–2923.

Der Kiureghian, A. and O. Ditlevsen (2009). "Aleatory or epistemic? Does it matter?" In: *Structural Safety* 31, pp. 105–112.

Dong, W. and H.C. Shah (1987). "Vertex method for computing functions of fuzzy variables". In: *Fuzzy Sets and Systems* 24, pp. 65–78.

Du, X. (2006). "Uncertainty analysis with probability and evidence theories". In: *Proc. of the ASME 2006 International Design Engineering Technical Conferences and Computers and Information in Engineering Conference. Volume 1: 32nd Design Automation Conference, Parts A and B*. USA.

Dubois, D. and H. Prade (1980). *Fuzzy Sets and Systems: Theory and Applications*. Academic Press.

Faes, M.G.R., M. Daub, S. Marelli, E. Patelli, and M. Beer (2021). "Engineering analysis with probability boxes: A review on computational methods". In: *Structural Safety* 93, p. 102092.

Fang, K.T, R. Li, and A. Sudjianto (2005). *Design and modeling for computer experiments*. Computer Science and Data Analysis Series. Chapman and Hall.

Ferson, S. and W.T. Tucker (2006). "Sensitivity analysis using probability bounding". In: *Reliability Engineering and System Safety* 91, pp. 1435–1442.

Finkel, D.E. (2003). *DIRECT optimization algorithm user guide*. Tech. rep. Center for Research in Scientific Computation, North Carolina State University.

Fox, C.R. and G. Ülkümen (2011). "Distinguishing two dimensions of uncertainty". In: *Perspectives on Thinking, Judging, and Decision Making.* Ed. by W. Brun, G. Keren, G. Kirkeboen, and H. Montgomery. Oslo: Universitetsforlaget. Chap. 17, pp. 21–35.

Gauchy, C., J. Stenger, R. Sueur, and B. Iooss (2022). "An information geometry approach to robustness analysis for the uncertainty quantification of computer codes". In: *Technometrics* 64, pp. 80–91.

Geffraye, G., O. Antoni, M. Farvacque, D. Kadri, G. Lavialle, B. Rameau, and A. Ruby (2011). "CATHARE 2 V2.5_2: A single version for various applications". In: *Nuclear Engineering and Design* 241, pp. 4456–4463.

Giuliani, M. and A. Castelletti (2016). "Is robustness really robust? How different definitions of robustness impact decision-making under climite change". In: *Climate Change* 135, pp. 409–424.

Göhler, S.M., T. Eifler, and T.J. Howard (2016). "Robustness metrics: consolidating the multiple approaches to quantify robustness". In: *Journal of Mechanical Design* 138, p. 111407.

Hacking, I. (1975). *The emergence of probability: A philosophical study of early ideas about probability, induction and statistical inference*. Cambridge University Press.

Hall, J.W., J.L. Lempert, K. Keller, A. Hackbarth, C. Mijere, and D.J. McInerney (2012). "Robust climate policies under uncertainty: a comparison of robust decision making and info-gap methods". In: *Risk Analysis* 32, pp. 1657–1672.

Hasofer, A. M. and N. C. Lind (1974). "Exact and invariant second-moment code format". In: *Journal of the Engineering Mechanics Division ASCE* 100, pp. 111–121.

Hastings, W. K. (1970). "Monte Carlo sampling methods using Markov chains and their applications". In: *Biometrika* 57, pp. 97–109.

Hayes, K.R., S.C. Barry, G.R. Hosack, and W.P. Gareth (2013). "Severe uncertainty and info-gap decision theory". In: *Methods in Ecology and Evolution* 4, pp. 601–611.

Hecht-Nielsen, N. (1989). "Theory of the backpropagation neural network". In: *International Joint Conference on Neural Networks, IJCNN*.

Hemez, F.M. and Y. Ben-Haïm (2004). "Info-gap robustness for the correlation of tests and simulations of a non-linear transient". In: *Mechanical Systems and Signal Processing* 18, pp. 1443–1467.

Hesterberg, T. C. (1996). "Estimates and confidence intervals for importance sampling Sensitivity Analysis". In: *Mathematical and Computer Modelling* 23, pp. 79–85.

Hohenbichler, M. and R. Rackwitz (1988). "Improvement of second-order reliability estimates by importance sampling". In: *Journal of engineering mechanics* 114, pp. 2195–2199.

Huang, X., J. Chen, and H. Zhu (2016). "Assessing small failure probabilities by AK–SS: An active learning method combining Kriging and Subset Simulation". In: *Structural Safety* 59, pp. 86–95.

Il Idrissi, M., N. Bousquet, F. Gamboa, B. Iooss, and J-M. Loubès (2022). "Quantile-constrained Wasserstein projections for robust interpretability analyses of numerical and machine learning models". In: *Preprint*.

Iooss, B. and L. Le Gratiet (2019). "Uncertainty and sensitivity analysis of functional risk curves based on Gaussian processes". In: *Reliability Engineering and System Safety* 187, pp. 58–66.

Iooss, B. and A. Marrel (2019). "Advanced methodology for uncertainty propagation in computer experiments with large number of inputs". In: *Nuclear Technology* 205, pp. 1588–1606.

Iooss, B., V. Verges, and V. Larget (2022). "BEPU robustness analysis via perturbed-law based sensitivity indices". In: *Proceedings of the Institution of Mechanical Engineers, Part O: Journal of Risk and Reliability* 236, pp. 855–865.

Ishigami, T. and T. Homma (1990). "An importance quantification technique in uncertainty analysis for computer models". In: *First International Symposium on Uncertainty Modeling and Analysis*, pp. 398–403.

Jaboviste, K., E. Sadoulet-Reboul, N. Peyret, C. Arnould, E. Collard, and G. Chevallier (2019). "On the compromise between performance and robustness for viscoelastic damped structures". In: *Mechanical Systems and Signal Processing* 119, pp. 65–80.

Jain, A.K., J. Mao, and K.M. Mohiuddin (1996). "Artificial neural networks: a tutorial". In: *Computer* 29, pp. 31–44.

Jiang, C., Z. Zhang, X. Han, and J. Liu (2013). "A novel evidence-based reliability analysis method for structures with epistemic uncertainty". In: *Computers and Structures* 129, pp. 1–12.

Jiang, C., Q. F. Zhang, X. Han, and Y. H. Qian (2014). "An non-probabilistic structural reliability analysis method based on a multidimensional parallelepiped convex model". In: *Acta Mechanica* 225, pp. 383–395.

Jones, D.R. and J.R.R.A. Martins (2021). "The DIRECT algorithm: 25 years later". In: *Journal of Global Optimization* 79, pp. 521–566.

Jones, D.R., C.D. Perttunen, and B.E. Stuckman (1993). "Lipschitzian optimization without the Lipschitz constant". In: *Journal of Optimization Theory and Applications* 79, pp. 157–181.

Kang, Z. and Y. Luo (2010). "Reliability-based structural optimization with probability and convex set hybrid models". In: *Structural and Multidisciplinary Optimization* 42, pp. 89–102.

Kang, Z. and W. Zhang (2016). "Construction and application of an ellipsoidal convex model using a semi-definite programming formulation from measured data". In: *Computer Methods in Applied Mechanics and Engineering* 300, pp. 461–489.

Kanno, Y., S. Fujita, and Y. Ben-Haïm (2017). "Structural design for earthquake resilience: Info-gap management of uncertainty". In: *Structural Safety* 69, pp. 23–33.

Knight, F.H. (1921). *Risk, Uncertainty and Profit*. Hart, Chaffner and Marx, New York.

Knoke, T. (2008). "Mixed forests and finance - Methodological approaches". In: *Ecological Economics* 65, pp. 590–601.

Koutsourelakis, P. S. (2004). "Reliability of structures in high dimensions. Part II. Theoretical validation". In: *Probabilistic Engineering Mechanics* 19, pp. 419–423.

Koutsourelakis, P. S., H. J. Pradlwarter, and G. I. Schuëller (2004). "Reliability of structures in high dimensions, Part I: algorithms and applications". In: *Probabilistic Engineering Mechanics* 19, pp. 409–417.

Kuczkowiak, S. (2014). "Modèle hybride incertain pour le calcul de réponse en fonctionnement d'un alternateur". PhD thesis. Université de Franche-Comté.

Labopin-Richard, T., F. Gamboa, A. Garivier, and B. Iooss (2016). "Bregman superquantiles. Estimation methods and applications". In: *Dependence Modeling* 4, pp. 76–108.

Lebrun, R. (2013). "Contributions à la modélisation de la dépendance stochastique". (in English). PhD thesis. Université Paris-Diderot – Paris VII.

Lemaire, M., A. Chateauneuf, and J.-C. Mitteau (2009). *Structural Reliability*. ISTE Ltd & John Wiley & Sons, Inc.

Lemaître, P., E. Sergienko, A. Arnaud, N. Bousquet, F. Gamboa, and B. Iooss (2015). "Density modification-based reliability sensitivity analysis". In: *Journal of Statistical Computation and Simulation* 85, pp. 1200–1223.

Lempert, R.J. and M.T. Collins (2007). "Managing the risk of uncertain threshold responses: comparison of robust, optimum, and precautionary approaches". In: *Risk Analysis* 27, pp. 1009–1026.

Li, L. (2012). "Sequential design of experiments to estimate a probability of failure". PhD thesis. Supélec.

Liu, J.S. (2001). *Monte Carlo Strategies in Scientific Computing*. Springer Series in Statistics. Springer New York.

Liu, T.J., C.H. Lee, and Y.S. Way (1997). "IIST and LSTF counterpart test on PWR station blackout transient". In: *Nuclear Engineering and Design* 167, pp. 357–373.

Liu, W., Z. Wang, X. Liu, N. Zeng, Y. Liu, and F.E. Alsaadi (2017). "A survey of deep neural network architectures and their applications". In: *Neurocomputing* 234, pp. 11–26.

Liu, X. and I. Elishakoff (2020). "A combined Importance Sampling and active learning Kriging reliability method for small failure probability with random and correlated interval variables". In: *Structural Safety* 82, p. 101875.

Luo, Y.J., Z. Kang, Z. Luo, and L. Alex (2008). "Continuum topology optimization with non-probabilistic reliability constraints based on multi-ellipsoid convex model". In: *Structural and Multidisciplinary Optimization* 39, pp. 297–310.

Marrel, A. and V. Chabridon (2021). "Statistical developments for target and conditional sensitivity analysis: Application on safety studies for nuclear reactor". In: *Reliability Engineering and System Safety* 214, p. 107711.

Matrosov, E.S., A.M. Woods, and J.J. Harou (2013). "Robust decision making and info-gap decision theory for water resource system planning". In: *Journal of Hydrology* 494, pp. 43–58.

Maugan, F.K. (2017). "Conception robuste de structure spatiale en présence de méconnaissance de modèle". PhD thesis. Université de Franche-Comté.

Mazgaj, P., J.-L. Vacher, and S. Carnevali (2016). "Comparison of CATHARE results with theexperimental results of cold leg intermediate break LOCA obtained during ROSA-2/LSTFtest 7". In: *EPJ Nuclear Sciences and Technology* 2.

McKay, M. D., R. J. Beckman, and W.J. Conover (2000). "A comparison of three methods for selecting values of input variables in the analysis of output from a computer code". In: *Technometrics* 42, pp. 55–61.

McPhail, C., H.R. Maier, J.H. Kwakkel, M. Giuliani, A. Castelletti, and S. Westra (2018). "Robustness metrics: how are they calculated, when should they be used and why do they give different results?" In: *Earth's Future* 6, pp. 169–191.

Melchers, R. E. (1989). "Importance sampling in structural systems". In: *Structural Safety* 6, pp. 3–10.

Metropolis, N. and S. Ulam (1949). "The Monte Carlo Method". In: *Journal of the American Statistical Association* 44, pp. 335–341.

Metropolis, N., A. W. Rosenbluth, M. N. Rosenbluth, and A. H. Teller (1953). "Equation of state calculations by fast computing machines". In: *The Journal of Chemical Physics* 21, pp. 1087–1092.

Molchanov, I. (2005). *Theory of Random Sets*. Springer.

Molga, M. and C. Smutnicki (2005). "Test functions for optimization needs". In: *Test functions for optimization needs*.

Morio, J. (2011). "Non-parametric adaptive importance sampling for the probability estimation of a launcher impact position". In: *Reliability Engineering and System Safety* 96, pp. 178–183.

Morio, J. and M. Balesdent (2015). *Estimation of Rare Event Probabilities in Complex Aerospace and Other Systems: A Practical Approach*. Woodhead Publishing, Elsevier.

Nataf, A. (1962). "Détermination des distributions dont les marges sont données". In: *Comptes Rendus de l'Académie des Sciences* 225. (in French), pp. 42–43.

Nelsen, R. B. (2006). *An introduction to Copulas*. Second ed. Springer Series in Statistics. Springer-Verlag New York.

Neumann, J. von and O. Morgenstern (1953). *Theory of games and economic behavior*. Princeton University Press.

Ni, B. Y., C. Jiang, and X. Han (2016). "An improved multidimensional parallelepiped nonprobabilistic model for structural uncertainty analysis". In: *Applied Mathematical Modelling* 40, pp. 4727–4745.

Oberkampf, W. L. and C. J. Roy (2010). *Verification and Validation in Scientific Computing*. Cambridge University Press.

Owhadi, H., C. Scovel, T. J. Sullivan, M. McKerns, and M. Ortiz (2013). "Optimal Uncertainty Quantification". In: *SIAM Review* 55, pp. 271–345.

Papadopoulos, V., D.G. Giovanis, N.D. Lagaros, and M. Papadrakakis (2012). "Accelerated subset simulation with neural networks for reliability analysis". In: *Computer Methods in Applied Mechanics and Engineering* 223, pp. 70–80.

Papadrakakis, M. and N.D. Lagaros (2002). "Reliability-based structural optimization using neural networks and Monte Carlo simulation". In: *Computer Methods in Applied Mechanics and Engineering* 191, pp. 3491–3507.

Perrin, G. and G. Defaux (2019). "Efficient evaluation of reliability-Oriented sensitivity indices". In: *Journal of Scientific Computing* 79, pp. 1433–1455.

Prosek, A. and B. Mavko (2007). "The state-of-the-art theory and applications of best-estimate plus uncertainty methods". In: *Nuclear Technology* 158, pp. 69–79.

Rackwitz, R. and B. Fiessler (1978). "Structural reliability under combined random load sequences". In: *Computers and Structures* 9, pp. 489–494.

Roach, T., Z. Kapelan, R. Ledbetter, and M. Ledbetter (2016). "Comparison of robust optimization and info-gap methods for water resource management under deep uncertainty". In: *Journal of Water Resources Planning and Management* 142, p. 04016028.

Rollón De Pinedo, A. (2021). "Statistical Analysis of the results of numerical simulations of accidental situations in Pressurized Water Reactors". PhD thesis. Université Grenoble Alpes.

Rosenblatt, M. (1952). "Remarks on a Multivariate Transformation". In: *Annals of Mathematical Statistics* 23, pp. 470–472.

Rubinstein, R. Y. and D. P. Kroese (2004). *The Cross-Entropy Method. A unified approach to combinatorial optimization, Monte-Carlo simulation and machine learning*. Information Science and Statistics. Springer-Verlag New York.

Sarazin, G., J. Morio, A. Lagnoux, M. Balesdent, and L. Brevault (2021). "Reliability-oriented sensitivity analysis in presence of data-driven epistemic uncertainty". In: *Reliability Engineering and System Safety* 215, p. 107733.

Schöbi, R. and B. Sudret (2017). "Structural reliability analysis for p-boxes using multi-level meta-models". In: *Probabilistic Engineering Mechanics* 48, pp. 27–38.

— (2019). "Global sensitivity analysis in the context of imprecise probabilities (p-boxes) using sparse polynomial chaos expansions". In: *Reliability Engineering and System Safety* 187, pp. 129–141.

Shafer, G. (1976). *A Mathematic Theory of Evidence*. Princeton University Press.

Silverman, B. W. (1986). *Density Estimation for Statistics and Data Analysis*. Chapman and Hall.

Simon, H. (1959). "Theories of decision-making in economic and behavioral science". In: *American Economic Review* 49, pp. 253–283.

Sniedovich, M. (2010). "A bird's view of info-gap decision theory". In: *The Journal of Risk Finance* 11, pp. 268–283.

— (2012). "Fooled by Local Robustness". In: *Risk Analysis* 32, pp. 1630–1637.

Song, J., P. Wei, M.A. Valdebenito, and M. Beer (2021). "Active learning line sampling for rare event analysis". In: *Mechanical Systems and Signal Processing* 147, p. 107113.

Stenger, J., F. Gamboa, M. Keller, and B. Iooss (2020). "Optimal uncertainty quantification of a risk measurement from a thermal-hydraulic code using canonical moments". In: *International Journal of Uncertainty Quantification* 10, pp. 35–53.

Straub, D., M. Ehre, and I. Papaioannou (2022). "Decision-theoretic reliability sensitivity". In: *Reliability Engineering and System Safety* 221, p. 108215.

Sueur, R., N. Bousquet, B. Iooss, and J. Bect (2016). "Perturbed-law based sensitivity indices for sensitivity analysis in structural reliability". In: *Proc. of the 8th International Conference on Sensitivity Analysis of Model Output (SAMO 2016)*. Le Tampon, Réunion Island, France.

Sueur, R., B. Iooss, and T. Delage (2017). "Sensitivity analysis using perturbed-law based indices for quantiles and application to an industrial case". In: *Proc. of the 10th International Conference on Mathematical Methods in Reliability (MMR 2017)*. Grenoble, France.

Takewaki, I. and Y. Ben-Haïm (2005). "Info-gap robust design with load and model uncertainties". In: *Journal of Sound and Vibration* 288, pp. 551–570.

Takewaki, I., K. Fujita, K. Yamamoto, and H. Takabatake (2011). "Smart passive damper control for greater building earthquake resilience in sustainable cities". In: *Sustainable Cities and Society* 1, pp. 3–15.

Tao, F., Q. Qi, L. Wang, and A.Y.C. Nee (2019). "Digital twins and cyber–physical systems toward smart manufacturing and industry 4.0: correlation and comparison". In: *Engineering* 5, pp. 653–661.

Tonon, F. and A. Bernardini (2000). "A random set approach to the optimization of uncertain structures". In: *Computers and Structures* 68, pp. 583–600.

Tonon, F., A. Bernardini, and A. Mammino (2000a). "Determination of parameters range in rock engineering by means of Random Set Theory". In: *Reliability Engineering and System Safety* 70, pp. 241–261.

Tonon, F., A. Bernardini, and A. Mammino (2000b). "Reliability analysis of rock mass response by means of random set theory". In: *Reliability Engineering and System Safety* 70, pp. 263–282.

Tvedt, L. (1990). "Distribution of quadratic forms in normal space – application to structural reliability". In: *Journal of engineering mechanics* 116, pp. 1183–1197.

— (2005). "Proban – probabilistic analysis". In: *Structural Safety* 28, pp. 150–163.

Valdebenito, M. A., H. A. Jensen, H. B. Hernández, and L. Mehrez (2018). "Sensitivity estimation of failure probability applying line sampling". In: *Reliability Engineering and System Safety* 171, pp. 99–111.

Valdebenito, M.A., M. Beer, H.A. Jensen, J. Chen, and P. Wei (2020). "Fuzzy failure probability estimation applying intervening variables". In: *Structural Safety* 83, p. 101909.

Wald, A. (1950). *Statistical decision functions*. Wiley.

Wang, X., Z. Qiu, and I. Elishakoff (2008). "Non-probabilistic set-theoretic model for structural safety measure". In: *Acta Mechanica* 198, pp. 51–64.

Wasserman, L. (2004). *All of Statistics: A Concise Course in Statistical Inference*. Springer Texts in Statistics. Springer Science+Business Media.

Wilf, H.S. (1960). "Maximally Stable Numerical Integration". In: *Journal of the Society for Industrial and Applied Mathematics* 8, pp. 537–540.

Wilson, G. (2013). "Historical insights in the development of Best estimate Plus Uncertainty safety analysis". In: *Annals of Nuclear Energy* 52, pp. 2–9.

Xiao, M., J. Zhang, L. Gao, S. Lee, and A.T. Eshghi (2019). "An efficient Kriging-based subset simulation method for hybrid reliability analysis under random and interval variables with small failure probability". In: *Structural and Multidisciplinary Optimization* 59, pp. 2077–2092.

Yang, X., Y. Liu, Y. Gao, Y. Zhang, and Z. Gao (2015). "An active learning kriging model for hybrid reliability analysis with both random and interval variables". In: *Structural and Multidisciplinary Optimization* 51, pp. 1003–1016.

Yuan, X. (2013). "Local estimation of failure probability function by weighted approach". In: *Probabilistic Engineering Mechanics* 34, pp. 1–11.

Yuan, X., Z. Zhenxuan, and Z. Baoqiang (2020). "Augmented line sampling for approximation of failure probability function in reliability-based analysis". In: *Applied Mathematical Modelling* 80, pp. 895–910.

Yuan, X., S. Liu, M.A. Valdebenito, J. Gu, and M. Beer (2021). "Efficient procedure for failure probability function estimation in augmented space". In: *Structural Safety* 92, p. 102104.

Zadeh, L. A. (1967). "Fuzzy sets as a basis for a theory of possibility". In: *Fuzzy Sets and Systems* 1, pp. 3–28.

Zhang, H., R.L. Mullen, and R.L. Muhanna (2010). "Interval Monte Carlo methods for structural reliability". In: *Structural Safety* 32, pp. 183–190.

Zhang, J. and M. Shields (2020). "On the quantification and efficient propagation of imprecise probabilities with copula dependence". In: *International Journal of Approximate Reasoning* 122, pp. 24–46.

Zhang, J., M. Xiao, L. Gao, and J. Fu (2018). "A novel projection outline based active learning method and its combination with Kriging metamodel for hybrid reliability analysis with random and interval variables". In: *Computer Methods in Applied Mechanics and Engineering* 341, pp. 32–52.

Zhang, X., Z. Lu, W. Yun, K. Feng, and Y. Wang (2020). "Line sampling-based local and global reliability sensitivity analysis". In: *Structural and Multidisciplinary Optimization* 61, pp. 267–281.

Zhang, Y. and A. Der Kiureghian (1994). "Two improved algorithms for reliability analysis". In: *Reliability and Optimization of Structural Systems: Proceedings of the 6th IFIP WG 7.5 Conference*. Ed. by R. Rackwitz, G. Augusti, and A. Borri. Springer US, pp. 297–304.

Zhang, Z., C. Jiang, G.G. Wang, and X. Han (2014). "First and second order approximate reliability analysis methods using evidence theory". In: *Reliability Engineering and System Safety* 137, pp. 40–49.

Zheng, J., Z. Luo, C. Jiang, B. Ni, and J. Wu (2018). "Non-probabilistic reliability-based topology optimization with multidimensional parallelepiped convex model". In: *Structural and Multidisciplinary Optimization* 57, pp. 2205–2221.

Zhu, L.P., I. Elishakoff, and J.H. Starnes Jr. (1996). "Derivation of multi-dimensional ellipsoidal convex model for experimental data". In: *Mathematical and Computer Modelling* 24, pp. 103–114.

Zio, E. and N. Pedroni (2010). "An optimized Line Sampling method for the estimation of the failure probability of nuclear passive systems". In: *Reliability Engineering and System Safety* 12, pp. 1300–1313.

— (2013). *Literature review of methods for representing uncertainty, Cahiers de la Sécurité Industrielle, Report No. 2013-03*. Tech. rep. Foundation for an Industrial Safety Culture, Toulouse, France.

Ülkümen, G., C.R. Fox, and B.F. Malle (2016). "Two dimensions of subjective uncertainty: clues from natural language". In: *Journal of Experimental Psychology* 145, pp. 1280–1297.

APPENDIX A

Formulations of weighted importance sampling, augmented space integral and augmented line sampling

All three methods introduced in this appendix have in common the idea of using a single set of samples for estimating several failure probabilities at different values of uncertain distribution parameters. Therefore, their use is particularly relevant when applying the IG method. This appendix reviews their formulations and presents some first results on two toy cases. It will be denoted by $f_{\mathbf{X},\mathbf{Y}}(\mathbf{x},\mathbf{y}|\boldsymbol{\theta})$ the joint pdf which is the product (as considering independent random variables) of the pdf $f_{\mathbf{X}}(\mathbf{x})$ of certain random variables and the pdf $f_{\mathbf{Y}}(\mathbf{y}|\boldsymbol{\theta})$ of random variables conditional to uncertain distribution parameters $\boldsymbol{\theta}$.

Weighted Importance Sampling

In Yuan (2013), the objective is to use the failure probability result obtained at a specific value of the distribution parameters $\widetilde{\boldsymbol{\theta}}$ to estimate failure probabilities at different values $\boldsymbol{\theta}$ without having to generate new samples. This framework is referred to as the weighted importance sampling (WIS) approach.

The basic idea is similar to classical importance sampling and to reverse importance sampling used in Chapter 7. For any $\boldsymbol{\theta}$, the failure probability is expressed as follows:

$$P_{\mathrm{f}}(\boldsymbol{\theta}) = \int_{\mathbb{R}_{n_{\mathbf{X}}+n_{\mathbf{Y}}}} \mathbb{1}_{\mathcal{F}_{\mathbf{x},\mathbf{y}}}(\mathbf{x},\mathbf{y})\, f_{\mathbf{X},\mathbf{Y}}(\mathbf{x},\mathbf{y}|\boldsymbol{\theta})\, d\mathbf{x}d\mathbf{y} = \int_{\mathbb{R}_{n_{\mathbf{X}}+n_{\mathbf{Y}}}} \mathbb{1}_{\mathcal{F}_{\mathbf{x},\mathbf{y}}}(\mathbf{x},\mathbf{y})\, \frac{f_{\mathbf{X},\mathbf{Y}}(\mathbf{x},\mathbf{y}|\boldsymbol{\theta})}{H(\mathbf{x},\mathbf{y})} H(\mathbf{x},\mathbf{y}) d\mathbf{x}d\mathbf{y} \quad \text{(A.1)}$$

where $H(\mathbf{x},\mathbf{y})$ is the importance sampling instrumental pdf to be defined by the user. Eq. A.1 may be rewritten as an expectation under $H(\mathbf{x},\mathbf{y})$:

$$P_{\mathrm{f}}(\boldsymbol{\theta}) = \mathbb{E}_H\left[\mathbb{1}_{\mathcal{F}_{\mathbf{x},\mathbf{y}}}(\mathbf{x},\mathbf{y})\, \frac{f_{\mathbf{X},\mathbf{Y}}(\mathbf{x},\mathbf{y}|\boldsymbol{\theta})}{H(\mathbf{x},\mathbf{y})}\right] \quad \text{(A.2)}$$

which may be estimated by generating N_{WIS} samples $\left(\mathbf{x}^{(j)},\mathbf{y}^{(j)}\right)$ from $H(\mathbf{x},\mathbf{y})$ as follows:

$$P_{\mathrm{f}}(\boldsymbol{\theta}) = \frac{1}{N_{\mathrm{WIS}}} \sum_{j=1}^{N_{\mathrm{WIS}}} \mathbb{1}_{\mathcal{F}_{\mathbf{x},\mathbf{y}}}\left(\mathbf{x}^{(j)},\mathbf{y}^{(j)}\right) \frac{f\left(\mathbf{x}^{(j)},\mathbf{y}^{(j)}|\boldsymbol{\theta}\right)}{H\left(\mathbf{x}^{(j)},\mathbf{y}^{(j)}\right)}. \quad \text{(A.3)}$$

Therefore, it can be seen that, no matter the value of $\boldsymbol{\theta}$, the indicator function (which is generally expensive to evaluate as it involves the computer model) is calculated with the same samples $\left(\mathbf{x}^{(j)}, \mathbf{y}^{(j)}\right)$ generated from H which is chosen at a fixed value of $\boldsymbol{\theta}$. Only the conditional pdf $f\left(\mathbf{y}^{(j)}|\boldsymbol{\theta}\right)$ needs to be reevaluated for each $\boldsymbol{\theta}$.

The performance of the method highly depends on the choice of the instrumental pdf. Indeed, the estimation in Eq. A.3 is considered as a local approximation as a better convergence will be achieved for values of $\boldsymbol{\theta}$ that are representative of the instrumental pdf H. However, such framework is compatible with the info-gap robustness analysis for relatively small horizons of uncertainty h as maximum failure probabilities are searched for around a nominal value $\widetilde{\boldsymbol{\theta}}$.

Augmented Line Sampling

In the Augmented Line Sampling (ALS) approach introduced in Yuan et al. (2020), the idea is to reuse the n_{ALS} line sampling roots obtained from an instrumental distribution without having to search for them again at each value $\boldsymbol{\theta}$. The failure probability is again expressed first with Eq. A.1. The corresponding LS estimator thus becomes:

$$P_{\text{f}}\left(\boldsymbol{\theta}\right) = \frac{1}{n_{\text{ALS}}} \sum_{j=1}^{n_{\text{ALS}}} p_{\text{f}}^{(j)}\left(\boldsymbol{\theta}\right) \frac{f\left(\mathbf{x}^{(j)}, \mathbf{y}^{(j)}|\boldsymbol{\theta}\right)}{H\left(\mathbf{x}^{(j)}, \mathbf{y}^{(j)}\right)} \tag{A.4}$$

where $p_{\text{f}}^{(j)}\left(\boldsymbol{\theta}\right) = \Phi\left(-r^{(j)}\left(\boldsymbol{\theta}\right)\right)$ is the conditionnal failure probability calculated from the roots that depend on $\boldsymbol{\theta}$.

By denoting $\mathbf{u}^{*,(j)}$ the points that intersect the lines with the LSF in the standard normal space obtained through the isoprobabilistic transformation T_H where $\mathbf{X}, \mathbf{Y} \sim H\left(\mathbf{x}, \mathbf{y}\right)$, the intersection points in the physical space are obtained as $\left(\mathbf{x}^{*,(j)}, \mathbf{y}^{*,(j)}\right) = T_H^{-1}\left(\mathbf{u}^{*,(j)}\right)$. Then, by denoting $T_{\boldsymbol{\theta}}$ the isoprobabilistic transformation considering that $\mathbf{X}, \mathbf{Y} \sim f\left(\mathbf{x}, \mathbf{y}|\boldsymbol{\theta}\right)$, the new intersection points are obtained as $\mathbf{u}_{\boldsymbol{\theta}}^{*,(j)} = T_{\boldsymbol{\theta}}\left(\mathbf{x}^{*,(j)}, \mathbf{y}^{*,(j)}\right)$. Finally, the corresponding roots are simply obtained from the scalar product $r^{(j)}\left(\boldsymbol{\theta}\right) = \langle \mathbf{u}_{\boldsymbol{\theta}}^{*,(j)}, \boldsymbol{\alpha} \rangle$.

Augmented Space Integral

The objective of the work proposed in Yuan et al. (2021) is to estimate the conditional failure probability $P_{\text{f}}\left(\boldsymbol{\theta}\right)$ by considering an augmented space where the uncertain distribution parameters follow an instrumental distribution such that $\boldsymbol{\Theta} \sim h_{\boldsymbol{\Theta}}\left(\boldsymbol{\theta}\right)$. Indeed, by considering F the failure event in the augmented space formed of $(\mathbf{X}, \mathbf{Y}, \boldsymbol{\Theta})$, the failure probability given $\boldsymbol{\theta}$ writes:

$$P_{\text{f}}\left(\boldsymbol{\theta}\right) = \mathbb{P}\left(F|\boldsymbol{\Theta} = \boldsymbol{\theta}\right) = \frac{h_{\boldsymbol{\Theta}}\left(\boldsymbol{\theta}|F\right)\mathbb{P}\left(F\right)}{h_{\boldsymbol{\Theta}}\left(\boldsymbol{\theta}\right)} \tag{A.5}$$

where $\mathbb{P}\left(F\right)$ is the failure probability in the augmented space expressed as:

$$\mathbb{P}\left(F\right) = \int_{\mathbb{R}^{n_{\boldsymbol{\theta}}}} \int_{\mathbb{R}^{n_{\mathbf{X}}+n_{\mathbf{Y}}}} I_F\left(\mathbf{x}, \mathbf{y}\right) f\left(\mathbf{y}|\boldsymbol{\theta}\right) h\left(\boldsymbol{\theta}\right) f\left(\mathbf{x}\right) d\boldsymbol{\theta} d\mathbf{x} d\mathbf{y} \tag{A.6}$$

After mathematical derivations to which the reader is referred to Yuan et al. (2021), the conditional failure probability finally reads:

$$P_{\text{f}}\left(\boldsymbol{\theta}\right) = \frac{1}{h\left(\boldsymbol{\theta}\right)} \int_{\mathbb{R}^{n_{\mathbf{X}}+n_{\mathbf{Y}}}} \frac{I_F\left(\mathbf{x}, \mathbf{y}\right) f\left(\mathbf{y}|\boldsymbol{\theta}\right)}{\Delta\left(\mathbf{y}\right)} f\left(\mathbf{x}, \mathbf{y}\right) d\mathbf{x} d\mathbf{y} = \frac{1}{h\left(\boldsymbol{\theta}\right)} \mathbb{E}_f\left[\frac{I_F\left(\mathbf{x}, \mathbf{y}\right) f\left(\mathbf{y}|\boldsymbol{\theta}\right)}{\Delta\left(\mathbf{y}\right)}\right] \tag{A.7}$$

where:

$$\Delta(\mathbf{y}) = \int_{\mathbb{R}^{n_\theta}} f_{\mathbf{Y}}(\mathbf{y}|\boldsymbol{\theta})\, d\boldsymbol{\theta} = \mathbb{E}_{\boldsymbol{\Theta}}\left[\frac{f_{\mathbf{Y}}(\mathbf{y}|\boldsymbol{\theta})}{h_{\boldsymbol{\Theta}}(\boldsymbol{\theta})}\right]. \tag{A.8}$$

Eq. A.8 can be solved either with integral numerical solvers, by sampling or even analytically in some configurations. It is important to notice that attributing a probability distribution to $\boldsymbol{\theta}$ only represents a numerical trick and not an added hypothesis. However, the choice of the instrumental distribution $h_{\boldsymbol{\Theta}}$ has an impact on the performance of the estimator. A simple choice is to assign uniform distributions to $\boldsymbol{\Theta}$ considering relevant bounds w.r.t. the epistemic uncertainty and w.r.t. the study.

In Yuan et al. (2021), Eq. A.7 is adapted to the Monte Carlo, importance sampling and subset simulation techniques. In the following, only the importance sampling technique is considered. In this case, as the random vector $\mathbf{Y}$ is already conditionned to $\boldsymbol{\Theta}$, an instrumental density is considered on $\mathbf{X}$ such that $H(\mathbf{x},\mathbf{y}) = H(\mathbf{x})\, f(\mathbf{y}|\boldsymbol{\theta})$ which transforms the failure proability expression to:

$$P_f(\boldsymbol{\theta}) = \frac{1}{h(\boldsymbol{\theta})}\int_{\mathbb{R}^{n_\mathbf{X}+n_\mathbf{Y}}} \frac{I_F(\mathbf{x},\mathbf{y})\, f(\mathbf{y}|\boldsymbol{\theta})}{\Delta(\mathbf{y})}\frac{f(\mathbf{x})}{H(\mathbf{x})} H(\mathbf{x},\mathbf{y})\, d\mathbf{x}d\mathbf{y} = \frac{1}{h(\boldsymbol{\theta})}\mathbb{E}_H\left[\frac{I_F(\mathbf{x},\mathbf{y})\, f(\mathbf{y}|\boldsymbol{\theta})}{\Delta(\mathbf{y})}\frac{f(\mathbf{x})}{H(\mathbf{x})}\right]. \tag{A.9}$$

In practice, the instrumental density $H(\mathbf{x})$ can be chosen based on the design point $\mathbf{x}^*$ obtained at a fixed value of $\boldsymbol{\theta}$.

Application to a front axle

The proposed toy case, also used in Yuan et al. (2020) and in Yuan et al. (2021), corresponds to an automobile front axle represented as an I-beam profile as depicted in Figure A.1.

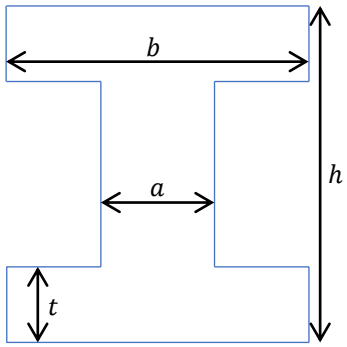

FIGURE A.1: I-beam profile of the automobile front axle.

The LSF is defined as:

$$g(\mathbf{x},\mathbf{y}) = \sigma_s - \sqrt{\frac{M}{W_x}^2 + \frac{T}{W_\rho}^2} \tag{A.10}$$

where $\sigma_s = 600$ Mpa is the yield stress, M is the bending moment, T is the torque and W_x and W_ρ are expressed as:

$$W_x = \frac{a(h-2t)^3}{6h} + \frac{b}{6h}\left[h^3 - (h-2t)^3\right] \tag{A.11}$$

and

$$W_\rho = 0.8bt^2 + 0.4\frac{a^3(h-2t)}{t}. \tag{A.12}$$

The characteristics of the six considered random variables are given in Table A.1 such that $\mathbf{X} = [M, T]^\top$ and $\mathbf{Y}(\boldsymbol{\theta}) = [a, t, b, h]^\top$. The nominal values of the uncertain means are set to $\widetilde{\boldsymbol{\theta}} = [13, 15, 65, 85]^\top$.

TABLE A.1: Input probabilistic modeling for the front axle.

Random variable	Distribution	Mean μ_{X_i}	Standard deviation σ_{X_i}
a (mm)	Normal	θ_a	0.65
t (mm)	Normal	θ_t	0.75
b (mm)	Normal	θ_b	3.25
h (mm)	Normal	θ_h	4.25
M (N.m)	Normal	3500	175
T (N.m)	Normal	3100	155

The three techniques, named WIS (Weighted Importance Sampling), ASI-IS (Augmented Space Integral with Importance Sampling) and ALS (Augmented Line Sampling), are used for estimating and comparing robustness curves with $\theta_i \in \left[\widetilde{\theta}_i(1-h), \widetilde{\theta}_i(1+h)\right]$ and $h \in [0, 0.1]$. WIS is applied by considering the instrumental pdf $H_{\text{WIS}}(\mathbf{x}, \mathbf{y}) = H_{\text{WIS}}(\mathbf{x}) H_{\text{WIS}}(\mathbf{y})$ composed of normal distributions centered around the design point $\mathbf{x}^*$ and $\mathbf{y}^*$ obtained from a FORM analysis at $\boldsymbol{\theta} = \widetilde{\boldsymbol{\theta}}$. The standard deviations are chosen as 10% of the design point values. ASI-IS is applied by attributing uniform distributions to $\boldsymbol{\theta}$ such that $\Theta_i \sim \mathcal{U}_{\Theta_i}\left(0.85\widetilde{\theta}_i, 1.15\widetilde{\theta}_i\right)$. The same importance sampling instrumental pdf as with WIS is used. The unique set of roots used for the application of ALS are the ones obtained for $\boldsymbol{\theta} = \widetilde{\boldsymbol{\theta}}$.

Figure A.2 presents the robustness curves (left) obtained using each method for $N = N_{\text{WIS}} = N_{\text{ASI-IS}} = N_{\text{ALS}} = \left\{1 \times 10^3, 5 \times 10^3, 20 \times 10^3\right\}$ and their relative error (right) w.r.t. the reference curve. The results are globally very precise even for $N = 1 \times 10^3$. However, it can be seen, especially with the WIS and ALS techniques, that the relative error becomes more important at higher horizons of uncertainty. This is less the case with the ASI-IS approach.

Application to a cantilever beam

The second toy case considers the same cantilever beam as in Chapter 7 where the LSF is based on the maximum Von Mises stress. The failure event is defined as the maximum Von Mises stress exceeding the yield strength set at $\sigma_y = 400$ MPa. The distributions parameters are given in Table A.2 with $\widetilde{\boldsymbol{\theta}} = [5, 42, 3, 3]^\top$. The same IG uncertainty models as in the previous toy case are used but the horizon of uncertainty goes up to 0.2. Therefore, the uniform distributions on the uncertain distribution parameters are now chosen as $\Theta_i \sim \mathcal{U}_{\Theta_i}\left(0.75\widetilde{\theta}_i, 1.25\widetilde{\theta}_i\right)$.

The same type of results as for the first toy case are presented in Figure A.3. In this case where the maximum horizon of uncertainty is twice as big as in the first toy case, the loss in precision with the increase of the horizon of uncertainty gets even more striking for all three techniques. Moreover, the ASI-IS approach brings poorer performances.

The two studied toy cases do not aim at ranking the three different techniques as their performances highly depend on their implementation, especially on the choices of instrumental distributions. Moreover, their performances also depend on the nominal performance of the failure probability estimator technique which itself depends on the studied case. However, these techniques seem very relevant to the application of IG on failure probabilities, especially when considering the lower values of the horizon of uncertainty.

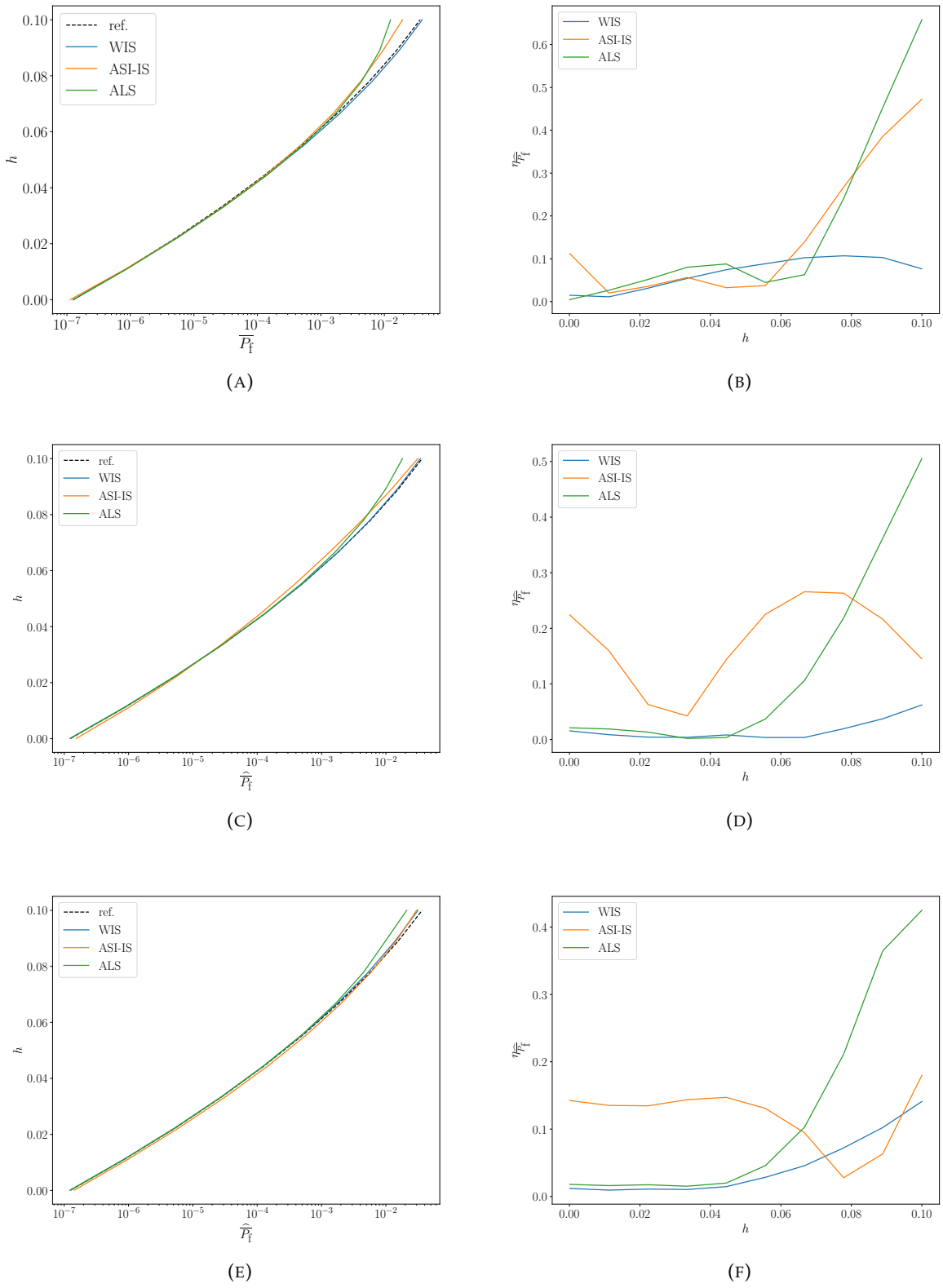

FIGURE A.2: Robustness curves (left) and relative erros (right) obtained from each approximation technique for $N = 1^3$ (top), $N = 5^3$ (middle) and $N = 20^3$ (bottom).

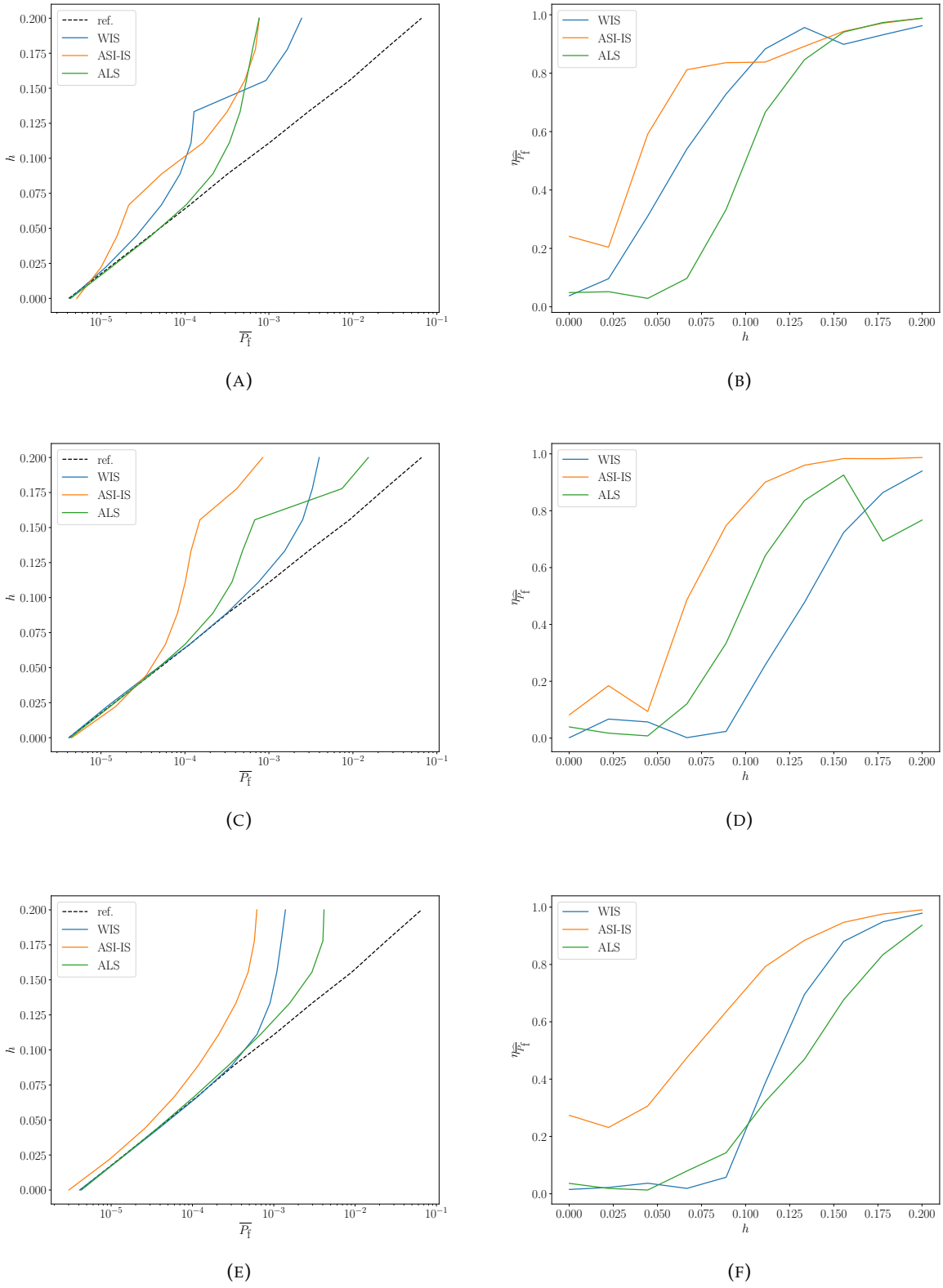

FIGURE A.3: Robustness curves (left) and relative erros (right) obtained from each approximation technique for $N = 1^3$ (top), $N = 5^3$ (middle) and $N = 20^3$ (bottom).

TABLE A.2: Input probabilistic modeling of $\mathbf{X}$.

Variable X_i	Distribution	param. 1	param. 2
$X_1 = P$ (kN)	Gumbel	$\beta = 12$	$\gamma = 1.2$
$X_2 = t$ (mm)	Normal	$\mu = \theta_1$	$\sigma = 0.25$
$X_3 = d$ (mm)	Normal	$\mu = \theta_2$	$\sigma = 2.1$
$X_4 = L_1$ (mm)	Uniform	$a = 115$	$b = 125$
$X_5 = L_2$ (mm)	Uniform	$a = 55$	$b = 65$
$X_6 = F_1$ (kN)	Normal	$\mu = \theta_3$	$\sigma = 300$
$X_7 = F_2$ (kN)	Normal	$\mu = \theta_4$	$\sigma = 300$
$X_8 = \theta_1$ (degrees)	Normal	$\mu = 5$	$\sigma = 1$
$X_9 = \theta_2$ (degrees)	Normal	$\mu = 10$	$\sigma = 2$
$X_10 = T$ (N.m)	Normal	$\mu = 90$	$\sigma = 9$

APPENDIX B

Search for the worst performances

The IG framework requires to search for a worst performance in each considered uncertainty space defined by the discretization of the horizon of uncertainty. There are multiple ways of finding these values and different techniques may be adapted and interchangeable during the process. Three main groups of techniques can be listed (see Chapter 4):

- the vertex method: the worst performance is supposed to be obtained at an unknown combination of extreme values of the uncertain parameters (vertices of the IG uncertainty space). This method requires 2^{n_e} evaluations where n_e is the number of uncertain parameters.
- the sampling method: random or selected samples from the uncertainty space are generated and evaluated. Then, the minimum or the maximum value is kept.
- the optimization method: an optimization algorithm, local or global, is used for efficiently reaching the minimum or the maximum value in the uncertainty space. This method is generally used when no hypothesis is made on the behavior of the QoI w.r.t. the uncertain parameters.

In this thesis, the optimization method was privileged mostly using the DIRECT algorithm available in the NLopt Python module. This choice was made in order to propose methodologies in the most penalizing IG framework, i.e. when strictly no hypothesis is considered. This appendix firstly describes how the DIRECT algorithm operates. Then, some numerical comparisons of the three mentionned searching techniques are analyzed on two toy cases.

DIRECT algorithm

The DIRECT algorithm was initially introduced in Jones et al. (1993) and its variants are well identified in Jones and Martins (2021). It is a deterministic optimization algorithm that only requires the bounds of the optimization space and a limit number of evaluations. After scaling the optimization space into the unit hypercube, the algorithm divides it into a series of smaller hyperrectangles. This process is illustrated in Figure B.1 where the maximum of the Ishigami function (see Eq. B.2) is searched for $x_1 \in [0,1]$ and $x_3 \in [0,1]$. The key point in the DIRECT algorithm, after performing the first iteration which is always the same, lies in the choice of the "potentially optimal" hyperrectangles to be divided into smaller hyperrectangles in which each center point is to be evalueted. This is performed based on Lipschitzian optimization. By denoting m the number of current hypperrectangles, $\mathbf{c_i}$ each corresponding center point and d_i the distance from $\mathbf{c_i}$ to its corresponding vertices, a hyperrectangle is said to be potentially

optimal if there exists some $K > 0$ such that (Jones and Martins, 2021):

$$f\left(\mathbf{c}_j\right) - Kd_j \leq f\left(\mathbf{c}_i\right) - Kd_i, \text{ for all } i = 1, \cdots, m \tag{B.1a}$$

$$f\left(\mathbf{c}_j\right) - Kd_j \leq f_{\min} - \epsilon \left|f_{\min}\right| \tag{B.1b}$$

where f is the objective function (to be minimized here), $f_{\min}$ the current minimum value and ϵ a small positive constant. In this sense, there may be several hyperrectangles that are potentially optimal during a same iteration. DIRECT presents several advantages and drawbacks. The main advantage is that it guarantees convergence to the global minimum for continuous functions without the need of gradient calculations. The main drawback is that, although the global zone containing the solution is quickly identified, its local refinement requires rather a lot of evaluations as other global searches are performed at the same time. It is often suggested to use DIRECT as a first global search and then a local optimizer in the identified zones from DIRECT.

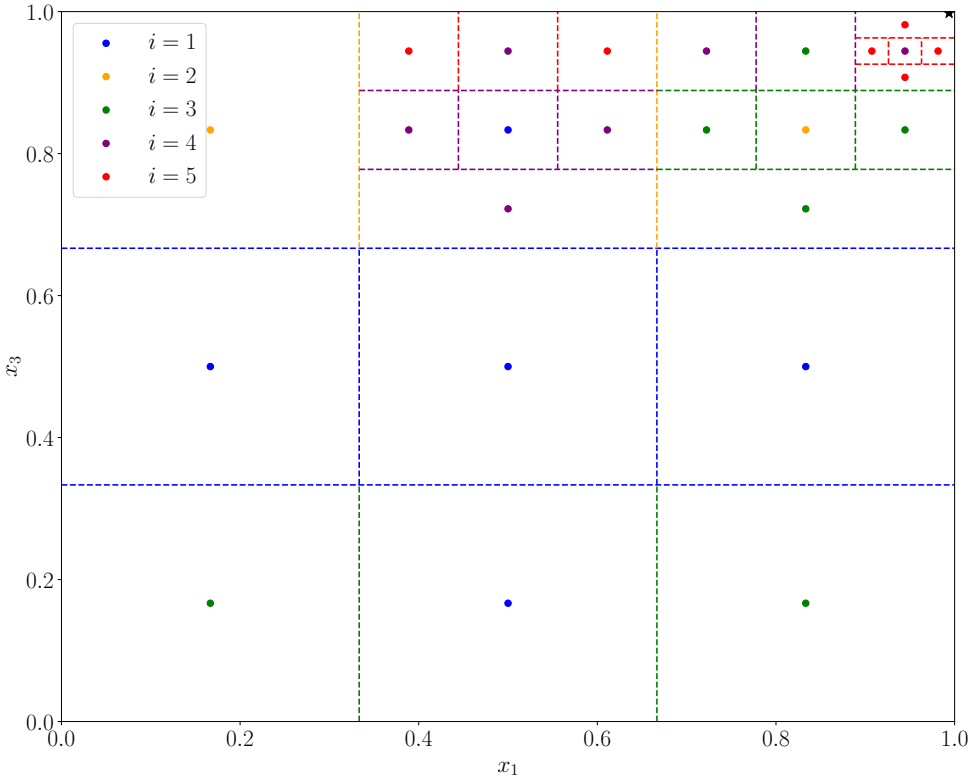

FIGURE B.1: Illustration of the first 5 iterations performed by the DIRECT algorithm on the Ishigami function.

Ishigami function

The use of the DIRECT algorithm for estimating robustness curves w.r.t. a failure probability is now compared with the use of the vertex method and a sampling method based on Latin Hypercube Sampling (LHS) (McKay et al., 2000). First, the following LSF based on the Ishigami function (Ishigami and Homma, 1990) is considered:

$$g(\mathbf{X}) = \sin(X_1) + 7\sin^2(X_2) + 0.1X_3^4\sin(X_1) + 3 \tag{B.2}$$

where $X_1 \sim \mathcal{N}(\theta_1, 1)$, $X_2 \sim \mathcal{N}(\theta_2, 1)$ and $X_3 \sim \mathcal{N}(\theta_3, 1)$. The failure probabilities are estimated with 50×10^3 MC samples. The nominal values of the uncertain means are given as $\widetilde{\boldsymbol{\theta}} = [-1.5, 0.5, 0.5]^\top$. 10 values of the horizon of uncertainty are considered for $h \in [0.1, 1]$. When applying the vertex method, only 8 failure probability evaluations are performed at a given h. Therefore, only 80 (plus the evaluation of the nominal failure probability) total evaluations are needed for estimating the entire robustness curve. The LHS-based method is performed by generating N_{LHS} samples once in the largest uncertainty space, i.e. for $\theta_1 \in [-3, 0]$, $\theta_2 \in [0, 1]$ and $\theta_3 \in [0, 1]$. This unique set of samples is used for estimating the entire robustness curve by selecting the maximum values in each uncertainty space contained in the largest one. In order to be comparable with the LHS-based method, the use of DIRECT is limited by a maximum number N_{OPT} of evaluations for the entire robustness curve. Therefore, each optimization process at a given h is allowed a maximum of $N_{\text{OPT}}/10$ evaluations.

Figure B.2 presents the robustness curves obtained with the three techniques for $N_{\text{LHS}} = N_{\text{OPT}} = 200$ and $N_{\text{LHS}} = N_{\text{OPT}} = 1000$. Except for the lower values of h ($h < 0.3$) for which there are less LHS candidates, the LHS and DIRECT-based methods give comparable curves. The robustness curve obtained using the vertex method coincides with the reference curve up to $h = 0.4$. Then, it progressively underestimates the robusntess. This means that there is at least one uncertain mean for which the maximum failure probabilites are not obtained at an extreme value.

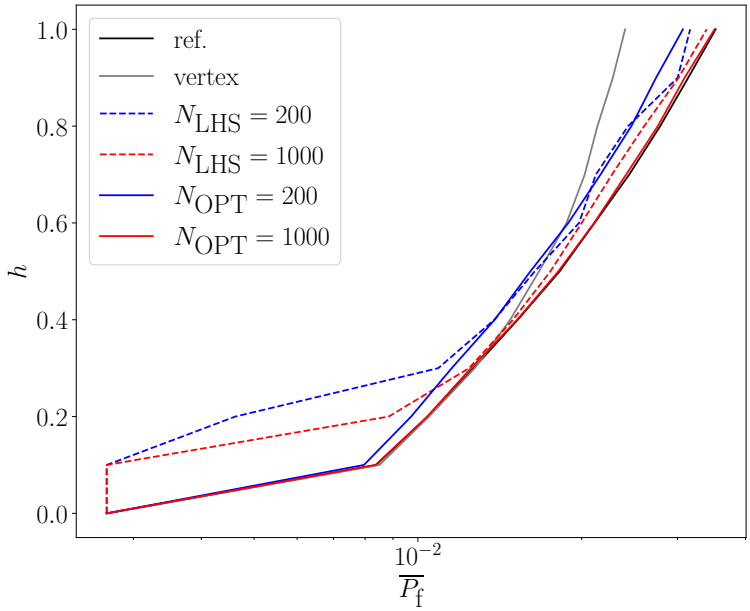

FIGURE B.2: Robustness curves for the Ishigami toy case using the vertex, the LHS-based and the DIRECT-based methods.

Cantilever beam

The same study is performed on the cantilever beam introduced in Chapter 7 considering the LSF based on the maximum Von Mises stress. The failure event is defined as the maximum Von Mises stress exceeding the yield strength set at $\sigma_y = 450$ MPa. The distributions parameters

are given in Table B.1 with $\widetilde{\boldsymbol{\theta}} = [12, 5, 42, 0.3, 0.3, 9]^\top$. The maximum failure probabilities are evaluated at 10 value of $h \in [0, 0.15]$.

TABLE B.1: Input probabilistic modeling of $\mathbf{X}$.

Variable X_i	Distribution	param. 1	param. 2
$X_1 = P$ (kN)	Gumbel	$\beta = \theta_1$	$\gamma = 1.2$
$X_2 = t$ (mm)	Normal	$\mu = \theta_2$	$\sigma = 0.25$
$X_3 = d$ (mm)	Normal	$\mu = \theta_3$	$\sigma = 2.1$
$X_4 = L_1$ (mm)	Uniform	$a = 115$	$b = 125$
$X_5 = L_2$ (mm)	Uniform	$a = 55$	$b = 65$
$X_6 = F_1$ (kN)	Normal	$\mu = 3$	$\sigma = \theta_4$
$X_7 = F_2$ (kN)	Normal	$\mu = 3$	$\sigma = \theta_5$
$X_8 = \theta_1$ (degrees)	Normal	$\mu = 5$	$\sigma = 1$
$X_9 = \theta_2$ (degrees)	Normal	$\mu = 10$	$\sigma = 2$
$X_10 = T$ (N.m)	Normal	$\mu = 90$	$\sigma = \theta_6$

The robustness curves obtained with each technique are given in Figure B.3 for $N_{\text{LHS}} = \{1000, 2000, 6000\}$ and $N_{\text{LHS}} = \{500, 1000, 2000\}$. The vertex method requires this time a total of $64 \times 10 = 640$ evaluations. In this case, using the vertex method yields the same robustness curve as the reference one. The DIRECT-based method performs better overall than the LHS-based method. From a general point of view, increasing the dimension of the uncertainty space affects the performances of the LHS and the DIRECT-based methods. It also increases exponentially the number of evaluations used by the vertex method.

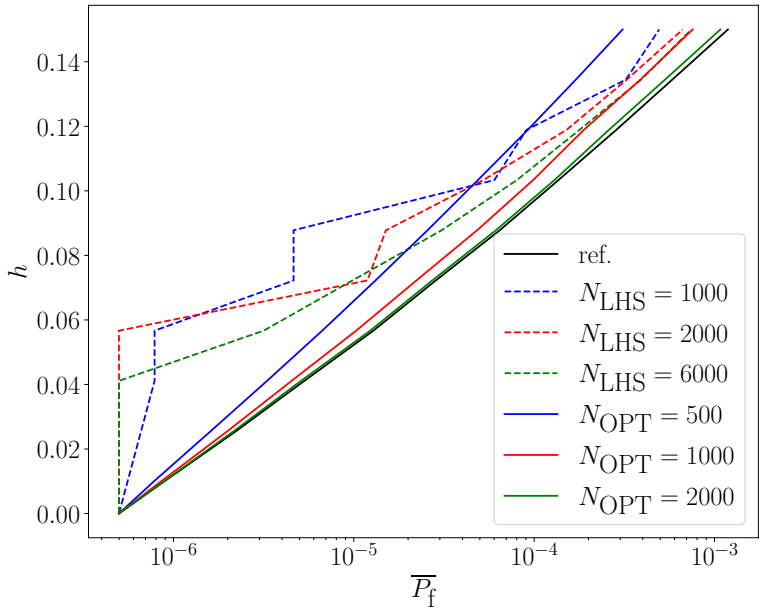

FIGURE B.3: Robustness curves for the cantilever toy case using the vertex, the LHS-based and the DIRECT-based methods.

APPENDIX C

Dependence in hybrid reliability analysis with random set theory

This thesis generally treated hybrid reliability problems by considering independency among and between the precise random variables $\mathbf{X}$ and the epistemic variables $\mathbf{Y}$ (except when considering the parallelepiped convex model). However, the random set framework is compatible with probabilistic dependency. Indeed, by transforming the HRA problem into a standard reliability analysis with unit uniform distributions, copulas are directly applicable for modeling dependency. In Alvarez et al. (2018), Frank and Gaussian copulas are used to model dependency between precise random variables and variables represented with free p-boxes.

However, dependency between random variables and epistemic variables has been much less studied than within the purely probabilistic framework. This appendix aims at providing some preliminary insights into the impact of dependency represented through copulas on the sampled random sets and, consequently, on the robustness.

To do so, the same two-degree-of-freedom damped oscillator introduced in Chapter 5 is considered where Table 5.1 and Table 5.2 recall the characteristics of the random variables and the epistemic variables respectively. The only difference is that dependency is considered between the random variable m_s and the epistemic variable F_s through the use of a normal copula $C\left(\alpha_{m_s}, \alpha_{F_s}, \rho_{m_s F_s}\right)$ where $\rho_{m_s F_s}$ is the coefficient of correlation between m_s and F_s.

First, Figure C.1 presents 1000 sampled random sets obtained when F_s is represented through a possibilistic triangular distribution, a possibilistic trapezoidal distribution and a free p-box composed of normal-based extreme cdfs. The samples are obtained for $\rho_{m_s F_s} = -0.7$ (left) and $\rho_{m_s F_s} = 0.7$ (right). These results are quite intuitive from a numerical point of view. Indeed, a positive coefficient of correlation means that values of α_{m_s} closer to one (respectively closer to zero) will also yield values of α_{F_s} closer to one (respectively closer to zero). Hence, for triangular and trapezoidal distributions, a higher (respectively lower) value of m_s will yield intervals around the nominal value that are narrower (respectively wider). The opposite happens for a negative coefficient of correlation. Considering the p-box representation on F_s, higher values of α_{m_s} will naturally lead to higher quantiles on both extreme cdfs bounding F_s. The interpretation seems less straightforward from a linguistic point of view. A positive coefficient of correlation with possibility distributions would mean that higher (respectively lower) values of m_s enhances (reduces) the confidence that F_s is closer to its nominal value.

Figure C.2 shows how the considered dependence may affect the robustness curve. In contrast to the results presented in Chapter 5, the fact of adding information to the IG uncertainty model does not automatically improve the robustness. However, when considering the possibilistic distributions on F_s, the impact of dependency increases with the horizon of uncertainty and vanishes when h tends to 0 as F_s reduces to its nominal value. When considering the p-box

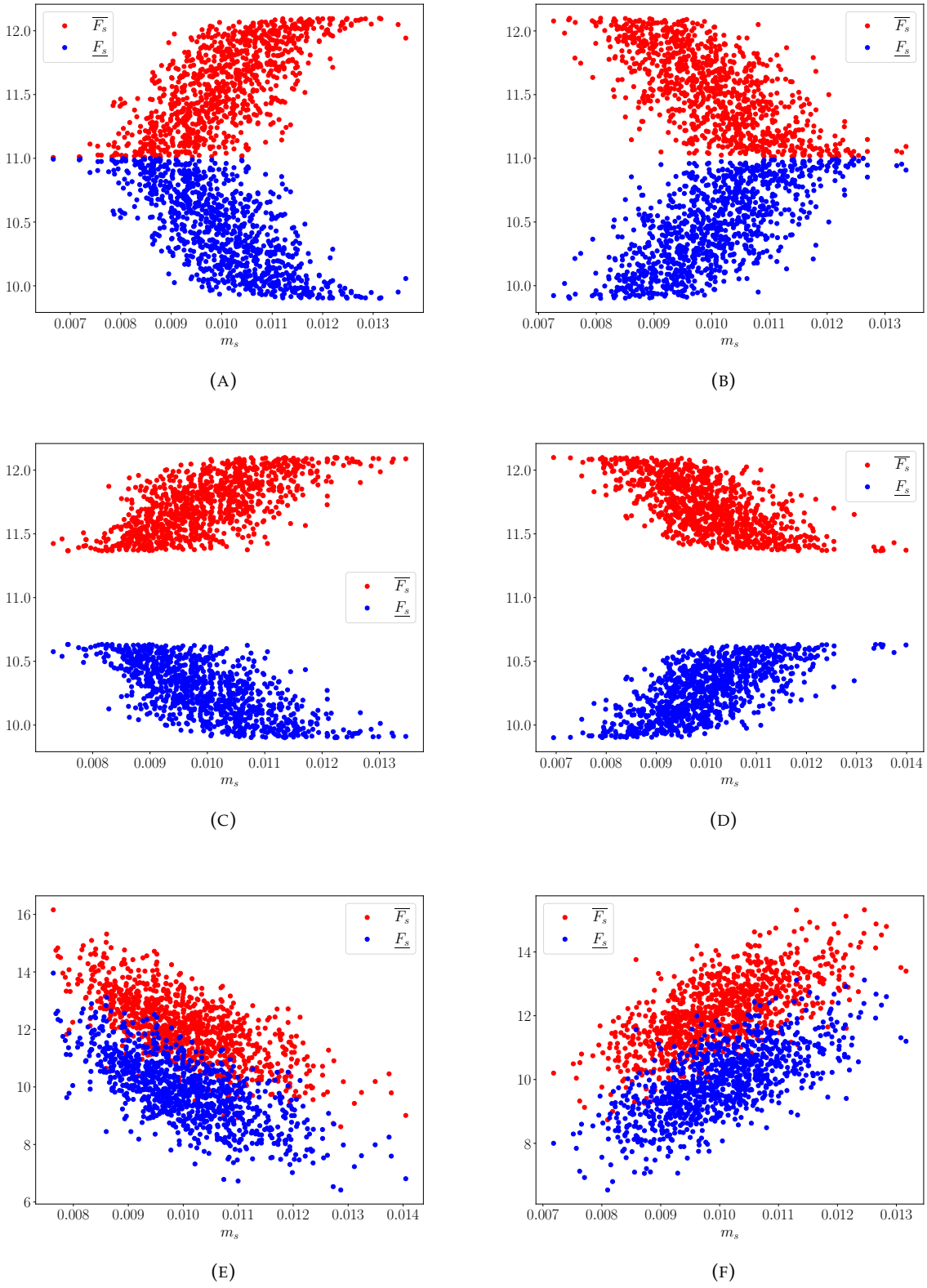

(A) (B)

(C) (D)

(E) (F)

FIGURE C.1: Sampled random sets considering $\rho_{m_s F_s} = -0.7$ (left) and $\rho_{m_s F_s} = 0.7$ (right) with a triangular distribution (top), a trapezoidal distribution (middle) and a p-box representation (bottom).

representation on F_s, the nominal configuration ($h = 0$) represents a unique cdf on F_s. Therefore, the dependency still has an impact even at $h = 0$.

It was shown in Chapter 5, in the context of no dependence, cases where different uncertainty representations are actually equivalent when applying random set theory. In particular, considering a symmetrical triangular possibilistic distribution with support $\left[\underline{Y}, \overline{Y}\right]$ and nominal value $\widetilde{Y}$ is equivalent to considering a p-box built from two uniform distributions in $\left[\underline{Y}, \widetilde{Y}\right]$ and in $\left[\widetilde{Y}, \overline{Y}\right]$. The objective is now to verify, only on the same considered toy case, if dependency affects this equivalence. Figure C.3 compares the sampled random sets obtained from the triangular representation and the uniform-based p-box one. It appears that the lower bounds of the random sets are identical between both representations. This is due to the fact that the upper uniform cdf coincides with the increasing part of the triangular distribution. The upper bounds are different, yet presenting a symmetrical behavior, as it is also the case with no dependence. Therefore, each upper bound has the same probability of occurence wether the triangular or the p-box representations are considered. The only difference is that the corresponding lower bounds are not the same. Hence, as it can be seen from Figure C.4, the robustness curves obtained from both representations also coincidence. Indeed, in this toy case, the lower value of the limit-state function (which leads to the estimation of the upper failure probability) is always obtained at $F_s = \overline{F_s}^{(j)}$ no matter if $F_s \in \left[\underline{F_s}^{\text{Tri},(j)}, \overline{F_s}^{(j)}\right]$ or if $F_s \in \left[\underline{F_s}^{\text{pbox},(j)}, \overline{F_s}^{(j)}\right]$.

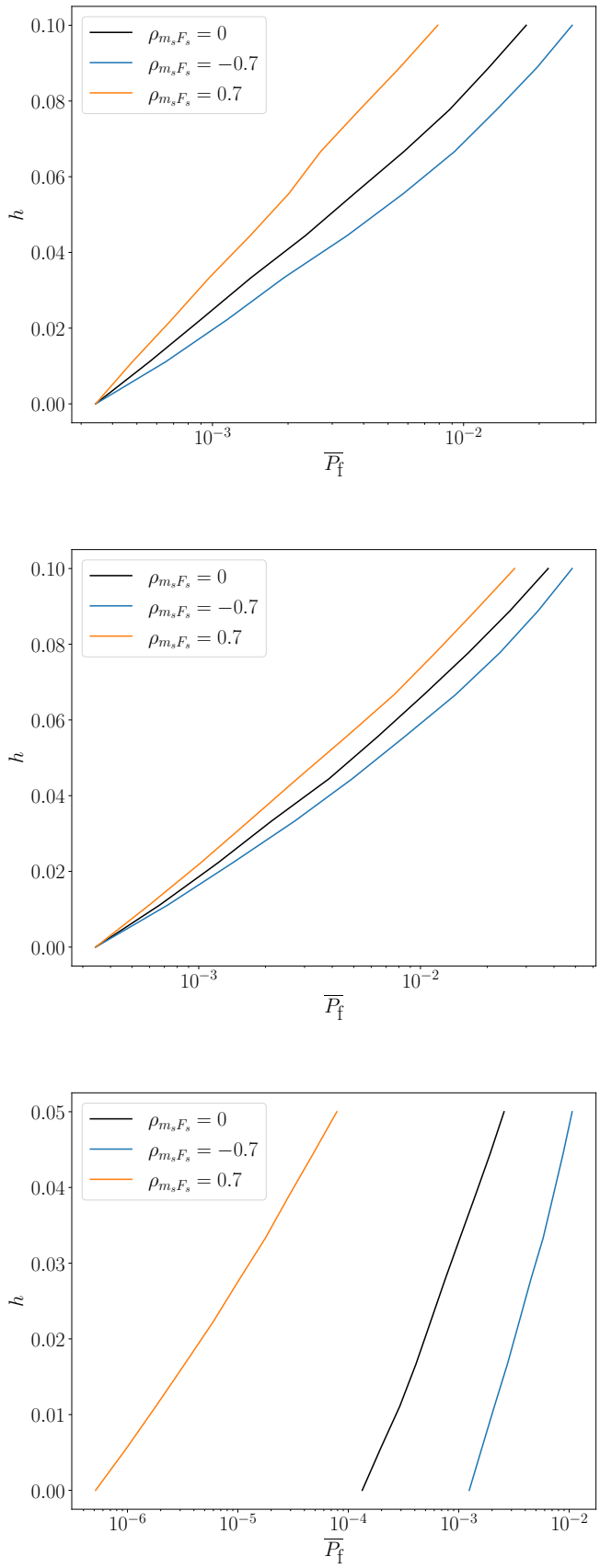

FIGURE C.2: Robustness curves considering dependency with a triangular distribution (top), a trapezoidal distribution (middle) and a p-box representation (bottom).

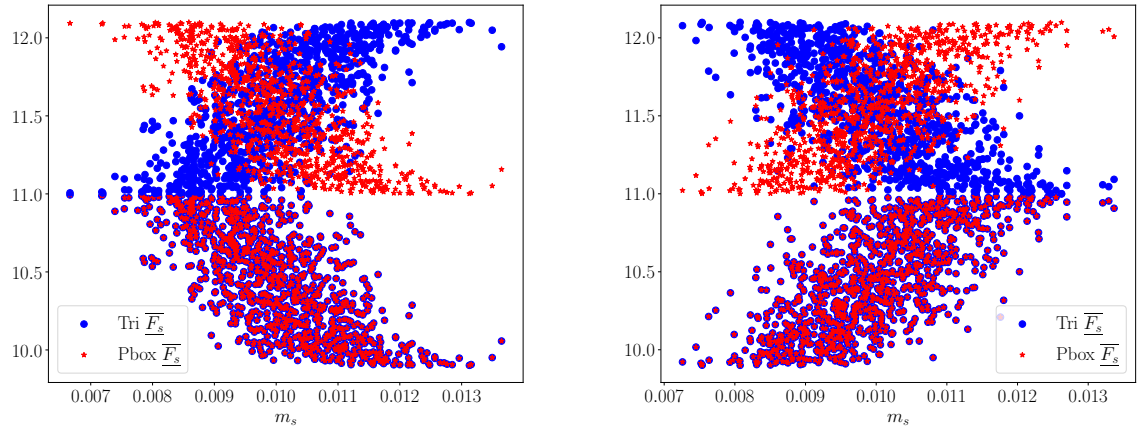

(A) (B)

FIGURE C.3: Sampled random sets considering $\rho_{m_s F_s} = -0.7$ (left) and $\rho_{m_s F_s} = 0.7$ (right) with a triangular distribution and its corresponding p-box representation.

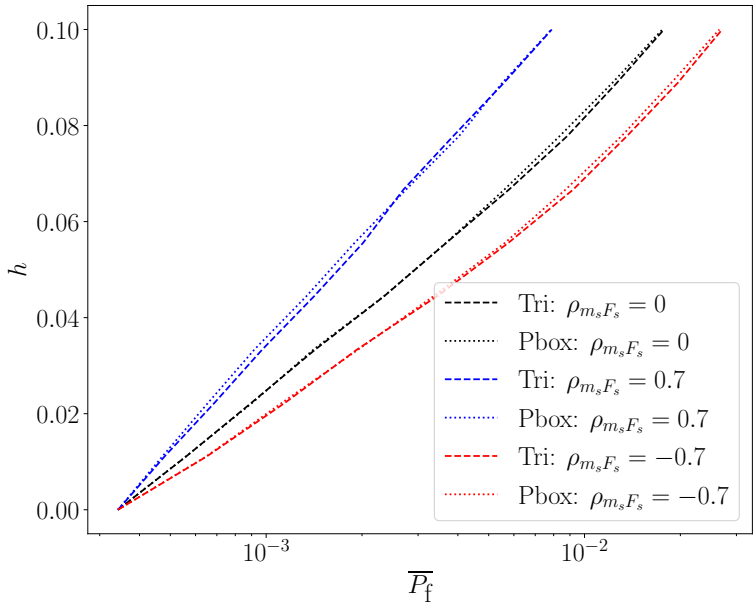

FIGURE C.4: Robustness curves obtained from the triangular distribution and its corresponding p-box representation considering dependency.

APPENDIX D

Multidimensional parallelepiped convex model

This appendix briefly presents the formulations implied in the construction of multidimensional parallelepiped (MP) convex models. The MP convex model was first introduced in Jiang et al. (2014) and then improved in Ni et al. (2016). Figure D.1 illustrates the shape of this type of convex model in two dimensions which results in a parallelogram.

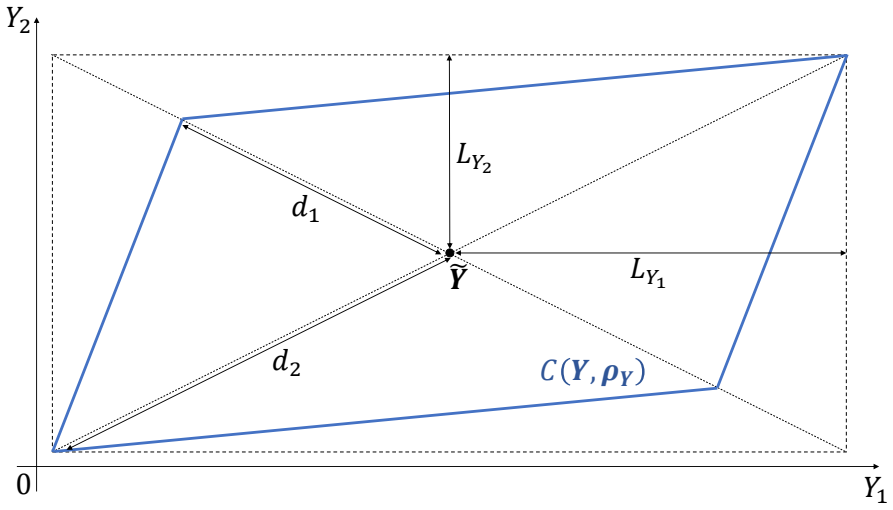

FIGURE D.1: Illustration of two-dimensional parallelepiped convex model.

It is used in Chapter 5 as it has the advantage of representing dependent and independent variables in a joint framework. Moreover, a sample that belongs to this convex set can directly be obtained from a sample $\mathbf{v} = (v_1, \cdots, v_{n_\mathbf{Y}})^\top$ of the hypercube $V = [-1, 1]^{n_\mathbf{Y}}$ with the following transformation:

$$Y_i = \frac{L_{Y_i}}{\sum_{j=1}^{n_\mathbf{Y}} |\boldsymbol{\rho}_{ij}|} \sum_{j=1}^{n_\mathbf{Y}} \rho_{ij} v_j + \widetilde{Y}_i, \; i = 1, 2, ..., n_\mathbf{Y} \tag{D.1}$$

where $\widetilde{Y}_i$ is the center point of the interval, L_{Y_i} is half the width of the interval and $\boldsymbol{\rho}$ is the correlation matrix composed of the coefficients of correlation $\rho_{ij} = \frac{d_2^{(ij)} - d_1^{(ij)}}{d_2^{(ij)} + d_1^{(ij)}}$ where $d_1^{(ij)}$ and $d_2^{(ij)}$ are half the diagonal lengths as depicted in Figure D.1. Figure D.2 shows the impact of the coefficient of correlation on the obtained convex set.

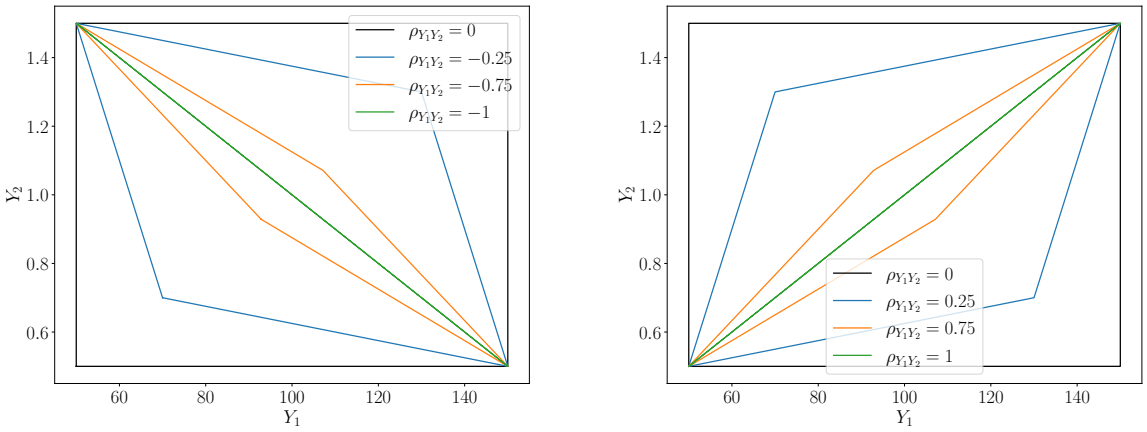

(A) (B)

FIGURE D.2: Two-dimensional parallelepiped convex model for different negative (A) and positive (B) coefficients of correlation.

An example of hybrid representation with random and MP convex variables can be found in Liu and Elishakoff (2020) where bounds on the failure probability are estimated using the importance sampling technique. Indeed, the fact that samples from the MP convex set are obtained direcly by sampling in the bounded hypercube $[-1, 1]^{n_{\mathbf{Y}}}$ without having to define any constraint function makes the optimization process easier.

APPENDIX E

Artificial neural networks architectures

This appendix explains in more details how the artificial neural networks (ANN) used in Chapter 6 were built. The first tuning parameters to be set when constructing ANNs are the number of hidden layers, the corresponding number of neurons and the activation functions to be used. There is no precise rule for assessing the right numbers of hidden layers and neurons. Generally, the higher the input dimension and the complexity of the response behavior, the more hidden layers and neurons are needed. Table E.1 presents the chosen architectures for ANN_1 and ANN_2 which are the same except for the output layer as the output of ANN_1 is a single classification probability ($p_1 \leq 0.5$ means that there is no root and $p_1 > 0.5$ means that are roots) and the output of ANN_2 corresponds to the two predicted roots. The activation functions are also the same with the use of "ReLU" except for the output layer where "sigmoid" is used for generating the classification probability and "linear" is used for the regression problem. Different architectures have not been tested as high performances of both ANNs were quickly achieved.

TABLE E.1: Architectures of ANN_1 and ANN_2.

Layer	Number of neurons		Activation function	
	ANN_1	ANN_2	ANN_1	ANN_2
Input layer	10	10	–	–
Hidden layer 1	64	64	ReLU	ReLU
Hidden layer 2	32	32	ReLU	ReLU
Hidden layer 3	16	16	ReLU	ReLU
Output layer	1	2	sigmoid	linear

The next parameters to define are the ones directly involved for the training process, namely the loss function, the loss function optimizer, the metric used for validation and the number of epochs. The choices made in the present paper are given in Table E.2. Both loss functions "binary crossentropy" and "mean squared error" are the most considered ones for classification and regression problems respectively. The loss optimizer "Adam" is very common in deep learning

TABLE E.2: Training parameters of ANN_1 and ANN_2.

Parameters	ANN_1	ANN_2
Loss function	binary crossentropy	mean squared error
Loss optimizer	Adam	Adam
Validation metric	accuracy	mean squared error
Epochs	50	50

and is known to converge efficiently. The validation metric is used to quantify the quality of the trained ANNs on the validation samples. It is very important as the trained ANNs that are saved are the ones that correspond to the epoch with the best validation metric. "Accuracy" (the proportion of correct classifications) and "mean squared error" are very common for classification and regression purposes respectively. The number of epochs plays an important role on the learning process. Too few epochs might lead to an underfit model which means that the training process did not enable the model to understand well all the features. Conversely, too many epochs might lead to an overfit model which means that it only performs well on the training inputs but not on new inputs. However, there are ways to circumvent this issue. In the present paper, a checkpoint is applied so that the model that is saved is the one that performs best on the validation data. Figure E.1 presents the convergence of the accuracy of ANN_1 and of the loss of ANN_2. The fact that the best configuration of ANN_2 is obtained at the last epoch suggests that more epochs might have improved the metric. However, both metrics are satisfactory.

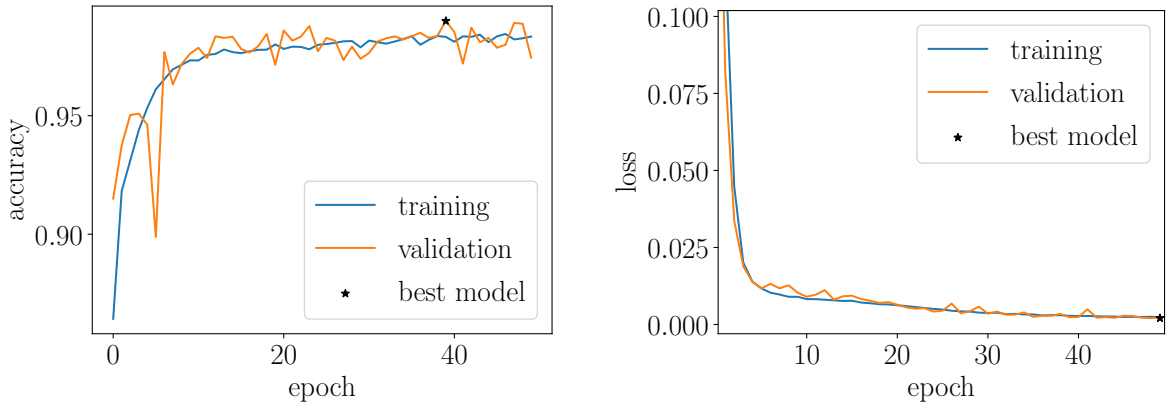

(A) (B)

FIGURE E.1: Evolution of the accuracy of ANN_1 (A) and the loss of ANN_2 (B) on the training and validation samples for $n_{\text{train}} = 3 \times 10^4$.

APPENDIX F

Résumé étendu de la thèse

Contexte

Contexte méthodologique.

Tout produit ou système industriel doit répondre à des critères de performance et de sûreté durant leur cycle complet de fonctionnement. De plus, la demande permanente d'améliorations technologiques et sociétales entraîne la création de systèmes de plus en plus complexes dont il faut maîtriser les risques accrus. La complexité de ces systèmes ainsi que le caractère non simulable de certains scénarios en conditions réelles ont mené au développement de codes de calcul basés sur des modèles physiques et mathématiques et sur des méthodes de résolution numérique. Ces codes de calcul permettent donc de simuler le comportement réel d'un système dans un certain environnement et donc de simuler ses niveaux de performance et de sûreté. Cependant, cette méthodologie fait appel à un certain nombre d'hypothèses de modélisation pour lesquelles la quantité d'information disponible permet rarement leur justification de manière triviale. C'est dans ce contexte que né la notion de prise en compte des incertitudes dans les modèles numériques afin de pouvoir quantifier un niveau de performance et de sûreté satisfaisant.

Le schéma dit ABCC' est souvent utilisé pour décrire le cadre de la prise en compte des incertitudes dans les modèles numériques. Ce schéma se décompose en les étapes suivantes :

- Etape A $\rightarrow$ Spécification du problème : identification des variables d'entrée et de sortie du système, définition d'un code numérique reliant les sorties aux entrées et choix d'une quantité d'intérêt en fonction de l'analyse ;
- Etape B $\rightarrow$ Modélisation des incertitudes : identification des différentes sources d'incertitude et choix du formalisme à adopter pour décrire ces incertitudes ;
- Etape C $\rightarrow$ Propagation des incertitudes : utilisation de techniques spécifiques afin de caractériser l'incertitude sur les variables de sorties à partir de la modèlisation des incertitudes en entrée ;
- Etape C' $\rightarrow$ Analyse inverse : utilisation de l'information sur les sorties du modèles afin d'obtenir de l'information sur les entrées du modèles.

Ce cadre général représente une idéalisation de la réalité nécessaire afin de mener des analyses de sûreté. Par conséquent, les décisions de sûreté qui en découlent se doivent d'être robustes par rapport aux hypothèses fortes de modélisation. C'est dans ce contexte que la méthode info-gap est investiguée. En particulier, il s'agit dans cette thèse d'évaluer la robustesse de quantités

d'intérêt fiabilistes décrivant la sûreté de systèmes critiques face aux hypothèses de modélisation des incertitudes des variables en entrée du code numérique.

Contexte industriel.

Cette thèse a été réalisée sous la forme d'une convention CIFRE en parteneriat avec le Département de Mécanique Appliquée du laboratoire FEMTO-ST (CNRS, Univ. Bourgogne Franche-Comté) et EDF R&D. Cette collaboration représente un example typique du besoin industriel pour une meilleure compréhension et une meilleure maîtrise de l'incertitude pouvant affecter des décisions propres à des systèmes industriels critiques.

Afin de demeurer un leader mondial de la production d'électricité, EDF peut compter sur un panel de systèmes hautement performants et complexes (e.g. centrales nucléaires et hydroélectriques). Ces systèmes industriels introduisent des risques à conséquences humaines, environnementales et économiques potentiellement graves qui se doivent d'être maîtrisés. Par conséquent, leur opérabilité représente une décision à responsabilité sociétale qui requiert des justifications rigoureuses.

La complexité des systèmes étudiés ainsi que la rareté et l'aspect non simulable des scénarios accidentels considérés ont poussé EDF à développer des méthodologies en lien avec le schéma classique du traitement des incertitudes dans les modèles numériques. De ce fait, la représentation probabiliste des incertitudes a progressivement pris place dans le but d'évaluer des quantités fiabilistes qui soient mieux représentatives de l'état de connaissances.

Cependant, les justifications provenant d'analyses probabilistes amènent souvent des préoccupations telles que :

- l'acceptabilité et l'interprétabilité de probabilités faibles mais non nulles ;
- l'utilisation de notions mathématiques plus complexes pour mener et justifier une propagation probabiliste des incertitudes ;
- la justification d'hypothèses probabilistes sur lesquelles l'estimation d'événements rares est très dépendante et pour lesquelles l'information est réduite.

C'est dans ce contexte que se place la motivation industrielle principale de cette thèse. La méthode info-gap (IG) est investiguée et adaptée à des quantitités fiabilistes afin de quantifier leur robustesse vis-à-vis de méconnaissances. En particulier, deux cas réels liés à EDF sont étudiés, à savoir l'étude de fiabilité des conduites forcées et l'étude d'un scénario accidentel de perte de réfrigérant dans le circuit primaire d'un réacteur à eau pressurisée.

Objectifs de la thèse

L'objectif principal de cette thèse est d'apporter des éléments méthodologiques afin de mener et d'interpréter des analyses de robustesse IG appliquées à des quantités fiabilistes dans le but de prendre des décisions sûres. Cet objectif général se décline en les objectifs suivants :

- O1 : Mener des analyses de robustesse confrontées simultanément à plusieurs sources d'incertitude ;
- O2 : Illustrer comment la méthode IG et le contexte d'évaluations fiabilistes peuvent être entremêlés dans le but de prendre des décisions sûres ;
- O3 : Quantifier l'impact du choix de la réprésentation des incertitudes épistémiques sur l'évaluation de la robustesse IG ;

- O4 : Proposer des solutions pour mener une analyse de robustesse IG appliquée à l'évaluation de probabilités de défaillance faibles liées à des domaines de défaillance complexes ;
- O5 : Proposer des solutions pour mener une analyse IG appliquée à l'estimation de quantiles d'ordre élevé issus de modèles numériques coûteux en temps de calcul.

En accord avec les objectifs listés ci-dessus, ce manuscrit est divisé en plusieurs chapitres dont le contenu est résumé dans la section suivante.

Etat de l'art

Chapitre 2 – Fiabilité des structures sous différentes sources d'incertitude.

L'application de la méthode IG à des quantités fiabilistes implique un processus composé de deux boucles imbriquées dont la boucle interne représente l'estimation de la quantité d'intérêt fiabiliste. Etant donc un point central de l'analyse de robustesse et étant potentiellement un problème complexe à résoudre pour des événements rares, ce chapitre vise à définir le contexte propre à la fiabilité des structures et à présenter une partie des différentes techniques d'estimation mises à disposition.

Une étape clé de l'analyse fiabiliste est la modélisation de l'incertitude qui peut prendre différentes formes (Hacking, 1975). En particulier, deux types d'incertitude sont communément dissociés, à savoir l'incertitude aléatoire (variabilité intrinsèque non réductible) et l'incertitude épistémique (liée à un manque de connaissances potentiellement réductible) (Der Kiureghian and Ditlevsen, 2009). Ce contexte a motivé le développement et l'application de plusieurs modélisations de l'incertitude en fonction de l'information considérée. Ce chapitre en présente quelques-unes ainsi que leur intégration dans le contexte de la fiabilité des structures à travers un example illustratif.

Dans un premier temps, les notions mathématiques principales de la fiabilité des structures sont introduites dans le cadre probabiliste, c'est à dire lorsque les grandeurs incertaines sont modélisées par des variables aléatoires. Les définitions de la fonction d'état limite et du domaine de défaillance permettent d'exprimer la quantité fiabiliste principalement étudiée dans cette thèse, à savoir une probabilité de défaillance. Les principales techniques numériques permettant l'estimation de la probabilité de défaillance sont présentées (Morio and Balesdent, 2015). Ces techniques incluent le passage de l'espace physique à l'espace standard, la méthode de Monte-Carlo, les méthodes FORM et SORM, le tirage d'importance, la simulation multi niveaux et le line sampling.

Dans un second temps, des modélisations alternatives (Beer et al., 2013; Zio and Pedroni, 2013) au cadre probabiliste sont décrites, à savoir les modèles convexes, la théorie de l'évidence, la théorie des possibilités et les p-box (probability box) paramétriques et non paramétriques. Un schéma synthétique est proposé permettant de décrire les liens entre ces différentes représentations de l'incertitude.

Chapitre 3 – Cas d'application industriels.

Ce chapitre vise à présenter plus en détail les deux cas d'application industriels qui motivent cette thèse. Le contexte industriel et l'étude fiabiliste propres à chacun d'eux sont donnés. Cela permet notamment d'apporter un cadre réel quant au besoin d'effectuer des analyses de robustesse.

La première application industrielle concerne l'étude de fiabilité des conduites forcées (Bryla et al., 2020; Ardillon et al., 2022) qui acheminent l'eau d'un barrage à une usine hydroélectrique. EDF en opère un grand nombre qui présentent des caractéristiques géométriques et mécaniques

variées. Ces structures vieillissantes subissent une perte d'épaisseur dû au phénomène de corrosion. Par conséquent, leur tenue mécanique se doit d'être justifiée à chaque instant et pour tout type de configuration. En particulier, les modes de défaillance relatifs à l'instabilité plastique et à la rupture en présence de défauts plans sont étudiés. Au modèle mécanique s'ajoute le cadre fiabiliste par la considération de certaines grandeurs physiques par des variables aléatoires. Dès lors, la quantité d'intérêt considérée est la probabilité de défaillance annuelle d'une configuration de conduite forcée que l'on souhaite inférieure à une probabilité de défaillance seuil. L'objectif est alors d'estimer la robustesse IG de cette estimation fiabiliste face aux hypothèses en entrée, notamment les valeurs de certains paramètres des distributions probabilistes. En particulier, la méthode IG permet de comparer la robustesse de différentes conduites forcées à performances nominales proches afin d'analyser si certaines configurations sont plus robustes que d'autres.

La deuxième application industrielle s'intéresse à un scénario accidentel hypothétique de perte de réfrigérant dans le circuit primaire d'un réacteur nucléaire à eau préssurisée causée par la présence d'une brèche. La chute de pression au primaire et la diminution de la quantité d'eau induisent alors une élévation de la température des crayons combustibles. Par conséquent, il est impératif de vérifier que cette température ne dépasse pas une valeur critique synonyme d'endommagement trop important du combustible. Les avancées dans la compréhension des phénomènes physiques en jeu ainsi que l'augmentation de la puissance de calcul informatique ont permis le développement de codes numériques dits de "Best Estimate models" permettant de simuler des transitoires thermohydrauliques. En France, cela a mené au code de calcul CATHARE développé conjointement par le CEA, EDF, Framatome et l'IRSN. Ce code permet donc, entre autres, de simuler le transitoire causé par la perte de réfrigérant afin d'en déduire la température maximale de la gaine du combustible. La disponibilité d'un tel code a alors permis de mettre en place le schéma numérique relatif à la quantification et propagation des incertitudes aléatoires. Cette méthodologie globale est dénomée par "Best Estimate Plus Uncertainty". En particulier, la modélisation probabiliste des paramètres considérés incertains donne lieu à l'estimation d'un quantile élevé (d'ordre 95% dans cette étude) à être comparé avec la température seuil. Cependant, la justification du choix des distributions paramétriques affectées aux variables aléatoires peut être remise en cause, notamment par l'Autorité de Sûreté Nucléaire. C'est ce contexte qui a poussé EDF a mener des analyses de robustesse afin d'évaluer l'impact des hypothèses probabilistes sur l'évaluation fiabiliste. Cette thèse propose d'utiliser la méthode IG afin de quantifier cette robustesse.

Chapitre 4 – Le contexte de robustesse info-gap.

Ce chapitre a pour but de présenter les éléments principaux relatifs au contexte IG (Ben-Haïm, 2006) et notamment son adaptation à des évaluations fiabilistes. Les fonctions qui sont centrales à la méthode sont introduites, à savoir les fonctions de robustesse et d'opportunité. La première permet de quantifier le niveau maximal d'incertitude autour d'une configuration nominale d'un système pour lequel une performance acceptable est garantie. La deuxième quantifie le niveau minimal d'incertitude autour d'une configuration nominale permettant d'espérer une performance particulièrement positive (ces critères de performance acceptable et de performance particulièrement positive sont à définir par l'analyste). Ce niveau d'incertitude, considérée comme épistémique, se traduit par la notion d'horizon d'incertitude qui est un nombre réel positif. Il permet de construire des ensembles convexes imbriqués autour d'une valeur nominale des paramètres considérés incertains. La recherche des performances extrêmes du système dans chacun de ces domaines d'incertitude permet la construction des courbes de robustesse et d'opportunité. Ces courbes permettent alors de classer différentes décisions en fonction de leur robustesse et de leur opportunité. La notion de valeur de l'information définie dans le contexte IG ainsi que certaines critiques addressées à cette méthode sont également discutées.

Ce chapitre permet également de comparer des analyses de robustesse dans différents contextes d'incertitude. En effet, la modularité de la méthode IG offre la possibilité de confronter des hypothèses de nature différente. Ici, les robustesses associées à deux fonctions d'état limite jouet sont évaluées et comparées en considérant l'incertitude épistémique sur :

- les variables d'entrée des fonction d'état limite directement ;
- des paramètres des distributions probabilistes affectées aux variables d'entrée ;
- la forme des distributions probabilistes affectées aux variables d'entrée ;
- la formulation des fonctions état limite (erreur de modèle).

Cette analyse a pour but principal d'illustrer la compatibilité et la pertinence de la méthode IG avec des analyses fiabilistes issues d'un formalisme probabiliste.

Cependant, la mise en relation de ces deux cadres méthodologiques implique un schéma numérique potentiellement challengeant à résoudre sans la considération de certaines hypothèses. Le coût numérique engendré par l'estimation de courbes de robustesse repose particulièrement sur les considérations suivantes :

- la méthode utilisée pour la recherche des performances extrêmes dans chaque ensemble convexe ;
- la performance globale de la technique utilisée pour l'estimation de la quantité d'intérêt fiabiliste (quantile ou probabilité de défaillance) ;
- la possibilité d'utiliser des métamodèles et des techniques à base d'échantillon unique avec un certain niveau de confiance ;
- le nombre d'horizons d'incertitude considéré pour approximer la courbe de robustesse.

Apports méthodologiques et applications

Chapitre 5 – Comparaison de la robustesse info-gap obtenue sous différentes réprésentations de l'incertitude.

Cette thèse se place dans un contexte présentant différentes sources d'incertitude. Par conséquent, différentes représentations de l'incertitude, telles que celles introduites au Chapitre 2, peuvent cohabiter dans une même étude fiabiliste. Il est souvent mention de fiabilité hybride pour décrire ce contexte.

Ce chapitre vise dans un premiers temps à poser le cadre théorique de la fiabilité hybride. Les variables aléatoires sont dissociées des variables épistémiques. Dans ce contexte, la probabilité de défaillance n'est plus unique mais est bornée par une probabilité minimale et une probabilité maximale. La considération simultanée de plusieurs modélisations de l'incertitude rend l'utilisation des techniques classiques d'estimation de probabilité de défaillance non triviale. Par conséquent, la théorie des random sets est appliquée afin d'uniformiser le problème hybride. En effet, cette théorie offre la possibilité de décrire une multitude de réprésentations de l'incertitude (probabiliste et autres) sous un même cadre probabiliste. En particulier, le problème de fiabilité hybride peut alors être ramené à deux problèmes de fiabilité ne considérant que des variables aléatoires probabilistes. Les techniques avancées d'estimation de probabilité de défaillance peuvent alors être employées pour évaluer les bornes de cette probabilité.

L'objectif principal de ce chapitre est d'évaluer l'impact qu'a le choix d'une modélisation de l'incertitude épistémique sur l'analyse de robustesse. Une méthodologie combinant la méthode IG et la modélisation par random sets est proposée dans ce but. Au lieu de ne considérer

que des ensembles convexes, le modèle d'incertitude IG est directement relié à la fonction random set pouvant décrire différentes réprésentations de l'incertitude. En particulier, les fonctions random sets considérées sont celles décrivant les réprésentations par des intervalles, par des ensembles convexes, par des distributions possibilistes, par des p-box et par des distributions probabilistes précises. Cette méthodologie permet notamment d'évaluer à quel point le passage d'une réprésentation de l'incertitude moins informative à une réprésentation plus informative (en passant d'une modélisation intervalle à une distribution possibiliste par exemple) resserre les bornes de la probabilité de défaillance en fonction de l'horizon d'incertitude IG considéré. Pour quantifier cet impact de manière plus précise, une métrique relative à la notion de valeur de l'information est définie.

Cette méthodologie est appliquée sur deux cas jouets ainsi que sur l'étude de fiabilité des conduites forcées. Différents groupes de comparaison sont analysés. Certains groupes permettent d'évaluer l'impact d'un ajout d'information sur les courbes de robustesse et d'opportunité tandis que d'autres permettent d'illustrer certaines équivalences entre différentes réprésentations de l'incertitude.

Chapitre 6 – Algorithmes basés sur la technique du line sampling pour l'évaluation robuste de la fiabilité des conduites forcées.

Ce chapitre développe un schéma méthodologique performant pour l'évaluation de la robustesse appliquée à la fiabilité des conduites forcées. En effet, les difficultés principales liées à cette application proviennent de la rareté des événements de défaillance pour lesquels des probabilités sont estimées ainsi que la particularité géométrique des domaines de défaillance induits. Par conséquent, des techniques avancées offrant un estimateur de la probabilité de défaillance globalement performant en termes de convergence et de temps de calcul sont requises afin d'obtenir des courbes de robustesse précises en un temps raisonnable. Ce chapitre investigue l'utilisation du line sampling dans ce but.

Dans un premier temps, l'étude de robustesse est appliquée au mode de défaillance par instabilité plastique en considérant l'incertitude épistémique à la fois sur des variables d'entrée et sur des paramètres de distribution probabiliste. Le domaine de défaillance associé à ce cas correspond de manière illustrative à une bande. Par conséquent, la technique du line sampling est adaptée du fait que chaque ligne présente deux racines (dont dépend le calcul de la probabilité de défaillance avec cette technique présentée dans le Chapitre 2). La recherche de ces racines n'impliquant qu'un faible nombre d'évaluations des fonctions d'état limite, l'estimateur proposé permet d'obtenir des courbes de robustesse en un temps réduit. De ce fait, il est possible d'estimer des courbes de robustesse pour une multitude de configurations nominales différentes afin d'évaluer si certaines d'entre elles se démarquent malgré des performances nominales proches.

Dans un deuxième temps, le mode de défaillance par rupture conditionnelle au succès d'une épreuve hydraulique est étudié. Ce cas d'étude est plus contraignant d'un point de vue de l'estimation de la probabilité de défaillance pour deux raisons :

- les fonctions d'état limite peuvent présenter des discontinuités ;
- la condition apportée par l'épreuve hydraulique implique un événement de défaillance composé d'une double intersections de trois événements.

L'impact majeur sur l'utilisation du line sampling est que certaines lignes ne présentent aucune racine tandis que d'autres en contiennent toujours deux. Dans ce contexte, trois algorithmes correspondant à trois formulations équivalentes de l'événement de défaillance sont proposés pour résoudre ce problème complexe de recherche de racines. En particulier, l'algorithme à base

de recherches séquentielles des racines permet de limiter le nombre total d'appels aux fonctions d'état limite.

Malgré la bonne performance des algorithmes proposés, la recherche des racines implique un nombre d'appels aux fonctions d'état limite relativement important. Ce nombre devient conséquent lors de l'application de la méthode IG qui requiert l'estimation de plusieurs centaines de probabilités de défaillance. Afin de réduire le nombre total de recherches de racines, une méthodologie à base de réseaux de neurones est adoptée. Un premier réseau de classification est utilisé dans le but de prédire l'existence ou non de racines pour une ligne donnée. Un deuxième réseau de régression prédit les valeurs des deux racines lorsque le premier estime qu'elles existent. Pour que les deux mêmes réseaux soient utilisés durant toute l'analyse IG, leur apprentissage s'effectue dans l'espace augmenté composé de l'espace probabiliste standard et de l'espace épistémique des paramètres de distribution. La méthodologie est appliquée sur un cas jouet représentatif et sur la fiabilité des conduites forcées. Les courbes de robustesse obtenues sont très précises pour un temps de calcul cumulé fortement réduit.

Chapitre 7 – Evaluation robuste d'un scénario accidentel propre à un système thermohydraulique industriel.

Ce chapitre applique la méthode IG sous différentes formes pour évaluer la robustesse des estimations du quantile d'ordre 95% et du superquantile d'ordre 75% de la température maximale de gaine lors d'une perte de réfrigérant au primaire. Bien que ces deux quantités fiabilistes soient en général plus simples à estimer que des probabilités de défaillance très faibles, le temps de calcul unitaire d'une simulation CATHARE d'environ 30 minutes rend l'étude fiabiliste, et donc l'application d'IG, challengeantes. De plus, le modèle considère 27 variables aléatoires représentées par des distributions paramétriques différentes.

Dans un premier temps, deux modèles d'incertitude IG originaux sont proposés. Le premier considère l'incertitude épistémique sur les paramètres de distribution dans l'espace standard. Cela permet une application et une interprétation plus aisées d'un unique horizon d'incertitude sur toutes les variables aléatoires. Le deuxième modèle considère une discrétisation de type Dempster-Shafer de la fonction de répartition nominale de chaque variable aléatoire ce qui permet de perturber la forme de la loi plutôt que ses paramètres. Cette représentation de l'incertitude revient à considérer des p-box non paramétriques et donc nécessite le retour au cadre des random set.

Dans un second temps, deux méthodes numériques sont investiguées afin de substituer le modèle coûteux CATHARE. La première méthode, dénomée Reverse Importance Sampling (RIS) et similaire au tirage d'importance, permet de réestimer le quantile et le superquantile perturbés de manière paramétrique à partir d'un unique jeu de données. Par conséquent, le code CATHARE n'est appelé que pour ce jeu de données et la seule opération à considérer est un ratio de densités qui n'est pas coûteux à évaluer. Pour l'utilisation de cette méthode, 3000 réalisations des variables aléatoires sont générées suivant leur distribution jointe nominale et les températures maximales correspondantes sont évaluées avec CATHARE. La deuxième méthode utilise à nouveau un réseau de neurones afin de simuler le comportement CATHARE. Ce réseau est entraîné à l'aide de 3000 nouvelles réalisations générées en considérant des lois uniformes sur les variables aléatoires dans leur support respectif.

Ces deux méthodes sont donc utilisées et comparées pour générer des courbes de robustesse sur un cas jouet et sur le cas de perte de réfrigérant au primaire. Des résultats comparables sont obtenus pour la robustesse du quantile pour laquelle les deux méthodes identifient le même groupe de variables les plus pénalisantes. Cependant, des écarts apparaissent pour les hauts horizons d'incertitude et quand le nombre de variables épistémiques considérées augmente.

Par contre, les robustesses du superquantile obtenues avec la méthode RIS sont particulièrement chaotiques et difficiles à interpréter. Les courbes obtenues avec l'utilisation du réseau de neurones s'avèrent bien plus stables.

Conclusion générale et perspectives

A travers cette thèse, IG est appliquée de plusieurs manières pour un même objectif : quantifier la robustesse d'évaluations fiabilistes face à certaines hypothèses. Les quantités d'intérêt fiabilistes sont passées d'une probabilité de défaillance très faible à un quantile d'ordre 95% et un superquantile d'ordre 75%. Les modèles d'incertitude IG ont été décrits à la fois par des fonctions random set, des p-box paramétriques dans l'espace physique et dans l'espace standard ainsi que des p-box non paramétriques basés sur une discrétisation de type Dempster-Shafer. Enfin, différentes techniques numériques ont été employées afin de faciliter l'application d'IG à des quantités fiabilistes. Des réseaux de neurones artificiels sont utilisés soit pour remplacer directement le code de simulation soit pour remplacer une étape intermédiaire durant l'estimation d'une probabilité de défaillance. Des méthodes de réestimation sont également considérées avec le "Weighted Importance Sampling" et le "Reverse Importance Sampling". Ce panel de concepts mathématiques montre la modularité du cadre IG ainsi que la dépendance de son implémentation avec le cas d'étude considéré. De plus, l'expansion constante offerte par la littérature de la boite à outils numériques couvrant divers domaines scientifiques rend l'application d'IG de moins en moins contraignante.

Finalement, les perspectives suivantes sont adressées :

- le placement d'IG par rapport à d'autres métriques ;
- la prise en compte d'une structure de dépendance dans les entrées ;
- l'application d'IG à des erreurs de modèles ;
- la contribution de l'analyse de sensibilité pour évaluer des courbes de robustesse ;
- l'utilisation de méthodes numériques adaptives ;
- l'extension d'IG à des mesures de robustesse moins conservatives.

Publications et communications

Les contributions présentées dans ce manuscrit ont donné lieu aux publications suivantes :

Jour. Pap. A. Ajenjo, E. Ardillon, V. Chabridon, B. Iooss, S. Cogan and E. Sadoulet-Reboul (2022). "An info-gap framework for robustness assessment of epistemic uncertainty models in hybrid structural reliability analysis". In: *Structural Safety* 96, pp. 102196.

A. Ajenjo, E. Ardillon, V. Chabridon, S. Cogan and E. Sadoulet-Reboul (2022). "Robustness evaluation of the reliability of penstocks combining line sampling and neural networks". *Preprint*.

Int. Conf. A. Ajenjo, E. Ardillon, V. Chabridon, S. Cogan and E. Sadoulet-Reboul (2021). "Info-gap robustness evaluation of a line-sampling-based reliability assessment of penstocks". In: *Proc. of the 13th International Conference on Structural Safety and Reliability (ICOSSAR 2021)*, Shanghai, China. (+Talk)

A. Ajenjo, E. Ardillon, V. Chabridon, S. Cogan and E. Sadoulet-Reboul (2021). "Robustness Evaluation of Reliability Assessments of Pensotcks Using Info-Gap Method". In: *Proc. of the 30th European Safety and Reliability Conference and the 15th Probabilistic Safety Assessment and Management Conference (ESREL 2020 PSAM 15)*, Venice, Italy. (+Talk)

A. Ajenjo, E. Ardillon, V. Chabridon, S. Cogan and E. Sadoulet-Reboul (2021). "An info-gap framework for comparing epistemic uncertainty models in hybrid structural reliability analysis". In: *Proc. of the 12th International Symposium on Imprecise Probability: Theories and Applications (ISIPTA 2021)*, Granada, Spain. (+Talk)

Nat. Conf. A. Ajenjo, E. Ardillon, V. Chabridon, S. Cogan and E. Sadoulet-Reboul (2022). "Application de la méthode info-gap aux analyses de fiabilité des conduites forcées". In: *11èmes Journées Fiabilité des Matériaux et des Structures (JFMS 2022)*, Clermont Ferrand, France. (+Talk)

A. Ajenjo, E. Ardillon, V. Chabridon, S. Cogan and E. Sadoulet-Reboul (2021). "Adapted line sampling and neural networks for evaluating the info-gap robustness of reliability estimates for penstocks". In: *MASCOT-NUM 2022*, Clermont Ferrand, France. (+Poster)

Résumé

Les systèmes de production d'électricité tels que les centrales nucléaires et hydroélectriques représentent des exemples typiques de systèmes complexes pour lesquels un haut niveau de sûreté est attendu. Ces évaluations de sûreté impliquent généralement l'utilisation de modèles numériques permettant de simuler le comportement du système étudié dans des conditions opérationnelles particulières. Cependant, ce contexte représente une idéalisation de la réalité confrontée à la présence de plusieurs sources d'incertitude généralement divisées en deux catégories : l'incertitude aléatoire (liée à une variabilité naturelle de certains phénomènes) et l'incertitude épistémique (liée à un manque de connaissance). Par conséquent, la quantification des incertitudes à travers les modèles numériques représente un intérêt grandissant dans la communauté scientifique dans le but d'évaluer la fiabilité d'un système. En particulier, des techniques de propagation de l'incertitude aléatoire permettent d'évaluer des quantités fiabilistes telles que des probabilités de défaillance faibles et des quantiles d'ordre élevé sur lesquelles des décisions liées à la sûreté sont justifiées. Cependant, ces évaluations impliquent généralement des hypothèses liées à un manque d'information qui est caractéristique des systèmes complexes et des événements rares. Dans ce contexte, il est impératif de considérer ces hypothèses dans la décision prise. Dans cette thèse, cela est fait en considérant le cadre info-gap permettant d'évaluer la robustesse d'estimations fiabilistes face à l'incertitude épistémique.

La méthode info-gap quantifie la notion de robustesse en évaluant le niveau maximal d'incertitude épistémique pour lequel le système garantit toujours une performance acceptable. Dans cette thèse, la méthode est appliquée à deux cas industriels : l'étude de fiabilité des conduites forcées et un scénario nucléaire accidentel lié à une perte de réfrigérant dans le circuit primaire. Dans un premier temps, les cadres méthodologiques et numériques associés à l'application d'info-gap sur des quantités fiabilistes sont présentés. Le contexte de fiabilité hybride est traité. En particulier, l'utilisation de la théorie des random sets permet d'évaluer l'impact de différentes représentations de l'incertitude sur l'évaluation de la robustesse. Dans un second temps, des méthodologies numériques dédiées, telles qu'une adaptation séquentielle du line sampling ou l'utilisation de réseaux de neurones artificiels, sont proposées afin d'appliquer efficacement la méthode info-gap aux deux cas industriels. Les solutions proposées apportent des arguments sur la compatibilité du cadre info-gap avec le cadre fiabiliste dans le but de prendre des décisions sûres.

Abstract

Power generation facilities such as nuclear and hydroelectric power plants are typical examples of complex industrial systems for which high safety standards must be met. These safety assessments generally rely on the use of computer models that simulate the real behavior of the studied system under specific operational conditions. However, this framework represents an idealization of reality as it faces various sources of uncertainty that are commonly separated into aleatory uncertainty (due to natural variability of physical phenomena) and epistemic uncertainty (due to lack of knowledge). As a consequence, uncertainty quantification in computer models gained much consideration over the past decades in order to evaluate the reliability of a system. In particular, techniques considering the propagation of aleatory uncertainty enable to evaluate risk-oriented quantities of interest such as low failure probabilities or high-order quantiles on which safety-related decisions are justified. However, these evaluations incorporate assumptions as, in practice, information is limited especially when considering complex systems and rare events. Therefore, it is crucial to address these assumptions. In this thesis, it is done by considering the info-gap framework in order to evaluate the robustness of reliability estimations to epistemic uncertainty.

The info-gap framework quantifies the notion of robustness by evaluating the highest level of epistemic uncertainty for which the system still guarantees an acceptable performance. In this thesis, it is applied to two real industrial cases, namely the reliability assessment of penstocks and the risk assessment of a nuclear accident related to a loss-of-coolant scenario. First, the methodological and numerical frameworks associated to the application of info-gap to reliability assessments are described. The context of hybrid reliability analysis is addressed. In particular, the use of random set theory enables to evaluate the impact of different uncertainty representations on the robustness evaluation. Secondly, dedicated numerical methodologies, such as a sequential line sampling technique and artificial neural networks, are proposed in order to efficiently apply the info-gap framework to both industrial cases. The proposed solutions bring insights on the compatibility of the info-gap framework with reliability estimates in order to take safe decions.